Thesis for the degree
Doctor of Philosophy

Submitted to the Scientific Council of the
Weizmann Institute of Science
Rehovot, Israel

עבודת גמר (תזה) לתואר
דוקטור לפילוסופיה

מוגשת למועצה המדעית של
מכון ויצמן למדע
רחובות, ישראל

By
Rei Chemke

מאת
רעי צ׳מקה

התלות המרדיונליות של טורבלנציה גאוסטרופית באטמוספירה
The latitudinal dependence of geostrophic turbulence in the atmosphere

Advisor:
Yohai Kaspi

מנחה:
יוחאי כספי

March 2017

אדר ה׳תשע״ז

Acknowledgements

First and foremost I would like to thank my advisor, Yohai Kaspi, who has equipped me with tools that allowed me to grow as a scientist. His scientific intuition and unique way of thinking enabled me to understand the importance of asking the right questions, and attacking problems from all different angles in simple and comprehensive ways. Concomitantly, through his devoted approach toward students, Yohai has taught me the invaluable importance of educating younger generations of scientists. By placing my academic career at the top of his priorities, Yohai has increased my eagerness in science, which I also hope to pass on to future scientists.

I would also like to acknowledge my colleagues here at Weizmann, Yani Yuval, Guy Dagan, Tom Dror, Morgan O'Neill, Eli Galanti, Marzia Parisi, Talia Tamarin and Hilla Afargan, who patiently taught me the proper way to conduct research, as well as helped me better understand the physics behind the general circulation of the atmosphere.

I hereby declare that this thesis summarizes my own independent research.

Abstract

The study of atmospheric and oceanic eddies is important for understanding the dynamics of the general circulation of the atmosphere and ocean and the governing scales within. Extant theories for the behavior of these eddies, such as geostrophic turbulence, rely on the theoretical work of two-dimensional turbulence. The latitudinal variations of the mean state (e.g., sphericity, temperature, wind, etc.) adds an additional complexity to geostrophic turbulence theory. In this thesis I studied the behavior of the eddies' energy cycle in both atmosphere and ocean as a function of latitude using both idealized GCM simulations and atmospheric and oceanic reanalysis data. The energy fluxes (i.e., eddy-mean and eddy-eddy interactions) and macroturbulent scales are found to show different behavior poleward and equatorward of a "supercriticality latitude". Poleward of this latitude, where the quasi-geostrophic flow is supercritical to baroclinic instability, a classic geostrophic turbulence picture appears with a barotropization of the flow together with an inverse energy cascade up to the Rhines scale. Equatorward of this latitude, the eddy-mean flow interactions play a major role in the balance. The effect of the nonlinear eddy-eddy interactions on the mean flow is further studied by comparing a set of full and quasi-linear idealized simulations. These interactions are found to have a minor effect on the jet scale, which thus coincides with the Rhines scale even when these interactions are absent. The eddy-eddy interactions are not a prerequisite for jet formation in the atmosphere, and even suppress their formation at high latitudes. For a global warming scenario the eddy flow is found be dominated by eddy-mean flow interactions and have a more baroclinic nature.

In the second part of the thesis we shift our focus to the dynamic-thermodynamic effects of atmospheric mass on atmospheric circulation. The many recently discovered terrestrial exoplanets as well as early Earth are expected to hold a wide range of atmospheric masses. In this study, high atmospheric mass planets are found to be more habitable due to both their higher surface temperature, and weaker meridional temperature gradient, which allows higher temperature at high latitudes, that may help to maintain liquid water on their surface. These changes are found to be related to the reduction of the convective fluxes and net radiative cooling. Changes in the temperature gradients are found to weaken and contract both the tropical (Hadley) and extratropical mean circulations.

תקציר

המחקר של הפרעות באטמוספירה ובאוקיינוס הוא חשוב להבנת הדינמיקה של הסירקולציה הגלובלית באטמוספרה ובאוקיינוס והסקלות השולטות בהן. תאוריות קיימות המתארות את ההתנהגות של ההפרעות האלו, כמו טורבלנציה גאוסטרופית, מתבססות על המחקר התאורטי של טורבלנציה דו ממדית. השינויים עם קו הרוחב של הזרימה הממוצעת (לדוגמה, הכדוריות, טמפרטורה, רוחות, וכדומה) מוסיפים סיבוכיות נוספת לתאוריית הטורבלנציה הגאוסטרופית. בתזה זו חקרתי את התנהגות מעגל האנרגיה של ההפרעות באטמוספרה ובאוקיינוס כפונקציה של קו רוחב בעזרת מודל אידאלי של הסירקולציה הגלובלית ותצפיות מהאטמוספרה ומהאוקיינוס. שטפי האנרגיה (אינטראקציות בין ההפרעות לזרימה הממוצעת ואינטרקציות בין ההפרעות לבין עצמן) והסקלות המקרו-טורבלנטיות הראו התנהגות שונה מעל ומתחת "קו רוחב סופרקריטי". מעל קו רוחב זה, איפה שהזרימה הקאוזי-גאוסטרופית היא סופר-קריטית לאי יציבות ברקולינית, נמצאה תמונה קלסית של טורבלנציה גאוסטרופית הכוללת ברוטרופיזציה של הזרימה יחד עם העברת אנרגיה לסקלות גדולות עד לסקלת ריינס. מתחת לקו רוחב זה, האינטראקציות בין הזרימה הממוצעת להפרעות משחקות תפקיד חשוב במאזן האנרגיה. על ידי השוואה בין סימולציות מלאות וקאוזי-לינאריות, חקרנו לעומק את ההשפעה של האינטראקציות הלא לינאריות בין ההפרעות לבין עצמן על הזרימה הממוצעת. האינטראקציות האלו נמצאו להשפיע רק בצורה מינורית על רוחב זרמי הסילון, ולכן עולה בקנה אחד עם סקלת ריינס גם כאשר האינטראקציות האלו חסרות. האינטראקציות בין ההפרעות לבין עצמן אינן תנאי מקדים להיווצרות זרמי סילון באטמוספרה, ואפילו מדכאות את ההיווצרות שלהם בקווי רוחב גבוהים. העלייה הצפויה של הטמפרטורות בעשורים הבאים נמצאה לשנות את מעגל האנרגיה של ההפרעות באטמוספרה ע"י חיזוק המבנה הברוקליני שלה והאינטרקציות בין הזרימה הממוצעת להפרעות.

בחלק השני של התזה חקרנו את ההשפעות הדינמיות-תרמודינמיות של מסת האטמוספירה על הסירקולציה באטמוספרה. המספר הרב של כוכבי לכת מחוץ למערכת השמש שהתגלה לאחרונה בנוסף לכדור הארץ הקדום, מכילים מנעד רחב של מסות אטמוספריות. במחקר הזה, כוכבי לכת עם מסה אטמוספרית כבדה נמצאו להיות בעלי פוטנציאל גבוה יותר להכיל חיים בשל טמפרטורת הקרקע היותר גבוהה שלהם וההפרש טמפרטורה הקטן יותר בין המשווה לקוטב, שמאפשר טמפרטורות גבוהות יותר בקווי רוחב גבוהים יותר, שיחד יכולות לאפשר להכיל מים בקרקע. השינויים הללו בשדה הטמפרטורה נגרמו בשל ההיחלשות של השטפים הקונבקטיבים ושל הקירור הקרינתי. השינויים בגרדיאנט הטמפרטורה גרמו להחלשה וכיווץ של הסירקולציה הממוצעת בטרופים ובחוץ-טרופים.

Contents

List of Abbreviations

Acronym	Definition
GCM	General Circulation Model
PE	Primitive Equation
QG	Quasi-Geostrophic
EKE	Eddy Kinetic Energy
QL	Quasi-Linear
NCEP	National Centers for Environmental Prediction
ECCO	Estimating the Circulation and Climate of the Ocean
NH	Northern Hemisphere
SH	Southern Hemisphere
PV	Potential Vorticity
WKBJ	Wentzel–Kramers–Brillouin-Jeffreys
CO_2	Carbon Dioxide
HH	Held and Hou (1980)
H00	Held (2000)
EP flux	Eliassen–Palm flux
MAPE	Mean Available Potential Energy
EAPE	Eddy Available Potential Energy
MKE	Mean Kinetic Energy

Chapter 1

Introduction

1.1 Geostrophic turbulence

One of the most robust phenomena in geophysical fluid dynamics is the emergence of jets. These jets have a large impact on the dynamics of the atmosphere and ocean mostly through eddy-mean flow interactions, and appear in both terrestrial and gas planets (e.g., Williams, 1978; Panetta, 1993; Schneider, 2006). Due to their strong dependence on temperature gradients and heat fluxes in the atmosphere, these jets shape and feed-off the zonal climatic bands on Earth. Furthermore, the wave patterns of these jets directly affect storm track variability (Blackmon, 1976; Blackmon et al., 1977).

In the atmosphere, large scale eddies (departures from zonal mean) play a major role in the meridional distribution of heat and momentum (Held, 1975; Held and Hoskins, 1985; Schneider, 2006). These eddies are mostly generated by baroclinic instability at midlatitudes, and decay barotropically, where they transfer barotropic kinetic energy to the zonal mean flow (Simmons and Hoskins, 1978; Lee and Kim, 2003). This sustains the more barotropic nature of the eddy-driven jet at midlatitudes, in contrast to the more baroclinic nature of the subtropical jet (Vallis, 2006). Studying the barotropization of the flow is thus essential for fully understanding midlatitude dynamics.

The study of large scale eddies within the framework of two-dimensional turbulence, is key for understanding atmospheric and oceanic turbulent flow (macroturbulence), and the mechanisms controlling jet dynamics. Even though baroclinic processes, involving vortex stretching, are one of the most important energy sources in the ocean and atmosphere (Eady, 1949; Simmons and Hoskins, 1978; Ferrari and Wunsch, 2009), Charney (1971) suggested that flow properties of geostrophic turbulence in the atmosphere and ocean resemble that of two-dimensional turbulence. Two prominent features of two-dimensional turbulence are the inverse energy cascade and forward enstrophy cascade (Fjortoft, 1953). These features have a clear signature in the energy spectrum, following a $k^{-5/3}$ and a k^{-3} spectral slope in the inverse energy cascade and forward enstrophy cascade regimes, respectively (Kraichnan, 1967). As energy cascades to larger scales it cannot keep accumulating, thus, a large scale dissipation process, such as bottom drag, is required (e.g., Rivera and Wu, 2000; Scott, 2001; Smith and Vallis, 2002; Danilov and Gurarie, 2002; Grianik et al., 2004; Vallis, 2006; Tsang and Young, 2009).

The Rhines–Salmon phenomenology (Rhines, 1977; Salmon, 1978) incorporated the behavior of two-dimensional turbulence in the energy cycle of geostrophic turbulence. While the baroclinic flow (i.e., the depth-dependent part of the flow) behaves as a passive tracer, advected by the barotropic flow (i.e., the depth-independent part of the flow), once barotropization occurs, the barotropic flow behaves as in two-dimensional turbulence, with an inverse energy cascade and a forward enstrophy cascade. The barotropization of the flow occurs at the Rossby deformation radius (Salmon, 1978; Smith and Vallis, 2001),

$$L_d = \frac{1}{|f|\pi} \int_0^H N dz, \tag{1.1}$$

where f is the Coriolis parameter, H is the column fluid depth and $N^2 = \frac{g}{\theta}\frac{\partial \theta}{\partial z}$ is the static stability, where g is gravity and θ is the potential temperature. Under baroclinic instability, the Rossby deformation radius follows the most unstable scale that linear f-plane theory predicts (Eady, 1949). As long as friction does not play a major role in the balance (Danilov and Gurarie, 2002), the inverse energy cascade in the barotropic mode is halted at the Rhines scale (Rhines, 1975),

$$L_\beta = \left(\frac{2U_{\rm rms}}{\beta}\right)^{0.5}, \tag{1.2}$$

where $U_{\rm rms}$ is the root mean square velocity and β is the meridional derivative of the Coriolis parameter. At this scale the turbulent regime changes to a Rossby wave regime (Rhines, 1975). Thus, in the presence of an inverse energy cascade, the Rhines and energy-containing scales should coincide (Holloway and Hendershott, 1977; Vallis and Maltrud, 1993; Held and Larichev, 1996; Danilov and Gurarie, 2000). Nonetheless, the inverse energy cascade continues up to the zero zonal wavenumber and formation of zonal jets occurs (e.g., Rhines, 1977; Williams, 1978; Rhines, 1994), with a meridional wavenumber following the Rhines scale (Rhines, 1975; Vallis and Maltrud, 1993; Panetta, 1993; Lee, 2005; Kaspi and Flierl, 2007; O'Gorman and Schneider, 2008c). When the ratio (scale separation) between the Rhines scale and the Rossby deformation radius, which follows the QG supercriticality (Held and Larichev, 1996),

$$S_c = \frac{f^2 u_z}{\beta H N^2}, \tag{1.3}$$

where u_z is the vertical shear of the zonal flow, is greater than one, eddy-eddy interactions are dominant and an inverse energy cascade occurs. Interestingly, in both QG models (Larichev and Held, 1995), the Rossby deformation radius was not found to coincide with the conversion scale of baroclinic to barotropic kinetic energy.

The lack of a clear scale separation between the Rhines scale and the deformation radius, and the fact that an inverse energy cascade, associated with two-dimensional turbulence, is not observed in the atmosphere (e.g., Baer, 1972; Boer and Shepherd, 1983; Nastrom and Gage, 1985), have raised questions regarding the significance of eddy-eddy interactions (Panetta, 1993; Schneider and Walker, 2006; Farrell and Ioannou, 2007; O'Gorman and Schneider, 2007; Constantinou et al., 2014; Marston, 2012; Srinivasan and Young, 2012; Bakas and Ioannou, 2014).

In the absence of such scale separation (supercriticality is equal or smaller than one), the eddy-eddy interactions should be negligible in the balance, implying that the Rossby deformation radius should follow the energy-containing wavenumber (Schneider and Walker, 2006; O'Gorman and Schneider, 2008c; Merlis and Schneider, 2009) and the width of the jet (Schneider and Walker, 2006). This implies on the major role of eddy-mean interactions in maintaining the jets (Shepherd, 1987b; Huang and Robinson, 1998; Farrell and Ioannou, 2007), and in adding energy at large scales through a shear-induced spectral transfer (e.g., Shepherd, 1987b; Huang and Robinson, 1998). Indeed, several studies showed that the spectral slope of the kinetic energy and the energy-containing wavenumber remain the same in simulations without eddy-eddy interactions (O'Gorman and Schneider, 2007; Chai and Vallis, 2014), as well as the meridional structure of the jets (Tobias et al., 2011; Constantinou et al., 2014; Marston, 2012; Srinivasan and Young, 2012; Tobias and Marston, 2013; Bakas and Ioannou, 2014).

On the other hand, other studies have shown that the supercriticality could vary above one (Zurita-Gotor, 2008; Jansen and Ferrari, 2012, 2013; Chai and Vallis, 2014). Thus, nonlinear eddy-eddy interactions become important (Zurita-Gotor and Vallis, 2009; Jansen and Ferrari, 2012; Chai and Vallis, 2014), and the energy-containing wavenumber coincides with the Rhines scale (Jansen and Ferrari, 2012; Chai and Vallis, 2014). At large supercriticality the energy-containing wavenumber does not correlate between simulations with and without eddy-eddy interactions (Chai and Vallis, 2014). Moreover, several studies observed an increase in the number of jets (the meridional energy-containing wavenumber) as the eddy-eddy interactions were removed (O'Gorman and Schneider, 2007; Chai and Vallis, 2014; Ait-Chaalal and Schneider, 2015).

Previous work that studied the behavior of the barotropic mode either used simplified models, which did not take into account the full vertical structure of the atmosphere (e.g, baroclinic processes), or did not consider the latitudinal dependence of the macroturbulent scale (e.g., the baroclinic conversion and energy-containing scales). Thus, here I examine the understanding of the energy cycle in the barotropic mode as a function of latitude, using an idealized General Circulation Model (GCM) and the available high resolution data assimilation for the atmosphere and ocean, which provide a sophisticated framework that contains all the necessary ingredients of the atmospheric and oceanic physics in the problem. Furthermore, as the important macroturbulent scales and energy fluxes in the barotropic energy cycle depend on the thermal structure of the atmosphere (Held and Larichev, 1996), studying the energy cycle in different climates provides better understanding of its behavior, with relevance for both past and future climates.

1.2 Atmospheric mass

The vast ongoing discovery of terrestrial exoplanets and the variety of atmospheric formation sources may lead to a wide range of atmospheric masses in these planets (Adams et al., 2008; Elkins-Tanton and Seager, 2008). The atmospheric composition is determined by both internal

processes (e.g., tectonic degassing, hydrodynamic and thermal escape of light gases, photosynthesis, silicate weathering, nitrification-dentirification, etc.), and external sources (e.g., nebular gases, asteroids and comets impacts, etc.)(Kasting and Catling, 2003; Seager, 2013). Even in our Solar System, atmospheric mass varies by orders of magnitude among the different planets. For example, while Venus' atmospheric mass is 92 times heavier than Earth's, Mars's atmospheric mass is much lighter, being only 0.006 bar.

Atmospheric mass not only varies among different planets, but also the same planets may be subject to changes in their surface pressure during their evolution. For example, while several studies have argued that high concentrations of N_2 may have resulted in a heavier atmosphere in early Earth's history (during the late Archean, $\sim$ 3 billion years ago) up to 10 times its present-day value (Goldblatt et al., 2009; Johnson and Goldblatt, 2015; Kavanagh and Goldblatt, 2015), others have argued that Earth's atmospheric mass was half as light as present-day value (Som et al., 2012; Marty et al., 2013; Som et al., 2016).

Atmospheric mass shields the surface from extreme shortwave radiation, enables heat transport from warm to cold regions, and through the greenhouse effect enables liquid water to be kept at the planet's surface (Forget and Pierrehumbert, 1997; Selsis et al., 2007; Seager, 2013). Thus, different atmospheric masses may result in various atmospheric thermodynamic and dynamic properties of the flow (Kaspi and Showman, 2015; Chemke et al., 2016b), which affect the planet's habitability (Charnay et al., 2013; Wolf and Toon, 2014; Chemke et al., 2016b). For example, it has been suggested that even low insolation terrestrial exoplanets (e.g., GJ581d, which discovered around the local red dwarf Gliese 581) may sustain liquid water on their surface under high atmospheric mass (i.e., high concentrations of greenhouse gases, von Paris et al., 2010; Wordsworth et al., 2010; Kaltenegger et al., 2011; Wordsworth et al., 2011).

As atmospheric mass plays a crucial role in affecting the planet's habitability, and may differ from planet to planet both in and out of our Solar System, and even during their history (Nishizawa et al., 2007; Goldblatt et al., 2009; Som et al., 2012; Marty et al., 2013; Johnson and Goldblatt, 2015; Kavanagh and Goldblatt, 2015; Som et al., 2016), this study aims to better understand the physics behind the different flow regimes under a range of atmospheric masses.

Among the different planetary parameters that may vary from planet to planet, atmospheric mass was found to increase the surface temperature (e.g., Charnay et al., 2013; Wolf and Toon, 2014; Kaspi and Showman, 2015; Chemke et al., 2016b). This warming has been related to three processes: (i) An increase in atmospheric mass results in pressure broadening of the absorption lines of greenhouse gases, which was found to overcome the increase in molecular (Rayleigh) scattering with atmospheric mass (Goldblatt et al., 2009; Wolf and Toon, 2014). (ii) Higher surface pressure results in a less stable moist adiabatic lapse rate. As the moist adiabatic lapse rate approaches the dry adiabatic lapse rate, the convective fluxes weaken, and thus leaving more heat at the surface (Goldblatt et al., 2009; Charnay et al., 2013).

In a series of simulations, Kaspi and Showman (2015) showed that the atmospheric mass not only modulates the surface temperature, but also affects the strength of the atmospheric circulation. As the atmospheric mass increases, the mean zonal wind decreases together with

the eddy momentum flux convergence, while the mean meridional mass transfer increases. Here, to better understand the dynamics in atmospheres with different masses, and further study the simulations of Kaspi and Showman (2015), we use a three-dimensional idealized GCM. As this model does not take into account processes that are less relevant for the effects of atmospheric mass on its dynamics (e.g., aerosols, chemical reactions, the diurnal and seasonal cycles), its idealization enables us not only to simulate the overall dynamics, but also to isolate the vertical and meridional dynamical and thermodynamical features of the atmosphere, under different atmospheric masses.

Chapter 2

Methods

2.1 Idealized global circulation model

The main toll of my thesis was an idealized aquaplanet moist general circulation model (GCM), based on the GFDL flexible modeling system (FMS). This is a 3D spherical coordinate primitive equation (PE) model of an ideal-gas atmosphere set at perpetual equinox similar to Frierson et al. (2006) and O'Gorman and Schneider (2008b). The lower boundary of the model is an ocean slab with no topography. The model does not contain a representation for ocean dynamics (heat transport, etc.), thus, the surface temperature only changes due to heat transport between the ocean slab and the lower layer of the atmosphere through radiative, sensible and latent heat fluxes. The parameterization of the surface fluxes (sensible heat, latent heat and water vapor) and the boundary layer are based on the Monin-Obukhov similarity theory. The model contains a constant latitudinal distribution of solar radiation at the top of the atmosphere and a standard two-stream gray radiation scheme for long wave radiation (Held, 1982; Goody and Yung, 1995), with optical depths that are only a function of latitude and pressure (Frierson et al., 2006).

The advantage of using an idealized GCM over a simpler model (e.g., radiative-convective model), is that the former solves the six nonlinear coupled primitive equations of the atmosphere; three momentum equations, thermodynamic equation, continuity equation and ideal gas equation. Hence, the idealized GCM provides a full description of the dynamical structure of the atmosphere. On the other hand, a full GCM, which includes chemistry, clouds, ocean circulation, land properties etc., could better mimic the atmosphere's processes, however, it will only increase the numbers of variables which affect the dynamics. Thus, it will limit my ability to isolate the basic physics which contribute the most to the dynamical processes in the atmosphere. In addition, as mentioned earlier the main advantage of this work over previous studies is the ability to use a PE model in high resolution (30 vertical sigma layers, horizontal resolution of $0.7^\circ \times 0.7^\circ$ and 6 hours temporal resolution). This provides me the privilege to observe the latitudinal variations in the atmosphere circulation and in particular, the latitudinal behavior of the important spectral fluxes and macroturbulent scale.

2.1.1 Multiple jets

In order to study the latitudinal behavior of the barotropic mode and its macroturbulent scales, we carried out a set of experiments where we systematically increased the planetary rotation rate up to 16 times Earth's rotation rate. This allows both separating the eddy-driven jet from the subtropical jet and to examine multiple jet regimes. Planets with higher rotation rates exhibit multiple zonal jets due to eddy length scales becoming smaller as rotation rate is increased (Williams and Holloway, 1982; Vallis and Maltrud, 1993; Cho and Polvani, 1996; Navarra and Boccaletti, 2002; Walker and Schneider, 2006; Kaspi and Schneider, 2011). Concomitantly, as the rotation rate of a planet is increased, the Hadley cell becomes narrower and less intense, resulting in more equatorward and weaker subtropical jets (e.g., Held and Hou 1980; Walker and Schneider 2006). Purely eddy-driven jets, which are distinct from the subtropical jets, form in our simulations only at rotation rates faster than Earth's rotation rate. In this study, we use the variation of rotation rate as a method of varying the eddy length scale. Alternatively, we could have varied the planetary radius or thermal Rossby number (e.g., Mitchell and Vallis, 2010), but for demonstrating the latitudinal dependence of the barotropic mode we find that varying only the rotation rate captures its behavior most clearly.

2.1.2 Climate change

In order to produce a range of climates, where the barotropic energy cycle is studied, the longwave optical thickness is increased, following O'Gorman and Schneider (2008a), representing an increase of greenhouse gases. The longwave radiation in the idealized GCM is represented using a standard two-stream gray radiation scheme, with a parameterized optical depth (Held, 1982; Goody and Yung, 1995),

$$\tau = \alpha \left[f_1 \sigma + (1 - f_1)\, \sigma^4 \right] \left[\tau_e + (\tau_p - \tau_e) \sin^2 \varphi \right], \tag{2.1}$$

where $f_1 = 0.1$, the linear and quartic terms approximate the linear decreasing of a well mixed longwave absorber (such as carbon dioxide) with pressure and the atmospheric structure of water vapor (due to the 0.25 scale height ratio of water vapor and pressure), respectively. $\tau_e = 8.4$ and $\tau_p = 2.2$ are the surface longwave optical depths at the equator and pole, respectively, and φ is latitude. Following O'Gorman and Schneider (2008b,a), α is the parameter that is varied between 0.4 and 4 (0.4, 0.5, 0.6, 0.7, 0.8, 0.9, 1.0, 1.2, 1.4 1.6, 2.0, 2.5, 3.0 3.5 4.0), to produce a range of 15 climates with global surface temperature that varies between 272 K and 306 K (272 K, 276 K, 279 K, 281 K, 284 K, 285 K, 287 K, 290 K, 292 K, 294 K, 298 K, 301 K, 303 K, 305 K, 306 K). As in O'Gorman and Schneider (2008b,a), $\alpha = 1$ represents Earth's present-day climate with global surface temperature of 287 K, equator to pole temperature difference of 40 K at the surface, subtropical jets and the edge of the Hadley cells at 26° and eddy-driven jets at 40°.

2.1.3 Quasi-linear simulations

In order to examine the effect of the nonlinear eddy-eddy interactions on macroturbulent scales, we remove these interactions from the momentum and temperature equations (O'Gorman and Schneider, 2007). We refer to these simulations as the quasi-linear (QL) simulations, and to the simulations with eddy-eddy interactions as the full simulations. The zonal mean temperature and momentum equations are similar in the QL and full simulations, as they both contain all the eddy-mean flow interactions (e.g., triad interactions involving the zero zonal wavenumber with another zonal wavenumber and its complex conjugate), including the contributions of the mean eddy fluxes (e.g., $\overline{v'\frac{\partial u'}{\partial y}}$, where u and v are the zonal and meridional velocities, and the bar and prime denote zonal mean and deviation from this mean, respectively). However, the eddy equations differ in the full and QL simulations as the purely eddy interactions (e.g., $\left(v'\frac{\partial u'}{\partial y}\right)'$, which involve triad interactions among three different zonal wavenumbers) are removed in the QL simulations. In this way, the spectrum is built only through eddy-mean interactions.

2.1.4 Atmospheric mass

The atmospheric mass per unit area can be calculated using the hydrostatic balance (Hartmann, 1994), as $dm = \frac{p_s}{g}$, where p_s is the surface pressure and g is the gravitational acceleration. For studying the effects of the atmospheric mass on its circulation a series of simulations are conducted using an idealized GCM, where the surface pressure is varied between 0.5 bar to 100 bar (0.5, 1, 3, 5, 7, 10, 15, 20, 30, 50, 100) while the gravitational acceleration is kept constant ($g = 9.81$), similar to Kaspi and Showman (2015). Alternatively, varying the gravitational acceleration (different mean density of the solid plant) and keeping the surface pressure constant would also enable studying the effects of atmospheric mass.

The model's temperature tendency equation is given by

$$\frac{\partial T}{\partial t} = -\mathbf{u}\cdot\nabla T + Q_{\text{adiab}} + Q_{\text{conv}} + Q_{\text{cond}} + Q_{\text{rad}} + Q_{\text{surf}}, \tag{2.2}$$

where T is the temperature field, $\mathbf{u}$ is the three dimensional velocity vector, the adiabatic heating is $Q_{\text{adiab}} = \frac{\kappa T\omega}{p}$, where ω is the vertical velocity in pressure coordinates and $\kappa = R_d/C_p$, with $R_d = 287\,\text{J}\,\text{kg}^{-1}\,\text{K}^{-1}$ and $C_p = 1004\,\text{J}\,\text{kg}^{-1}\,\text{K}^{-1}$ are the gas constant of dry air and the specific heat of air, respectively. Latent heat release per unit mass is calculated through convection (Q_{conv}) and condensation (Q_{cond}) processes, respectively (Betts, 1986; Betts and Miller, 1986). The convection scheme relaxes the water vapor towards a profile of 70% relative humidity relative to the moist adiabatic lapse rate. The condensation scheme prevents the specific humidity from exceeding saturation by precipitating the condensed water vapor (Frierson et al., 2006). Vapor saturation is calculated using the Clausius–Clapeyron relation. The heating due to solar and longwave radiation (Q_{rad}) is calculated as,

$$\text{Q}_{\text{rad}} = \frac{1}{\text{C}_\text{p}}\frac{d(\text{Q}_\text{s} - \text{Q}_\text{l})}{d\text{m}}, \tag{2.3}$$

where Q_s and Q_l are the net solar and longwave fluxes, respectively. Heat exchange between the slab ocean and the lowest atmospheric level, through diffusive and heat fluxes, are calculated in Q_{surf}.

2.2 Observations

2.2.1 Atmosphere

Since this research covers a wide range of planetary parameters using the above idealized GCM, an important tool for confirming any theoretical conclusion is by comparison to reanalysis data. The NCEP Reanalysis 2 data (Kanamitsu et al., 2002) provided by the NOAA/OAR/ESRL PSD, and available at `http://www.esrl.noaa.gov/psd/`, is a state-of-the-art analysis, which produces winds, temperature and geopotential fields with 17 vertical pressure levels, 6 h temporal and $2.5° \times 2.5°$ horizontal resolutions. I was able to look at long term averages on Earth and eventually support our GCM's conclusions.

2.2.2 Ocean

The Cube92 version of The ECCO2 state estimate averaged every 3 days (`ftp://ecco2.jpl.nasa.gov/data1/cube/cube92/lat_lon/quart_90S_90N/`) provides flow velocity, potential temperature and salinity of the ocean. The ECCO2 synthesizes a high-resolution global-ocean ($0.25° \times 0.25°$ with 50 vertical layers of thicknesses varying from 10 m at the top to approximately 450 m at the bottom) and sea-ice configuration of the MIT ocean GCM (Marshall et al., 1997), with the available satellite (sea surface temperature and height) and in-situ (vertical profiles of temperature and salinity) data. The primitive equations for the ocean are solved on a cube-sphere grid projection (Adcroft et al., 2004) with bathymetry (Menemenlis et al., 2008). A Green function method is used to minimize the misfits between the GCM and observations (Menemenlis et al., 2005). The solution of the governing equations is constrained to observations by adjusting several control parameters based on the model-data misfit. The partial-cell formulation (Adcroft et al., 1997) is used to account for the discontinuity of the bathymatery.

2.3 The zonal spectral barotropic EKE budget

In several of the chapters it was necessary to compute the zonal spectral barotropic EKE budget for each latitude. A similar latitudinal analysis was done by Saltzman (1957) only for the EKE. Unlike previous studies which investigated the spectral EKE equation using two-dimensional spectra (e.g., Lambert, 1984; Koshyk and Hamilton, 2001; Jansen and Ferrari, 2012; Chai and

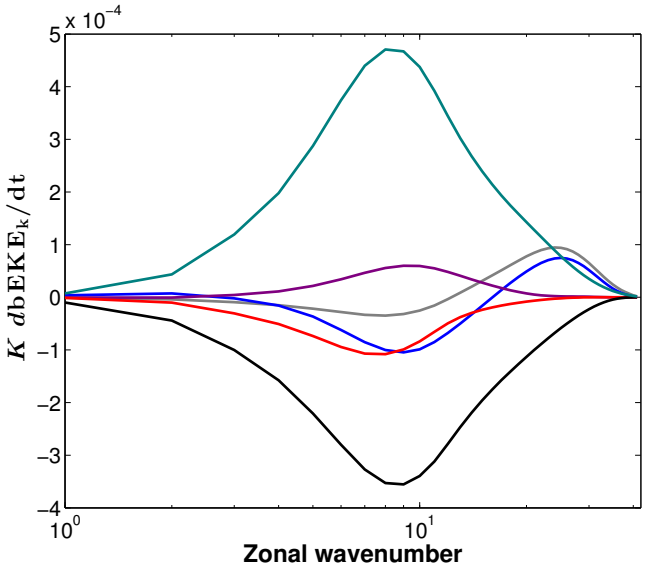

Figure 2.1: The components of the barotropic EKE equation (m^2s^{-3}) summed over all latitudes as a function of zonal wavenumber for present-day simulation. conversion of baroclinic EKE (turquoise); conversion of barotropic eddy available potential energy (purple); eddy-mean flow interactions (red); eddy-eddy interactions (blue); barotropic EKE loss by diffusion (black); the sum of all components (gray).

Vallis, 2014), here we compute the one-dimensional Fourier spectra of the barotropic EKE for each latitude. The zonal spectral barotropic EKE budget is computed as follows,

$$\frac{1}{2}\frac{\partial \mathrm{bEKE}}{\partial t} = EE + EM + P + CT + F \tag{2.4}$$

where

$$\mathrm{bEKE}_k = \left\langle |[u]'_k|^2 + |[v]'_k|^2 \right\rangle \tag{2.5}$$

is the zonal spectral barotropic EKE, u and v are the zonal and meridional velocities, respectively, angle brackets denote a time mean, squared brackets denote a vertical average, and prime denotes the deviation from zonal mean (after taking the vertical average). The subscript k denotes the zonal spectral components with a zonal wavenumber k. The terms on the right hand side of Eq. 2.4 are as follows,

$$EE = \Bigg\langle \mathrm{Re}\Bigg\{ -[u]'^{*}_k \Big(\big([\mathbf{u}]' \cdot \nabla [u]'\big)_k - \big(\frac{[u]'[v]' \tan\varphi}{a}\big)_k \Big) - [v]'^{*}_k \Big(\big([\mathbf{u}]' \cdot \nabla [v]'\big)_k + \big(\frac{[u]'[u]' \tan\varphi}{a}\big)_k \Big) \Bigg\} \Bigg\rangle, \tag{2.6}$$

contains the nonlinear eddy-eddy interactions,

$$EM = \Big\langle \mathrm{Re}\Big\{ -[u]_k'^{*}\Big(\big(\overline{[\mathbf{u}]}\cdot\nabla[u]'\big)_k + \big([\mathbf{u}]'\cdot\nabla\overline{[u]}\big)_k - \big(\frac{\overline{[u]}[v]'\tan\theta}{a}\big)_k - \big(\frac{[u]'\overline{[v]}\tan\varphi}{a}\big)_k\Big) - [v]_k'^{*}\Big(\big(\overline{[\mathbf{u}]}\cdot\nabla[v]'\big)_k + \big([\mathbf{u}]'\cdot\nabla\overline{[v]}\big)_k + 2\big(\frac{\overline{[u]}[u]'\tan\varphi}{a}\big)_k\Big)\Big\}\Big\rangle, \quad (2.7)$$

contains the eddy-mean interactions,

$$P = \Big\langle \mathrm{Re}\Big\{ -[\mathbf{u_H}]_k'^{*}\Big(\big(\nabla_H[\phi]'\big)_{\mathbf{k}} + \big(\frac{R[T]}{p_s}\nabla_H p_s\big)_k'\Big)\Big\}\Big\rangle, \quad (2.8)$$

contains the conversion of barotropic eddy potential energy to barotropic EKE,

$$CT = \Big\langle \mathrm{Re}\Big\{ -[u]_k'^{*}\Big(\big[\mathbf{u}^+\cdot\nabla u^+\big]_k' - \big[\frac{u^+v^+\tan\varphi}{a}\big]_k'\Big) - [v]_k'^{*}\Big(\big[\mathbf{u}^+\cdot\nabla v^+\big]_k' + \big[\frac{u^+u^+\tan\varphi}{a}\big]_k'\Big)\Big\}\Big\rangle, \quad (2.9)$$

contains the conversion of baroclinic EKE to barotropic EKE, and F contains the friction and diffusion terms, where $\mathbf{u}$ denotes the three dimensional velocity vector, φ is latitude, * denotes a complex conjugate, the overbar denotes a zonal mean, the subscript H denotes a horizontal vector, ϕ is geopotential, T is temperature, p_s is the surface pressure, R is the specific gas constant, a is Earth's radius and $^+$ denotes deviation from vertical average. The term of conversion of barotropic eddy potential energy (Eq. 2.8) is different than the usual term presented by Lorenz (1955), as here we do not integrate over the entire domain, but rather keep our analysis as a function of latitude. Thus, as we do not add the continuity equation we manage to keep the conversion term of barotropic eddy potential energy as simple as possible. In addition, as the model is in σ coordinates, the gradient of the surface pressure is added to the conversion of barotropic eddy potential energy term.

As the spectral analysis is conducted in zonal wavenumber space, Eqs. 2.6-2.9 hold both the energy transfers in the zonal direction, and the lateral transport between different latitudes. In addition, studying the energy transfers in the zonal direction enables both observing their latitudinal variations, as well as the important zonal macroturbulent scales. Note that due to the isotropization of the flow by eddy-eddy interactions (Shepherd, 1987b; Chemke and Kaspi, 2016a), an inverse energy cascade towards smaller zonal wavenumbers is accompanied by an inverse energy cascade towards smaller total wavenumbers. In a statistical steady state the sum over all latitudes and zonal wavenumbers of the right-hand side of Eq. 2.4 vanishes (Fig. 2.1) .

2.3.1 Eddy scales

The energy-containing zonal wavenumber is calculated from the zonal spectrum of the barotropic eddy meridional velocity, similar to O'Gorman and Schneider (2008c),

$$k_e^2 = \frac{\sum_k |[v]'_k|^2}{\sum_k k^{-2} |[v]'_k|^2}. \tag{2.10}$$

As in O'Gorman and Schneider (2008c), we find that using the squared zonal wavenumber in the denominator provides the energy-containing zonal wavenumber to be closest to the peak of the zonal spectrum of the barotropic eddy meridional velocity. The length scale of k_e is calculated for each latitude as,

$$L_e = \frac{2\pi a \cos(\varphi)}{k_e}. \tag{2.11}$$

The coincidence of the length scale of the energy-containing zonal wavenumber (Eq. 2.11) and the jet scale (Fig. 3.18) supports our choice of the power of k in Eq. 2.10. The Rhines scale and Rossby deformation radius are converted to zonal wavenumbers using Eq. 2.11. The conversion wavenumber of baroclinic to barotropic EKE is calculated as the centroid of Eq. 2.9,

$$k_{CT} = \frac{\sum_k kCT}{\sum_k CT}. \tag{2.12}$$

This method produces wavenumber closest to the peak of the conversion of baroclinic to barotropic EKE (Fig. 3.19a).

The Rhines wavelength is calculated as,

$$\lambda_\beta = 2\pi L_\beta, \tag{2.13}$$

where $L_\beta = \frac{\mathrm{EKE}^{0.25}}{\beta^{0.5}}$ is the Rhines scale (Scott and Wang, 2005; O'Gorman and Schneider, 2008c; Abernathey and Wortham, 2015), where EKE is the vertically averaged eddy kinetic energy. The Rossby deformation wavelength is calculated as,

$$\lambda_d = 2\pi L_d, \tag{2.14}$$

where L_d is the Rossby deformation (Eq. 1.1). Their corresponding zonal wavenumbers are calculated using Eq. 2.11.

Chapter 3

Geostrophic turbulence

3.1 Poleward migration of eddy-driven jets

On Earth, due to the relatively large typical eddy length scale compared to the size of the planet, the eddy driven jet usually is partially merged with the subtropical jet and captures a significant part of the baroclinic zone. As a result, and due to the seasonal variations, it is difficult to identify any mechanism of poleward migration, resulting in both previous observational and modeling studies using various filtering methods in order to identify these migrating anomalies (Feldstein, 1998; Lee et al., 2007). Here, in order to isolate only the eddy driven jets and to examine multiple jet regimes (where jet migration is more pronounced), we study a series of simulations where we vary the rotation rate of the planet. This allows both separating the eddy driven jet from the subtropical jet, and studying the dependence of the poleward migration on the rotation rate of the planet, which turns out to be important for understanding the poleward migration. Planets with higher rotation rates exhibit multiple zonal jets due to eddy length scales becoming smaller as rotation rate is increased (Williams and Holloway, 1982; Vallis and Maltrud, 1993; Cho and Polvani, 1996; Navarra and Boccaletti, 2002; Walker and Schneider, 2006; Kaspi and Schneider, 2011). Concomitantly, as the rotation rate of a planet is increased, the Hadley cell becomes narrower and less intense, resulting in more equatorward and weaker subtropical jets (e.g., Held and Hou 1980; Walker and Schneider 2006). Purely eddy driven jets, which are distinct from the subtropical jets, form in our simulations only at rotation rates faster than Earth's rotation rate.

In this study we use the variation of rotation rate as a method of varying the eddy length scale. Alternatively, we could have varied the planetary radius or thermal Rossby number (e.g., Mitchell and Vallis, 2010), but for demonstrating the jet migration we find that varying only the rotation rate captures this mechanism most clearly. Experimenting with fast rotation rates and thus a regime of multi-eddy driven jets, enables the quantitative study of the poleward migration of these jets. We carry out a set of experiments using an idealized global circulation model where we systematically increase the planetary rotation rate up to 16 times Earth's rotation rate (Ω_e) (Sec. 2.1.1). Each simulation has 30 vertical sigma layers at T170 horizontal resolution ($0.7° \times 0.7°$). Simulation results presented here have a 6 hour temporal resolution (model time step is 150 seconds), and have been zonally and vertically averaged, in addition

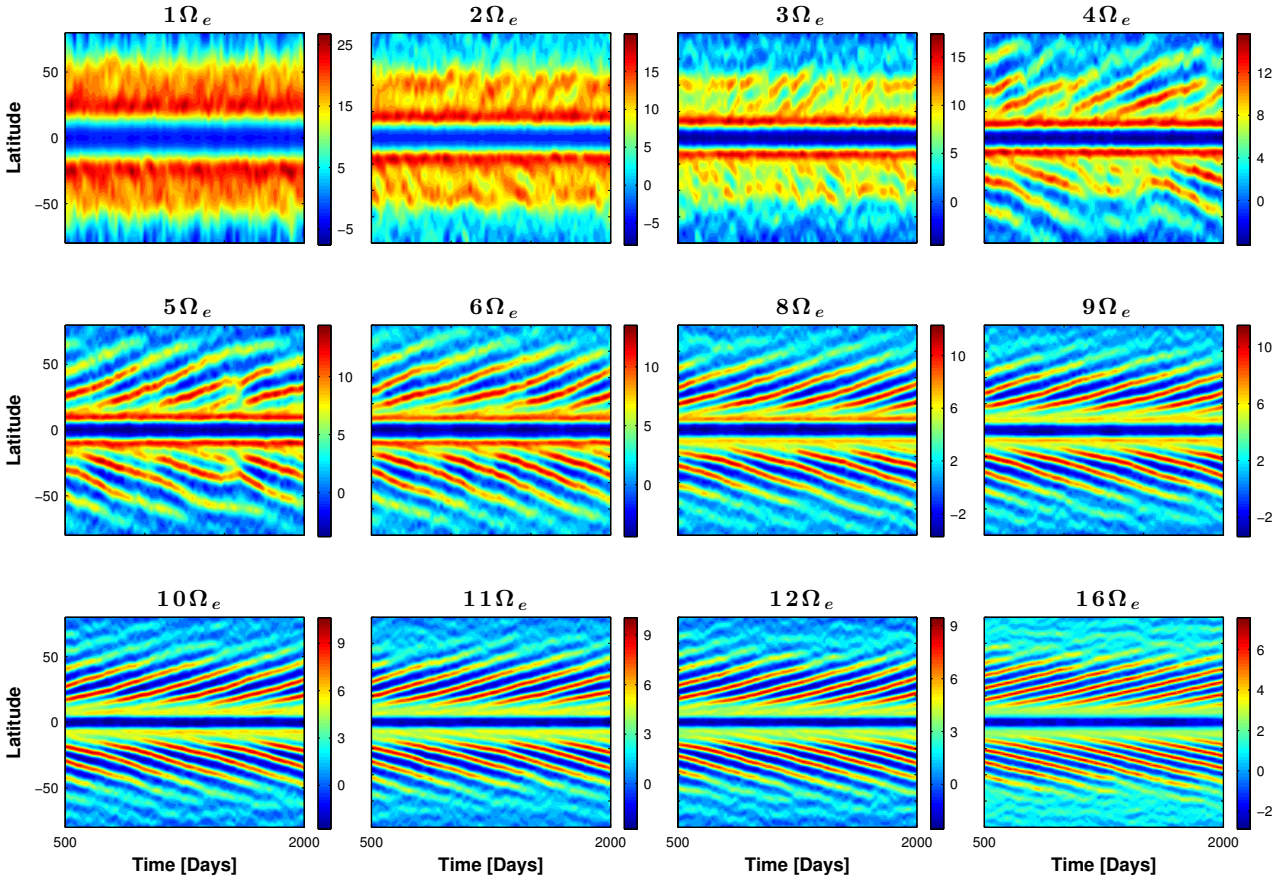

Figure 3.1: Hovmoller diagrams of zonal and vertical averaged zonal wind ($\overline{u}$, $\mathrm{m\,s^{-1}}$) as a function of time for different simulations at rotation rates between Ω_e and $16\Omega_e$. Note the different color scales for each panel.

to a running time average of 20 days. The atmosphere reaches a periodic jet migration state by day 200, and the results represent the last 1500 days of 2000 day runs. The periodic jet migration state in these simulations is a state where the eddy driven jets are constantly forming near the subtropical jet and migrating polewards. Thus, the simulation results we present are not at steady state.

3.1.1 Jet migration

In this section, we present a set of simulations with rotation rates faster than Earth's (hence smaller eddy length scales), where the eddy driven jets and their poleward migration are isolated. We begin with demonstrating the jet migration over a series of simulations, and then proceed to explain the migration mechanism. Figure 3.1 shows Hovmoller diagrams, from simulations at different rotation rates, of the zonal and vertical averaged zonal wind, $\overline{u}$. Four interesting properties can be seen in this plot: First, a clear separation between the eddy driven jet and the subtropical jet begins at rotation rates faster than $2\Omega_e$. Different than the observations and previous modeling studies where the migration referred to the zonal wind anomalies (Riehl et al., 1950; Dickey et al., 1992; Feldstein, 1998; Lee et al., 2007; Chan et al., 2007), here

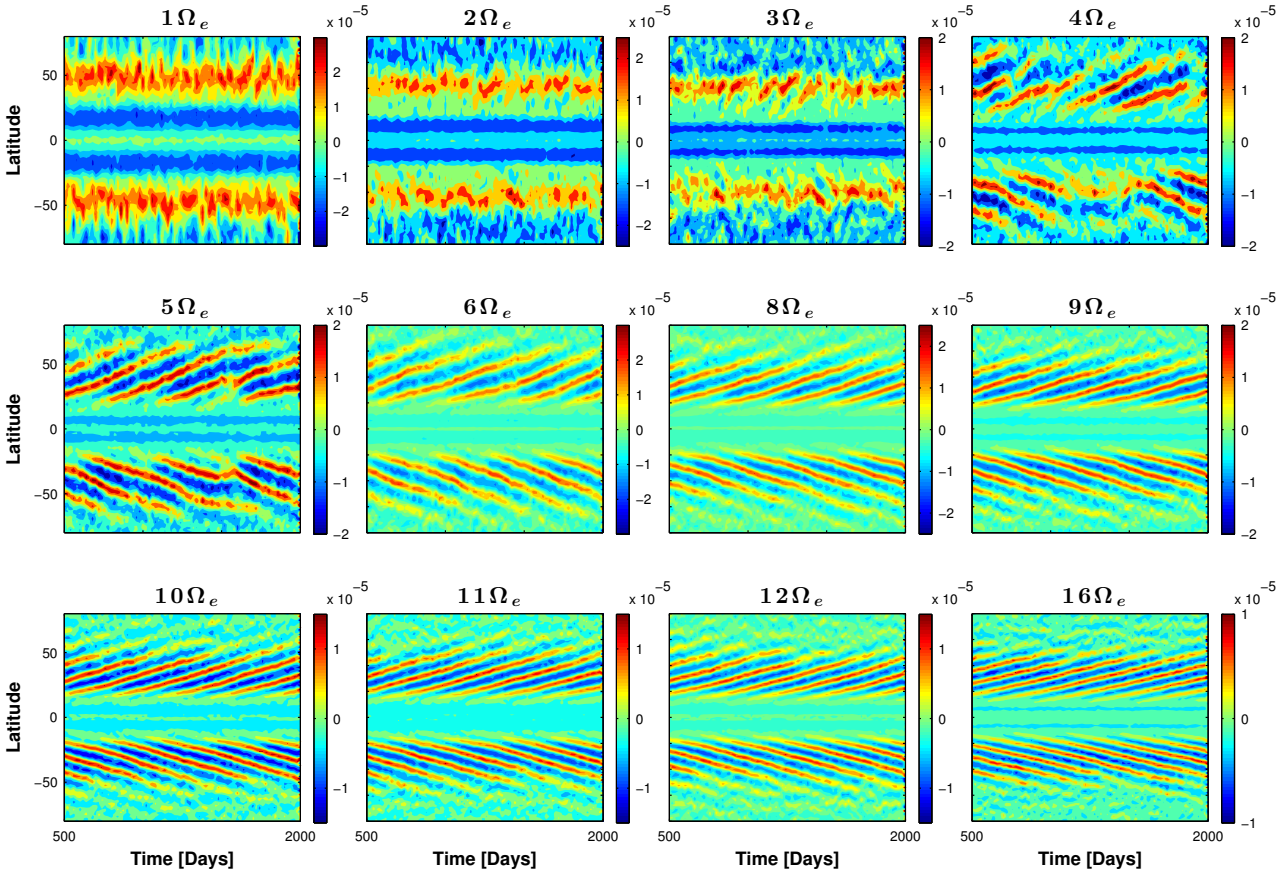

Figure 3.2: Hovmoller diagrams of zonal and vertical averaged eddy momentum flux convergence (N_y, $\mathrm{m\,s^{-2}}$) as a function of time for different simulations at rotation rates between Ω_e and $16\Omega_e$. Note the different color scales for each panel.

the poleward migration of the eddy driven jets themselves is clear. Second, the subtropical jet does not change its latitudinal location with time, and is determined by the latitudinal extent of the Hadley cell, which moves equatorward with increasing rotation rate (Held and Hou, 1980; Walker and Schneider, 2006). Third, the number of the jets, as in Williams and Holloway (1982), shows an increases with rotation rate; and fourth, the rate of poleward migration of the eddy driven jets decreases with rotation rate. These last two points will be discussed in detail in section 3.1.3. Furthermore, as pointed out by Son and Lee (2006) in the context of zonal wind anomalies, the continuous migration of the eddy driven jet is different from the phenomena of jet meandering (zonal index, e.g., Robinson, 2000), or from the jet's meridional shift due to external forcing in a steady state (e.g., Kidston et al., 2011; Barnes and Thompson, 2014; Lorenz, 2014a,b; Zurita-Gotor et al., 2014).

The vertically integrated zonal momentum QG equation to leading order is given by

$$\frac{\partial \overline{u}}{\partial t} = -\frac{1}{a\cos^2\varphi}\frac{\partial(\overline{u'v'}\cos^2\varphi)}{\partial\varphi} + F, \tag{3.1}$$

where primes denote deviation from the zonal mean (overbars), a is Earth's radius, φ is latitude, v is meridional velocity and F represents surface drag. This shows how the eddy momentum flux convergence can accelerate or decelerate the jet (Vallis, 2006). As a result of the vertical

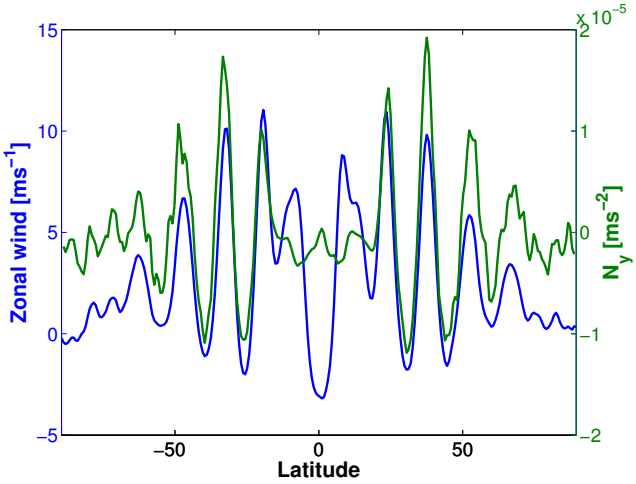

Figure 3.3: Vertical and zonal mean zonal wind ($\overline{u}$, blue), and eddy momentum flux convergence (N_y, green) as a function of latitude for a specific time in the $8\Omega_e$ simulation. Results are smoothed with a 20-day running mean.

integration, the Coriolis term ($f\overline{v}$) in the QG momentum equation vanishes due to mass conservation. In addition, mainly due to the zonal average, the mean momentum flux convergence terms are small compared to the eddy momentum flux convergence terms. Figure 3.2 shows Hovmoller diagrams similar to those in Figure 3.1 only for the zonal mean eddy momentum flux convergence, N_y (following the notation of Hoskins et al. (1983), and in spherical coordinates),

$$N_y \equiv -\frac{1}{a\cos^2\varphi}\frac{\partial(\overline{u'v'}\cos^2\varphi)}{\partial\varphi}. \tag{3.2}$$

The eddy momentum flux convergence shows the same signature of migration as the jets themselves, and the correlation between the momentum flux convergence regions (Figure 3.2) and the extratropical jets (Figure 3.1) indicates that indeed these jets are eddy driven. The lack of momentum flux convergence at the location of the equatormost and non migrating jet, indicates that this is a subtropical jet, located at the edge of the Hadley cell. Only for the lowest rotation rate cases this separation between the subtropical and eddy driven jet is not distinct.

3.1.2 Jet migration mechanism

Carrying on the results of the previous section, here we propose a mechanism for the poleward migration of the eddy driven jets, by focusing first on one simulation with a rotation rate of $8\Omega_e$. In the next section we will attempt to show the consistency of this mechanism for all other rotation rates we explored, in addition to the rotation rate's effect on the jet migration.

Figure 3.3 shows a latitudinal cross section of $\overline{u}$ and N_y for a specific time of this simulation. It shows the latitudinal correlation in each eddy driven jet between $\overline{u}$ and N_y, and the lower values of N_y at the latitudes of the subtropical jets. Moreover, N_y has a poleward bias around each eddy driven jet. In order to demonstrate this poleward bias more clearly, and to show

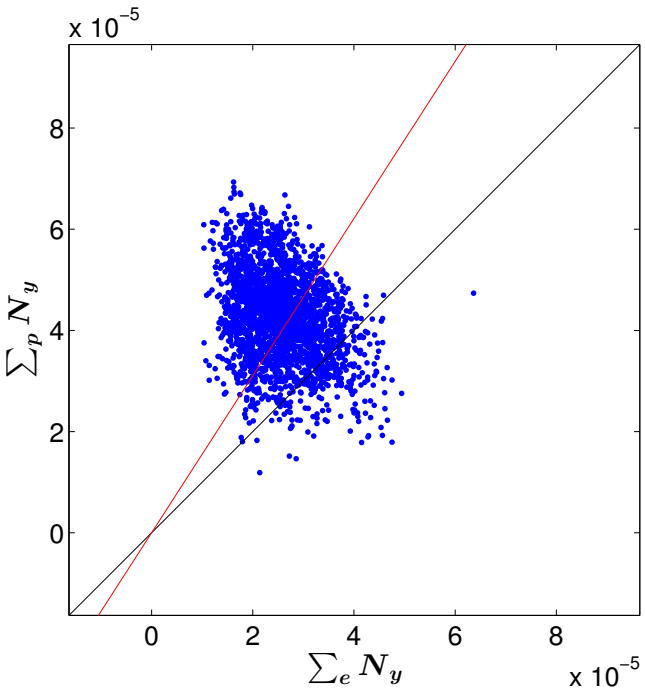

Figure 3.4: The sum over the poleward ($\sum_p$) vs. equatorward ($\sum_e$) flanks of the eddy momentum flux convergence (N_y, $\mathrm{m\,s^{-2}}$) for all jets in the $8\Omega_e$ simulation. Each dot represents a jet in a certain time and latitude. The black line represents a line where the sum of the eddy momentum flux convergence over the poleward flank ($\sum_p N_y$) is equal to the sum of the eddy momentum flux convergence over the equatorward flank ($\sum_e N_y$). The red line represents the best fit for the data based on a linear regression analysis.

how robust this bias is for all the eddy driven jets through the entire simulation, we sum N_y (ΣN_y) separately over the poleward and equatorward flanks of each eddy driven jet, and plot ΣN_y over the poleward flank ($\Sigma_p N_y$) vs. ΣN_y over the equatorward flank ($\Sigma_e N_y$) for each jet (Figure 3.4). The meridional width of each flank is defined as the distance between the latitude of maximum vertical averaged mean zonal wind within each jet, and its closest latitude of minimum or zero zonal wind. Summing over the full latitudinal width of the jet flanks, and not comparing only the closest poleward and equatorward points around the jet's peak enables accumulating better statistics for each jet, and thus accounting the total effect that the eddy momentum flux convergence has on the whole jet and not just on its peak. This also accounts for the meridional structure of both the eddy driven jet and eddy momentum flux convergence. In addition it accounts for the migration of the jet even in cases where the peak of the jet (represented by a single point) has not moved meridionally or moved in a different direction. Each dot in Figure 3.4 represents an eddy driven jet at a specific time and latitude. The black line represents the line where $\Sigma_p N_y$ equals $\Sigma_e N_y$ for a given jet (i.e., a slope of unity in this plot). A jet (dot) for which its $\Sigma_p N_y$ is larger than its $\Sigma_e N_y$, appears therefore above the black line, and vice verse. In Figure 3.4, 88% of the jets experience a larger poleward bias in ΣN_y (placed above the black line). This means that statistically most of the jets through the 1500 days of this model run ($8\Omega_e$), experience a poleward bias in ΣN_y.

In order to quantify the magnitude of this poleward bias, we perform a linear regression

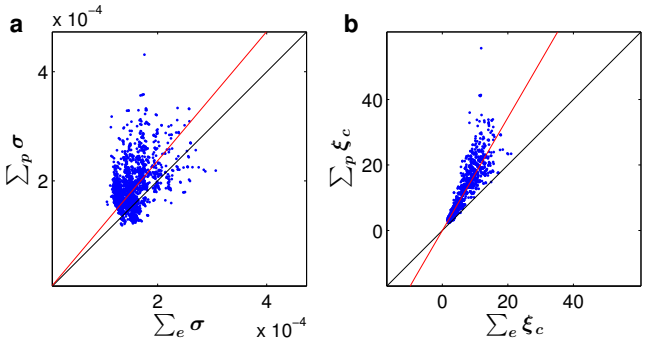

Figure 3.5: The sum over the poleward ($\sum_p$) vs. equatorward ($\sum_e$) flanks of a. the Eady growth rate, σ, s^{-1}; and b. the supercriticality parameter, ξ_c for all jets in the $8\Omega_e$ run. Each dot represents a jet at a certain time and latitude. In each plot the black line represents a line where the sum over the poleward flank is equal to the sum over the equatorward flank. The red line represents the best fit for the data based on a linear regression analysis.

analysis (red line) on the data presented in Fig. 3.4. When the slope of this line equals that of the black line (1:1), the mean magnitude of the poleward bias equals to that of the equatorward bias. In Figure 3.4, the slope of this line is about 1.55, which means that most of the jets experience a strong poleward bias of ΣN_y. Following on Eq. 3.1 this poleward bias around each eddy driven jet at every given instant is consistent with the poleward jet migration with time. Therefore, over most instances of the simulation time, the momentum flux convergence in Eq. 3.1 is stronger on the poleward flank of the jets, and therefore supports a poleward migration of the jets. Similarly, previous studies have also shown the importance of eddy momentum flux convergence in propagating the mean zonal wind anomalies (e.g., Feldstein, 1998; Lee et al., 2007; James and Dodd, 1996), as expected from Eq. 3.1.

The group velocity of Rossby waves propagates away from the source region. Therefore, in the presence of Rossby waves there will be an eddy momentum flux convergence at the source region (in our case, the baroclinic unstable region) (Vallis, 2006). Using a QG model, Riviere (2009) showed that the waves with the largest growth rates are dominant in shifting the jet poleward. Hence, an increase in baroclinic growth can enhance poleward propagation of the jet. Thus, we next analyze the meridional location of baroclinicity (eddy generation) in order to study its location relative to the eddy momentum flux convergence and the eddy driven jet.

As the simplest possible baroclinicity measure, we first use the Eady growth rate, σ, (Eady, 1949; Pedlosky, 1987) which represents the growth rate of the most unstable waves as a simple local measure for the baroclinicity (e.g., Stone 1966; Ioannou and Lindzen 1986; Hoskins and Valdes 1990; Lorenz and Hartmann 2001; Chan et al. 2007; Smith 2007; Merlis and Schneider 2009),

$$\sigma = \frac{fU_z}{S}, \tag{3.3}$$

where f is the Coriolis parameter, U_z is the vertical shear of the zonal wind and $S = \left(\frac{g}{\bar{\theta}}\frac{\partial \bar{\theta}}{\partial z}\right)^{1/2}$ is the static stability. Despite the fact that the Eady growth rate was developed as an f plane theory, Lindzen and Farrell (1980) showed that the Eady growth rate is also suitable to

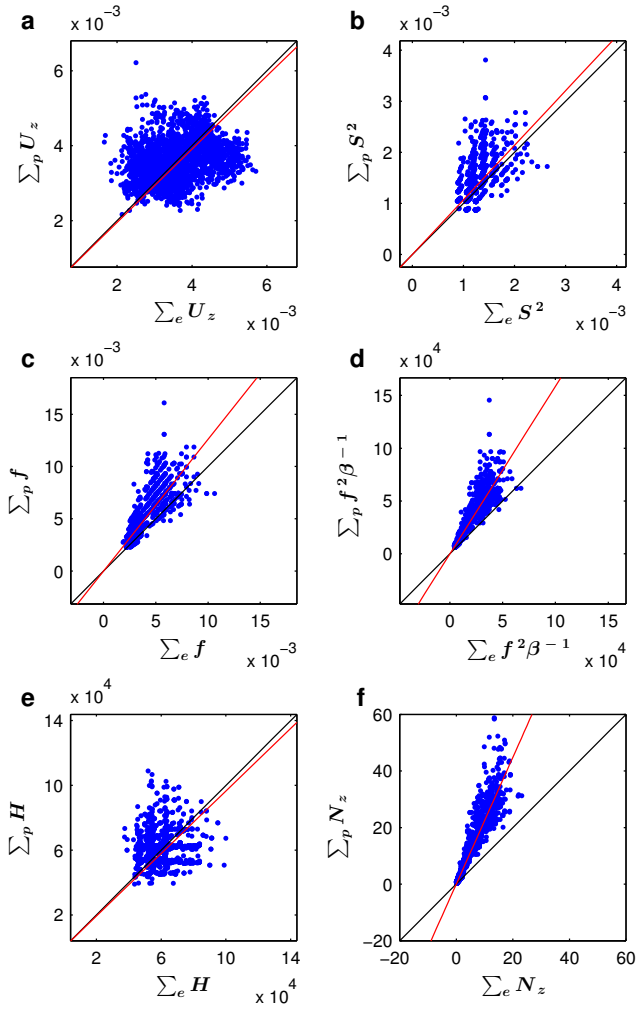

Figure 3.6: The sum over the poleward ($\sum_p$) vs. equatorward ($\sum_e$) flanks of a. the vertical shear of the zonal wind, U_z [s^{-1}]; b. the static stability, S^2 [s^{-2}]; c. the Coriolis parameter, f [s^{-1}]; d. $f^2\beta^{-1}$ [$m\,s^{-1}$]; e. the tropopause height, H [m]; f. the sum of the divergence of the vertical component of the EP flux for all jets in the $8\Omega_e$ run. Each dot represents a jet at a certain time and latitude. In each plot the black line represents a line where the sum over the poleward flank is equal to the sum over the equatorward flank. The red line represents the best fit for the data based on a linear regression analysis.

represent the growth rate of the most unstable waves on a beta plane as in Charney's model (Charney, 1947). Nonetheless, we will later investigate the jet migration mechanism with other measures of baroclinicity such as the supercriticality parameter (e.g., Held and Larichev, 1996). Figure 3.5a shows the sum over the poleward and equatorward flanks, defined as for the momentum flux convergence in Figure 3.4, but for the zonally and vertically averaged Eady growth rate. As for N_y, the Eady growth rate also shows a clear poleward bias around the jet's core. About 83% of the jets experience a poleward bias in the Eady growth rate, with a 1.18 larger magnitude than the equatorward bias (red line).

To better understand why the Eady growth rate has a robust poleward bias around the jet's core, we implement the same analysis on all three components of the Eady growth rate: U_z, S and f (Figures 3.6a,b and c, respectively). As for the Eady growth rate itself, we look at the vertical average of all three components. The vertical shear of the zonal wind (Figure 3.6a) is

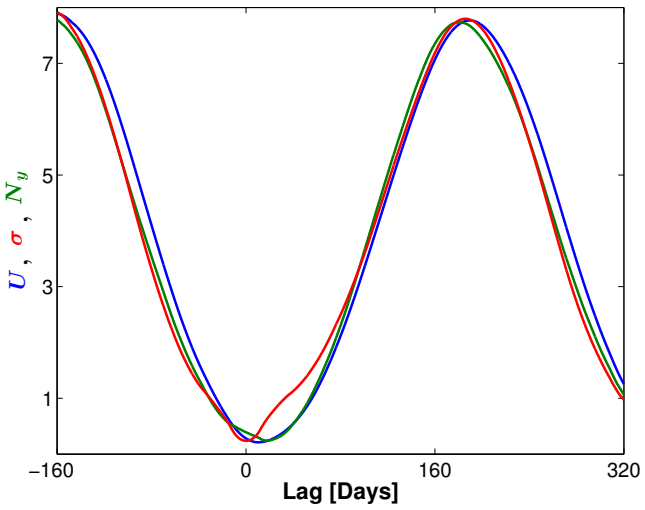

Figure 3.7: The composite time series over all latitudes of the mean zonal wind (blue), $\mathrm{m\,s^{-1}}$, Eady growth rate (red), $10^{-5}\ \mathrm{s^{-1}}$ and the eddy momentum flux convergence (green), $10^{-5}\ \mathrm{m\,s^{-2}}$ for the $8\Omega_e$ simulation. The reference time for this composition (lag 0 day) is the minimum in the Eady growth rate around each cycle (between two consecutive maxima of the mean zonal wind).

symmetric around the jet's core. Only 55% of the jets experience a poleward bias in U_z with approximately the same magnitude as the equatorward bias (only 0.97 larger). Thus, U_z does not contribute to the above poleward bias in the Eady growth rate.

Chan et al. (2007) showed that the meridional change of the static stability in the ocean can have a profound effect on the direction of the eddy driven jet's migration. In the atmosphere, the vertically integrated static stability generally increases poleward. Thus, it can cause an equatorward bias in the Eady growth rate. However, as can be seen in Figure 3.6b the static stability is also symmetric around the jet's core; only about 52% of the jets experience a poleward bias in static stability, with approximately the same magnitude as the equatorward bias, which is only 1.07 times larger. Hence, relative to its magnitude, the static stability does not vary much with latitude, and also does not contribute to the poleward bias in the Eady growth rate.

The Coriolis parameter, however, has a clear poleward bias (Figure 3.6c) as expected from its latitudinal dependence. 91.41% of the jets experience a poleward bias with a 1.26 times larger magnitude than the equatorward bias. In fact since f is a trigonometric function, we expect that all the jets should experience a poleward bias in f. However, some of the jets (8.59%) experience an equatorward bias in the Coriolis parameter measure. This occurs since the structure of the jets is not always meridionally symmetric (Figure 3.6a). This asymmetry results in a wider equatorward flank than a poleward flank for some jets. Thus, in a small subset of the cases, the summed Coriolis parameter is larger on the equatorward flank of these jets, even though the value of f always increases poleward. Despite this asymmetry in some of the cases, statistically, the meridional structure of the jets is symmetric around the jet core (Figure 3.6a). Repeating this analysis of the poleward bias without accounting for the meridional structure of the jets (e.g., by summing over the same amount of latitudes poleward

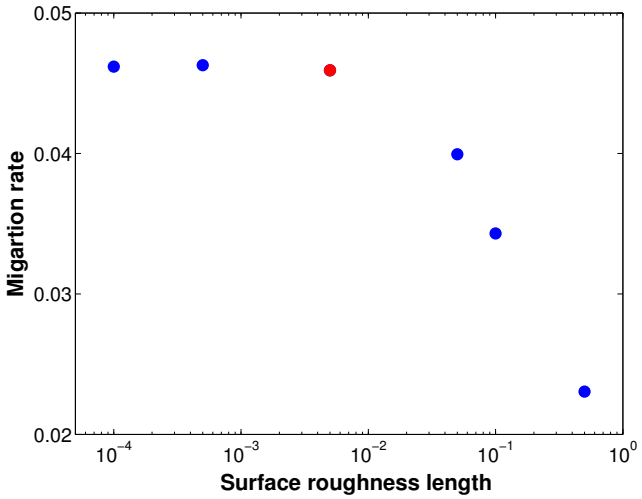

Figure 3.8: The migration rate, $\mathrm{m\,s^{-1}}$ as a function of the surface roughness length, m. The red dot represents the value of surface friction used in the presented simulations.

and equatorward of the jet's core) produces the same behavior in all of the above components.

Therefore, the poleward bias of the Eady growth rate around the jet's core is primarily due to the sphericity of the planet (the latitudinal increase of the Coriolis parameter). Since the Eady growth rate was derived from a f-plane theory, and in order to account for the sphericity of the planet (the β-effect in QG), we also examine the supercriticality, ξ_c, as a measure for baroclinicity,

$$\xi_c = \frac{f^2 U_z}{\beta H S^2}, \tag{3.4}$$

which was found to be suitable for two layer models (Phillips, 1954; Held and Larichev, 1996), continually stratified models (Charney, 1947) and GCMs (Schneider and Walker, 2008), where $\beta = \frac{\partial f}{\partial y}$ and H is the tropopause height. Figure 3.5b shows the same type of analysis as in Figure 3.5a but for the supercriticality parameter. The height of the tropopause is calculated as the height where the the static stability reaches a threshold value of 0.015 s $^{-1}$ and is symmetric around the jet's core (Fig. 3.6e). The supercriticality has a robust poleward bias around the jet core; about 99% of the jets experience a poleward bias with a 1.72 larger magnitude than the equatorward bias. As in the Eady growth rate case, the main contributors to the poleward bias in supercriticality are its Coriolis related parameters, $f^2\beta^{-1}$ (Figure 3.6d).

The eddy-mean flow energy cycle describes the conversion of mean available potential energy to mean kinetic energy through eddy heat and momentum fluxes (Lorenz, 1955). Simmons and Hoskins (1978) showed that the perturbation life cycle plays an important role in this cycle. As the perturbation grows through baroclinic instability while subtracting potential energy from the mean flow, it eventually decays barotropically and returns kinetic energy to the mean flow by eddy momentum fluxes. In our simulations, in addition to the poleward biased eddy momentum flux convergence, the divergence of the vertical component of the EP flux, following Edmon et al. (1980), also has a poleward bias around the jet's core (Figure 3.6f). About 82% of the jets experience a poleward bias in the divergence of the vertical component of the EP

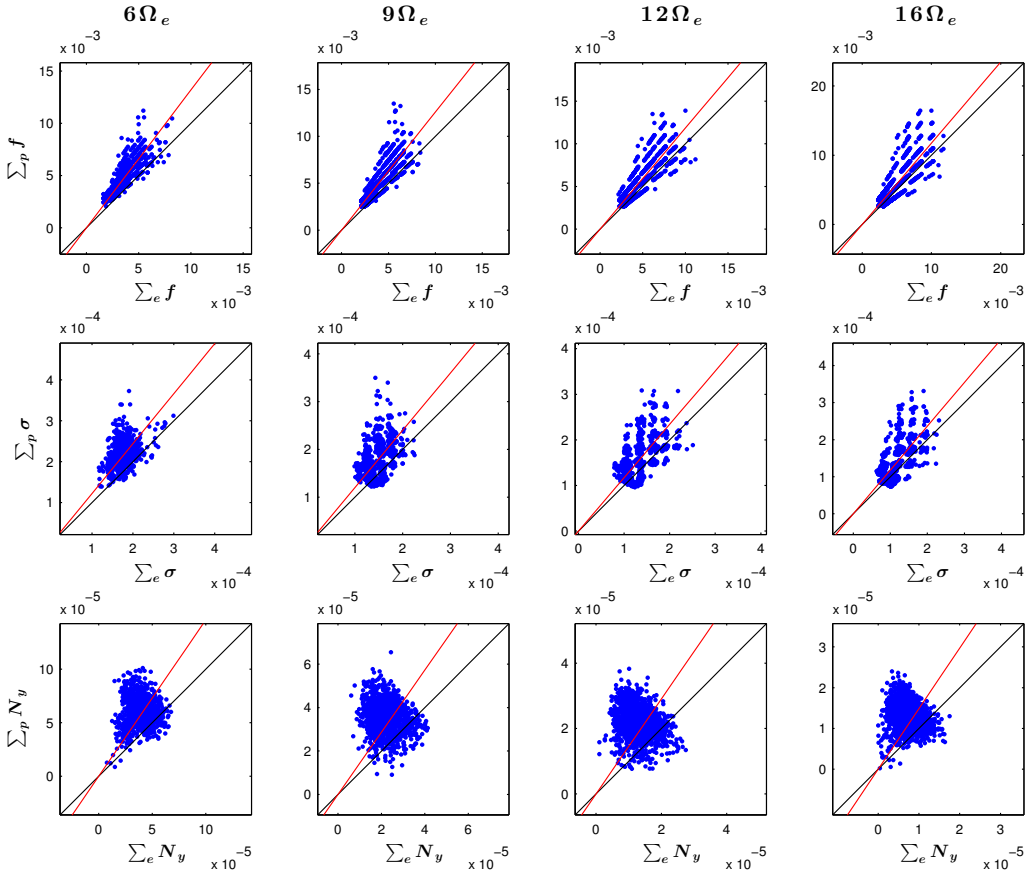

Figure 3.9: First, second and third rows are the same as Figures 3.6c, 3.5a and 3.4, respectively, only for 6 (first column), 9 (second column), 12 (third column) and 16 (fourth column) Ω_e runs. Bias values appear in Table 3.1.

flux, with a 2.25 larger magnitude than the equatorward bias (red line).

To examine the causality between the mean zonal wind, Eady growth rate and eddy momentum flux convergence, we produce a composite of these fields at all latitudes and times (blue, red and green lines in Fig. 3.7, respectively). The reference time for this composition (lag 0 in Fig. 3.7) is the minimum in the Eady growth rate around each cycle (between two consecutive maxima of the mean zonal wind). Choosing a different reference time (e.g., the minimum or maximum of the mean zonal wind) produces the same results. For ease of comparison the Eady growth rate and eddy momentum flux convergence were rescaled using a linear regression analysis with the mean zonal wind. Around each peak of the mean zonal wind (blue line, Fig. 3.7), the left branch is what we referred to as the poleward flank in Fig. 3.3 (since when looking from a specific latitude the poleward flank appears prior to the arrival of the peak). At the flanks of the jets (i.e., at times between 0-100 days and after 250 days) the Eady growth rate precedes the eddy momentum flux convergence that precedes the mean zonal wind. However, around the jet's core (i.e., at times between 100-250 days), the eddy momentum flux convergence precedes the Eady growth rate, which precedes the mean zonal wind.

At the flanks of the jet, the vertical shear of the zonal wind is weak, and thus the poleward bias in the Coriolis parameter causes the poleward bias in baroclinicity, which results in the bias of the eddy momentum flux convergence. Around the jet's core, on the other hand, the

Ω_e	U_z [s^{-1}]	S^2 [s^{-2}]	H [m]	f [s^{-1}]	$f^2\beta^{-1}$ [$m\,s^{-1}$]	σ [s^{-1}]	ξ_c	N_y [$m\,s^{-1}$]
6	53.38%, 0.97	71.30%, 1.10	52.59%, 0.99	97.12%, 1.32	99.95%, 1.71	90.48%, 1.22	100.00%, 1.78	90.68%, 1.46
9	55.90%, 0.99	55.84%, 1.07	47.93%, 0.97	86.81%, 1.25	99.67%, 1.54	80.65%, 1.21	99.93%, 1.77	87.26%, 1.45
12	55.61%, 0.99	53.00%, 1.07	42.23%, 0.97	79.96%, 1.21	98.15%, 1.42	76.10%, 1.21	98.53%, 1.70	86.99%, 1.45
16	58.37%, 1.00	56.72%, 1.06	43.08%, 0.95	73.20%, 1.18	78.40%, 1.37	72.51%, 1.20	87.57%, 1.71	86.38%, 1.46

Table 3.1: The percentage of jets which experienced a poleward bias, and the magnitude of the poleward bias relative to the equatorward bias for each property for several rotation rate simulations.

baroclinicity is more affected by the strong vertical shear of the zonal wind, which decreases the poleward bias in the Eady growth rate. In both regions, the increase of the mean zonal wind can further increase the baroclinicity and/or the eddy momentum flux convergence (as can be seen by the latter times in Fig. 3.7). This growth occurs at the expense of these properties at equatorward latitudes, thus producing the poleward migration (Fig. 3.1). This suggests that while the forcing of the migration of the jets at their flanks is due to the poleward bias of baroclinicity (due to the sphericity of the planet), at their cores, the eddy momentum flux convergences drives the migration. Robinson (2000) discussed the importance of the eddies in driving the poleward drift of both the mean zonal wind and the baroclinicity (as occurs at the jets' core in our simulations) through the equatorward propagation of momentum fluxes aloft (due to the sphericity of the planet). Thus, the sphericity of the planet plays an important role in affecting the poleward migration of the jets in both the flanks and the core of the jet.

In Lee et al. (2007) the migration of zonal wind anomalies starts in the tropics due to midlatitude wave breaking, while in our simulation the migration of the jets occurs only in the extratropics. However, the latter stages of their mechanism (the drift of zonal wind anomalies by eddy momentum flux convergence) is similar in both cases. In the extratropics, Lorenz (2014b) showed that the reflecting level is responsible for the poleward shift of the zonal wind anomalies, even by imposing the convergence of the vertical EP flux (i.e., no asymmetry in baroclinicity). This mechanism can also be suitable to explain the poleward biased eddy momentum flux convergence around the jet's core.

In steady state simulations surface drag plays a major role as it balances the eddy momentum flux convergence (e.g., James and Gray, 1986; Panetta, 1993; Robinson, 1996, 2000; Cai and Shin, 2014; Eq. 3.1). However, as in Lee et al. (2007), we have found that systematically experimenting with variation of surface drag (by varying the surface roughness length) in these simulations (including cases where we significantly reduce the surface drag) has only a very minor affect on the jets and their migration (Fig. 3.8). This is consistent with the fact that in Eq. 3.1 the leading order balance is between the zonal wind tendency and eddy momentum flux convergence. However, as we increase the surface friction beyond a certain value it begins to take an important role in the balance, and as a result the migration rate decreases (Fig. 3.8).

Furthermore, in the presented simulations both the divergence of the EP flux and measures of baroclinicity show a poleward bias around the jet's core (Figures 3.4, 3.5 and 3.6f), while the convergence of the EP flux occurs equatorward of the latitude of maximum baroclinic growth

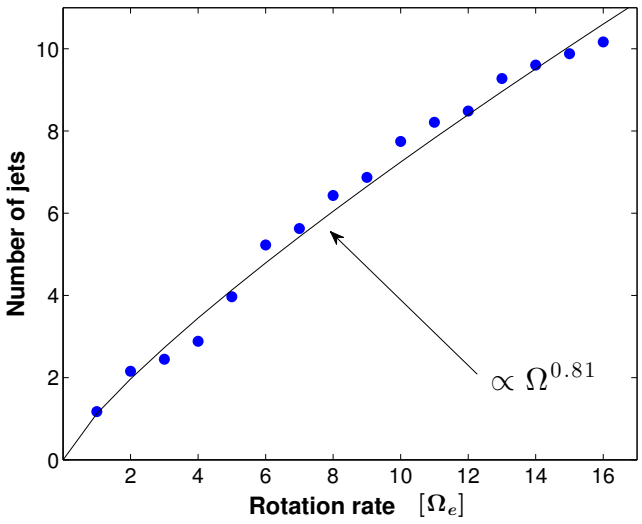

Figure 3.10: The average number of eddy driven jets as a function of rotation rate.

(Fig. 3.7), as in Robinson (2000), and of the jet's position (Fig. 3.3). However, the important role that friction plays (closing the mean meridional circulation in a steady state) in Robinson's mechanism seems to be of secondary importance in these simulations (Fig. 3.8).

3.1.3 The properties of the poleward migration over multiple rotation rates

To demonstrate the robustness of the mechanism presented in section 3.1.2 we preform the same analysis for N_y, Eady growth rate, the supercriticality and their variables, on representative model runs with different rotation rates (6, 9, 12 and 16 Ω_e). The results are summarized in Table 3.1. The symmetry in U_z, S^2 and H around the jet's core is robust for all rotation rates, as the percentage of jets which experience a poleward bias is around 50%, and the ratio between the magnitude of the poleward bias and equatorward bias is around 1. In addition, the static stability develops a poleward bias at low rotation rates, which decreases the poleward bias in baroclinic growth as discussed in section 3.1.2.

The poleward Coriolis bias within the jet width decreases with rotation rate (Figure 3.9 and Table 3.1). There are two competing mechanisms which affect the magnitude of the Coriolis parameter's poleward bias. On one hand, as the rotation rate increases, the Coriolis parameter grows more rapidly with latitude, which causes the poleward bias to increase. On the other hand, as the rotation rate increases the number of eddy driven jets increases as well ($n_{\text{jet}} \propto \Omega^{0.81}$) due to the decrease in the eddy length scale (Figure 3.10), and therefore the width of each one of the multiple baroclinic regions and the variation of the Coriolis parameter within each jet decreases. Since the number of jets increases with rotation rate, while the radius of the planet remains constant, the space between the jets decreases with rotation rate. Figure 3.11 shows the eddy driven jet spacing as a function of latitude and rotation rate, where the jet spacing is defined as the length between two consecutive maxima of the zonal wind. The narrowing of the flanks causes the magnitude of the summed Coriolis parameter to decrease in both flanks,

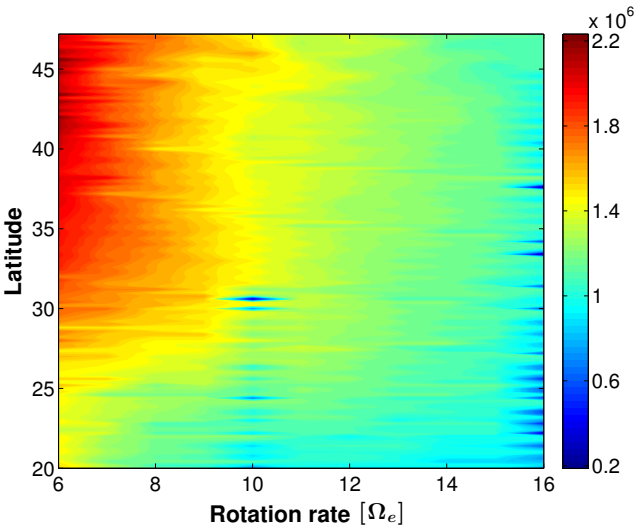

Figure 3.11: Jet spacing [m] as function of latitude and rotation rate.

and thus to a total decrease in the magnitude of the poleward bias and resulting migration rate. The simulations show that the narrowing of the jets dominates the migration rate, over the increase in the value of the Coriolis parameter. The importance of the jet scaling on their meridional migration was also discussed by Thompson (2010) in the context of topographic variations.

The poleward bias of the Coriolis parameter, leads also to a poleward bias in the Eady growth rate and supercriticality (Figure 3.9 and Table 3.1). The mean net bias (Σ_p minus Σ_e) in Figure 3.12a demonstrates the effect of the jet narrowing on the poleward biased Eady growth rate and supercriticality with rotation rate. The poleward bias of N_y is robust in all the rotation rates (Figure 3.9 and Table 3.1), and also shows a decrease in the poleward bias of N_y as the rotation rate increases (Figure 3.9 and Table 3.1). Note that in Figure 3.9 even though the N_y bias ratio (red line) does not change with rotation rate, the actual bias value decreases, as consistent also with Figure 3.12b. Figure 3.12b also shows that the poleward bias of N_y is robust in all rotation rates (positive values) and that the mean net bias decreases with rotation rate, and is $\propto \Omega^{-1.2}$.

Based on our proposed mechanism for the poleward migration of the jets (section 3.1.2), the migration rate should be proportional to the net eddy momentum flux convergence, since this is the force that acts on the jets to propagate them poleward. Hence, we expect that the rate of migration should decrease with rotation rate as can be seen by comparing the slopes of the jet propagation with time in the Hovmoller plots in Figure 3.1. Feldstein (1998) showed that in observations the poleward propagation speed decreases towards the midlatitude and increases towards high latitudes. For the quantitative calculation of the migration rate (Figure 3.12c), we treat the meridional variations in the migration rate as a second order process, and fit a linear trend over the entire baroclinic zone (from the subtropical jet to the latitude where the jets vanish) for all the jets in each rotation rate. Only simulations with a continuous migration were taken into account (simulations with a rotation rate larger than $5\Omega_e$). Figure 3.12c shows that the migration rate of the eddy driven jets decreases with rotation rate and is $\propto \Omega^{-0.44}$.

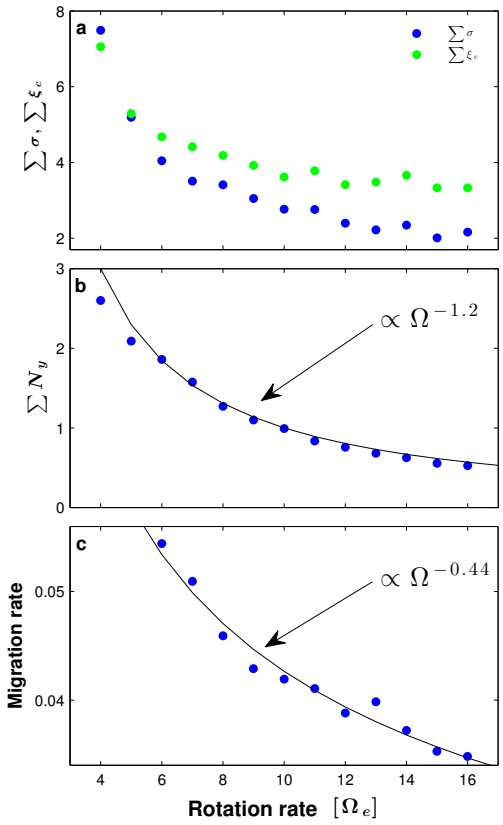

Figure 3.12: Dependence on rotation rate. a. Net Eady growth rate (10^{-5} s^{-1}, blue) and the supercriticality parameter (green). Net refers to the sum of the Eady growth rate or supercriticality on the poleward flank minus the sum on the equatorward flank. b. Net eddy momentum flux convergence (10^{-5} $m\,s^{-2}$, N_y). Net refers to the sum of the eddy momentum flux convergence on the poleward flank minus the sum on the equatorward flank. For the analysis of panels a and b only simulations with a clear separation between the subtropical jet and the eddy driven jets were taken into account ($\Omega > 3\Omega_e$). c. Jet's migration rate [ms^{-1}]. Only simulations with a continuous migration where taken into account for the analysis in panel c ($\Omega > 5\Omega_e$).

Figure 3.13 indeed shows the nearly linear relation between the jet migration and the net eddy momentum flux convergence.

Nonetheless, due to the dependence of jet spacing on latitude as can be inferred from Figure 3.11, care should be taken when developing such scaling. In addition, unlike Feldstein (1998), in our simulations the maximum propagation speed occurs at midlatitudes, although the meridional variations of the migration rate are small compared with its variations with rotation rate. The maximum propagation speed occurs at midlatitudes due to two reasons: First, as the jets propagate to higher latitudes the variations of the Coriolis parameter around their flanks (the beta effect) become smaller, which decrease the poleward bias of the baroclinic growth rate and N_y and thus the rate of migration. On the other hand, the jet spacing increases with latitude (Figure 3.11), thus, as explained previously for different rotation rates, at higher latitudes the wider jets could have a stronger poleward bias. As a result, the maximum propagation speed occurs at midlatitudes.

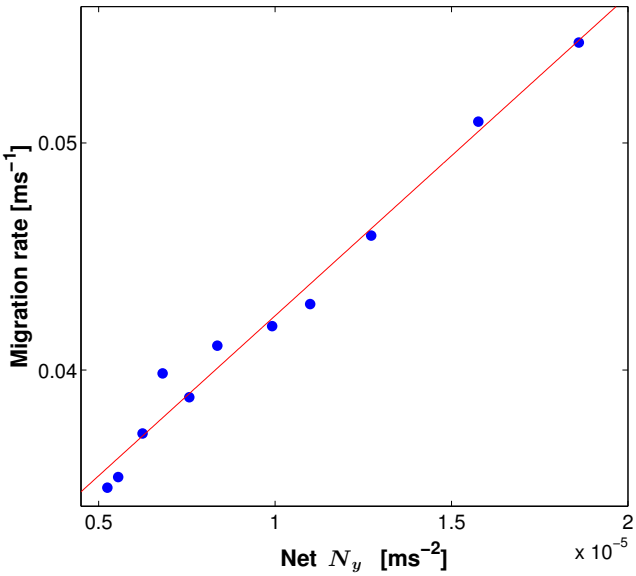

Figure 3.13: Jet migration rate as a function of net eddy momentum flux convergence for different rotation rates. Net refers to the sum of the eddy momentum flux convergence on the poleward flank minus the sum on the equatorward flank. The red line is a linear fit, and has a slope of 1.4×10^3.

3.1.4 Discussion

In this study we show using a high resolution idealized moist GCM (the poleward migration of the eddy-driven jets does not depend on moisture processes, thus, repeating these simulations while eliminating the moisture effects give the same results) that poleward migration of baroclinic eddy driven jets, can be generated due to an asymmetry in the eddy momentum flux convergence around the jet core. The larger eddy momentum flux convergence on the poleward flanks of the jets is consistent with an asymmetry in baroclinic growth around the jet's core. The type of bias (poleward or equatorward) in baroclinic growth, which we parameterize by the Eady growth rate and supercriticality, is determined by the ratio between the meridional change of the Coriolis parameter and the static stability. In all simulations presented here the static stability is nearly symmetric around the jet's core. Hence, the Coriolis parameter is the main contributor to the poleward biased Eady growth rate and supercriticality. At the flanks of the jets, the baroclinic growth precedes the increase of the eddy momentum flux convergence, and thus drives the poleward migration of the jets due to the sphericity of the planet (the Coriolis parameter). On the other hand, around the jet's core the eddy momentum flux convergence precedes the baroclinic growth. A possible mechanism for the latter was discussed by Robinson (2000), where the EP flux convergence (which occur equatorward of their latitude of generation, due to the sphericity of the planet) shifts the baroclinicity and the mean zonal wind poleward, thorough a mean meridional circulation. Thus, the sphericity of the planet plays a major role in shifting the jet poleward (e.g., Nakamura, 1993; Balasubramanian and Garner, 1997; Lorenz and Hartmann, 2001; Riviere, 2009; Thompson, 2010). Son and Lee (2006) showed that the behavior of zonal anomalies is sensitive to the meridional temperature gradient forcing. Here, similarly, the vertical shear of the zonal wind times the Coriolis parameter (the meridional

temperature gradient, using thermal wind balance) affects the properties of the migration. Beyond the possible application of this mechanism to the observed migrating anomalies in the extratropics (Riehl et al., 1950; Dickey et al., 1992; Feldstein, 1998), this work points to the general tendency of baroclinically driven jets to propagate meridionally with time.

The ratio between the Coriolis parameter and the static stability in the Eady growth rate and supercriticality, which was found to play a major role in determining the migration properties in this study and in Chan et al. (2007), also appears in the stretching term of the QG potential vorticity (QGPV). Riviere (2009) showed the effect that the absolute vorticity and stretching terms in the PV gradient have on the meridional location of the jet. While the absolute vorticity terms cause anticyclonic wave breaking and a poleward shift of the jet, the stretching term causes cyclonic wave breaking and an equatorward shift of the jet. The poleward biased Eady growth (Figures 3.5a and 3.9) implies that the Coriolis parameter causes a meridional asymmetry in the stretching term that leads to a meridional asymmetry in the shape of the jet, which may eventually cause a poleward migration. The supercriticality, however, contains the ratio between the stretching term and only the β term from the absolute vorticity. The poleward biased supercriticality (Figure 3.5b and Table 3.1) implies that both the stretching term and β may contribute to the poleward migration of the jets.

As discussed in the introduction, it is difficult to test the jet migration mechanism on Earth using observational data. However, the regions of maximal momentum flux convergence on Earth have a strong correlation to the strongly baroclinic regions, and baroclinically generated cyclones on average do migrate poleward downstream of their source regions (Coronel et al., 2015). This phenomenon is particularly evident in the Atlantic and Pacific storm track regions (Orlanski, 1998; Riviere, 2009; Kaspi and Schneider, 2013), and it is possible that the poleward migration of zonal anomalies is also related to this spatial poleward tilt.

Lee (2005) used the Rhines scale (Eq. 2.13), and the supercriticality from Phillips (1956) in order to state that the number of eddy driven jets is $n_{\text{jet}} \propto (\frac{a}{\Theta_m})^{0.5}$, where a is the planet radius and Θ_m is half of the potential temperature difference between the equator to pole. Lee's model suggests that the number of eddy driven jets should be $\propto \Omega^{0.5}$. Figure 3.10 shows that in our simulations, the number of eddy driven jets is $n_{\text{jet}} \propto \Omega^{0.81}$, and by including the subtropical jet, $n_{\text{jet}} \propto \Omega^{0.52}$. Since in these simulations the jet scaling follows the Rhines scale (Chemke and Kaspi, 2015a, 2016a), and in Lee (2005) the width of the baroclinic zone was taken to be constant, the above discrepancy could be explained by the variations of the width of the baroclinic zone with rotation rate.

O'Gorman and Schneider (2008c) showed that the meridional jet spacing approximately matches the eddy length, which does not vary much with latitude, and the Rhines scale. This coincides with our finding regarding the dependence of the jet space on rotation rate (Figure 3.11). However, our results do show that the space between the jets increases with latitude, as was pointed out by Huang and Robinson (1998), and this increase becomes more moderate with rotation rate (Figure 3.11). We further discuss the properties of the jet spacing on a multiple jet planet in Chemke and Kaspi (2015a, 2016a).

Williams (2003) showed that an equatorward migration of eddy driven jets can occur in a Jupiter parameter regime, due to an asymmetry in the eddy momentum fluxes, which are larger on the equatorward side of the jets. Following on the mechanism presented here, such a case may exist if the static stability on Jupiter increases poleward faster than the Coriolis parameter. However, all wind and thermal structure data for Jupiter are limited to the outer cloud level, and therefore currently we have no estimates for the static stability, nor do we know the depth to which the dynamic weather layer may extend (Kaspi, 2013). If indeed the observed jets on Jupiter are mainly eddy driven (Salyk et al., 2006), then Jupiter lies in the regime where such poleward migration is possible, however current detailed wind observations, which all rely on cloud tracking have been interpolated only for very specific and short times during spacecraft flybys (e.g., Choi and Showman, 2011).

3.2 The latitudinal dependence of atmospheric jet scales and macroturbulent energy cascades

The dependence of the macroturbulent scales on both latitude and rotation rate, motivated us not to integrate them over some baroclinic zone as done in previous studies (e.g., Schneider and Walker, 2006; Jansen and Ferrari, 2012), but investigate the jet scales and energy cascades as function of latitude and rotation rate. Using the simulations of the latitudinally migrating eddy-driven jets (Chemke and Kaspi, 2015b) (Sec. 2.1.1) we were enabled preforming this analysis over a continuos range of latitudes at high rotation rates. The high rotation rates allow a better scale separation between the jet, Rhines and Rossby scales and the radius of the planet.

3.2.1 Jet spacing

In this work we use the simulations of Chemke and Kaspi (2015b) where we have shown that at high rotation rates the eddy driven jets are clearly separated from the subtropical jets, and due to the sphericity of the planet migrate poleward with time (Fig. 3.1). The constantly migrating eddy driven jets at midlatitudes and high rotation rates enables analyzing these jets with latitude across the entire baroclinic zone, and to map their spacing as a function of latitude and rotation rate (Fig. 3.11). The jet space is calculated as the meridional distance between two consecutive peaks of the zonal mean zonal wind[1]. Due to the periodic migration of the eddy driven jets (Fig. 3.1), we were able to accumulate statistics about the jets spacing at each latitude. The average of the jet spacing through all times at each latitude and rotation rate is plotted in Fig. 3.11. As simulations at higher rotation rates have more jets (Chemke and Kaspi, 2015b), the space between the jets decreases with rotation rate. Thus, as in Schneider and Walker (2006), the total energy-containing wavenumber at $k = 0$ increases with rotation

[1]Calculating the jet width as the meridional distance between two consecutive minimum points of the zonal mean zonal wind produces the same picture as in Fig. 3.11.

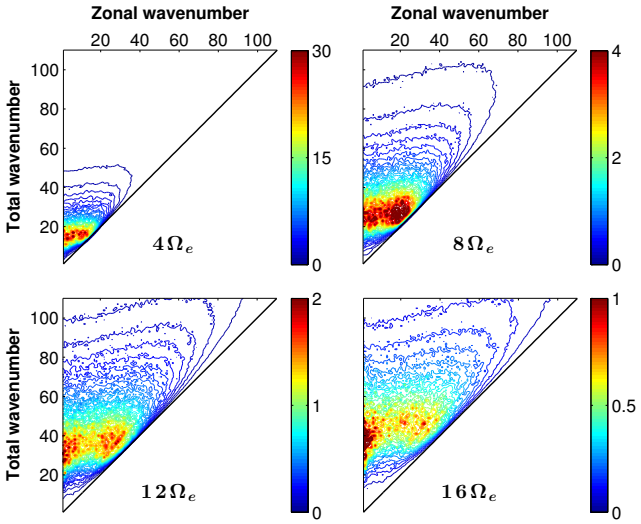

Figure 3.14: The 2D spectrum, computed using spherical harmonics as basis functions (Boer and Shepherd, 1983), of the barotropic EKE (10^{-2} m^{2}s^{-2}) in the 4, 8, 12 and 16Ω_e simulations as a function of zonal and total wavenumbers.

rate (Fig. 3.14). In addition, the jet spacing increases with latitude, as was pointed out by Huang and Robinson (1998) and Kidston and Vallis (2010).

As mentioned in the introduction, both the Rhines scale and the Rossby deformation radius have been related to the jet width. The fact that the jet spacing increases with latitude implies that the Rossby deformation radius likely does not solely set the jet spacing latitude by latitude. Based on Fig. 3.11, Fig. 3.15 shows the ratios between both the Rhines scale and the jet spacing, and the Rossby deformation radius and the jet spacing as a function of latitude for all simulated jets at all rotation rates presented in Fig. 3.11. The Rhines scale, following Rhines (1975), is calculated using Eq. 2.13[2].

The Rossby deformation radius is calculated using Eq. 2.14 multiplied by π,

$$L_D = 2\pi \frac{NH}{f} \tag{3.5}$$

where f is the Coriolis parameter, H is the tropopause height calculated as the height where the the static stability reaches a threshold value of 0.015 s^{-1} and $N^2 = \frac{g}{\theta}\frac{\partial \theta}{\partial z}$ is the vertically averaged static stability below the tropopause height (similar to Frierson et al., 2006), where g is gravity and θ is the potential temperature. The Rossby deformation radius is found to be proportional to the deformation radius which is calculated as $f^{-1}\int N_p dp$ when applying the Liouville-Green or WKBJ approximation on the Sturm–Liouville eigenvalue problem for the vertical structure of the vertical velocity (Gill, 1982; Chelton et al., 1998), where $N_p = \frac{g^2\rho}{\theta}\frac{\partial \theta}{\partial p}$,

[2]We also explore other ways of calculating the Rhines scale, such as the barotropic Rhines scale using the barotropic EKE (deviation from zonal mean of the vertically averaged EKE, Sec. 2.3) as done in previous studies (e.g., Haidvogel and Held, 1980; Schneider and Walker, 2006; Jansen and Ferrari, 2012; Chai and Vallis, 2014), and the Rhines scale based on the Rayleigh–Kuo stability criterion as suggested by Farrell and Ioannou (2007). Even though that the Rhines scale and the barotropic Rhines scale were found to be similar, none of these scales were found to have better scaling with the jet space and the scale of the energy-containing eddies, than the scale in Eq. 2.13 as discuss further below.

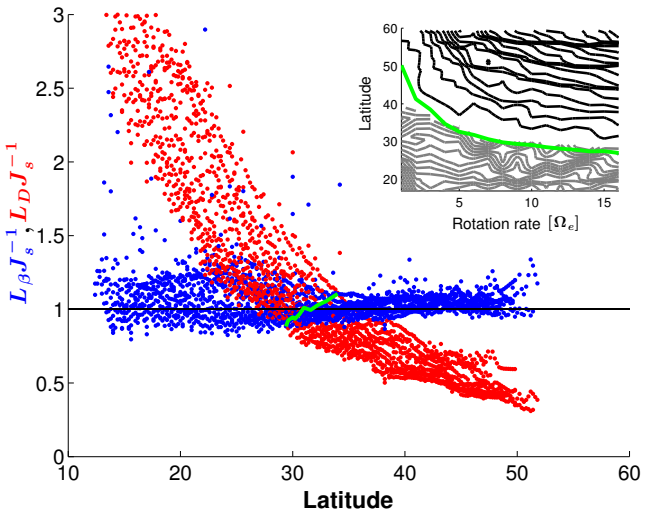

Figure 3.15: The ratio between the Rhines scale and the jet spacing (blue), and between the Rossby deformation radius and the jet spacing (red) as a function of latitude for all simulations presented in Fig. 3.11. Each dot represents a single jet at a single latitude and rotation rate. The green line shows the supercriticality latitude where the Rhines scale equals the Rossby deformation radius. The small corner panel shows the dependency of this latitude as a function of rotation rate. The black and gray contours show where the QG supercriticality, $c_s S_c$, is larger and smaller than one, respectively. For demonstration purposes in this panel, $c_s = 1.5$ is an empirical constant chosen to best separate values larger and smaller than one around the supercriticality latitude. This choice does not affect the shape of the supercriticality with rotation rate (which follows the supercriticality latitude).

p is pressure and ρ is the density.

Three interesting properties can be seen in Fig. 3.15: First, the jet space seems to be well correlated with the Rhines scale, as suggested also by previous studies (e.g., Williams, 1978; Panetta, 1993; Vallis and Maltrud, 1993; Thompson, 2010), through all latitudes and rotation rates. Second, for each rotation rate there is a latitude where the Rhines scale is equal to the Rossby deformation radius (green line). Thus, poleward of these latitudes the Rhines scale (blue dots) is larger than the Rossby deformation radius (red dots), and equatorward of these latitudes the Rossby deformation radius is larger than the Rhines scale (Theiss, 2004). As mentioned in the introduction, Held and Larichev (1996) showed that the QG supercriticality follows the ratio of the Rhines scale and the Rossby deformation radius. The small panel of Fig. 3.15 shows how this latitude separates the QG supercriticality (Phillips, 1954; Held and Larichev, 1996),

$$S_c = \frac{f^2 u_z}{\beta H N^2}, \tag{3.6}$$

where u_z is the vertical shear of the zonal wind, between values larger (black contours) and smaller (gray contours) than one for each rotation rate. Thus, in order to not confuse with the critical latitude related to Rossby waves, we assign this latitude as the "supercriticality latitude", since poleward of this latitude the QG supercrticality is larger than one (Fig. 3.15 small panel) where inverse cascade could occur, and vice verse. The increase of the supercriticality with latitude is consistent with Jansen and Ferrari (2015) where an increase of $f\beta^{-1}$, while keeping

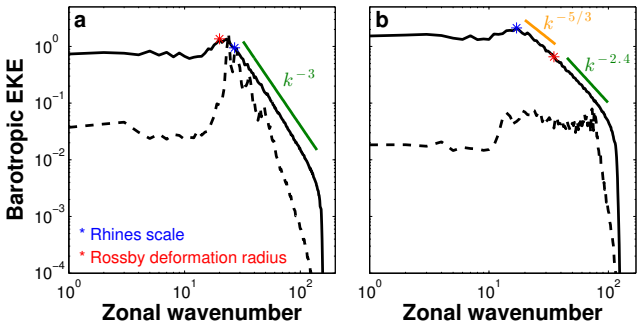

Figure 3.16: The zonal spectrum of the barotropic EKE (m^2s^{-2}) in the $8\Omega_e$ simulation as a function of zonal wavenumber with (solid black line) and without (dashed black line) eddy-eddy interactions for a. a latitude where the Rhines scale is smaller than the Rossby deformation radius (25°), and b. a latitude where the Rhines scale is larger than the Rossby deformation radius (45°). The spectrum of the barotropic EKE without eddy-eddy interactions is divided by 5 for a simpler comparison. The blue and red asterisks are the Rhines and Rossby zonal wavenumbers (Sec 2.3.1), respectively. In panel a, the green line follows a k^{-3} slope. In panel b, the orange and green lines follow a $k^{-5/3}$ and a $k^{-2.4}$ slope, respectively.

the planet size constant, increases the supercriticality. The supercriticality latitude decreases with rotation rate, and this decrease becomes more moderate with rotation rate. This can be due to the opposite affects of the Coriolis parameter and the vertical shear of the zonal wind to increase and decrease, respectively, with rotation rate. If indeed the baroclinic energy is converted to barotropic energy at the Rossby deformation radius, as suggested by Salmon (1978), and the halting scale of the inverse cascade is the Rhines scale, as suggested by Rhines (1975), then this scale separation enables inverse energy cascade to occur only poleward of the supercriticality latitude. These points will be discussed in sections 3.2.2 and 3.2.3 in more detail.

Third, poleward of this latitude where inverse cascade could occur, the Rhines scale is indeed more correlated with the jet space. This coincides with O'Gorman and Schneider (2008c) who showed that the eddy length scale was approximately the Rhines scale and the jet spacing as well. However, here the spacing between the jets increases with latitude, getting more moderate with rotation rate (Fig. 3.11). Equatorward of this latitude, where the Rossby deformation radius is larger than the Rhines scale, the Rhines scale still correlates, although not as well, with the jet space but better than the Rossby deformation radius.

The fact that the latitude where the Rossby deformation radius equals the Rhines scale increases as the rotation rate decreases (small panel of Fig. 3.15), causes the width of the region where an inverse cascade can occur (where the Rhines scale is larger than the Rossby deformation radius) to decrease with decreasing rotation rate. On Earth, the Rhines scale and the Rossby deformation radius are nearly equal only at very high latitudes. This may explain why previous studies observed only the enstrophy cascade in the atmosphere with no inverse cascade (Baer, 1972; Boer and Shepherd, 1983; Lindborg, 1999; Nastrom and Gage, 1985; Koshyk and Hamilton, 2001).

3.2.2 Zonal Spectrum of the barotropic EKE

In order to understand the energy transport and jet scaling equatorward and poleward of the supercriticality latitude, we first examine the zonal spectrum of the barotropic EKE and then analyze its zonal spectral budget (section 3.2.3).

The meridional jet spacing (the Rhines scale, Fig. 3.15) does not necessarily play an important role in the energy transfers in the zonal direction. For example, Vallis and Maltrud (1993) and Huang and Robinson (1998) showed the anisotropic nature of the Rhines scale. Nonetheless, as we show below the Rhines and the jet scales have a crucial role in affecting the processes which transport energy to the jet scale at each latitude in the zonal direction. Moreover, Huang and Robinson (1998) show this anisotropic nature of the Rhines scale by observing the energy-containing wavenumber of the kinetic energy in a zonal and total wavenumbers space. In our simulations, on the other hand, the energy-containing wavenumber has a relative isotropic behavior, as it is almost parallel to the zonal wavenumber axis (Fig. 3.14). As in Boer and Shepherd (1983) and Shepherd (1987b), at large total wavenumbers and small zonal wavenumbers the turbulent regime of the barotropic flow becomes less isotropic. The fact that the contours of the barotropic EKE are spread along lines of constant total wavenumbers (Fig. 3.14), implies that an inverse energy cascade in the zonal direction (toward smaller zonal wavenumbers with higher energy) is accompanied with an inverse energy cascade toward smaller total wavenumbers as well.

To demonstrate the latitudinal behavior of the barotropic EKE, we show its zonal spectrum for the $8\Omega_e$ simulation at a latitude equatorward (Fig. 3.16a) and poleward of the supercriticality latitude (Fig. 3.16b). We show only a sample of two latitudes, as these latitudes provide a representative picture of the barotropic EKE spectrum equator and poleward of the supercriticality latitude. We later show that these latitudes properly represent these two distinct regimes. At latitudes where the Rhines scale is smaller than the deformation radius (Fig. 3.16a) the barotropic EKE spectrum follows a k^{-3} slope of forward enstrophy cascade, as found on Earth, from the Rhines zonal wavenumber (blue asterisk, Sec. 2.3.1) down to the viscosity scale[3]. This slope implies that nonlinear eddy-eddy interactions do not transport energy to larger scales. At latitudes where the Rhines scale is larger than the deformation radius (Fig. 3.16b) the spectral slope between the Rhines and Rossby zonal wavenumbers (red asterisk, Sec. 2.3.1) indeed follows a -5/3 slope, as expected from the inverse cascade in 2D turbulence. Thus, eddy-eddy interactions transfer energy upscale from the deformation scale up to the jet scale. In addition, the spectral slope due to enstrophy cascade, from the Rossby zonal wavenumber to the viscosity scale, at latitudes poleward of the supercriticality latitude is shallower than the expected -3 slope of enstrophy cascade. These two points are further explained in section 3.2.3. The energy plateau at large scales in Fig. 3.16b implies that the energy reaches the zero zonal wavenumber (the jet) as in Vallis and Maltrud (1993) by following the same contour of energy at the Rhines scale in their dumbbell figures. This can also be seen in Fig. 3.14 by following the energy con-

[3]We assign the viscosity scale at $k = 100$ where the zonal spectrum of the barotropic kinetic energy becomes extremely sharp. Despite the apparent arbitrariness of this choice, through all of the simulations this scale is always found to occur at the upper edge of the regime were viscosity starts to play a major role.

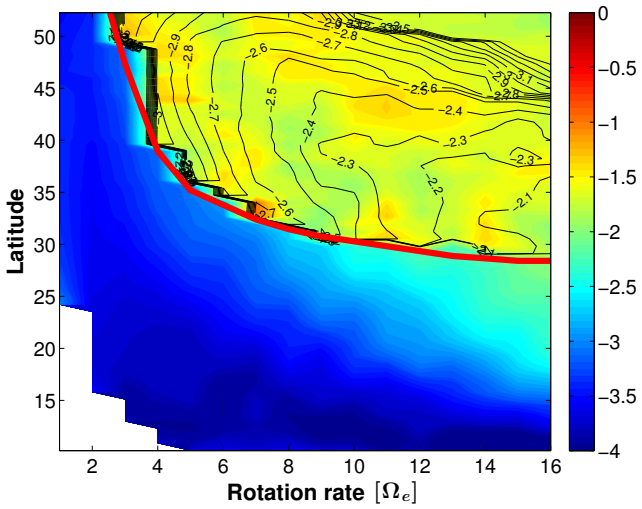

Figure 3.17: The spectral slope as function of latitude and rotation rate. This is calculated as the power of the zonal wavenumber of a straight line fitted to the barotropic EKE spectrum for each latitude and rotation rate. The red line shows the latitude at each rotation rate where the Rhines scale equals the Rossby deformation radius. Below this line, the slope is fitted from the Rhines wavenumber down to $k = 100$. Above the red line the slope is fitted between the Rhines wavenumber and the Rossby wavenumber. The contours show the spectral slope between the Rossby wavenumber and $k = 100$. The white area contains latitudes equatorward to the subtropical jet in each rotation rate.

taining wavenumber contours, which separate two regimes at lower and higher wavenumbers with lower barotropic EKE. Alternatively, the maintenance of the jets can be by eddy-mean interactions (e.g., Shepherd, 1987b; Panetta, 1993; Huang and Robinson, 1998; Robinson, 2006; Farrell and Ioannou, 2007) which we discuss in the next section.

In order to see how robust this picture is, we calculate the above three slopes and plot the power of each slope as a function of rotation rate and latitude (Fig. 3.17). Each slope is calculated by fitting a linear trend to the log of the barotropic EKE over its specific wavenumber range. The red line shows the supercriticality latitude for each rotation rate. This line clearly separates between latitudes where the spectral slope is close to -3 between the Rhines zonal wavenumber and the viscosity scale (equatorward of the supercriticality latitude), and latitudes where the spectral slope is close to -5/3 between the Rhines and the Rossby zonal wavenumbers (poleward of the supercriticality latitude) for each rotation rate. The black contours show the spectral slopes between the Rossby zonal wavenumber down to the viscosity scale, only for latitudes poleward of the supercriticality latitude. Through all latitudes and rotation rates this slope is shallower than the -3 slope of enstrophy cascade. As will we show later, this is due to the fact that the conversion of baroclinic to barotropic EKE is spread through a wide range of scales (Larichev and Held, 1995). For Earth parameters, this supercriticality latitude is poleward of the baroclinic region, which causes the atmosphere to show at each latitude inside the baroclinic region a spectral slope of -3, with no hint for inverse cascade (Fig. 3.17); consistent with Earth observations (e.g., Baer, 1972; Boer and Shepherd, 1983; Lindborg, 1999; Nastrom and Gage, 1985; Koshyk and Hamilton, 2001). This coincides with Frierson et al. (2006), who showed that on Earth through most of the baroclinic zone the deformation radius

is larger than the Rhines scale.

At latitudes equatorward of the supercriticality latitude, the jet, Rhines and Rossby zonal wavenumbers do not coincide with the energy-containing zonal wavenumber, k_e, calculated as in O'Gorman and Schneider (2008c) from the zonal spectrum of the barotropic meridional velocity (Sec. 2.3.1). However, at latitudes poleward to the supercriticality latitude, the jet, Rhines and the energy-containing zonal wavenumbers are almost indistinguishable, as in Jansen and Ferrari (2012); Chai and Vallis (2014) and in Schneider and Walker (2006) at simulations where their supercriticality was one. This could be robustly seen in Fig. 3.18; the jet scale is well correlated with the length scale of the energy-containing zonal wavenumber (L_e, Sec 2.3.1), at latitudes poleward of the supercriticality latitude (blue dots) for all rotation rates. This coincides with Rhines' claim that the Rhines scale is the scale where inverse cascade is being arrested (Rhines, 1975). On the other hand, for latitudes equatorward of the supercriticality latitude (red dots) the jet scale is smaller than the length scale of the energy-containing zonal wavenumber. Schneider and Liu (2009) showed that in Jupiter simulations the Rhines scale and the length scale of the energy-containing zonal wavenumber coincide poleward to a certain latitude. However, different from our simulations they found an opposite dependence of the spectral slope on latitude (Liu and Schneider, 2014); in their simulations at equatorial latitudes the zonal kinetic energy spectrum show a $k^{-5/3}$ power law, but at midlatitudes the spectrum follows a k^{-3} slope.

Although the above picture strongly agrees with Rhines (1975) and Salmon (1978) at latitudes poleward of the supercriticality latitude where an inverse cascade occurs up to the jet scale, there are some features which require further explanation. First, it seems that even though the Rossby deformation radius coincides with the scale where inverse cascade begins (as can be seen by the -5/3 regime poleward of the supercriticality latitude), it fails to show the expected -3 slope of the enstrophy cascade (contours), but rather a shallower spectrum. Second, at high rotation rates ($> 9\Omega_e$) the spectrum of the barotropic EKE below the supercriticality latitude is shallower than the k^{-3} that was observed at lower rotation rates (Fig. 3.17); and third, through most of the latitudes equatorward of the supercriticality latitude the slopes get steeper than -3 as the latitude decreases (Fig. 3.17). These points are further discussed below.

3.2.3 Zonal spectral barotropic EKE budget

For interpretation of these results (Figs. 3.15 and 3.17), we proceed to analyze the different components in the barotropic EKE equation (Sec. 2.3) similar to Larichev and Held (1995), only that here as a function of latitude. This would allow first to determine whether or not the Rossby deformation radius is indeed the scale where baroclinic energy is converted to barotropic energy. And second, to observe the behavior of eddy-eddy and eddy-mean interactions poleward and equatorward of the supercriticality latitude, in order to better understand the processes of energy transport at latitudes where inverse cascade does and does not occur.

The results below are shown for the $8\Omega_e$ simulation as it captures the characteristics both

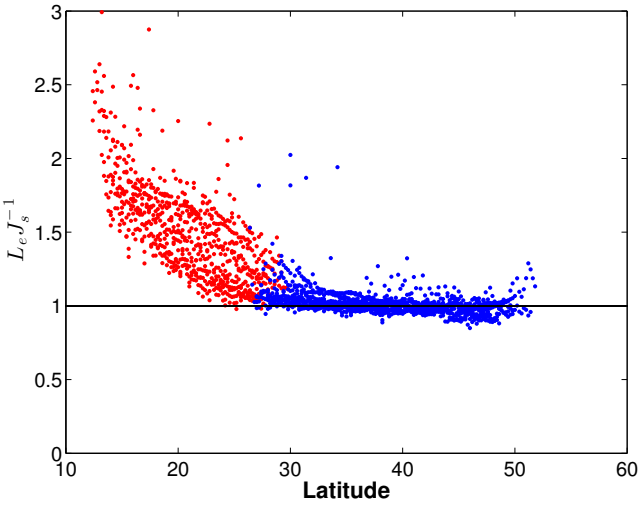

Figure 3.18: The ratio of the length scale of the energy-containing zonal wavenumber, calculated from the zonal spectrum of the barotropic meridional velocity (Sec. 2.3.1) and the jet space as a function of latitude for all rotation rates. The blue (red) dots represents latitudes poleward (equatorward) of the latitude where the Rhines scale is equal to the Rossby deformation radius.

above and below the supercriticality latitude. Hence, it is a representative picture of the behavior that occurs both at low and high rotation rates. Figure 3.19 shows four of the components of the barotropic EKE budget as function of latitude and zonal wavenumber. In each plot the Rhines zonal wavenumber (gray line), Rossby zonal wavenumber (black line) and the conversion zonal wavenumber (white line), which is calculated as the centroid (Eq. 2.12) of the conversion term (Eq. 2.9), are shown. In addition, the supercriticality latitude (blue line) and the conversion latitude, where the Rhines scale is equal to the conversion scale of baroclinic to barotropic EKE (red line), are plotted as well.

Most of the energy influx is from the baroclinic EKE (Fig. 3.19a). This influx is being transferred to larger (inverse cascade) and smaller scales (enstrophy cascade) by the eddy-eddy interactions (Fig. 3.19d). This transfer occurs mostly poleward of the supercriticality latitude and continues beyond the Rhines scale up to $k = 0$ (the energy plateau in Fig. 3.16 and following the energy-containing wavenumber contours in Fig. 3.14). At all latitudes above the supercriticality latitude, the Rhines scale captures well the upscale cascade by the eddy-eddy interactions (Fig. 3.19d). Thus, the arrest of the inverse cascade reaches larger scales at higher latitudes. This is opposite than the behavior documented by Scott and Wang (2005) who showed that the scale of the arrest of the inverse energy cascade in the ocean surface decreases with latitude. The eddy-mean interactions also remove energy around the supercriticality latitude, however, they add energy mostly equatorward of the supercriticality latitude at large scales (Fig. 3.19c). The conversion of barotropic EKE to eddy potential energy occurs at large scales while at intermediate scales barotropic eddy potential energy is converted to barotropic EKE. Note, that the different terms presented in Fig. 3.19 contain not only the transport of barotropic EKE among different scales but also the lateral transport between different latitudes. This point is further discussed in section. 3.2.5.

The Rossby deformation radius manages to separate accurately latitudes where the -5/3

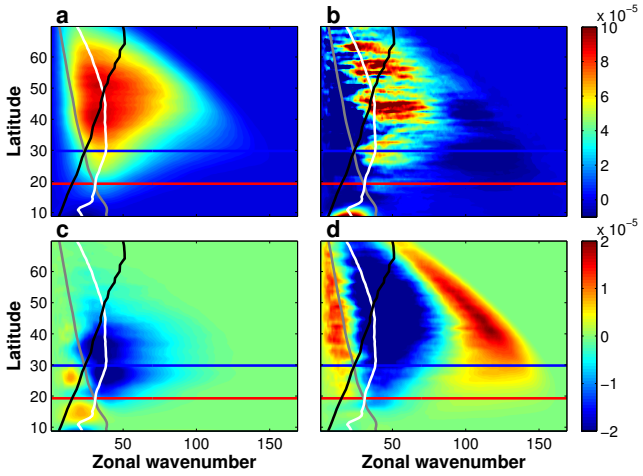

Figure 3.19: Components of the barotropic EKE equation (m^2s^{-3}, Sec. 2.3) in the $8\Omega_e$ run as a function of latitude and zonal wavenumber. a. conversion of baroclinic EKE. b. conversion of barotropic eddy potential energy multiplied by 5. c. eddy-mean interactions. d. eddy-eddy interactions. The gray, black and white lines are the Rhines, Rossby and the conversion zonal wavenumbers, respectively. The blue and red lines are the supercritical and conversion latitude, respectively. Each component is multiplied by the wavenumber and smoothed with a 20-point running mean.

slope of inverse cascade does and does not occur (Fig. 3.17); however, the corresponding Rossby zonal wavenumber does not coincide with the conversion zonal wavenumber (Fig. 3.19a). Alternatively, the supercriticality latitude could have been defined as the ratio between the Rhines scale and the conversion scale from baroclinic to barotropic EKE (Salmon, 1978). However, this does not give three distinct regimes of the spectral slopes as shown by using the Rossby deformation radius (Fig. 3.17)[4]. Thus, further investigation is needed for a better understanding of the role of the Rossby deformation radius in the energy cycle.

One reason that can explain the inability of the conversion zonal wavenumber or the Rossby zonal wavenumber to separate between the inverse energy cascade and the enstrophy cascade at each latitude, is the wide range where baroclinic EKE is being converted to barotropic EKE (Figs. 3.19a and. 3.20a). This was pointed out by Larichev and Held (1995), who showed that as a result of the broad conversion to the barotropic mode, the -5/3 slopes in the barotropic mode are steeper. One possibility is that this non-localization of energy conversion causes the slope, due to the enstrophy cascade, to become shallower at latitudes poleward of the supercriticality latitude (Fig. 3.17). However, the -5/3 slope caused by the inverse energy cascade is less affected by this broadness (Fig. 3.17) since this broadness occurs mostly at wavenumbers larger than the Rossby and conversion zonal wavenumbers, as can be seen in Fig. 3.19a and from the long tail of the orange line in Fig. 3.20a.

As a result of the mismatch between the Rossby deformation radius and the conversion scale, there is a region between the supercriticality latitude and the conversion latitude (thus,

[4]The inability of the conversion latitude to produce such a sharp transition as occurs around the supercriticality latitude (Fig. 3.17), is also found for other conversion scales computed by different weighted mean methods (e.g., Chai and Vallis, 2014 used the inverse centroid of the conversion from eddy available potential energy to EKE, as in Schneider and Walker, 2006).

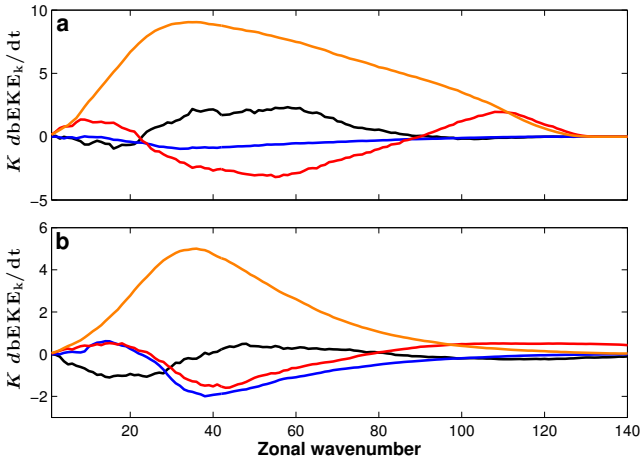

Figure 3.20: Components of the barotropic EKE equation (10^{-5} m^{2}s^{-3}, Sec. 2.3) as a function of zonal wavenumber at latitudes a. poleward of the supercriticality latitude (45°) and b. equatorward of the supercriticality latitude (25°), in the $8\Omega_e$ run as in Fig. 3.19: Conversion from baroclinic EKE to barotropic EKE (orange line), conversion from barotropic eddy potential energy to barotropic EKE (black line), transfer of barotropic EKE by eddy-eddy interactions (red line) and transfer from barotropic mean kinetic energy to barotropic EKE (blue line).

between the red and blue lines) where the influx from the baroclinic EKE still occurs at scales smaller than the Rhines scale (Fig. 3.19a). Thus, at these latitudes the energy still needs to be transferred upscale to the jet scale. Indeed, eddy-eddy interactions are transferring energy upscale as well as down scale at these latitudes (Fig. 3.19d). However, equatorward of the supercriticality latitude the slopes follow more the spectral slope of an enstrophy cascade, k^{-3}, (Figs. 3.16 and 3.17), rather than an inverse energy cascade. This could imply that an inverse cascade by eddy-eddy interactions equatorward of the supercriticality latitudes is weak, and thus negligible in affecting the spectrum of the barotropic EKE to follow a $k^{-5/3}$ slope. Eddy-eddy interactions do seem to be weaker equatorward of the supercriticality latitude, however their magnitude at large scales is similar to the magnitude of both the eddy-mean interactions and the conversion to barotropic eddy potential energy (Figs. 3.19b-d, and 3.20). In addition, unlike poleward latitudes where inverse cascade is observed, at these latitudes the jet scale is smaller than the length scale of the energy-containing zonal wavenumber (Fig. 3.18). We further discuss the role of eddy-eddy interactions poleward and equatorward of the supercriticality latitude in the next section.

We next focus on how the energy budget behaves equatorward of the conversion latitude (thus, equatorward of the red line), where the input to the barotropic EKE occurs at scales larger than the Rhines scale (Fig. 3.19). In terms of Vallis and Maltrud (1993)'s dumbbell figures, at these latitudes the influx of barotropic EKE occurs inside the dumbbell in the wave regime. The anisotropic nature of this regime disables us to infer any conclusions on the meridional jet spacing by studying the energy spectrum in the zonal direction. However, it is a unique regime and it is important to understand it in the zonal direction as well.

Figure 3.21 is similar to Fig. 3.19 but only for latitudes equatorward of the conversion latitude. First, we can see that the magnitude of the different components in the barotropic EKE

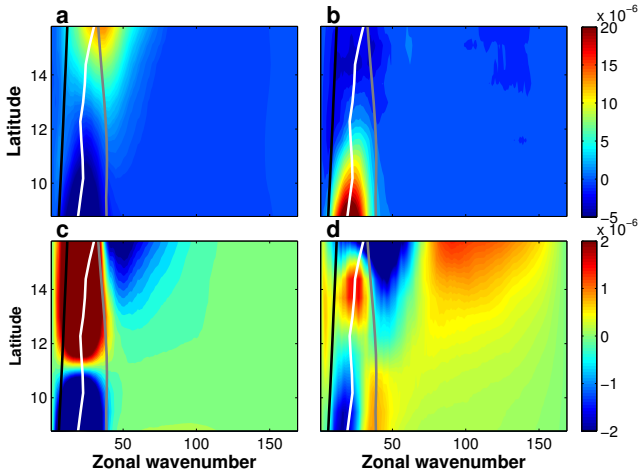

Figure 3.21: Components of the barotropic EKE equation (Sec. 2.3) in the $8\Omega_e$ run as a function of latitude and zonal wavenumber, as in Fig. 3.19 only for latitudes where the Rhines scale is smaller than the conversion scale of baroclinic EKE. a. conversion of baroclinic EKE. b. conversion of barotropic eddy potential energy. c. eddy-mean interaction. d. eddy-eddy interaction.

equation (Eq. 2.4) is an order of magnitude smaller than poleward of the conversion latitude. Second, at these latitudes the influx is mostly from barotropic eddy potential energy (Fig. 3.21b) rather than baroclinic EKE (Fig. 3.21a) as in the poleward latitudes (Fig. 3.19a). Moreover, only at these latitudes, the barotropic EKE is converted to baroclinic EKE at low latitudes and small wavenumbers (Fig. 3.19a). Different than the higher latitudes, here the eddy-mean interactions (Fig. 3.21c), which are stronger than the eddy-eddy interactions (Fig. 3.21d), transfer this influx from potential energy to higher latitudes. On the other hand, as the separation between the conversion wavenumber and the Rhines wavenumber grows (moving to lower latitudes) the eddy-eddy interactions remove the influx of barotropic eddy potential energy at large scales and transfer it down to the Rhines zonal wavenumber (Fig. 3.21d). At latitudes close to the conversion latitude we can see the remnants of the influx from the baroclinic EKE and the outflux by both the eddy-eddy and eddy-mean interactions, in addition to the energy transfer to small scales by the eddy-eddy interactions.

3.2.4 The role of eddy-eddy interactions

In order to further analyze whether the eddy-eddy interactions are important poleward and equatorward of the supercriticality latitude, we remove the eddy-eddy interactions from the momentum and temperature equations as in O'Gorman and Schneider (2007). As a result, in these simulations only the eddy-mean interactions can control the shape of the energy spectrum. The dashed black lines in Fig. 3.16 show the spectrum of the barotropic EKE in the simulation where we removed the eddy-eddy interactions. Although Fig. 3.16 shows only the spectrum of the barotropic EKE from two different latitudes (poleward and equatorward of the supercriticality latitude), their properties are found to be robust through all latitudes in this simulation.

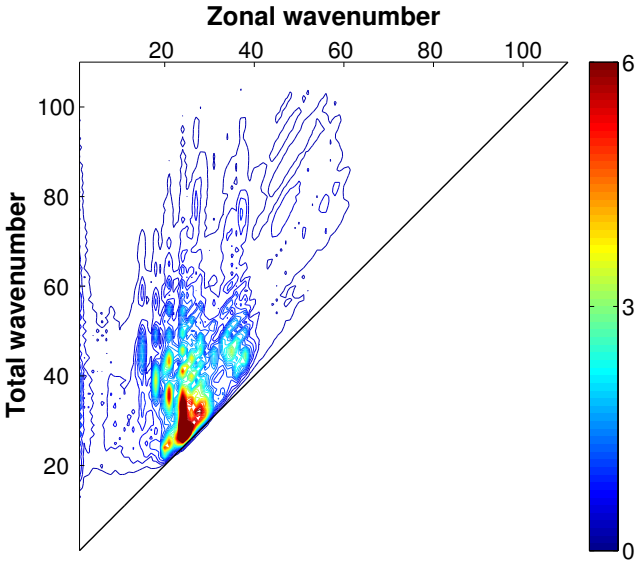

Figure 3.22: The 2D spectrum of the barotropic EKE (10^{-2} m^{2}s^{-2}), as in Fig. 3.14 only for the $8\Omega_e$ simulation without eddy-eddy interactions, as a function of zonal and total wavenumbers.

Similar to O'Gorman and Schneider (2007) and Chai and Vallis (2014), the barotropic EKE at intermediate scales, in the simulation with eddy-eddy interactions, is smaller than in the simulation where these interactions are absent (Fig. 3.16a). O'Gorman and Schneider (2007) suggested that the presence of eddy-eddy interactions reduces the competence to convert energy to barotropic energy and thus reduces the total barotropic kinetic energy. In addition, the removal of eddy-eddy interactions causes the spectrum to be less smooth (Fig. 3.16), likely as a result of the lack of energy transfer between different scales by these interactions (O'Gorman and Schneider, 2007).

The spectrum of the barotropic EKE at latitudes poleward of the supercriticality latitude (Fig. 3.16b) does not follow a $k^{-5/3}$ slope anymore, but rather a much shallower slope. As discussed in Shepherd (1987a), the tendency of the eddy-eddy interactions to spread the barotropic EKE along lines of constant total wavenumber (Fig. 3.14) vanishes in this simulation when they are absent (Fig. 3.22). Hence, similar to Berloff and Kamenkovich (2013a,b), the energy-containing wavenumber is more isolated in the spectral space (Figs. 3.16a and 3.22). This can also be observed in the simulation with eddy-eddy interactions, as the energy-containing zonal wavenumber (peaks of solid black lines in Fig. 3.16) is more (less) isolated at latitudes equatorward (poleward) of the supercriticality latitude, where eddy-eddy interactions are less (more) pronounced (note the logarithmic scale). These points strengthen the findings of sections 3.2.2 and 3.2.3 on the importance of eddy-eddy interactions, especially poleward of the supercriticality latitude, in transferring energy to larger scales.

On the other hand, equatorward of the supercriticality latitude the spectral slope at large scales qualitatively remains as in the simulation with the eddy-eddy interactions (Fig. 3.16a). Due to the lack of energy input by the eddy-mean interactions at small scales (as also occurs in the simulation with eddy-eddy interactions, Fig. 3.19), the spectral slope becomes steeper at small scales. This could imply that as the eddy-eddy interactions weaken moving equatorward

from the supercriticality latitude (Fig. 3.19d), the spectral slope should also become steeper (as can be seen in Fig. 3.17). Furthermore, equatorward of the conversion latitude, where eddy-eddy interactions are negligible (Fig. 3.21d), the tendency of the eddy-mean interactions to transfer energy to poleward latitudes along lines of constant zonal wavenumber (Fig. 3.21c), can also be seen in the simulation without eddy-eddy interactions where the barotropic EKE is more elongated along lines of constant zonal wavenumber (Fig. 3.22).

The importance of eddy-mean flow interactions, as seems to be the case equatorward of the supercriticality latitude (Figs. 3.19c and 3.20b), had been discussed in previous studies through shear-induced spectral transfer from the point of view of transient-stationary interactions (e.g., Shepherd, 1987b; Huang and Robinson, 1998). As in Huang and Robinson (1998), also here these interactions mostly involve eddies smaller than the Rhines scale (Fig. 3.19c), even though it correlates with the jet space (Fig. 3.15). Large scale eddies also contribute to the spectral budget of the barotropic EKE (Fig. 3.19c). The lack of inverse cascade emphasizes the major role of eddy-mean interactions in maintaining the jets (Shepherd, 1987b; Huang and Robinson, 1998; Farrell and Ioannou, 2007) and adding energy at large scales. Therefore, other mechanisms other than an inverse energy cascade should explain the fact that the Rhines scale still coincides with the jet space, equatorward of the supercriticality latitude. This point is beyond the scope of this paper and further discussed in the next section.

On Earth, the fact that the region between the supercriticality latitude and the subtropical jet covers the entire baroclinic zone (Fig. 3.17), may explain the fact that an inverse cascade is not observed in atmospheric observations (Baer, 1972; Boer and Shepherd, 1983; Lindborg, 1999; Nastrom and Gage, 1985; Koshyk and Hamilton, 2001). Different than the higher rotation rate simulations, on Earth the relative large ratio between the eddy scale and the size of the planet, causes only a small separation between the Rhines scale, the Rossby deformation radius and the conversion scale at all latitudes. As a result, the minor role of eddy-eddy interactions in this regime at higher rotation rates (Fig. 3.19d) is not found in our Ω_e simulation.

3.2.5 Discussion

In this study we show the importance of the Rossby deformation radius in affecting the spectrum of barotropic kinetic energy, by distinguishing between latitudes where an inverse cascade does and does not occur (Fig. 3.17). However, different than the classic picture (e.g., Salmon, 1978), this scale does not coincide with our measures of the conversion scale from baroclinic to barotropic EKE. Due to the mismatch between the Rossby deformation radius and the conversion scale, the influx from baroclinic to barotropic EKE at latitudes equatorward of the supercriticality latitude, occurs at scales smaller than the Rhines scale. However, the spectrum of the barotropic EKE follows a k^{-3} slope. The lack of inverse cascade implies on the minor role of eddy-eddy interactions in transferring energy upscale, and on the importance of eddy-mean interactions at these latitudes. In addition, since the length scale of the energy-containing zonal wavenumber at these latitudes is larger than the jet scale, other mechanisms besides an

inverse energy cascade should explain the latitudinal coincident of the Rhines and jet scales. For example, Farrell and Ioannou (2007) showed that the barotropic jet scale could be determined by the Rayleigh–Kuo stability criterion (Kuo, 1949); thus, with no inverse cascade, the jet scale should coincide with the Rhines scale, defined as $L_\beta = \left(\frac{U_{\max}}{\beta}\right)^{0.5}$, and could differ from the length scale of the energy-containing zonal wavenumber.

Several studies have showed that even by removing the nonlinear eddy-eddy interactions (quasi-linear models), the meridional structure of the jets remains similar to that in the full nonlinear simulations (e.g., O'Gorman and Schneider, 2007; Constantinou et al., 2014; Srinivasan and Young, 2012; Tobias and Marston, 2013). Thus, implying that eddy-eddy interaction and inverse energy cascade might not be a prerequisite for jet formation. However, the different latitudinal spread of the ratio between the Rhines and jet scales poleward and equatorward of the supercriticality latitude (Fig. 3.15) implies that eddy-eddy interactions and inverse energy cascade do affect the meridional structure of the flow especially when it is highly nonlinear (e.g., poleward of the supercriticality latitude).

The spectrum of the barotropic EKE at latitudes equatorward of the supercriticality latitude at rotation rates higher than $9\Omega_e$ follows a shallower slope than the predicted -3 of enstrophy cascade as in 2D turbulence (Fig. 3.17). This is not due to not properly resolving the small scales eddies, as simulations at T213 (0.56°) show the same behavior. One possibility is that as the rotation rate increases, the input of barotropic energy from both the barotropic eddy potential and baroclinic energies becomes broader at latitudes equatorward of the supercriticality latitude. As a result, the spectral slope can become shallower as occurs to the enstrophy cascade poleward of the supercriticality latitude. Alternatively, the decrease in accumulation of barotropic EKE by eddy-mean interactions at scales around the Rhines scale can also lead to a shallower slope.

Our results show that the jet scale is proportional to the Rhines scale (Fig. 3.15). Assuming the jet and Rhines scales are equal, Lee (2005) suggested that the number of eddy driven jets should be $\propto \Omega^{0.5}$. However, in Chemke and Kaspi (2015b) the number of eddy driven jets follows, $n_{\text{jet}} \propto \Omega^{0.81}$. These results may be different since in our simulations the baroclinic zone increases as the rotation rate increases (Fig. 3.17), while in Lee (2005) a constant width of baroclinic zone was taken into account.

The different terms in Fig. 3.19d (Eqs. 2.6-2.9) contain not only the transport of barotropic EKE between different scales but also the lateral transport between different latitudes. However, by looking at Fig. 3.19d, it seems that most of the energy transfer is between different zonal scales and not between different latitudes. Theiss (2004) showed that the nonlinear interactions are responsible for the equatorward cascade of EKE, which we do not observe in our simulations. By summing the eddy-eddy and eddy-mean interactions over all zonal wavenumbers at each latitude, we observe the absence of the net lateral transport of barotropic EKE; The eddy-eddy interactions decrease by an order of magnitude once they are summed over all zonal wavenumbers with no coherent behavior of an equatorward cascade. Hence, these interactions transfer most of the barotropic EKE between different scales, and do not seem to

cascade energy towards the equator. The eddy-mean interactions, on the other hand, tend to remove the barotropic EKE through most latitudes.

Choi and Showman (2011) showed using the spectrum of cloud patterns imaged from the Cassini spacecraft that 2D turbulence inverse and enstrophy cascades could occur on Jupiter. Their transition scale between the -5/3 slope and -3 slope of was found to be between ∼1,000 and ∼3,000 km at latitude of 45°. The planetary Rossby number of Jupiter, $\frac{U}{\Omega R}$, should be ∼7 times smaller than that of Earth, as its radius is ∼11 times larger than Earth's radius, its rotation rate is ∼2.5 times faster and its mean tropospheric winds are on average 4 times faster than those on Earth (Vasavada and Showman, 2005). The Rossby deformation radius (which is found to be a potential transition scale in our simulations) at 45° in the $7\Omega_e$ simulation is indeed ∼1,000 km. On the other hand, other studies have shown that an inverse cascade does not necessarily occur on Jupiter (e.g., Schneider and Liu, 2009). Theiss (2006) showed that by including the latitudinal dependency of the deformation radius in the dispersion relation of Rossby waves, the Rhines effect on Jupiter separates latitudes where coherent jets appear, and where the flow is governed by vortices. This is consistent with Theiss (2004), Sayanagi et al. (2008) and Scott and Polvani (2007) findings, however the fact that jets appear in our simulations even poleward of the supercriticality latitude (Figs. 3.1,3.15 and 3.18), could imply that the shallow atmosphere approximations in our PE model are not necessarily applicable to Jupiter's flow.

3.2.6 Conclusions

In this study we have used an idealized GCM at high rotation rates to allow a clear separation between the eddy driven jet and the subtropical jet in the atmosphere. As the meridional jet spacing (latitudinal location) has an important affect on climate and weather systems, this separation enables us to scale the meridional spacing of the eddy driven jets and study the macroturbulence behavior. Different from previous studies, the multiple jet regime and their constant poleward migration at high rotation rates allow us to study the jet properties, macroturbulence and energy cascades *latitute-by-latitude* and not just averaged over some baroclinic zone. Our main conclusions are as follows:

- The Rhines scale is able to predict the jet spacing latitude-by-latitude over a wide range of simulations with different rotation rates (Fig. 3.15).
- We show the presence of the supercriticality latitude: a latitude where the Rhines scale is equal to the Rossby deformation radius. We find that at latitudes poleward of the supercriticality latitude, where the Rhines scale is larger than the Rossby deformation radius, inverse energy cascade occurs from the Rossby deformation radius up to the Rhines scale with a spectral slope which follows a $k^{-5/3}$ slope as in two-dimensional turbulence (Fig. 3.17). In addition, at these latitudes, eddy-eddy interactions play a major role in

cascading the barotropic EKE to larger and smaller scales (Fig. 3.19d). At these latitudes the length scale of the energy-containing zonal wavenumber coincides with the jet scale (Fig. 3.18).

- At latitudes equatorward of the supercriticality latitude, where the Rhines scale is smaller than the Rossby deformation radius, there is a sharp transition to a regime where the spectral slope between the Rhines scale down to the viscosity scale follows a k^{-3} slope, similar to the enstrophy cascade in two-dimensional turbulence (Fig. 3.17).

- In our Earth like simulations the supercriticality latitude is placed poleward of the baroclinic zone, causing it to produce only the k^{-3} slope of enstrophy cascade with no hint of inverse cascade (Fig. 3.17), as observed in Earth's atmosphere.

- Due the non-local input of energy, mostly at small scales, from baroclinic to the barotropic EKE (Figs. 3.19a and. 3.20a), the spectral slope of enstrophy cascade at latitudes poleward of the supercriticality latitude, from the Rossby deformation radius down to the viscosity scale is shallower than the predicted k^{-3} slope (Fig. 3.17).

- Even though the Rossby deformation radius does not coincide with the scale where energy is being transferred from baroclinic to barotropic EKE (Fig. 3.19a), it still produces a sharp transition between latitudes where inverse cascade does and does not occur (Fig. 3.17).

- As a result of the previous point at latitudes equatorward of the supercriticality latitude, the influx of baroclinic to barotropic EKE still occurs at scales smaller than the Rhines scale, even though that the deformation radius is larger than the Rhines scale (Fig. 3.19a). Eddy-eddy interactions transfer energy upscale at these latitudes (Fig. 3.19d), although, the spectral slope is similar to a k^{-3} of enstrophy cascade (Fig. 3.17). This implies that eddy-eddy interactions at these latitudes are too weak to affect the spectral slope. This, combined with the fact that the length scale of the energy-containing zonal wavenumber is larger than the jet scale at these latitudes (Fig. 3.18), emphasizes the minor role of the halting scale of the inverse energy cascade and the importance of eddy-mean interactions equatorward of the supercriticality latitude.

- By removing the eddy-eddy interactions from our model, we demonstrate the point above, and show that the spectral slope at these latitudes remains qualitatively the same at large scales due to eddy-mean interactions (Fig. 3.16). The importance of eddy-eddy interactions at latitudes poleward of the supercriticality latitude is also shown. In addition, at latitudes equatorward of the supercriticality latitude the eddy-eddy interactions transfer energy to larger and smaller scales (Fig. 3.19d), while the eddy-mean interactions add energy only at large wavenumbers (Fig. 3.19c). As a result, when eddy-eddy interactions are removed the eddy-mean interactions alone produce at small scales a steeper spectral slope than the -3 of enstrophy cascade (Fig. 3.16). Thus, as we move to lower latitudes

where the eddy-eddy interactions weaken (Fig. 3.19d), the spectral slope steepens as well (Fig. 3.17).

- At latitudes lower than the conversion latitude, where the Rhines scale is smaller than the conversion scale of baroclinic eddy kinetic and barotropic eddy potential energy to barotropic EKE, the eddy-mean interactions transfer the influx of energy from barotropic eddy potential energy to higher latitudes, while the eddy-eddy interactions spread it down to the Rhines scale. However, these transfers are much weaker than those at latitudes poleward of the conversion scale (Fig. 3.21).

3.3 Barotropic kinetic energy and enstrophy transfers in the atmosphere

In this study, the spectral properties of the atmospheric barotropic mode are investigated for the first time as a function of latitude using NCEP reanalysis data (Sec. 2.2.1). This is different than previous studies, which investigated the global spectral behavior of the atmosphere at different pressure levels (Boer and Shepherd, 1983; Shepherd, 1987b; Trenberth and Solomon, 1993; Burgess et al., 2013) or observed the vertical average eddy fields (Straus and Ditlevsen, 1999). The reanalysis data enables studying the barotropic mode in a more realistic framework than previous idealized studies, as it provides the best available realization of the observed atmospheric dynamics.

The barotropic EKE (Eq. 2.5) and eddy potential enstrophy (Z) zonal spectra,

$$\mathrm{bZ}_k = \left\langle |[q]'_k|^2 \right\rangle, \tag{3.7}$$

are calculated around each latitude circle (Saltzman, 1957), where angle and squared brackets denote a time mean and vertical average, respectively, primes represent deviation from zonal mean and k is the zonal wavenumber with a corresponding wavelength (Eq. 2.11). $q = \zeta + f + \frac{\partial}{\partial p}\left(\frac{f_0^2}{S^2}\frac{\partial \psi}{\partial p}\right)$ is the QG potential vorticity (QGPV, Charney and Stern, 1962) in pressure coordinates (p), where ζ is relative vorticity, f is the Coriolis parameter, f_0 is a constant midlatitude value of f, $\psi = \frac{\phi}{f}$ is the streamfunction, where ϕ is the geopotential, and $S^2 = -\frac{1}{\rho\theta^+}\frac{\partial \widetilde{\theta}}{\partial p}$, where ρ is density, $\widetilde{\theta}$ is a reference profile of the potential temperature, and θ^+ is the deviation from that reference profile (Hoskins et al., 1985; Vallis, 2006). For studying the spectral behavior of the zonal barotropic EKE, three terms of its tendency equation are computed; the baroclinic to barotropic conversion (Eq. 2.9), the eddy-mean flow interactions (Eq. 2.7), and the eddy-eddy interactions (Eq. 2.6). A fourth term that denotes the conversion of barotropic eddy potential energy to EKE is less relevant for studying the interactions among different scales (Fig. 6.1 in appendix 6.1). Similar terms are, respectively, computed for the Z tendency equation;

$$qCT = -\mathrm{Re}\left\langle [q]^{'*}_k \left[\mathbf{u}^+ \cdot \nabla q^+\right]'_k \right\rangle, \tag{3.8}$$

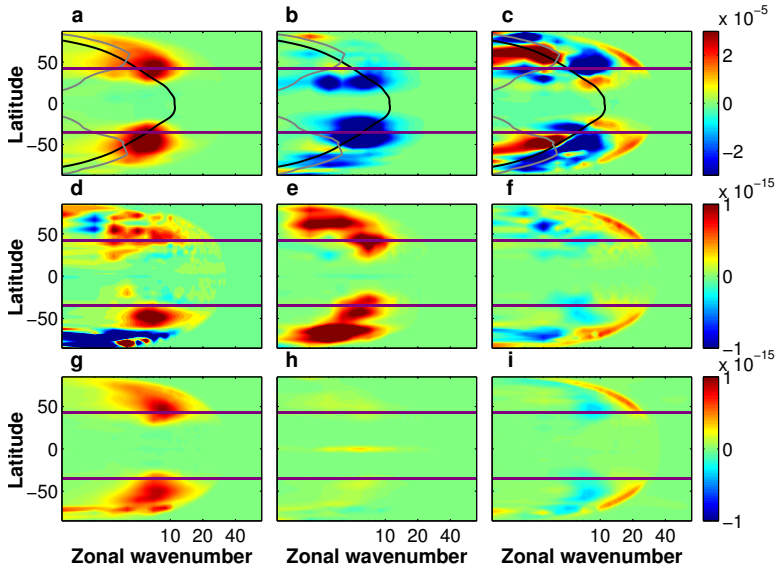

Figure 3.23: Components of the barotropic EKE equation (first row, a-c, m^2s^{-3}) and Z equation (s^{-3}) using QGPV (second row, d-f) and QGPV with constant f and S^2 (third row, g-i) as a function of latitude and zonal wavenumber. (a) conversion of baroclinic EKE divided by 5 (Eq. 2.9); (b) EKE eddy-mean flow interactions (Eq. 2.7); (c) EKE eddy-eddy interactions (Eq.2.6); (d) and (g) Z conversion of baroclinic to barotropic (Eq. 3.8); (e) and (h) Z eddy-mean flow interactions (Eq. 3.9); (f) and (i) Z eddy-eddy interactions (Eq. 3.10). The gray and black lines in panels a-c are the Rossby and Rhines wavenumbers, respectively. The purple lines are the supercriticality latitude, where the QG-supercriticality equals one. Each component is multiplied by the zonal wavenumber.

$$qEM = -\mathrm{Re}\Big\langle [q]_k'^{*}\big(\overline{[\mathbf{u}]}\cdot\nabla[q]' + [\mathbf{u}]'\cdot\nabla\overline{[q]}\big)_k\Big\rangle, \tag{3.9}$$

and,

$$qEE = -\mathrm{Re}\Big\langle [q]_k'^{*}\big([\mathbf{u}]'\cdot\nabla[q]'\big)_k\Big\rangle. \tag{3.10}$$

Eqs. 3.8-3.10 also include the spherical metric terms as described in Sec 2.3. On one hand, the one-dimensional Fourier analysis allows investigating the meridional structure of the barotropic mode, and the important zonal macroturbulent scales. On the other hand, it contains the lateral transport of EKE and Z among different latitudes. These transfers are found to be less important than the transfers calculated in Eqs. 2.6-2.9 (Fig. 6.2 in appendix 6.1). The isotropic nature of small scale eddies (e.g., Shepherd, 1987b) may suggest that energy transfers to different energetic zonal wavenumbers represent similar transfers in total wavenumber space.

3.3.1 Barotropization of EKE

The main source of EKE in the barotropic mode, is the conversion from all baroclinic modes to the barotropic mode (barotropization, Fig. 3.23a). The barotropization of the flow spans the entire extratropics, with a maximum value at midlatitudes. The non-monotonic behavior of the barotropization with latitude may be explained using Held and Larichev (1996) scaling

theory; the barotropization should increase with the barotropic root mean square velocity ($U_{\rm rms}$), vertical shear of the zonal wind (u_z) and the Coriolis parameter (f), and decrease with increasing stratification ($N^2 = \frac{g}{\theta}\frac{\partial\theta}{\partial z}$, where g is gravity) and tropopause height (H). As some of the parameters are affected by processes in the energy cycle, the understanding of cause and effect is limited. Furthermore, different than previous modeling studies (e.g., Held and Larichev, 1996; Smith and Vallis, 2001, 2002; Thompson and Young, 2007; Venaille et al., 2012), the reanalysis data cannot provide systematic investigation of the relative importance of the above parameters in affecting the latitudinal behavior of the barotropization. Thus, it is elucidated based on the relations found in these studies. Fig. 3.24 shows the dependence of the mean barotropization on the above zonal mean parameters. The mean barotropization in Fig. 3.24 is calculated as the sum of the barotropization through all wavenumbers at latitudes where the mean barotropization is larger than 30% of its maximum value. Thus, each circle corresponds to a specific latitude, where blue (red) circles correspond to latitudes poleward (equatorward) of the latitude of maximum mean barotropization and closed (open) circles correspond to the northern (southern) hemisphere.

In the ocean, the EKE is surface intensified and thus limits the baroclinic-barotropic transfer. This was suggested to occur due strong stratification in both oceanic models (Smith and Vallis, 2001; Fu and Flierl, 1980) and at low latitudes in reanalysis data (Chemke and Kaspi, 2016b). In the atmosphere, since the stratification increases poleward (Fig. 3.24a), an inverse relation with the barotropization (as suggested by Held and Larichev, 1996) is found only at high latitudes (blue circles, Fig. 3.24a), which follows $N^{-10.2\pm1.3}$ (the $\pm$ denotes its 95% confidence interval and $R^2 = 0.92$). This suggest the stratification might only explain the decrease of the barotropization at high latitudes (Fig. 3.23a).

The barotropic EKE, which is used for calculating $U_{\rm rms}$, indeed tends to increase the barotropization in both hemispheres (open and closed circles, Fig. 3.24b), but it has low statistical significance, and shows stronger dependence in the northern hemisphere (NH)($\propto$ bEKE$^{0.74\pm0.37}$ and $R^2 = 0.48$, closed circles) than in the southern hemisphere (SH) ($\propto$ bEKE$^{0.1\pm0.23}$ and $R^2 = 0.05$, open circles). While the vertical shear of the zonal wind barely changes in the SH (open circles, Fig. 3.24c), due to the double jet structure in the extratropics, and at low latitudes in the NH (closed red circles), it tends to increase the barotropization at high latitudes in the NH ($\propto u_z^{1.54\pm0.2}$ and $R^2 = 0.96$, closed blue circles). The large differences between the two hemispheres in the dependence of the barotropization on the barotropic EKE and vertical shear, suggests that they are less likely to explain the symmetric behavior of the barotropization in both hemispheres (Fig. 3.23a).

A direct relation between the Coriolis parameter and barotropization occurs only at low latitudes (red circles, Fig. 3.24d) where the barotropization increases, and follows $f^{1.86\pm0.27}$ ($R^2 = 0.93$). As the tropopause height decreases with latitude in the extratropics, it presents an inverse relation with the barotropization only at low latitudes (red circles, Fig. 3.24e), which follows $H^{-2.86\pm0.73}$ ($R^2 = 0.82$). Following the World Meteorological Organization (WMO) definition, the tropopause height is defined as the lowest height where the mean lapse rate is

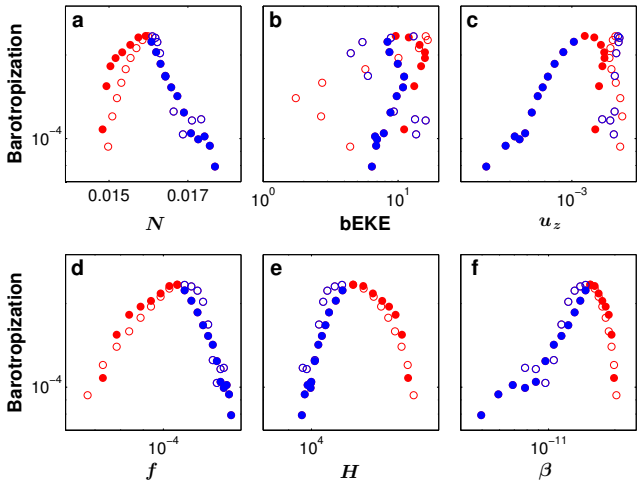

Figure 3.24: Mean baroclinic to barotropic EKE conversion (m^2s^{-3}) for different latitudes in the extratropics as a function of (a) mean static stability (N, s^{-1}), (b) barotropic EKE ($bEKE$, m^2s^{-2}), (c) vertical shear of the zonal wind (u_z, s^{-1}), (d) Coriolis parameter (f, s^{-1}), (e) tropopause height (H, m), and (f) β-term (β, $m^{-1}s^{-1}$). Each circle represents a specific latitude. The blue (red) circles correspond to latitudes poleward (equatorward) of the latitude of maximum mean barotropization. The closed (open) circles correspond to the northern (southern) hemisphere.

$2\,\mathrm{Km}^{-1}$. The β-term (meridional derivative of the Coriolis parameter) affects the barotropization only at high supercriticality, where due to an inverse energy cascade it enters the energy-containing scale (e.g., the Rhines scale, Held and Larichev, 1996). The purple lines in Fig. 3.23 (supercriticality latitudes) mark the meridional transition between vertically averaged values of QG-supercrticality ($S_c = \frac{f^2 u_z}{\beta H N^2}$, following Held and Larichev, 1996) above and below unity. Thus, only at high latitudes (where the QG-supercriticality increases above unity) the β-term might affect the barotropization. As the β-term decreases with latitude it shows a direct relation to barotropization (as was shown in Smith and Vallis, 2001) at high latitudes (blue circles, Fig. 3.24f), which follows $\beta^{1.1\pm0.17}$ ($R^2 = 0.88$). This is different than the inverse relation found in Held and Larichev (1996), at high supercriticality. At low latitudes, on the other hand, there is an inverse relation between the β-term and barotropization. In this subcritical region, the eddy-mean interactions play a crucial role in the balance and the eddy-eddy interactions are weaker (Fig. 3.23b and c and Sec. 3.3.2). Venaille et al. (2012) showed that the opposite effect of the β-term on barotropization is due to the tendency of large meridional PV gradient to overcome the layer-wise conservation of eddy PV (Sec. 3.3.3), which encourages a depth-independent flow only in a turbulent regime (i.e., where the QG-supercriticality is above unity) and a depth-dependent flow in a Rossby wave regime (i.e., where the QG-supercriticality is below unity). In summary, at low latitudes, the increase of the barotropization may be explained by the increase and decrease of the Coriolis parameter and the tropopause height, respectively. At high latitudes, on the other hand, the increase of the stratification together with the decrease of the β-term, may explain the decrease of the barotropization.

According to the Rhines-Salmon two-layer phenomenology, the barotropization of the flow should occur at the Rossby wavenumber. However, through all latitudes the Rossby wavenum-

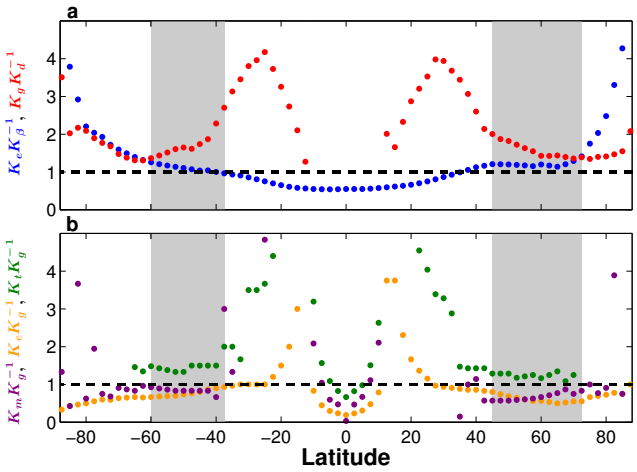

Figure 3.25: Ratios of macroturbulent wavenumbers as a function of latitude. (a) The ratio of the conversion and Rossby wavenumbers (red circles), and the ratio of the energy-containing and Rhines wavenumbers (blue circles). (b) The ratio of the energy-containing and conversion wavenumbers (orange circles), the ratio of the transition (see text for definition) and conversion wavenumbers (green circles), and the ratio of the most unstable and conversion wavenumbers (purple circles). The shaded areas represent latitudes where an explicit inverse energy cascade occurs according to Fig. 3.23c.

ber (gray line in Fig. 3.23) is smaller than the conversion wavenumber (red circles in Fig. 3.25a), which is defined as the wavenumber of maximum baroclinic-barotropic conversion at each latitude (from Fig. 3.23a). The Rossby wavenumber is calculated using Eq. 2.11, and the Rossby wavelength using Eq. 2.14. Since at these scales baroclinic instability is expected to produce EKE (Eady, 1949; Salmon, 1978), the most unstable wavenumber (K_m) is calculated following Smith (2007), by preforming a QG linear stability analysis, and compared to the conversion wavenumber (purple circles, Fig. 3.25b). Different than the Rossby wavenumber, the most unstable wavenumber does follow the conversion wavenumber through all latitudes, especially in the SH. Similar behavior was shown to occur in both atmospheric idealized GCMs (Chemke and Kaspi, 2015a, 2016a; Jansen and Ferrari, 2012) and oceanic reanalysis (Chemke and Kaspi, 2016b). Thus, the barotropization of the flow is likely concentrated at midlatitudes since it is coupled to baroclinic instability (Salmon, 1978; Vallis, 2006), which is mostly important at midlatitudes, and due to the latitudinal dependence of the sphericity parameters, stratification and tropopause height.

3.3.2 Inverse energy cascade in the barotropic mode

The input of barotropic energy from the baroclinic modes is transferred by advection among different scales. The barotropic eddy-mean flow interactions remove this input of energy and transfer it directly to the zero zonal wavenumber (Fig. 3.23b), which maintains the barotropic zonal mean eddy-driven jets (Held, 1975; Simmons and Hoskins, 1978). While in the NH the eddy-mean flow interactions are localized around 25°N, in the SH they are spread at midlatitudes with a maximum around 42°S. Different than the global stratospheric analysis of Burgess

et al. (2013), here the barotropic eddy-mean flow interactions do not add EKE to other scales beside the zero zonal wavenumber. Eddy-eddy interactions also play a major role in the balance, but only at high latitudes (Fig. 3.23c), as was also shown in idealized atmospheric GCM simulations (Chemke and Kaspi, 2015a, 2016a) and oceanic reanalysis data (Chemke and Kaspi, 2016b). A classic 2D-turbulence picture emerges at these latitudes, where the eddy-eddy interactions spread the input of EKE from the baroclinic modes both upscale and down scale. Similar behavior was shown to occur globally using a 2D spectra of reanalysis data (Boer and Shepherd, 1983; Shepherd, 1987b; Straus and Ditlevsen, 1999; Burgess et al., 2013). The presence of eddy-eddy interactions at high latitudes may also contribute to the decrease in barotropization at these latitudes (Chemke and Kaspi, 2016a).

Barotropic inverse energy cascade occurs when the conversion of baroclinic to barotropic wavenumber is larger than the energy-containing wavenumber (K_e, defined at each latitude as the wavenumber where the spectrum of the barotropic meridional velocity is at maximum, O'Gorman and Schneider, 2008c; Kidston et al., 2011; Chemke and Kaspi, 2016a). Indeed, the conversion wavenumber exceeds the energy-containing wavenumber (orange circles, Fig. 3.25b) at latitudes where, according to Fig. 3.23c, inverse energy cascade takes place (shaded areas in Fig. 3.25). At higher latitudes, the conversion wavenumber is still larger than the energy-containing wavenumber, however inverse energy cascade is suppressed since the input of energy from the baroclinic modes vanishes (Fig. 3.23a). At lower latitudes in the extratropics these scales almost coincide, which limits the inverse energy-cascade. Furthermore, despite the effect of bottom drag on the energy-containing scale (e.g., Danilov and Gurarie, 2002; Smith and Vallis, 2002; Thompson and Young, 2007), the Rhines and energy-containing wavenumbers coincide at latitudes of inverse cascade (blue circles, Fig. 3.25a) as expected from Rhines (1975)'s theory and was shown to occur in both idealized GCM simulations (Jansen and Ferrari, 2012; Chai and Vallis, 2014; Chemke and Kaspi, 2016a) and oceanic reanalysis data (Chemke and Kaspi, 2016b). This is also evident by the fact that the Rhines wavenumber follows the inverse energy transfer of eddy-eddy interactions (Fig. 3.23c). The Rhines wavenumber is calculated using Eq. 2.11, where the Rhines wavelength using Eq. 2.13 (Rhines, 1975).

As the Rossby and conversion wavenumbers do not match, the supercriticality latitudes (purple lines in Fig. 3.23) do not follow latitudes where the Rossby and Rhines wavenumbers coincide (the crossing of the gray and black lines in Fig. 3.23). Nonetheless, latitudes where inverse energy cascade is observed are separated by the supercriticality latitudes (Fig. 3.23c), which can explain its occurrence only at high latitudes (Chemke and Kaspi, 2015a). This addition of barotropic EKE to large scales only at high latitudes, contributes the barotropic nature of the eddy-driven jet.

Despite the pronounced inverse energy cascade in both hemispheres (Fig. 3.23c), the zonal barotropic EKE spectrum (Eq. 2.5) follows a $-5/3$ slope at large scales only in the NH, while in the SH a steeper slope between -2.5 and -3, as was found globally in Straus and Ditlevsen (1999) (orange lines in Figs. 3.26a, 3.26c and 3.26e). However, in both hemispheres the slopes have low statistical significance. The slopes are determined at each latitude through linear

least-squares fitting of the spectrum in log-log space. The fitting algorithm finds the best-fit slopes below the energy-containing wavenumber and till the dissipation range, where the spectrum rapidly declines. Due to the small scale separation between the energy-containing (blue asterisks, Fig. 3.26) and conversion (red circles, Fig. 3.26) wavenumbers, there is no significant region where the spectrum follows $k^{-5/3}$, which causes the large uncertainty in the slopes' values at high latitudes (Fig. 3.26e). Furthermore, the broad input of baroclinic EKE (Fig. 3.23a) may explain the steeper slopes in the SH at large scales (Larichev and Held, 1995).

At low latitudes the upper branch of the spectrum ranges between a slope of -2.5 and -3.8 (orange lines in Figs. 3.26b, 3.26d and 3.26e). In 2D-spectra analysis the tropics contribute more to the resulted spectrum, which might explain why previous reanalysis 2D-spectra studies (e.g., Boer and Shepherd, 1983; Trenberth and Solomon, 1993; Burgess et al., 2013) showed a similar range of slopes through all heights. A steeper slope than the -3 slope, expected from 2D-turbulence (Kraichnan, 1967), is also found at smaller scales at high latitudes, where the spectrum follows a -4 slope (green lines in Figs. 3.26a, 3.26c and 3.26e), which might occur due to the parameterizations of bottom drag and dissipation processes in the reanalysis (Rivière et al., 2004; Thompson and Young, 2006; Arbic and Scott, 2008; Jansen and Held, 2014). Similar to several previous studies (Boer and Shepherd, 1983; Shepherd, 1987b; Trenberth and Solomon, 1993; Straus and Ditlevsen, 1999) there is no signature of a shallower spectral slope in mesoscales as found by Nastrom and Gage (1985), and was shown to occur in both 1D (Koshyk and Hamilton, 2001; Hamilton et al., 2008) and 2D spectra (Burgess et al., 2013; Hamilton et al., 2008). This may be explained by the fact that the shallower slope in mesoscales was found to occur mostly in the stratosphere (Burgess et al., 2013), while the barotropic spectrum in Fig. 3.26 includes all heights. Even though the spectral slopes do not show the classic behavior of 2D-turbulence, the transition wavenumber (K_t), which separates the two slopes at each latitude, implies the existence of two turbulent regimes at smaller and larger wavenumbers. The transition wavenumber is found to follow the conversion wavenumber mostly at high latitudes, where inverse energy cascade takes place (green circles, Fig. 3.25b). This may indicate that the forward Z and inverse energy cascade at large and small wavenumbers by eddy-eddy interactions (Fig. 3.23c), are triggered by the barotropization of the flow (Fig. 3.23a).

3.3.3 Barotropic eddy enstrophy balance

Similar to the barotropization of EKE, the Z also undergoes barotropization in the extratropics, reaching a maximum value at midlatitudes (Fig. 3.23d). In spite of the layer-wise conservation of QG potential enstrophy in pressure coordinates, the mean meridional PV gradient together with diabatic heating and dissipation terms enable the barotropization of the Z mostly poleward of the supercritical latitude (Venaille et al., 2012). Concomitantly, the eddy-eddy interactions transfer the Z to smaller scales (forward cascade, Fig. 3.23f) as expected from the two-layer baroclinic turbulence phenomenology (Rhines, 1977; Salmon, 1978). Forward Z cascade, calculated using the relative vorticity alone, was also shown to occur in 2D-spectra analysis (Boer

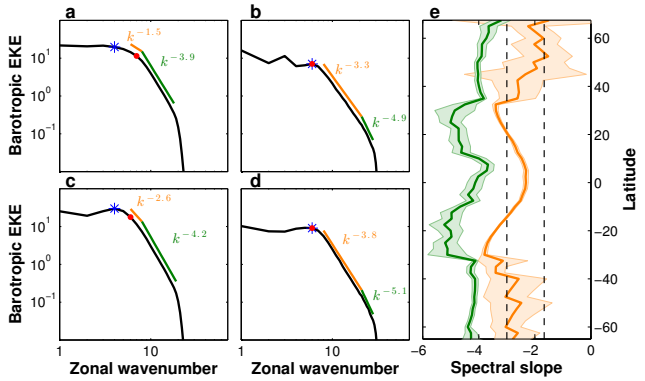

Figure 3.26: The zonal spectrum of the barotropic EKE (m^2s^{-2}) as a function of zonal wavenumber at (a) 52°N (b) 27°N (c) 52°S and (d) 27°S. The blue asterisk and red dot are the energy-containing wavenumber and conversion wavenumber of baroclinic to barotropic EKE, respectively. The orange and green lines are the best linear fit slopes. (e) The spectral slopes as function of latitude with shading representing the 95% confidence intervals. The two vertical dashed lines correspond to the -5/3 and -3 slopes.

and Shepherd, 1983; Straus and Ditlevsen, 1999; Burgess et al., 2013). Similar to the inverse energy cascade (Fig. 3.23c), forward Z cascade occurs poleward of the supercriticality latitudes, pointing to the importance of the supercriticality in assessing the role of eddy-eddy interactions in the atmosphere. The forward Z cascade latitudinal distribution might be also related to the filamentation of PV in critical latitudes (Thorncroft et al., 1993).

Most of the barotropic Z transfers occurs from the mean flow to the eddies (Fig. 3.23e). The dominant term in Eq. 3.9, which is responsible for most of this Z transfer is $-[v]'[q]'\frac{\partial[q]}{a\partial\vartheta}$ (Fig. 3.23e). This term contributes to the growth of waves (increases Z) as it is everywhere positive (Held, 1975; Held and Hoskins, 1985). As the meridional gradient of the QGPV is everywhere positive, the meridional flux, $[v]'[q]'$, must be everywhere negative (downgradient), and this may occur if it is diffusive (Green, 1970; Held and Larichev, 1996). In the Rhines-Salmon phenomenology, the eddy-mean flow interactions do not play a major role in the balance as the Coriolis parameter and static stability were taken as constants (i.e., small meridional QGPV gradient). Repeating the calculations of the Z transfers (Eqs. 3.8-3.10) for the QGPV only with constant f and S^2, shows similar picture to the classic two-layer phenomenology, where the main balance of Z in the barotropic mode is between the barotropization and the forward Z cascade (Fig. 3.23g-i). Thus, in Earth's atmosphere, the significant meridional QGPV gradient strengthens the role of eddy-mean flow interactions in adding Z to the eddies, at the expense of the baroclinic-barotropic transfer.

3.4 The latitudinal dependence of the oceanic barotropic eddy kinetic energy and macroturbulence energy transport

Using high-resolution satellite data, there has been extensive effort to understand the energy spectral fluxes at the ocean surface (e.g., Scott and Wang, 2005; Schlösser and Eden, 2007;

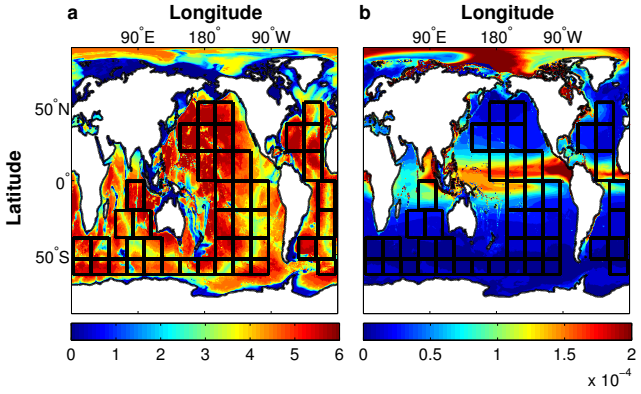

Figure 3.27: a. The bathymetry of the ocean (km) and b. the mean static stability (s^{-2}, see text for definition). The black boxes show the regions used for the analysis.

Bühler et al., 2014; Klocker and Abernathey, 2014). As these fluxes mostly represent the first baroclinic mode (Wunsch, 1997), Stammer (1997) argued using altimetric data, that the energy-containing scale at the surface follows the first deformation radius. Scott and Wang (2005) found an inverse energy cascade at the ocean surface, which differs from the forward cascade in the first baroclinic mode in the Rhines-Salmon phenomenology. Several modeling studies have verified this finding (Schlösser and Eden, 2007; Scott and Arbic, 2007).

Different than these studies, here we focus on understanding the behavior of the oceanic energy fluxes in the barotropic mode. The high-resolution modern state estimate provides an opportunity to examine our understanding of the energy cycle in the barotropic mode in the ocean. While previous studies investigated the barotropic mode using models (e.g., Fu and Flierl, 1980; Smith and Vallis, 2001; Venaille et al., 2011), the high-resolution ECCO2 data synthesizes our best physical understanding of the ocean with observations (Sec. 2.2.2). Thus, in this study the theoretical geostrophic turbulence picture can be more realistically examined, as more realistic components (e.g., bottom topography, wind forcing) are taken into account. The global coverage of the ECCO2 also allows studying the barotropic spectral fluxes as a function of latitude. The latitudinal dependence found using the ECCO2 in this study, which shows 'classic' barotropic behavior only at high latitudes, was found recently to occur in atmospheric GCM simulations as well (Chemke and Kaspi, 2015a).

For calculating the energy spectrum and spectral fluxes in the barotropic mode, a 2D Fourier decomposition is implemented on 43 land-free regions with 96 grid points in the zonal direction (i.e., 23.75° wide), and with the same width in the meridional direction (Fig. 3.27). While smaller regions do not entirely capture the energy-containing scale, larger regions do not add information for the scale analysis discussed in this paper. As discussed in Scott and Wang (2005), even though the ocean does not have periodic boundary conditions, assumed for the Fourier analysis, the results are robust over different region sizes. Similar to Scott and Wang (2005) and Schlösser and Eden (2007) a Hamming window is applied prior to the Fourier decomposition, and the resulted data is smoothed with a 20-point running mean. As the strongest spatial variations of the barotropic mode occur in the meridional direction, the longitudinal variations of the barotropic mode are beyond the scope of this paper, and unless otherwise

stated, the analysis is implemented on each region and the results show their zonal mean.

The spectrum of the barotropic eddy kinetic energy (EKE) is calculated as follows,

$$\mathrm{bEKE}_K = \left\langle |[u]'_K|^2 + |[v]'_K|^2 \right\rangle, \tag{3.11}$$

where u and v are the zonal and meridional velocities, angle brackets denote a time mean, squared brackets denote a vertical average, and prime denotes the deviation from zonal mean of each region. The subscript K denotes the spectral components with a total horizontal wavenumber $K = \sqrt{k_x^2 + k_y^2}$ (wavelength, $L = K^{-1}$), where k_x and k_y are the zonal and meridional wavenumbers, respectively. For studying the eddy behavior in the barotropic mode, each field is first vertically averaged prior to the computation of the deviation from zonal mean. Two components of the barotropic EKE tendency equation are studied here, the conversion of baroclinic to barotropic EKE,

$$CT = \left\langle -[\mathbf{u_h}]'^{*}_K \cdot \left[\mathbf{u}^{+} \cdot \nabla \mathbf{u}^{+}_{\mathbf{h}}\right]'_K \right\rangle, \tag{3.12}$$

and the nonlinear eddy-eddy interactions,

$$EE = \left\langle -[\mathbf{u_h}]'^{*}_K \cdot \left([\mathbf{u}]' \cdot \nabla [\mathbf{u_h}]'\right)_K \right\rangle, \tag{3.13}$$

where $\mathbf{u}$ denotes the three dimensional velocity vector, * denotes a complex conjugate, the subscript h denotes the horizontal components of the vector, and $^+$ denotes deviation from vertical average. Eqs. 3.12 and 3.13 are calculated in spherical coordinates.

3.4.1 Barotropization at high latitudes

Although the fundamental theory of geostrophic turbulence (Rhines, 1977; Salmon, 1978; Fu and Flierl, 1980) was found to be suitable for QG two-layer models (e.g., Larichev and Held, 1995) and continually stratified models (e.g., Smith and Vallis, 2001, 2002), the barotropic behavior of the flow shows a strong latitudinal dependence in GCMs (Venaille et al., 2011; Chemke and Kaspi, 2015a). The ECCO2 analysis reveals a similar latitudinal behavior in the ocean (Fig. 3.28). The barotropization of the flow (conversion of baroclinic to barotropic EKE) mostly occurs at high latitudes, poleward of 40° (Fig. 3.28a), with a corresponding inverse energy cascade by eddy-eddy interactions at these latitudes (Fig. 3.28b). Note, that different than the two-layer phenomenology (e.g., Salmon, 1978; Larichev and Held, 1995), here the conversion from baroclinic to barotropic may involve multiple baroclinic modes and not only the first baroclinic mode.

What causes the barotropization of the flow to be more pronounced at high latitudes? The factors that mostly affect barotropization processes according to the scaling theory of Held and Larichev (1996), in addition to bottom topography, are the r.m.s barotropic velocity (U_{rms}), the Coriolis parameter (f) and its meridional derivative (β), the stratification (N^2) and zonal shear

(u_z). Several studies showed that bottom friction inhibits the barotropization of the flow and weakens the barotropic inverse energy cascade (Treguier and Hua, 1988; Smith and Vallis, 2002; Arbic and Flierl, 2004; Arbic et al., 2007; Scott and Arbic, 2007; Venaille et al., 2011). However, as steep bottom topography exists through all latitudes (Fig. 3.27a), while the strongest barotropization occurs at high latitudes, particularly in the southern ocean (Fig. 3.28a), bottom topography does not explain the strong barotropization of the flow at high latitudes. This can be further seen by comparing the dependence of barotropization (B_t, calculated as the maximum conversion of baroclinic to barotropic EKE), on bathymetry variance (B_v) through all regions (Fig. 3.29a). Even though an inverse relation between barotropization and bathymetry variance might be expected, the variations in bathymetry have a low effect on barotropization, with even a small tendency to increase it ($B_t \propto B_v^{0.83}$, Fig. 3.29a). Nonetheless, bottom topography may still play a significant role in the balance, as the spatial (Beckmann et al., 1994; Böning et al., 1996; Smith et al., 2000; Jansen and Held, 2014) and vertical resolutions at depth (Sec. 2.2), and the different parameterizations of bottom drag (Rivière et al., 2004; Thompson and Young, 2006; Arbic and Scott, 2008), may affect both the dissipation of energy and the stratification of the flow.

Previous studies showed that similar to bottom topography, near-surface stratification also tends to weaken the barotropization (Fu and Flierl, 1980; Smith and Vallis, 2001, 2002). While uniform stratification results in an efficient barotropization from all baroclinic modes, non-uniform stratification results in energy transfers from high baroclinic modes to the first mode, and from there inefficiently to the barotropic mode. Fig. 3.27b shows the mean stratification of the water column above the pycnocline, calculated using the static stability, $N^2 = \frac{g}{\rho_0}\frac{\partial \rho_\theta}{\partial z}$, following Chelton et al. (1998), where g is gravity, ρ_0 is background density and ρ_θ is the potential density. The strongest stratification occurs at low latitudes, while it is weaker and hence more uniform at high latitudes. The strong barotropization at high latitudes, may imply that its latitudinal variation is affected by the stratification (Fig. 3.28a). As the largest stratification occurs near the ocean surface, its latitudinal variations are less affected by bottom topography. By comparing the dependence of barotropization (B_t), on stratification (N^2), the stratification clearly decreases the barotropization ($B_t \propto N^{-2.4}$, Fig. 3.29b).

Similar to the barotropization, the U_{rms} (defined as bEKE$^{0.5}$) is also larger at high latitudes. Large values of barotropic EKE may imply a stronger energy cycle at these latitudes. The barotropic EKE indeed tends to increase the barotropization ($B_t \propto bEKE^{0.93}$, Fig. 3.29c). The vertical shear of the zonal flow also weakly increases the barotropization, but it is not statistically significant ($B_t \propto u_z^{0.8}$, Fig. 3.29d). The sphericity parameters (the Coriolis parameter and its meridional derivative), on the other hand, may also explain the latitudinal dependence of the barotropization, as the Coriolis parameter and the β-effect tend to increase and decrease the barotropization of the flow, respectively ($B_t \propto f^2\beta^{-5.3}$, Fig. 3.29e and f). Thus, the main factors affecting the latitudinal variations of the barotropization are the stratification, sphericity of the planet and barotropic EKE.

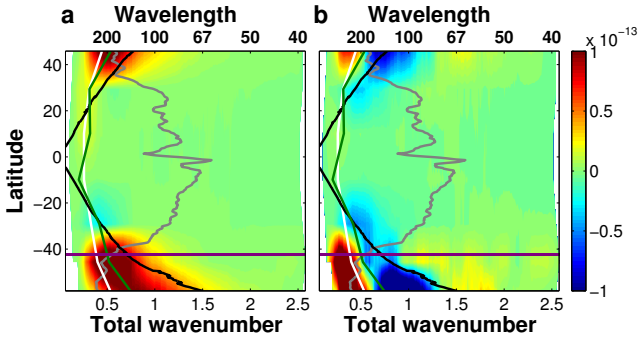

Figure 3.28: Components of the barotropic EKE equation (m^2s^{-3}, Eqs. 3.12 and 3.13) as a function of latitude and total wavenumber ($10^{-5}\,m^{-1}$) and wavelength (km). a. conversion from baroclinic EKE to barotropic EKE divided by 5. b. transfer of barotropic EKE by eddy-eddy interactions. The black, gray, green and white lines are the Rossby $\left(K_d = (2\pi L_d)^{-1}\right)$, Rhines $\left(K_\beta = (2\pi L_\beta)^{-1}\right)$, conversion ($K_g$) and energy-containing (K_e) wavenumbers, respectively. The purple line shows the latitude where poleward (equatorward) of it the QG supercriticality is larger (smaller) than one. The white areas represent unresolved large and small scales at different latitude bands. Each component is multiplied by the wavenumber.

3.4.2 Barotropic inverse energy cascade

The strong barotropization at high latitudes, does not necessarily ensure a barotropic inverse energy cascade at these latitudes as well. For an inverse energy cascade to occur, there must be a scale separation between the conversion scale of baroclinic to barotropic EKE and the energy-containing scale (Salmon, 1978). Indeed, the inverse energy cascade at high latitudes (Fig. 3.28b) is consistent with a scale separation between the conversion wavenumber of baroclinic to barotropic EKE (K_g, green line in Fig. 3.28) and the energy containing wavenumber (K_e, white line in Fig. 3.28). The energy-containing and conversion wavenumbers are defined as the wavenumbers where the barotropic energy spectrum (Eq. 3.11) and the conversion of baroclinic to barotropic EKE (Fig. 3.28a and Eq. 3.12) are at maximum, respectively. At lower latitudes, the energy-containing wavenumber and the conversion wavenumber of baroclinic to barotropic EKE nearly coincide. To better understand the latitudinal dependence of these scales, we now investigate different parameterizations for them.

Different than the classic Rhines-Salmon phenomenology, the region-averaged Rossby deformation wavenumber does not coincide with the conversion wavenumber (black and green lines in Fig. 3.28a and red dots in Fig. 3.30a). The Rossby deformation wavenumber is defined as, $K_d = (\lambda_d)^{-1}$, where λ_d is the Rossby deformation wavelength calculated using Eq. 2.14 (Scott and Wang, 2005; Abernathey and Wortham, 2015). Following Smith (2007), we calculate the most unstable wavenumber (K_m) by applying a linear normal-mode instability analysis on the linearized quasi-geostrophic (QG) potential vorticity equation. Using the region-averaged time mean flow, density and meridional potential vorticity gradient, the eigenvalues are calculated at each region presented in Fig. 3.27. As discussed in Smith (2007), for accounting only the energetically important wavenumbers the growth rate is normalized by the eddy available potential energy, which is calculated using the variance of the potential temperature field (e.g., Lorenz,

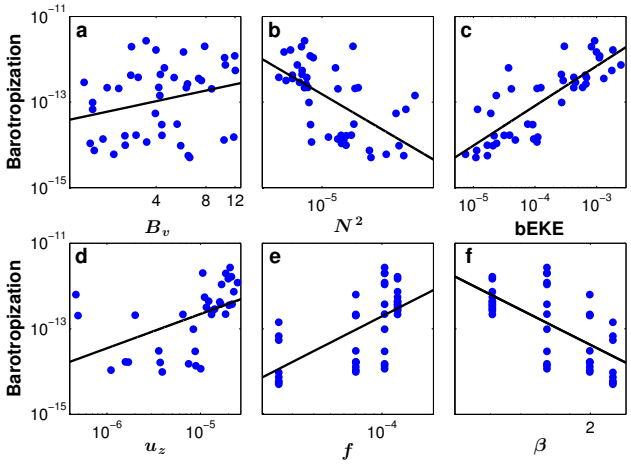

Figure 3.29: Maximum baroclinic to barotropic EKE conversion (B_t, $\mathrm{m^2 s^{-3}}$) at each region presented in Fig. 3.27 as a function of a. the variance of bathymetry (B_v, $10^5\,\mathrm{m}$), b. the mean static stability (N^2, $\mathrm{s^{-2}}$), c. the barotropic eddy kinetic energy ($bEKE$, $\mathrm{m^2 s^{-2}}$), d. the vertical shear of the zonal flow (u_z, $\mathrm{s^{-1}}$), e. the Coriolis parameter (f, $\mathrm{s^{-1}}$) and f. the meridional derivative of the Coriolis parameter (β, $10^{-11}\,\mathrm{m^{-1} s^{-1}}$). The black lines represent the best fits, and follow 0.83 ± 0.96 ($R^2 = 0.068$), -1.2 ± 0.4 ($R^2 = 0.36$), 0.93 ± 0.2 ($R^2 = 0.67$), 0.8 ± 0.5 ($R^2 = 0.24$), 2 ± 0.8 ($R^2 = 0.36$) and -5.3 ± 2 ($R^2 = 0.4$) slopes in panels a-f, respectively, where the errors represent the 95% confidence interval.

1955; Saltzman, 1957; Boer, 1975). The conversion wavenumber does coincide with the most unstable wavenumber (similar to Jansen and Ferrari, 2012; Berloff and Kamenkovich, 2013b), through almost all latitudes, except at latitudes near the equator where there may not be baroclinic instability (orange dots, Fig. 3.30b). These results are different than in Schlösser and Eden (2007), where the deformation radius was found to be proportional to the conversion scale near the ocean surface. In the barotropic mode, on the other hand, at high (low) latitudes the conversion wavenumber, and hence the most unstable wavenumber (as was shown by Venaille et al. (2011) and Tulloch et al. (2011)), are smaller (larger) than the Rossby deformation wavenumber (red dots, Fig. 3.30a). The congruity of the conversion and the most unstable wavenumbers, emphasizes the role of baroclinic instability in the barotropization of the flow (Qiu et al., 2008), and may explain the increase of the conversion wavenumber with latitude (green line in Fig. 3.28a), as the main controlling parameters in baroclinic instability are the Coriolis parameter, stratification and zonal mean shear (e.g., Eady, 1949; Phillips, 1954).

In agreement with Rhines (1975), and with idealized atmospheric GCM simulations (Jansen and Ferrari, 2012; Chemke and Kaspi, 2015a), only at high latitudes where inverse energy cascade occurs (Fig. 3.28b), indeed the Rhines wavenumber, K_β, follows the energy-containing wavenumber (white and gray lines in Fig. 3.28 and blue dots in Fig. 3.30a). The Rhines wavenumber is defined as, $K_\beta = (\lambda_\beta)^{-1}$, where λ_β is the Rhines wavelength calculated using Eq. 2.13 (Scott and Wang, 2005; Abernathey and Wortham, 2015). Different than surface observations (e.g., Stammer, 1997), here the Rossby deformation wavenumber does not follow the barotropic energy-containing wavenumber (black and white lines in Fig. 3.28). Even though this picture differs from the Rhines–Salmon phenomenology, since the conversion wavenumber does not follow the Rossby deformation wavenumber, the ratio between the Rhines scale and

Rossby deformation radius does predict regions where inverse energy cascade does and does not occur (poleward and equatorward of where the black and gray lines meet in Fig. 3.28).

The QG supercriticality was suggested by Held and Larichev (1996) to follow the ratio of the Rhines scale and Rossby deformation radius. The horizontal purple line in Fig. 3.28 shows the latitude where the QG supercriticality, $S_c = \frac{f^2 u_z}{\beta H N^2}$, equals one. While in the southern ocean, values of QG supercriticality larger than one, do follow latitudes where the Rhines scale is larger than the Rossby deformation radius and where inverse energy cascade occurs (similar to Chemke and Kaspi, 2015a), in the northern ocean, on the other hand, values of QG supercriticality are everywhere smaller than one. At low latitudes, where the QG supercriticality is smaller than one and the inverse energy cascade is inhibited (Fig. 3.28b), the Rhines wavenumber is larger than the energy-containing wavenumber (blue dots in Fig. 3.30a). Several studies showed the presence of a more isotropic regime, governed by eddies, poleward of the latitude where the Rhines scale is larger than the Rossby deformation radius, while equatorward of this latitude a more wave regime (Theiss, 2004; Chelton et al., 2007; Eden, 2007; Sayanagi et al., 2008; Klocker and Abernathey, 2014). The ratio between the barotropic energy-containing zonal and meridional wavenumbers does show a mild evidence for more zonally elongated eddies at low latitudes, and more isotropic flow at high latitudes (Fig. 3.30c).

Bottom drag has also been found to decrease the energy-containing scale (Smith and Vallis, 2002; Arbic and Flierl, 2004; Thompson and Young, 2007). The energy-containing scale decreases at high latitudes on both hemispheres (white line Fig. 3.28), however, strong topographic variations occur through all latitudes. Bottom topography could also decrease the inverse energy cascade strength (Treguier and Hua, 1988; Scott and Arbic, 2007). In the southern ocean, however, where bottom topography might play an important role (Wunsch and Ferrari, 2004; Masich et al., 2015), the inverse cascade is largest (Fig. 3.28b). Thus, in spite the dominant bottom topography, the presence of strong inverse energy cascade at high latitudes, in both hemispheres, suggests the importance of the supercriticality (the sphericity parameters, stratification and vertical shear) in affecting the inverse cascade (Smith and Vallis, 2002), through the scale separation of the conversion scale (baroclinic instability) and the energy-containing scale (the Rhines effect). Again, care should be taken before ignoring the effects of bottom drag, as it may be subjected to the parameterization (Arbic and Scott, 2008) and the coarse horizontal and vertical (near the ocean floor) resolutions of the model.

3.4.3 The spectrum of the barotropic EKE

To further analyze the barotropic inverse energy cascade, the spectral slopes of the barotropic EKE (Eq. 3.11) are calculated and shown in Fig. 3.31. The spectral slopes are calculated in log-log space at each region using a linear least-squares fit algorithm, applied to find the best (largest coefficient of determination) one or two slopes for the energy spectrum, beyond the roll-off of the spectrum near the energy containing-wavenumber (K_e) and down to $1.2 \times 10^{-5}\,\mathrm{m}^{-1}$ in order to avoid fitting submesoscales. Different than the conversion of EKE from baroclinic to

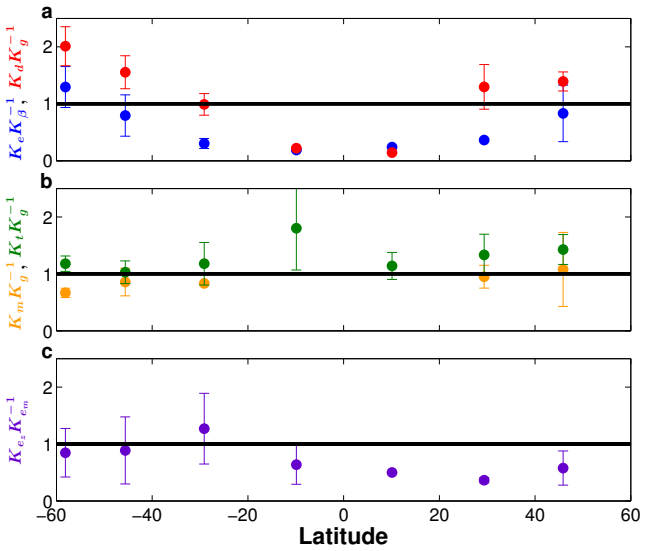

Figure 3.30: Ratio of macroturbulent scales as a function of latitude. a. The ratio of the region-averaged Rossby wavenumber (K_d) and the conversion wavenumber of baroclinic to barotropic EKE (K_g, red dots), and the ratio of the energy-containing wavenumber (K_e) and the region-averaged Rhines wavenumber (K_β, blue dots). b. The ratio of the most unstable wavenumber (K_m) and the conversion wavenumber of baroclinic to barotropic EKE (K_g, orange dots), and the ratio of the transition wavenumber (K_t) and the conversion wavenumber of baroclinic to barotropic EKE (K_g, green dots). At the two closest latitudes to the equator the ratios between the most unstable and conversion wavenumbers are off the y-axis limit. c. The ratio of the zonal (K_{e_z}) and meridional (K_{e_m}) energy-containing wavenumbers. The error bars represent the standard deviation along each latitudinal band.

barotropic and the inverse energy cascade by eddy-eddy interactions (Fig. 3.28), which intensify with latitude, the spectral slopes do not show such latitudinal behavior (Fig. 3.31).

Following the classic arguments of 2D-turbulence (Kraichnan, 1967), we expect to find at large scales of the spectrum the -5/3 slope, only at latitudes where inverse energy cascade is observed (Fig. 3.28b). However, steeper slopes than -5/3 appear through almost all latitudes, especially at high latitudes (Fig. 3.31e). Larichev and Held (1995) suggested that a broad input of baroclinic energy to the barotropic mode at large scales could affect the spectral slopes. This might explain the steeper slopes, as the conversion of baroclinic to barotropic does not occur at a specific scale, but rather through a wide range of scales (Fig. 3.28a). The spectral slope at small scales follows a -4 slope through all latitudes, which is steeper than -3 slopes of forward enstrophy cascade in 2D-turbulence (Kraichnan, 1967), likely due to dissipation processes at small scales. Near the grid scale the forward energy cascade in Fig. 3.28b may be an artifact of the coarse resolution (Jansen and Held, 2014). The transition wavenumber (K_t, the wavenumber where the slope changes discontinuously in Fig. 3.31a-d, where the two best fit segments meet) coincides with the conversion wavenumber of baroclinic to barotropic EKE, mostly in the southern ocean (red asterisk in Fig 3.31 and green dots in Fig. 3.30b). This again emphasizes that the energy source for the different behavior at small (inverse energy-cascade) and large (forward enstrophy cascade) wavenumbers is likely related to baroclinic instability.

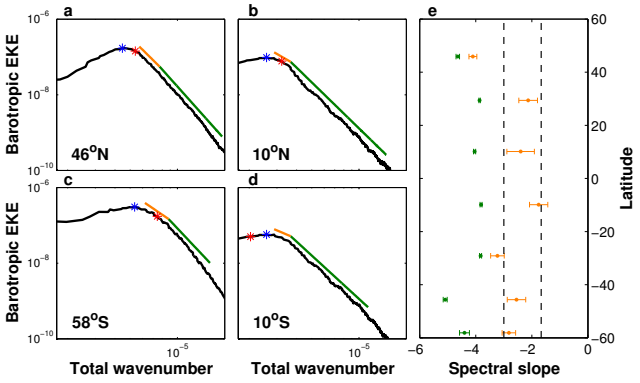

Figure 3.31: The spectrum of the barotropic EKE (m^2s^{-2}) as a function of total wavenumber (m^{-1}) for latitude bands centered at a. 46°N, b. 10°N, c. 58°S and d. 10°S. The blue and red asterisks are the energy-containing wavenumber (K_e) and the conversion wavenumber of baroclinic to barotropic EKE (K_g), respectively. The orange and green lines are the best linear fit slopes. e. The spectral slopes as function of latitude with error bars of 95% confidence interval. The two vertical dashed lines correspond to the -5/3 and -3 spectral slopes.

3.5 Atmospheric barotropic energy transfer response to global warming

The projected changes in temperature due to global warming will have a profound effect on the behavior of midlatitude eddies. Using an idealized moist global circulation model the atmospheric barotropic energy balance (Sec. 2.3) is studied over a wide range of climates. In this study, following O'Gorman and Schneider (2008a), the longwave optical thickness is increased, representing an increase of greenhouse gases, to produce a range of climates where the barotropic energy cycle is studied (Sec. 2.1.2). As the important macroturbulent scales and energy fluxes in the barotropic energy cycle depend on the thermal structure of the atmosphere, the wide range of climates provides better understanding of its behavior, with relevance for both past and future climates. Each simulation has 30 vertical sigma layers at T42 horizontal resolution (2.8° × 2.8°). Unless otherwise stated, the results represent the time average of the last 2500 days of 3500 day runs, in order to ensure that a statistically steady-state is reached. As the model is idealized (i.e., lacks land, clouds, chemical reactions, etc.) it does not capture the exact energy fluxes in warmer and colder climates, but its simplicity provides isolating the physical understanding of their behaviors in a realistic 3D framework.

3.5.1 Barotropization of the flow

The two sources of barotropic EKE are the conversion of baroclinic EKE (barotropization, Eq. 2.9) and of barotropic eddy available potential energy (Eq. 2.8). Fig. 3.32 shows these different components (right hand side in Eq. 2.4) as a function of latitude and zonal wavenumber for three different climate simulations. The conversion of baroclinic EKE, which is the main source of barotropic EKE, is concentrated in the extratropics (cf. Chemke et al., 2016a for a discussion on the latitudinal distribution of the barotropization) and reveals two interesting behaviors as the longwave optical thickness increases (first column in Fig. 3.32). First, it shows

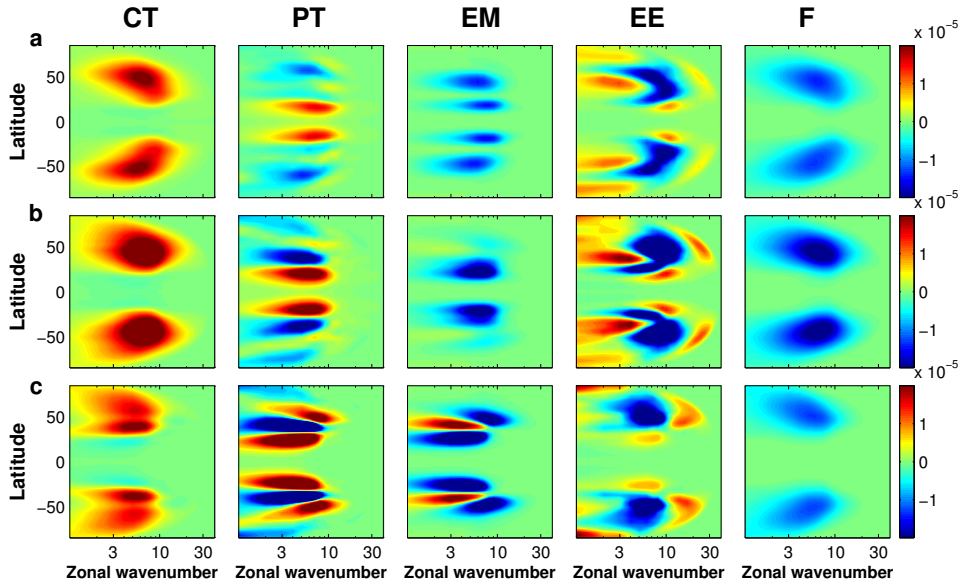

Figure 3.32: The components of the barotropic EKE equation (m^2s^{-3}) for different climate simulations with surface temperature of: (a) 272 K, (b) 287 K and (c) 306 K. Conversion of baroclinic EKE (divided by 5, Eq. 2.9) (first column), conversion of barotropic eddy available potential energy (divided by 2, Eq. 2.8) (second column), eddy-mean flow interactions (divided by 2, Eq. 2.7) (third column), eddy-eddy interactions (Eq. 2.6) (fourth column) and dissipation (divided by 5, fifth column). The red and blue colors denote addition and subtraction of barotropic EKE, respectively. As the axes are semi-logarithmic, each component is multiplied by the zonal wavenumber.

a non-monotonic behavior at midlatitudes as the climate warms. This can be further observed by summing the barotropization over all zonal wavenumbers at each latitude, which shows that it reaches a maximum value in simulations around present-day climate, and it is weaker in colder and warmer climates (Fig. 3.33a). Second, the barotropization of the flow shows a poleward shift as the climate becomes warmer (Fig. 3.33a).

3.5.1.1 The non-monotonic behavior of the barotropization

To elucidate the non-monotonic behavior of the barotropization at midlatitudes as the long-wave optical thickness increases (Fig. 3.33a), the variables controlling the barotropic-baroclinic energy transfers (CT), according to the scaling theory of Held and Larichev (1996), are investigated (Fig. 3.34),

$$CT \propto \mathrm{bEKE}^{1.5} N^{-2} u_z^2 H^{-2} f^2 \beta^{-0.5}, \tag{3.14}$$

where the barotropic EKE (bEKE) and vertical shear of the zonal wind (u_z), were found to have a direct relation with the barotropization, and the static stability (N) and tropopause height (H), were found to have an inverse relation with the barotropization. f and β are the Coriolis parameter and its meridional derivative, respectively, which do not vary between these simulations. Although some deviations from the scaling theory were found (e.g., Thompson and Young, 2006, 2007), it still allows some understanding of the behavior of the barotropization, as

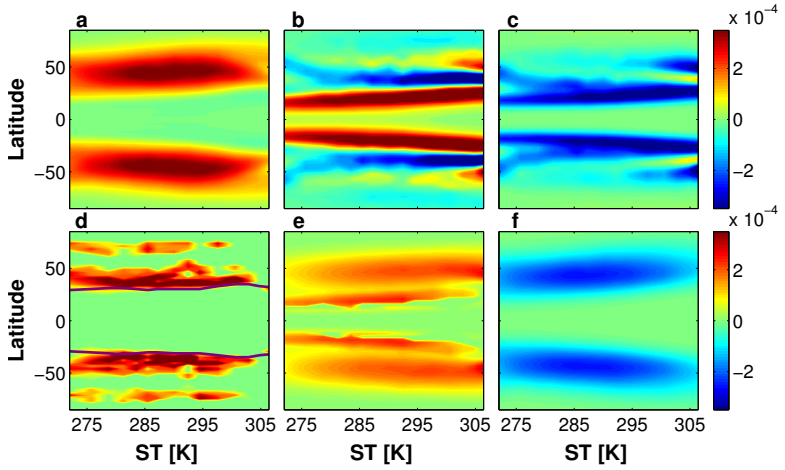

Figure 3.33: The components of the barotropic EKE equation (m^2s^{-3}) summed at each latitude over all zonal wavenumbers as a function of latitude and surface temperature (ST). (a) conversion of baroclinic EKE (divided by 5); (b) conversion of barotropic eddy available potential energy; (c) eddy-mean flow interactions; (d) the inverse energy cascade by eddy-eddy interactions (summed over zonal wavenumbers where there is an addition of energy to larger scales); (e) the forward energy cascade by eddy-eddy interactions (summed over zonal wavenumbers where there is an addition of energy to smaller scales) (divided by 5); (f) loss of barotropic EKE by dissipation (divided by 5). The purple lines in panel d correspond to latitudes where the QG supercriticality equals one.

was shown in both models (e.g., Smith and Vallis, 2001, 2002; Venaille et al., 2011, 2012; Chemke and Kaspi, 2015a) and reanalysis data (Chemke and Kaspi, 2016b; Chemke et al., 2016a). Different than previous studies (Held and Larichev, 1996; Smith and Vallis, 2002; Venaille et al., 2012), here these parameters are not systematically isolated, and their importance in affecting the barotropization in different climates is thus based on the findings of these studies.

Fig. 3.35 shows the dependence of the mean barotropization on the different parameters (Note that the Fig. 3.35 uses logarithmic axes). The mean barotropization in Fig. 3.35 is calculated at each simulation as the mean over the extratropics of its sum over all zonal wavenumbers (Fig. 3.33a). The extratropics are defined from the poleward edge of the Hadley cell to the poles, where the poleward edge of the Hadley cell is defined as the latitude where the mean meridional mass streamfunction first changes sign at the height of its maximum value (e.g., Walker and Schneider, 2006). The abscissa parameters in Fig. 3.35 are calculated at each simulation as the mean over the extratropics of their zonal and vertical average values (Fig. 3.34). The vertical averages (pressure weighted) are taken up to the tropopause height, which is defined based on the World Meteorological Organization (WMO) as the lowest level where the mean temperature reaches $2\,Kkm^{-1}$. Each circle in Fig. 3.35 represents a single simulation, where the blue and red circles correspond to climates colder and warmer than present-day climate (black circles), respectively.

3.5.1.1.1 Static stability The static stability, which was suggested to have an inverse relation with barotropization (Held and Larichev, 1996), shows a non-monotonic behavior at

midlatitudes and decreases at high latitudes as the climate becomes warmer (Fig. 3.34a). Similar to O'Gorman and Schneider (2008a), the static stability at midlatitudes reaches a minimum value at climates similar to present-day, and is larger at colder and warmer climates. The dry static stability, which is defined as $N^2 = \frac{g}{\theta}\frac{\partial \theta}{\partial z}$, where g is gravity and θ is the potential temperature, is used rather than a moist static stability (e.g., Frierson, 2006; O'Gorman, 2011), as it better captures the behavior of the eddies (cf. Sec. 3.5.4) and of the barotropization in different climates. As the longwave optical thickness increases, the potential temperature lapse rate (θ_z) shows a similar non-monotonic behavior with a minimum value around present-day climate, which explains the non-monotonic behavior of the static stability (Fig. 3.36a). Using Stone (1978)'s theory, which states that the eddy fluxes act to maintain the atmosphere in a state that is marginally critical to baroclinic instability (i.e., $\triangle_z \theta \sim \triangle_y \theta$), O'Gorman and Schneider (2008a) suggested that in cold climates the atmosphere may be more stable than present-day due to stronger meridional temperature gradient (Stone, 1978; Held, 1982; Schneider, 2004; O'Gorman and Schneider, 2008a). In warm climates, on the other hand, moist processes may act to stabilize the atmosphere through an increase of the surface equivalent potential temperature gradient and the moist adiabat (Juckes, 2000; Frierson, 2006, 2008). Stronger stratification decreases the barotropization as the energy is transferred from all baroclinic modes to the barotropic mode, indirectly and incompletely through the first baroclinic mode (Fu and Flierl, 1980; Smith and Vallis, 2001). Thus, the opposite tendency of the static stability and the barotropization, results in a non-direct dependence in both cold ($\propto N^{-2.5\pm1}$, the $\pm$ represents the 95% confidence interval with $R^2 = 0.92$) and warm ($\propto N^{-9\pm0.9}$ with $R^2 = 0.99$) climates (Fig. 3.35a). The moist stratification, on the other hand, decreases as the climate becomes warmer (Fig. 3.36b), and thus, it is a less relevant metric for the barotropization than the dry stratification, as it may only explain the increase of the barotropization in cold climates. As was also shown in Frierson (2006, 2008), in warmer climates than present-day, the moist potential temperature lapse rate does not change much, which may be due to stronger convective fluxes (Juckes, 2000).

3.5.1.1.2 Tropopause height Similar to previous studies (e.g., Thuburn and Craig, 1997; Lorenz and DeWeaver, 2007; O'Gorman and Schneider, 2008a; Frierson, 2008; Vallis et al., 2015), the tropopause height, which is also expected to have an inverse relation with barotropization according to Held and Larichev (1996), increases as the longwave optical thickness increases (Fig. 3.34b). The increase of the tropopause height is related to the increase of the potential temperature lapse rate at midlatitudes in warm climates (Fig. 3.36a) and the overall increase of surface temperature (Thuburn and Craig, 1997). In the tropics, the monotonic increase of the potential temperature lapse rate through all climates may further increase the tropopause height. An inverse relation between the tropopause height and barotropization is found in warm climates, (red circles in Fig. 3.35b, $\propto H^{-2.13\pm0.57}$ with $R^2 = 0.93$), and thus may explain the decrease of the barotropization at those climates.

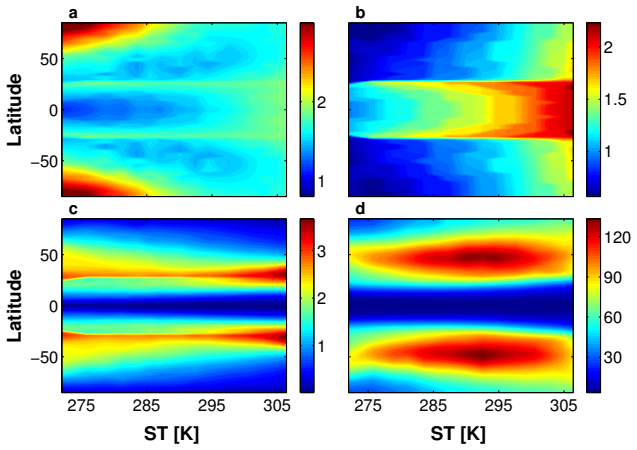

Figure 3.34: Zonal and vertical averaged components as a function of latitude and surface temperature (ST). (a) static stability (10^{-4}, s^{-2}), (b) tropopause height (10^4, m), (c) vertical shear of the zonal wind (10^{-3}, s^{-1}) and (d) barotropic EKE (m^2s^{-2}). The vertical averages are taken up to the tropopause height.

3.5.1.1.3 Vertical shear of the zonal wind Similar to the stratification, the vertical shear of the zonal wind behaves differently at mid and high latitudes as the climate becomes warmer (Fig. 3.34c). Fig. 3.37 shows the mean meridional mass streamfunction (colors) and mean zonal wind (contours) for three different simulations. As further discussed below, as the climate becomes warmer the jet becomes stronger at midlatitudes (as it merges with the subtropical jet), as was also found in future-projected climates (e.g., Lorenz and DeWeaver, 2007), and weaker at high and low latitudes. This causes the poleward flank of the eddy-driven jet to shift equatorward, which contracts the baroclinic zone. Thus, while at high latitudes, the vertical shear of the zonal wind decreases, at midlatitudes it increases (Fig. 3.34c). As a result, its averaged value over the extratropics shows a non-monotonic behavior as the climate becomes warmer, reaching a minimum value around present-day climate (Fig. 3.35c). This results in a non-direct relation with the mean barotropization in both cold ($\propto {u_z}^{-2.48\pm0.6}$ with $R^2 = 0.97$) and warm ($\propto {u_z}^{-8.54\pm3.07}$ with $R^2 = 0.88$) climates, which is opposite than what was found in previous studies (Held and Larichev, 1996; Smith and Vallis, 2002; Chemke and Kaspi, 2016b).

3.5.1.1.4 Barotropic EKE Similar to the barotropization, the vertically averaged EKE was shown to have a non-monotonic behavior at midlatitudes as the longwave optical thickness increases (O'Gorman and Schneider, 2008a), which was attributed to changes in the thermal structure of the atmosphere (e.g., stratification, tropopause height and meridional temperature gradient). The barotropic EKE also shows a non-monotonic behavior (Fig. 3.34d), with a maximum value around present-day climate. Thus, as expected from the scaling theory of Held and Larichev (1996), the barotropization has a direct relation with the barotropic EKE in both cold ($\propto \text{bEKE}^{1.1\pm0.09}$ with $R^2 = 0.99$) and warm ($\propto \text{bEKE}^{3.62\pm0.29}$ with $R^2 = 0.99$) climates. Note, as the above parameters are affected by barotropization processes (especially the barotropic EKE), cause and effect arguments are limited. Thus, changes in the thermal

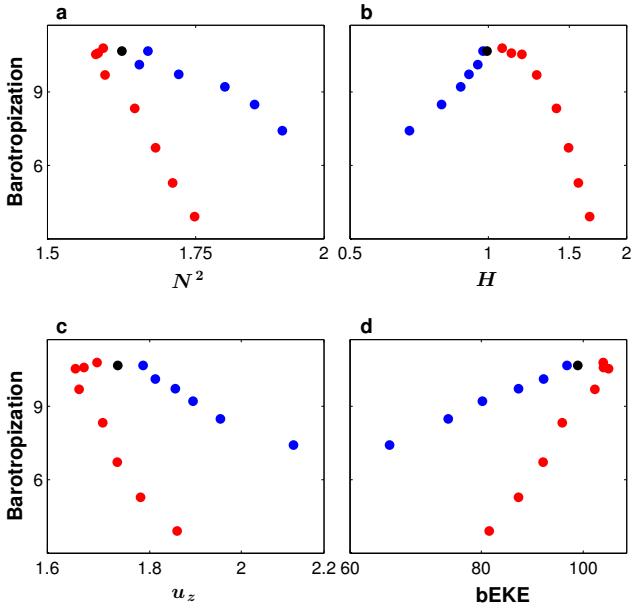

Figure 3.35: The extratropical mean barotropization (10^{-4}, m^2s^{-3}) as a function of the extratropical mean of the zonal and vertical averages of (a) static stability (10^{-4}, s^{-2}), (b) tropopause height (10^4, m), (c) vertical shear of the zonal wind (10^{-3}, s^{-1}) and (d) barotropic EKE (m^2s^{-2}). Each circle represents the mean value of the extratropics in a single simulation. The blue and red circles correspond, respectively, to climates colder and warmer than present-day climate (black circles). Note that the figure uses logarithmic axes.

structure of the atmosphere may result in the non-monotonic behavior of the barotropic EKE at midlatitudes, by affecting the barotropization of the flow and/or the vertically averaged EKE (O'Gorman and Schneider, 2008a).

3.5.1.1.5 Barotropic dissipation The dissipation of barotropic EKE also shows a non-monotonic behavior at midlatitudes as the climate becomes warmer, reaching a minimum value (maximum subtraction of barotropic EKE) around present-day climate (Fig. 3.33f). This is similar to the non-monotonic behavior of the barotropic EKE, as these two are coupled. Previous studies showed that the barotropic dissipation may alter the energy fluxes and macroturbulent scales in the baroclinic-barotropic energy cycle (e.g., Arbic and Flierl, 2004; Thompson and Young, 2006, 2007). Although dissipation was found in previous studies to weaken both the barotropization and the barotropic inverse energy cascade (e.g., Treguier and Hua, 1988; Smith and Vallis, 2002; Arbic et al., 2007; Scott and Arbic, 2007; Venaille et al., 2011, 2014), here these fluxes reach maximum values when the dissipation is strongest (Fig. 3.33a,d and f), due to their strong relation with the barotropic EKE.

In summary, the non-monotonic behavior of the barotropization at midlatitudes as the climate becomes warmer is mostly related to the non-monotonic behavior of the stratification. In addition, the increase in mean temperature and lapse rate in warm climates results in an increase of the tropopause height, which may decrease the barotropization in these climates.

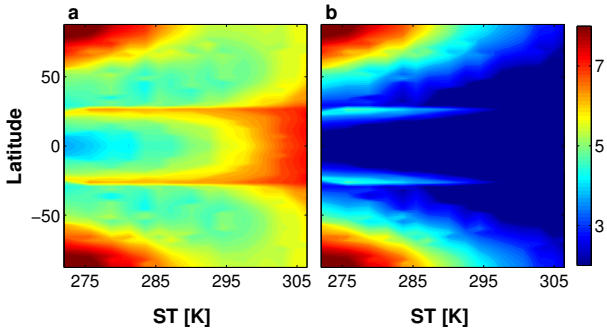

Figure 3.36: Zonal and vertical averaged of (a) potential temperature lapse rate (θ_z, Kkm^{-1}) and (b) moist potential temperature lapse rate (θ_{e_z}, Kkm^{-1}) as a function of latitude and surface temperature (ST). The vertical averages are taken up to the tropopause height.

3.5.1.2 The poleward shift of the barotropization

As the barotropization is triggered by baroclinic instability (Salmon, 1978; Vallis, 2006), its poleward shift may be associated with the poleward shift of the baroclinic zone found in both observation (e.g., Thompson et al., 2000) and model projections of global warming (e.g., Hall et al., 1994; Kushner et al., 2001; Yin, 2005; Bengtsson and Hodges, 2006; Lorenz and DeWeaver, 2007; Meehl et al., 2007; Vallis et al., 2015). Indeed, among the variables controlling the barotropization, only the static stability shows a similar poleward shift (Fig. 3.34a). Figure 3.38 shows that through all climates the weighted mean latitude of the barotropization propagates poleward in concert with the mean latitude of the inverse static stability. The reason behind the poleward shift of the static stability is thus the main concern of this section.

The poleward shift of the baroclinic zone, under global warming, is a broadly covered subject with several proposed mechanisms, including an increase in tropopause height and upper-troposphere changes in baroclinicity (Lorenz and DeWeaver, 2007; Lu et al., 2008; Rivière, 2011), meridional changes in baroclinic instability (Frierson et al., 2007; Lu et al., 2008; Kodama and Iwasaki, 2009) and critical latitude dynamics (Chen and Held, 2007; Lu et al., 2008; Kidston et al., 2011; Kidston and Vallis, 2012; Lorenz, 2014a). Thus, a new mechanism is not suggested here, but these mechanisms are rather discussed in respect to the results of the presented simulations. As the complexity of the idealized GCM does not allow isolating the relative importance of these mechanisms, which can be done in a simpler model by controlling the different variables (e.g., tropopause height, vertical stability, etc.), falsification or validation these mechanisms is done by studying them through all simulations.

3.5.1.2.1 Tropospheric static stability As discussed above, in warmer climates than present-day, the potential temperature lapse rate (θ_z) acts to stabilize the atmosphere (due to the increase of the surface equivalent potential temperature gradient and the moist adiabat, Juckes, 2000; Frierson, 2006, 2008) more at low-mid latitudes than at high latitudes (Fig. 3.36a), which may encourage baroclinic instability processes to occur more at higher latitudes, and shift the baroclinic zone poleward (Lu et al., 2008; Kodama and Iwasaki, 2009). On the other hand, although the poleward shift of the energy cycle occurs through all climates (Fig. 3.33), in colder

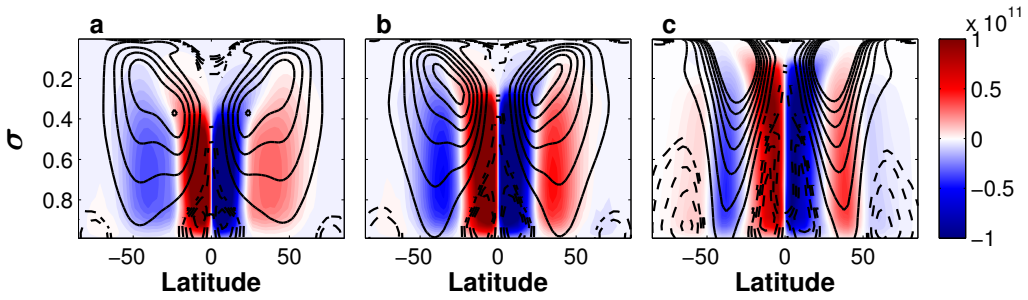

Figure 3.37: The mean meridional mass streamfunction (kgs^{-1}, colors) and mean zonal wind (ms^{-1}, contours) as a function of sigma ($\sigma = p/p_s$) and latitude for simulations with surface temperature of (a) 279 K, (b) 287 K and (c) 306 K. The solid and dashed contours in panels a-c correspond to westerly and easterly winds, respectively. Positive contours have a 5 ms^{-1} spacing with maximum values of 25, 30 and 35 ms^{-1} in panels a, b and c, respectively. Negative contours have a 1 ms^{-1} spacing with minimum values of -5 ms^{-1} in all panels.

climates than present-day, the potential temperature lapse rate acts to stabilize the atmosphere more at high latitudes than at mid-low latitudes, which suppresses the poleward shift. In other words, the increase in the static stability, which was found in previous studies (Frierson, 2006), occurs only in warmer climates than present-day. Moreover, through all climates the moist potential temperature lapse rate is higher at high latitudes than low-mid latitudes (Fig. 3.36b). Thus, the increase in static stability can not solely explain the poleward shift.

3.5.1.2.2 Upper-level baroclinicity The extratropical stratosphere is expected to cool as the longwave optical thickness is increased, mostly due to the stronger emission of longwave radiation in the stratosphere (Vallis et al., 2015). Lorenz and DeWeaver (2007) suggested that an increase in the tropopause height (H) poleward of the jet location together with the extratropical stratospheric cooling, may alter the meridional temperature gradient aloft, and result in a poleward shift of the baroclinic zone. Fig. 3.39 shows the temperature difference (in colors) between simulations with surface temperature of 279 K and 287 K and their corresponding tropopause heights. The extratropical stratosphere indeed cools as the longwave optical thickness is increased (blue colors above the purple line in Fig. 3.39). As a result, an increase in the tropopause height (purple and green lines in Fig. 3.39) results in stronger meridional temperature gradient on the poleward flank of the subtropical jet and across the eddy driven jet, below the tropopause height (Fig. 3.39). This destabilizes the troposphere at high latitude (Figs. 3.34a and 3.36a) and may push the barotropization poleward.

From an eddy life cycle point of view, Rivière (2011) suggested that an enhanced upper-troposphere baroclinicity (Fig. 3.39) may decrease the high wavenumber cut-off, which would increase the abundance of long wavelengths, and increase the eddies' phase speed (Wittman et al., 2007) as further discussed below. These wavelengths favor anticyclonic breaking that leads to a poleward shift of the jets (e.g., Balasubramanian and Garner, 1997; Orlanski, 2003; Riviere, 2009). This may also explain the increase of the energy-containing zonal scale (Fig. 3.40a) in these simulations. The energy-containing zonal wavenumber is calculated at each latitude as

the inverse centroid (Schneider and Walker, 2006; O'Gorman, 2011; Chai and Vallis, 2014) of the zonal spectrum of the barotropic meridional eddy velocity,

$$k_e = \frac{\sum_k |[v]'_k|^2}{\sum_k k^{-1} |[v]'_k|^2}, \tag{3.15}$$

which produces wavenumbers closest to the peak of the spectrum. The energy-containing wavelength is calculated using Eq. 2.11.

3.5.1.2.3 Critical latitude dynamics As the climate becomes warmer the subtropical and eddy-driven jets merge, and form a stronger and narrower jet at midlatitudes (Fig. 3.37). This results in a weakening of the mean zonal winds on both the poleward and equatorward flanks of the jets. Consistent with Chen and Held (2007)'s mechanism, the eddy momentum flux convergence ($-\frac{1}{a\cos^2\varphi}\frac{\partial\left(\overline{u'v'}^*\cos^2\varphi\right)}{\partial\varphi}$, where a is Earth's radius and φ is latitude) phase speed increases as the climate becomes warmer (Fig. 3.41). This together with a decrease in the mean zonal wind on the equatorward flank cause the critical latitude on the equatorward flank of the jet to shift poleward (compare dashed gray and black lines in Fig. 3.41c), which may push the baroclinic source at the surface poleward (Robinson, 2000; Chen et al., 2007) and destabilize the atmosphere at higher latitudes. The eddy momentum flux convergence phase speed is calculated following Randel and Held (1991), at the height of maximum eddy momentum flux divergence at high latitudes, in segments of consecutive 50 days averaged over 550 days.

Even though the energy-containing zonal scale does increase with longwave optical thickness (Fig. 3.40a), which decreases the eddies' relative phase speed (absolute phase speed minus the mean zonal wind) in the source regions (Fig. 3.41d-f) (Kidston et al., 2010, 2011), the critical latitude on the poleward flank shifts equatorward rather than poleward (compare dashed gray and black lines in Fig. 3.41c). This occurs due to a decrease in the zonal wind at high latitudes, which merges the dissipation and source latitudes on the poleward flank of the jet, and may suppress the poleward shift. Furthermore, the decrease in mean zonal wind on the poleward flank (Fig. 3.41), may also decrease the wave reflection, and thus the poleward momentum fluxes (Kidston and Vallis, 2012; Lorenz, 2014a).

In aggregate, the most relevant contributors to the poleward shift of the barotropization in these simulations are changes in the upper troposphere baroclinicity and in critical latitude dynamics on the equatorward flank of the jet. These changes destabilize the atmosphere at higher latitudes as the climate becomes warmer (Figs. 3.34a and 3.36a) and thus contribute to the observed poleward shift of the barotropization. Note, that changes in baroclinicity poleward of the jet's core, may push the jet poleward, and even modulate the eddies' phase speed (Wittman et al., 2007) and thus the critical latitude as well. Thus, as baroclinicity is coupled to the critical latitude processes, determining cause and effect between the two is limited.

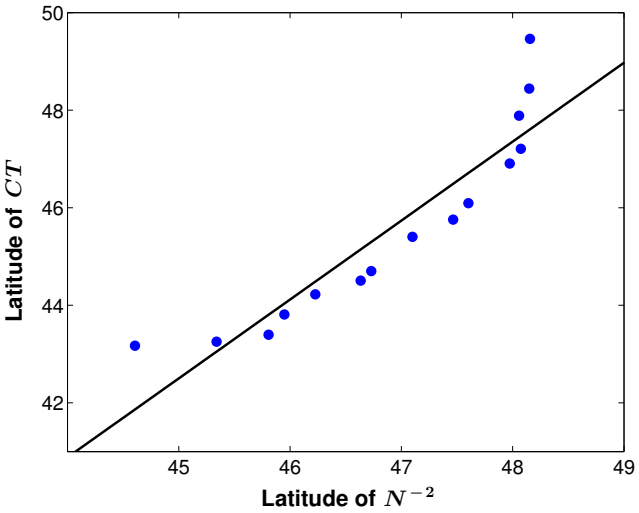

Figure 3.38: The extratropical weighted mean latitude of the barotropization (Eq. 2.9) as a function of the extratropical weighted mean latitude of the inverse static stability (N^{-2}). The black line shows the best linear fit and follows $y = 1.6(\pm 0.4) \cdot x - 30.3$ with $R^2 = 0.85$. The $\pm$ represent the 95% confidence interval.

3.5.2 Barotropic eddy available potential energy

The second source of barotropic EKE is the conversion of barotropic eddy available potential energy (second column in Fig. 3.32). While in Lorenz's energy cycle (Lorenz, 1955) this is the main source of EKE, here it accounts only the conversion that occurs in the barotropic mode, and as a result it is smaller than the conversion of baroclinic to barotropic EKE. Nonetheless, its latitudinal structure in different climates also affects the behavior of the barotropic eddy-mean flow and eddy-eddy interactions, as further discussed below (Secs. 3.5.3-3.5.4). Different than the barotropization (Fig. 3.33a), the conversion of barotropic eddy available potential energy increases as the longwave optical thickness increases, mostly due to the increase in the zonal wind variance and meridional barotropic geopotential gradient (Fig. 3.42), and shows a triple behavior with latitude. Note, that as the flux of barotropic eddy available potential energy affects the barotropic EKE, it is difficult to determine weather the increase in wind variance is the cause or effect of this increase with surface temperature. Similar to the increase of the barotropic meridional geopotential gradient, which is related to the meridional temperature gradient through hydrostatic balance, Wu et al. (2010) showed that the eddy available potential energy increases in warmer climates due to the stronger warming of low latitude vs mid-high latitudes in the upper troposphere. Summing the conversion of barotropic eddy available potential energy over all wavenumbers at each latitude, shows that it also migrates poleward as the climate becomes warmer (Fig. 3.33b). In addition, while at low and high latitudes the barotropic eddy available potential energy is converted to barotropic EKE, at midlatitudes barotropic EKE is converted to barotropic eddy available potential energy (Fig. 3.33b). This triple structure in latitude is further discussed below (Sec. 3.5.3), and found to be related to the contraction of the latitudinal extent of the mean flow at midlatitudes.

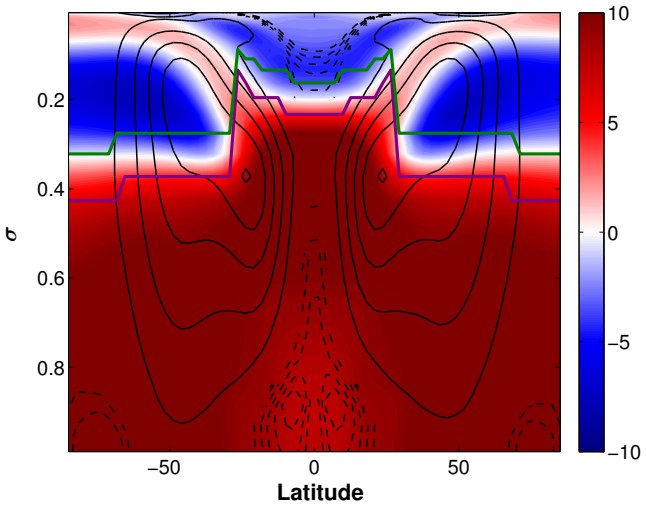

Figure 3.39: Temperature difference (colors) as a function of sigma ($\sigma = p/p_s$) and latitude between simulations with surface temperature of 287 K and 279 K. The black contours correspond to the mean zonal wind (ms^{-1}) in the simulation with surface temperature of 279 K. The solid and dashed contours correspond to westerly and easterly winds, respectively. Positive contours have a 5 ms^{-1} spacing with maximum values of 25 ms^{-1}. Negative contours have a 1 ms^{-1} spacing with minimum values of -5 ms^{-1}. The purple and green lines, respectively correspond to the tropopause height in simulations with surface temperature of 279 K and 287 K.

3.5.3 Eddy-mean flow interactions

The barotropic eddy-mean flow interactions play a major role in maintaing the barotropic component of the mean zonal wind (eddy-driven jet) at midlatitudes (Held, 1975; Held and Hoskins, 1985; Lee and Kim, 2003), and show three interesting properties as the climate becomes warmer (third column in Fig. 3.32). First, these interactions remove the conversion of barotropic eddy available potential energy to barotropic EKE, at low and high latitudes, and transfer it to the zonal mean flow. Second, summing the eddy-mean flow interactions over all wavenumbers, shows that similar to the conversion of barotropic eddy available potential energy, these interactions also increase and migrate poleward as the longwave optical thickness increases (Fig. 3.33c), and third, in warm climates, the eddy-mean flow interactions transfer barotropic EKE from the mean flow to the eddies (red colors in Fig. 3.33c).

The dominant term in Eq. 2.7 that is responsible for most of the energy transfer is $-[u]'[v]'\overline{[u]}_y$. Investigating its mean and eddy components separately (Fig. 3.43), provides a deeper understanding on the latitudinal structure of the eddy-mean flow interactions. Whether the barotropic EKE is transferred from the eddies to the mean flow, or the other way around, can be understood using the Orr mechanism (Orr, 1907; Lindzen, 1988; Vallis, 2006). When the eddies tilt into (with) the shear, $-\overline{[u]'[v]'[u]}_y > 0$ ($-\overline{[u]'[v]'[u]}_y < 0$), the EKE is transferred from the mean flow (eddies) to the eddies (mean flow). Fig. 3.43 shows the meridional derivative of the zonal mean barotropic wind (in colors, $\overline{[u]}_y$) and the zonal mean barotropic meridional momentum fluxes (in contours, $\overline{[u]'[v]'}$), as a function of latitude and surface temperature. In the northern (southern) hemisphere, the meridional derivative of the zonal mean barotropic wind is positive (negative) at low latitudes and negative (positive) at high latitudes due to the

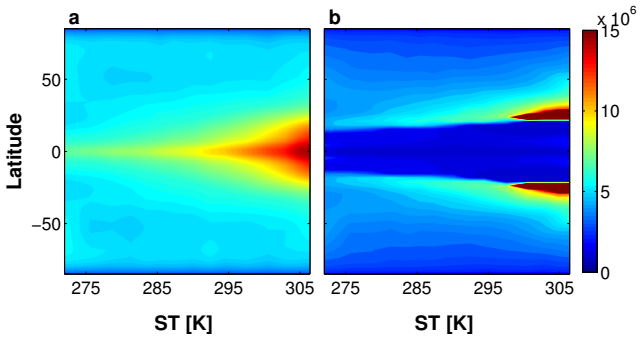

Figure 3.40: Macroturbulent scales (m) as a function of latitude and surface temperature (ST). (a) The zonal energy-containing scale and (b) the zonal conversion scale of baroclinic to barotropic EKE. The zonal energy-containing and conversion scales are calculated using Eq. 2.11 and their corresponding zonal wavenumbers using the inverse centroid (Eq. 3.15) of the zonal spectrum of the barotropic meridional eddy velocity and the conversion of baroclinic to barotropic EKE (Eq. 2.9), respectively.

presence of the jet streams at midlatitudes. Similarly, the northern (southern) hemisphere's eddy momentum fluxes are also positive (negative) at low latitudes and negative (positive) at high latitudes, as they converge momentum into the eddy-driven jet. As a result, in both high and low latitudes, $-\overline{[u]'[v]'[u]}_y < 0$, which results in transfer of EKE from the eddies to the mean flow (blue colors in Fig. 3.33c). On the other hand, in warm climates at midlatitudes the energy is transferred from the mean flow to the eddies, $-\overline{[u]'[v]'[u]}_y > 0$. This occurs due to the equatorward migration of the meridional derivative of the zonal mean barotropic wind at high latitudes, which penetrates the region of the poleward momentum fluxes.

The equatorward migration of $\overline{[u]}_y$ at high latitudes, due to the merging of the subtropical and eddy-driven jets with warming climate, implies the contraction of the poleward flank of the barotropic jet stream. At high altitudes, the decrease in the mean zonal wind (Fig. 3.37) migrates the critical latitude on the poleward flank equatorward, as discussed above (Fig. 3.41). In warm climates this result in a wider region poleward of the critical latitude where eddies dissipate. Indeed, at these latitudes there is stronger eddy momentum flux divergence as the climate becomes warmer (blue colors at high latitudes in Fig. 3.41). As the vertical integral of the eddy momentum flux convergence balances the wind at the surface (Held and Hoskins, 1985; Vallis, 2006), the stronger eddy momentum flux divergence in warm climates, further increase the easterlies at the surface (dashed contours at high latitudes in Fig. 3.37a-c), which further increases and migrates equatorward $\overline{u}_y$ at the surface. The increase of $\overline{u}_y$ in both high and low altitudes in warm climates, explains the increase in $\overline{[u]}_y$, which increases the barotropic eddy-mean flow interactions as the longwave optical thickness increases (Fig. 3.33c). The contraction of the poleward flank of the barotropic mean flow at high latitudes as the climate becomes warmer migrates equatorward the meridional derivative of the zonal mean barotropic wind into the region of the poleward momentum fluxes, which causes an energy transfer from the mean flow to the eddies in warm climates.

On one hand, the reduced phase speeds of the eddies and the equatorward contraction of the poleward flank of the mean flow in warm climates, may be two independent results of changes

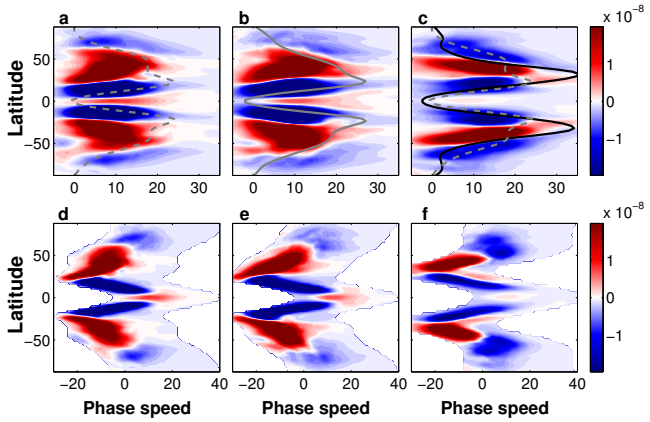

Figure 3.41: Eddy momentum flux convergence ($-\frac{1}{a\cos^2\varphi}\frac{\partial\left(\overline{u'v'}^*\cos^2\varphi\right)}{\partial\varphi}$, ms^{-2}, colors) as a function of latitude and (a)-(c) phase speed (top row) and (d)-(f) relative phase speed (bottom row) for simulations with surface temperature of (a), (d) 279 K, (b), (e) 287 K and (c), (f) 306 K. The red and blue colors correspond to convergence and divergence of momentum, respectively. The eddy momentum flux convergence is calculated at the height of its minimum value at high latitudes, and multiplied by the cosine of latitude. The dashed gray, solid gray and black lines correspond to the mean zonal wind at the same height. In panel c, the mean zonal wind from simulations with surface temperature of both 279 K (dashed gray), and 306 K (black), are plotted.

in the thermal structure of the atmosphere. On the other hand, previous studies suggested that changes in the eddies' phase speed may result in latitudinal displacement of the mean flow (e.g., Chen et al., 2007; Chen and Held, 2007; Lorenz, 2014a). Determining cause and effect in these processes is beyond the scope of this paper.

3.5.4 Eddy-eddy interactions

According to the Rhines-Salmon two-layer phenomenology, the barotropic eddy-eddy interactions transfer the barotropic EKE both upscale and downscale (Rhines, 1977; Salmon, 1978). The fourth column in Fig. 3.32 shows the energy transfers by eddy-eddy interactions. These interactions remove the input from the baroclinic modes, and transfer it both upscale (inverse energy cascade) and downscale (forward energy cascade). While the forward energy cascade occurs through the entire extratropics, the inverse energy cascade occurs only at mid-high latitudes. Summing the inverse energy cascade (i.e., summing the positive values of the eddy-eddy interactions at each latitude from the zero zonal wavenumber to the first zero crossing) through all climates, shows a similar behavior to the barotropization, with a maximum value around present-day climate (Fig. 3.33d). However, different than the barotropization, the inverse energy cascade by eddy-eddy interactions does not migrate poleward as the climate becomes warmer, but rather remains at the same latitudinal location.

Inverse energy cascade can occur if there is a scale separation between the energy-injection scale and the energy-containing scale. In geostrophic turbulence the injection scale is the scale where EKE is converted from the baroclinic to the barotropic mode (Rhines, 1977; Salmon,

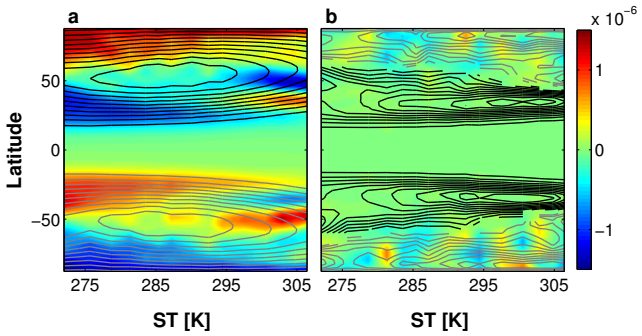

Figure 3.42: The zonal mean of the different components of the dominant term in the conversion of barotropic eddy available potential energy (Eq. 2.8), $-[\mathbf{u_h}]' \cdot \nabla_h[\phi]'$. (a) The meridional gradient of the eddy geopotential (colors) and the meridional wind variance (contours). (b) The zonal gradient of the eddy geopotential (colors) and the zonal wind variance (contours). The black and gray contours correspond to positive and negative values, respectively.

1978). Fig. 3.44a shows the ratio between the conversion scale of baroclinic to barotropic EKE (L_g) and the energy-containing scale (L_e) for all simulations as a function of latitude. The conversion scale is computed using Eqs. 3.15 and 2.11, only with the zonal spectrum of the conversion of baroclinic to barotropic EKE (Eq. 2.9), rather than the barotropic meridional eddy velocity. In most climates, the energy-containing scale is larger than the conversion scale beyond latitude 30°, which coincides with the latitudinal location of the inverse energy cascade (Fig. 3.33d). This occurs since through all climates the conversion scale decreases more rapidly with latitude than the energy-containing scale (Fig. 3.40). As the climate becomes warmer, the conversion scale increases, mostly at low-mid latitudes (Fig. 3.40b). This decreases the scale separation between the energy-containing and conversion scales (Fig. 3.44a), and further limits the inverse energy cascade (Fig. 3.33c).

Parameterizing the energy-containing and conversion scales may help understanding the latitudinal behavior of the inverse energy cascade. In agreement with Rhines (1975), at latitudes where inverse energy cascade occurs (Fig. 3.33d), the Rhines wavelength and energy-containing scale coincide (Fig. 3.44b). The Rhines wavelength, λ_β, is defined using Eq. 2.13 only with the barotropic EKE. The conversion scale is associated with EKE production through baroclinic instability, and thus is expected to occur, according to the Rhines-Salmon two-layer phenomenology, at the Rossby deformation wavelength (Salmon, 1978). Indeed, in warm climates the conversion scale follows both the Rossby deformation wavelength (red circles in Fig. 3.44c) and the most unstable scale (red circles in Fig. 3.44d). While in colder climates the conversion scale is larger than the Rossby deformation wavelength (blue circles in Fig. 3.44c), it is smaller than the most unstable scale (blue circles in Fig. 3.44d). The Rossby deformation wavelength, λ_d is defined using Eq. 2.14[5] (Chelton et al., 1998; Scott and Wang, 2005; Abernathey and Wortham, 2015). The most unstable scale is computed using Eq. 2.11, where the most unstable zonal wavenumber is computed, following Smith (2007), at each latitude by solving the linearized quasi-geostrophic (QG) potential vorticity equation, and looking for

[5]Using the dry static stability in the Rossby deformation radius definition, rather than a moist static stability (e.g., Frierson, 2006; O'Gorman, 2011) provides better agreement with the conversion scale.

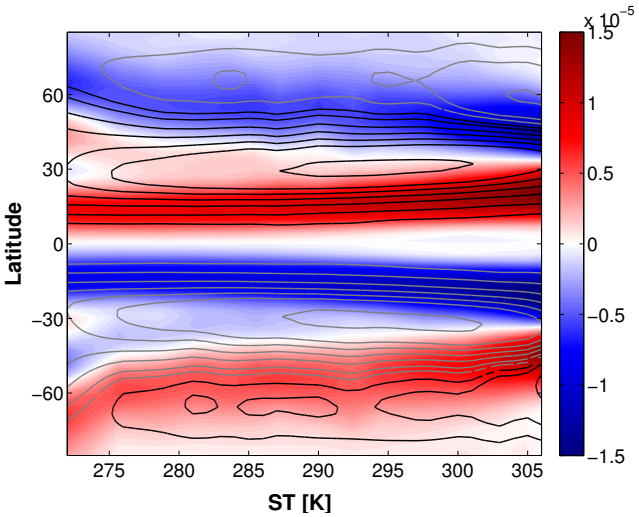

Figure 3.43: The meridional gradient of the barotropic mean zonal wind (colors, $\overline{[u_y]}$, s^{-1}) and the barotropic mean eddy momentum fluxes (contours, $\overline{[u]'[v]'}$, ms^{-2}) as a function of latitude and surface temperature (ST). The gray and black contours correspond to negative (southward) and positive (northward) momentum fluxes, respectively. The positive (negative) contours correspond to (-)14, (-)10, (-)8, (-)6, (-)4, (-)2 and (-)0.8 ms^{-2}.

the wavenumbers with the fastest growth rate, after normalizing them by the eddy available potential energy (EAPE, Lorenz, 1955). The agreement of the conversion scale with both the Rossby deformation wavelength and most unstable scale, suggest that its monotonic increase (Fig. 3.40b), with longwave optical thickness, is due to the monotonic increase of the tropopause height (O'Gorman, 2011), which increases the deformation radius, and upper-level baroclinicity (Rivière, 2011), which decreases the high wavenumber cut-off.

According to the scaling theory of Held and Larichev (1996) the ratio between the Rhines and Rossby wavelengths, should follow the QG supercriticality, and thus separates cases where inverse energy cascade does and does not occur (e.g., in two-dimensional turbulence inverse energy cascade is expected to occur when the energy-containing scale is larger than the energy injection scale) (Jansen and Ferrari, 2012; Chemke and Kaspi, 2015a, 2016b; Chemke et al., 2016a). The purple lines in Fig. 3.33d correspond to latitudes where the QG supercriticality ($S_c = C_s \frac{u_z f^2}{\beta N^2 H}$) equals one (supercriticality latitudes), which indeed separate latitudes where inverse energy cascade does and does not occur[6]. Since the Rossby wavelength follows the conversion scale, through all climates, up to a constant of proportionality (Fig. 3.44c), the QG supercriticality is multiplied by their scale ratio ($C_s = L_g L_d^{-1}$), which causes the supercriticality latitudes to mark the transition of where inverse energy cascade occurs. Note, as the scaling theory of Held and Larichev (1996) was developed based on the assumption of a large scale separation between the Rhines scale and Rossby deformation radius (i.e., large supercriticality), which does not occur close to the supercriticality latitudes, the presence of this constant of proportionality may also be related to the limitation of applying this theory in these simulations. The supercriticality latitudes also follow the most equatorward and poleward latitudes where the

[6]The dry static stability is used for the calculation of the QG supercriticality as it is found better to capture the behavior of the eddies than using a moist static stability, even in warm climates.

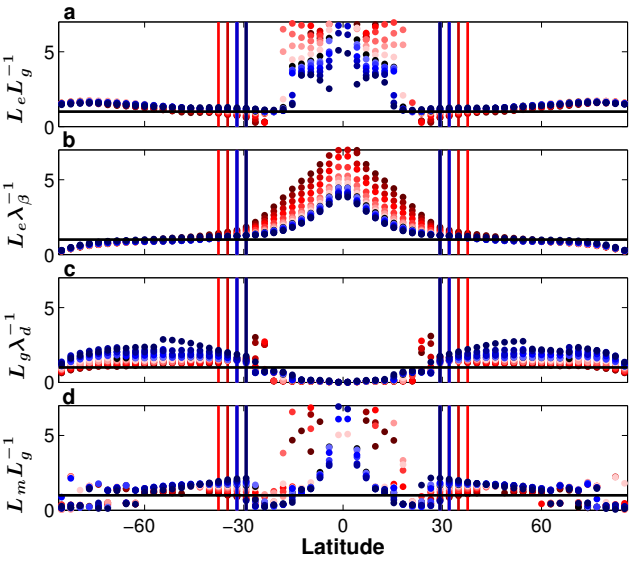

Figure 3.44: Scales ratio as a function of latitude. (a) the ratio of the energy-containing (L_e) and conversion of baroclinic to barotropic (L_g) scales, (b) the ratio of the energy-containing scale (L_e) and Rhines wavelength (λ_β), (c) the ratio of the conversion of baroclinic to barotropic scale (L_g) and Rossby wavelength (λ_d) and (d) the ratio of the most unstable (L_m) and conversion of baroclinic to barotropic (L_g) scales. Each color corresponds to a different climate simulation, warmer (colder) colors correspond to warmer (colder) climates. The vertical colored lines respectively correspond to the latitudes where the QG supercriticality equals one for the different climates.

energy-containing scale equals the Rhines scale and the conversion scale, respectively (vertical lines in Fig. 3.44a and b). The QG supercriticality has similar values through all latitudes in different simulations, mostly due to the similar latitudinal tendencies of the static stability and vertical shear of the zonal wind through all climates (Fig. 3.34a and c). This results in a similar latitudinal location of the inverse energy cascade in most simulations (Fig. 3.33d).

Different than the inverse energy cascade, summing the forward energy cascade (i.e, summing the positive values of the eddy-eddy interactions at each latitude from the second zero crossing) through all climates, shows an increase as the climate becomes warmer together with the poleward shift of the energy cycle (Fig. 3.33e). The increase in the addition of barotropic EKE to small scales should flatten the energy spectrum, however, as the forward energy cascade is shifted to larger scales, as the climate becomes warmer (fourth column in Fig. 3.32), the energy spectrum eventually steepens (not shown). Since the investigation of the energy cycle is done at each latitude, and not globally, the eddy-eddy interactions (fourth column in Fig. 3.32) also contain the lateral transport of barotropic EKE between different latitudes. Summing the eddy-eddy interactions over all zonal wavenumbers at each latitude produces the net lateral transport (Fig. 3.45). The eddy-eddy interactions not only transfer the conversion of baroclinic EKE to smaller and larger zonal scales, but also equatorward. In a QG framework, inverse energy cascade includes both the transfer of energy to larger scales and to larger deformation radii. The later implies both the barotropization of the flow (smaller vertical wavenumbers) and, due to its latitudinal variation, an equatorward cascade of EKE (Theiss, 2004).

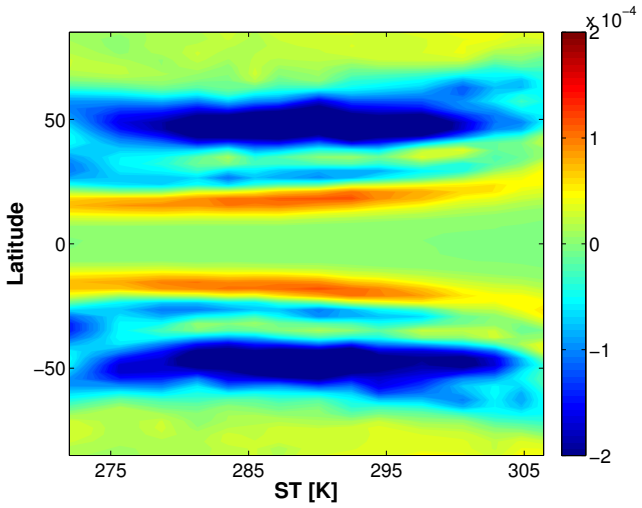

Figure 3.45: The net lateral transport of eddy-eddy interactions (Eq. 2.6 summed over all zonal wavenumbers) as a function of latitude and surface temperature (ST).

3.5.5 Conclusions

In this study the kinetic energy transfers in the barotropic mode are studied for the first time as a function of latitude through a wide range of climates. Following O'Gorman and Schneider (2008a,b), this is done by increasing the longwave optical thickness (which represent an increase of greenhouse gases) in an idealized moist GCM, such that the surface temperature varies between $272 - 306\,\mathrm{K}$. Investigating the behavior of the energy cycle in cold and warm climates provides a better understanding of both the dependence of the energy cycle on the thermal structure of the atmosphere, and the dynamics of past and future projected climates.

Similar to the observed poleward shift of the baroclinic zone in the last decades and in global warming projections, the barotropic energy cycle also shifts poleward as the climate becomes warmer (Fig. 3.33). Using the scaling arguments of Held and Larichev (1996) the poleward shift of the baroclinic to barotropic conversion of EKE (barotropization) is driven by the poleward movement of the static stability. Several mechanisms are found to be consistent with the poleward shift of the static stability; the increase of the tropopause height and upper level baroclinicity and changes in critical latitude dynamics on the equatorward flank of the jet. As the latter is also affected by changes in the jet location, and thus baroclinicity, it is difficult to determine cause and effect.

The barotropization is found to have a non-monotonic behavior at midlatitudes as the longwave optical thickness increases (Fig. 3.33a). The barotropization reaches a maximum value around present-day climate, and it is weaker in colder and warmer climates. The non-monotonic behaviors of the stratification (Fig. 3.34a) contributes to the non-monotonic behavior of the barotropization. In warm climates, the increase in both lapse rate and mean temperature, increase the tropopause height (Fig. 3.34b), and can also explain the reduction in barotropization in these climates. The barotropic EKE (Fig. 3.34d) shows a non-monotonic behavior as the climate becomes warmer, however, causality arguments here are limited as the barotropic EKE and the barotropization are coupled.

The eddy-mean interactions strengthen and shift poleward as the longwave optical thickness increases (Fig. 3.33c). In addition, these interactions transfer kinetic energy from the eddies to the mean flow at low and high latitudes, and from the mean flow to the eddies at midlatitudes in warm climates. As the climate becomes warmer, the subtropical and eddy-driven jets merge, which decreases the mean zonal wind at high latitudes (Fig. 3.37a-c), and results in an equatorward shift of the critical latitude on the poleward flank of the jet (Fig. 3.41). This results in an overall increase of the meridional shear of the zonal mean barotropic wind at high latitudes (Fig. 3.43), which increases the eddy-mean flow interactions. In addition, the equatorward shift causes the meridional shear of the zonal mean barotropic wind at high latitudes to intrude into the region of the poleward momentum fluxes, which results, according to the Orr mechanism, in a transfer of kinetic energy from the mean flow to the eddies in warm climates.

The inverse and forward energy cascades by eddy-eddy interactions show different behavior as the longwave optical thickness increases. The inverse energy cascade does not shift poleward and shows a non-monotonic behavior as the longwave optical thickness increases, reaching a maximum value around present-day climate (Fig. 3.33d). In agreement with geostrophic turbulence theory, the inverse energy cascade occurs at latitudes where the energy-conversion scale (which follows the Rhines scale, Fig. 3.44b) is larger than the baroclinic-barotropic conversion scale (which follows the Rossby deformation wavelength up to a constant of proportionality, Fig. 3.44c). Thus, QG supercriticality values of one, which are suggested to follow the ratio of the Rhines and Rossby deformation scales, indeed mark the latitudinal transition of where inverse energy cascade begins (Fig. 3.33d). The similar latitudinal distribution of the QG supercriticality through all climates, thus, results in a similar latitudinal extent of the inverse energy cascade. The forward cascade, on the other hand, increases and shifts poleward as the climate becomes warmer (Fig. 3.33e).

The findings of this study imply that in future projected climates and also in warmer periods during Earth's early history where the greenhouse gas concentration was higher the present-day values, the eddy flow should be dominated by eddy-mean flow interactions, and have a more baroclinic nature. Interestingly, cold climates hold larger values of QG supercriticality than warm climates (not shown), mostly due to the monotonic decrease of the vertical shear of the zonal wind at mid-high latitudes with surface temperature (Fig. 3.34c). The low values of supercriticality in warm climates imply that at large scales baroclinic advection may play an important role in the balance (Held and Larichev, 1996). Thus, in order to fully understand the energy cycle of different climates the baroclinic modes should also be studied.

For the different phenomena captured in this study (e.g., poleward shift and the non-monotonic behavior of the barotropization) several mechanisms were found applicable. The complexity of the idealized GCM limits the understanding of cause and effect, and so the ability to determine the relative importance of these mechanisms, as it is difficult to isolate them in a GCM. Thus, using simpler models that allow isolating the different roles of the thermodynamically components of the atmosphere (e.g., static stability, tropopause height, etc.), would further elucidate the mechanism behind the behavior of the barotropic energy cycle in different

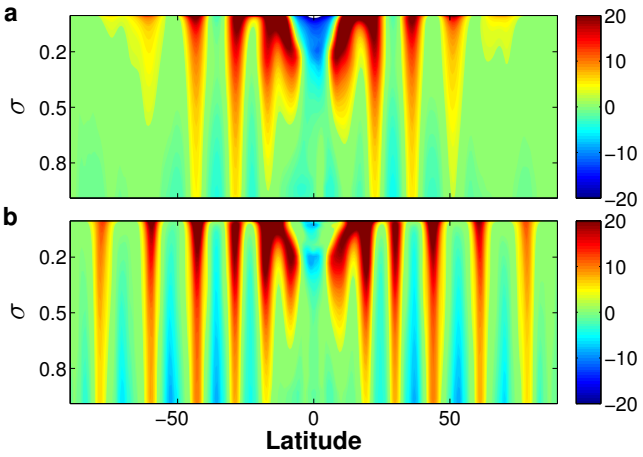

Figure 3.46: Snapshot of the mean zonal wind (ms^{-1}) as a function of sigma and latitude for the $8\Omega_e$ simulations with eddy-eddy interactions (a), and without eddy-eddy interactions (b).

climates. In addition, studying the different roles of changes in the lower and upper tropospheric thermal structure will also deepen the understanding of the mechanisms controlling this behavior.

3.6 The effect of eddy–eddy interactions on jet formation and macroturbulent scales

The turbulent behavior of large scales in the atmosphere suggests the importance of eddy–eddy interactions in controlling the atmospheric energy spectrum. In particular, studying their effect on the energy-containing scales in the atmosphere is crucial for developing a better understanding of the physical processes at synoptic scales. In this study, we examine the importance of the eddy– eddy interactions in controlling the macroturbulent scales. Because of their latitudinal dependence (Chemke and Kaspi, 2015a), we study their effect by comparing idealized GCM simulations with and without eddy–eddy interactions as a function of latitude (Sec. 2.1.3).

We carry out a set of simulations where we systematically increase the planetary rotation rate up to 8 times Earth's rotation rate (Ω_e). Increasing the rotation rate enables studying multiple-jet planets at all latitudes (due to the poleward migration of the eddy-driven jets, Chemke and Kaspi, 2015b), and thus to accumulate better statistics on the meridional and zonal containing scales. At high rotation rates the eddy length scale is relatively small compared to the planet size (e.g., Schneider and Walker, 2006; Kaspi and Showman, 2015), which provides a wide separation among the important macroturbulence scales (e.g., the Rhines scale, Rossby deformation radius, scale of barotropic to baroclinic energy conversion, etc.). Each simulation has 30 vertical sigma layers at T170 horizontal resolution ($0.7° \times 0.7°$). Unless otherwise stated, the results represent the time average of the last 500 days of 2000 day simulations.

3.6.1 The width of the jet

As discussed in section 1, previous studies (O'Gorman and Schneider, 2007; Chai and Vallis, 2014) showed that in Earth-like simulations when the eddy-eddy interactions were removed, the jets were compressed towards the equator and an additional jet emerged at higher latitudes. Figure 3.46 shows a snapshot of the meridional-height cross section of the mean zonal wind in the full and QL $8\Omega_e$ simulations. Similar to Tobias and Marston (2013) the mean zonal wind intensifies in the QL simulation, particularly at high latitudes, as in Marston (2012). In order to see how robust this phenomenon is, we calculate the number of eddy-driven jets[7] through a series of simulations with different rotation rates (Fig. 3.47a). As the rotation rate increases, the eddy length scale decreases, which increases the number of jets in the atmosphere (e.g., Williams and Holloway, 1982; Navarra and Boccaletti, 2002; Kaspi and Schneider, 2011; Chemke and Kaspi, 2015b), since their meridional scale correlates with the Rhines scale (Rhines, 1975; Vallis and Maltrud, 1993; Panetta, 1993; Lee, 2005; O'Gorman and Schneider, 2008c; Chemke and Kaspi, 2015a). The number of the eddy driven jets in the QL simulations (red dots in Fig. 3.47a) is larger by $\sim 58\%$ than in the full simulations (blue dots in Fig. 3.47a). This can also be seen by observing the mean zonal wind in the full and QL $8\Omega_e$ simulations (Fig. 3.46).

The presence of eddy-driven jets in the QL simulations at latitudes where these jets were absent in the full simulations (Fig. 3.46), implies that the production of the zonal jets through local processes in spectral space of nonlinear eddy-eddy interactions (e.g., Rhines, 1977; Williams, 1978; Rhines, 1994) is less important in such atmospheric simulations (e.g, Farrell and Ioannou, 2007; Constantinou et al., 2014; Marston, 2012; Srinivasan and Young, 2012). The maintenance of jets by eddy-mean flow interactions (e.g., Shepherd, 1987b; Panetta, 1993; Huang and Robinson, 1998; Robinson, 2006; Farrell and Ioannou, 2007), is further discussed in the next section.

O'Gorman and Schneider (2007) suggested that the meridional wavenumber of the mean flow is smaller in the full simulation, due to the tendency of eddy-eddy interactions to inverse cascade energy near the zero zonal wavenumber to smaller meridional wavenumbers. This could imply a narrowing of the jet's width as the eddy-eddy interactions are removed. However, similar to Constantinou et al. (2014) and Srinivasan and Young (2012), when the eddy-eddy interactions are removed in our simulations, the width of the jet remains similar to the width of the jet in the full simulations (95% of the jets have either increase or decrease their width in less than 20%), through all latitudes and rotation rates (Fig. 3.48a). The width of the jet is defined as the meridional distance between two consecutive minima values of the mean zonal wind.

The increase in the number of eddy driven jets in these simulations (Fig. 3.47a), is due to an increase in the latitudinal width of the region where these jets appear (Fig. 3.47b). We refer to this region as the 'jet region'. By comparing the mean zonal wind for the QL and full $8\Omega_e$ simulations (Fig. 3.46), the jet region becomes wider (stronger eddy-driven jets appear at

[7]We define an eddy-driven jet to be where its maximum vertical and zonal averaged velocity is larger than 50% of the maximum vertical and zonal averaged velocity of the strongest jet. This avoids low values of zonal wind for the calculation of the number of eddy-driven jets. The results are not sensitive to taking a lower or higher percentage. Defining an eddy-driven jet as a local maximum of the zonal wind that resides in the baroclinic zone (e.g., the latitudinal extent of the baroclinic zone is defined where 30% of the maximum value of the eddy heat flux is observed near the surface, Schneider and Walker, 2006), produces the same results.

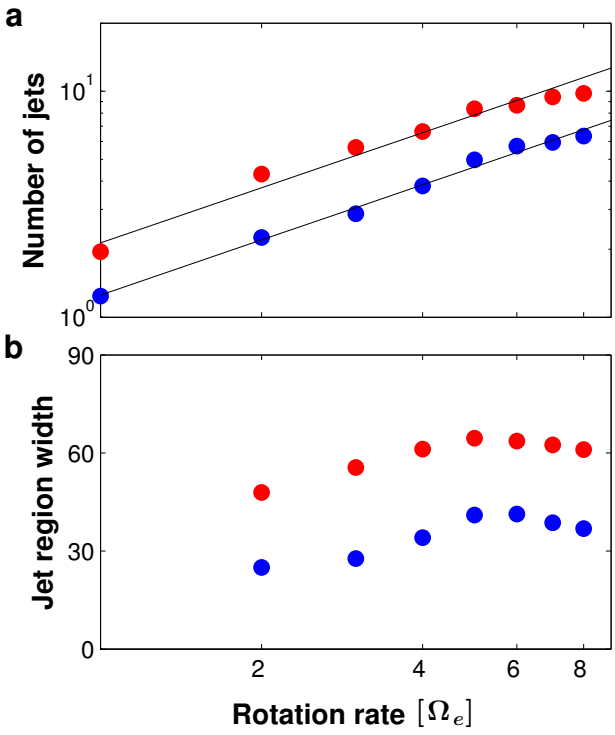

Figure 3.47: a. The number of eddy-driven jets in both hemispheres as a function of rotation rate, for simulations with (blue) and without (red) eddy-eddy interactions. b. The latitudinal width of the jet region for simulations with (blue) and without (red) eddy-eddy interactions. The two black lines in panel a follow $C_{1,2} \cdot \Omega^{0.81}$ where $C_1 = 1.58C_2$. The width of the jet region is defined as the distance between the most equatorward and poleward eddy-driven jets. Only simulations where the eddy-driven jets are clearly separated are taken into account for the analysis of panel b ($\Omega > \Omega_e$).

higher latitudes) as the eddy-eddy interactions are removed. This increase in the width of the jet region is found to occur through all rotation rates (Fig. 3.47b). The latitudinal jet region increases in the QL simulations (red dots in Fig. 3.47b) on average by $\sim 70\%$ compared to the full simulations (blue dots in Fig. 3.47b). Hence, most of the change in the meridional structure of the zonal wind in the QL simulations comes from the expansion of the jet region (Fig. 3.46b), and not from a change in the jets' width (Fig. 3.48a). The increase in the QL simulations of the jet region ($\sim 70\%$) is larger than the increase in the number of eddy-driven jets ($\sim 58\%$), since the jets that appear at higher latitudes are wider (Fig. 3.46) due to the latitudinal dependence of the Rhines scale (Huang and Robinson, 1998; Kidston and Vallis, 2010; Chemke and Kaspi, 2015b,a).

The width of the jet region displays a non-monotonic dependence on rotation rate, in both full and QL simulations. For the lower rotation rates, the jet region increases with rotation rate (Fig. 3.47b) mainly due to the decrease in the latitudinal extent of the Hadley cell (Held and Hou, 1980; Walker and Schneider, 2006). On the other hand, at higher rotation rates, the jet region slowly decreases with rotation rate, which might be due to the weakening of the poleward eddy heat flux with rotation rate (Hunt, 1979; Kaspi and Showman, 2015), which limits the edge of the baroclinic and jet regions.

The width of the jets in the QL simulations is found to scale with the Rhines scale, and not with the Rossby deformation radius (Fig. 3.48b) through all latitudes and rotation rates, as was shown to occur in the full simulations as well (Chemke and Kaspi, 2015a). The Rhines scale is defined using Eq. 2.13. The Rossby deformation radius is defined using Eq. 2.14 multiplied by π,

$$L_D = 2\pi \frac{NH}{f}, \tag{3.16}$$

where H is the tropopause height calculated as the height where the static stability reaches a threshold value of 0.015 s^{-1}, and $N = \left(\frac{g}{\theta}\frac{\partial\theta}{\partial z}\right)^{1/2}$ is the vertically averaged static stability below the tropopause height (similar to Frierson et al., 2006), where g is gravity and θ is the potential temperature[8]. The conversion between wavenumbers (k) and length scales (L) is computed at each latitude using Eq. 2.11.

The correlation of the width of the jet and the Rhines scale, latitude by latitude through all rotation rates, in the QL simulations, implies that the width of the jet can not be determined by an inverse energy-cascade argument through eddy-eddy interactions. Similarly, in the full simulations, where eddy-eddy interactions were found to be weak (equatorward of the supercriticality latitude), the jets' width correlates with the Rhines scale. While the above correlation in the QL simulations occurs similarly at all latitudes (Fig. 3.48b), in the full simulations the width of the jet coincides better with the Rhines scale poleward of the supercriticality latitude, where eddy-eddy interactions were found to be important (see Fig. 8d in Chemke and Kaspi, 2015a). This suggests that the eddy-eddy interactions do have some effect on the width of the jet, mostly poleward of the supercriticality latitude. Nonetheless, as the ratio between the width of the jets in the full and QL simulations behaves similarly poleward (blue dots in Fig. 3.48a) and equatorward (red dots in Fig. 3.48a) of the supercriticality latitude, this effect may be of less importance.

3.6.2 Macroturbulent scales

The effect of eddy-eddy interactions on the meridional structure of the flow can be further understood by comparing the different components in the budget of the zonal barotropic EKE (following the analysis of Larichev and Held, 1995, but here as a function of latitude, as in Chemke and Kaspi, 2015a). Even though the meridional structure of the mean flow and eddies are also affected by meridional macroturbulent scales (Simmons, 1974; Vallis and Maltrud, 1993; Huang and Robinson, 1998; Huang et al., 2001; Barry et al., 2002), here we study the effect of eddy-eddy interactions on the meridional structure of the jets using the zonal spectrum

[8]The Rossby deformation radius is similar to the Rossby deformation radius calculated when applying the WKBJ approximation on the eigenvalue problem for the vertical structure of the QG streamfunction (Gill, 1982; Chelton et al., 1998). The 2π factor represents the conversion to wavelength. Rhines scales calculated using the barotropic EKE (e.g., Haidvogel and Held, 1980; Schneider and Walker, 2006; Jansen and Ferrari, 2012; Chai and Vallis, 2014), the energy cascade rate (Held and Larichev, 1996) or using the Rayleigh–Kuo stability criterion (Farrell and Ioannou, 2007), were found to be less consistent with the width of the jet and with the halting scale of the inverse energy cascade (Chemke and Kaspi, 2015a) than the Rhines scale in Eq. 2.13.

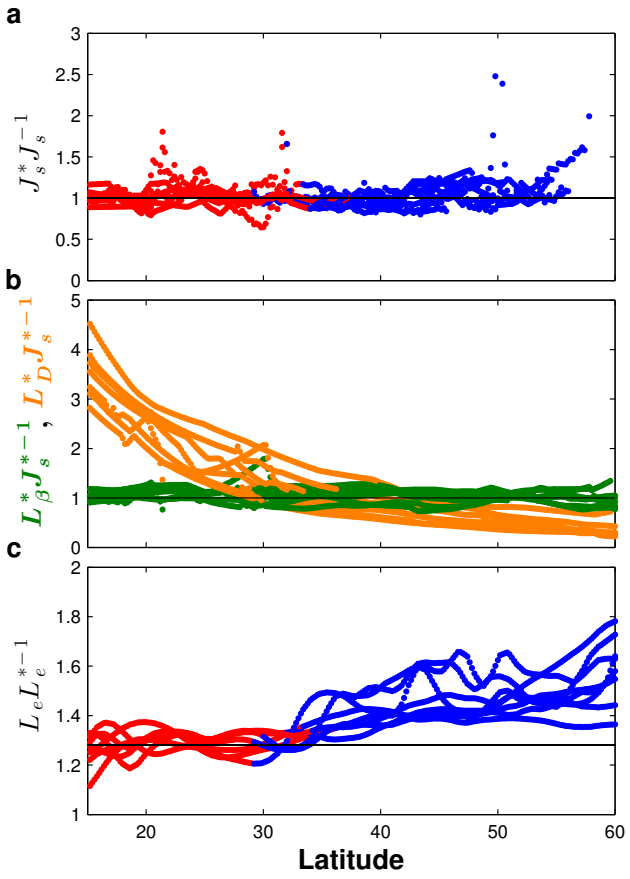

Figure 3.48: Scale properties as a function of latitude for all rotation rates. In all panels each dot represents a ratio at a single latitude and rotation rate. a. The ratio between the width of the jets in the QL (denoted with an asterisk) and full simulations. b. The ratio between the Rhines scale and the width of the jet (green), and between the Rossby deformation radius and the width of the jet (orange) in the QL simulations. c. The ratio between the length scale of the energy-containing zonal wavenumber, calculated from the zonal spectrum of the barotropic eddy meridional velocity (Eq. 2.10), in the full and QL (denoted with an asterisk) simulations. In panels a and c the blue (red) dots represent latitudes poleward (equatorward) of the supercriticality latitude.

(see appendix 2.3); this is done mainly due to two reasons: first, this allows studying the effect of eddy-eddy interactions as a function of latitude (both poleward and equatorward of the supercriticality latitude). Second, the eddy-eddy interactions also have a latitudinal effect on other zonal macroturbulent scales (e.g., the baroclinic conversion and energy-containing scales), which are further analyzed below. The components in the barotropic EKE equation (Sec. 2.3) are presented only for the $8\Omega_e$ simulation, as it captures the properties both above and below the supercriticality latitude (Fig. 3.49). A similar analysis was conducted in previous studies (e.g., Lambert, 1984; Koshyk and Hamilton, 2001; Jansen and Ferrari, 2012; Chai and Vallis, 2014), only for the EKE using two-dimensional spectra. The black line in each panel of Fig. 3.49 shows the supercriticality latitude from the full simulation, where the Rhines scale (blue line, Eq. 2.13) is equal to the Rossby deformation radius (white line, Eq. 3.16). The gray line shows the conversion from baroclinic to barotropic EKE zonal wavenumber, calculated as the centroid of Eq. 2.9. This definition provides conversion wavenumbers that are closest to the maximum

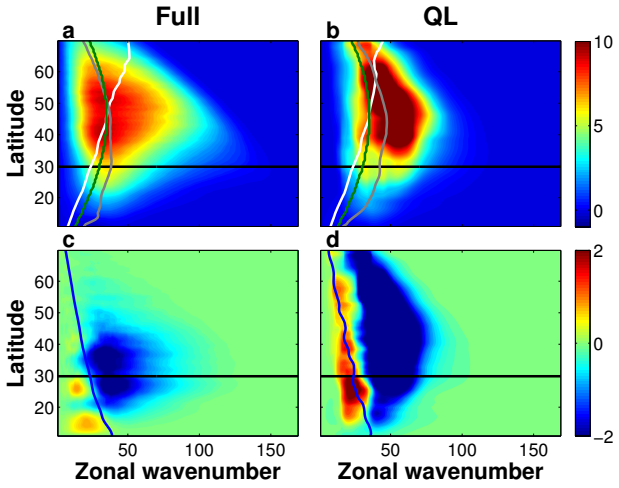

Figure 3.49: Components of the barotropic EKE equation (10^{-5} m^{2}s^{-3}, Eqs. 2.9 and 2.7) in the $8\Omega_e$ run as a function of latitude and zonal wavenumber. The left (right) column presents a simulation with (without) eddy-eddy interactions of conversion of baroclinic EKE (top), and eddy-mean interactions (bottom). Each component is multiplied by the wavenumber and smoothed with a 20-point running mean. The black, gray, blue, green and white lines correspond to the supercriticality latitude (where the Rhines scale is equal to the Rossby deformation radius) from the full simulation, the conversion wavenumber of baroclinic to barotropic EKE, the Rhines scale, the maximum baroclinic growth wavenumber and the Rossby deformation wavenumber (see text for definitions), respectively.

of Eq. 2.9.

It has been suggested that the presence of eddy-eddy interactions reduces the conversion of potential to kinetic energy, which can explain the increase in the kinetic energy in the QL simulations (e.g., O'Gorman and Schneider, 2007; Chai and Vallis, 2014). In the QL simulations, the conversion from baroclinic to barotropic EKE indeed strengthens (the maximum conversion is 1.6 larger in the QL simulations, poleward of the supercriticality latitude), compared to the full simulations, mostly at intermediate scales (Berloff and Kamenkovich, 2013a,b), while it weakens at large and small scales (compare Fig. 3.49a and 3.49b). This is consistent with the increase of barotropic EKE in the QL simulations at intermediate scales, and a decrease at large and small scales (Chemke and Kaspi, 2015a). Due to this opposite behavior at different scales, it might suggest that the mean EKE in the full and QL simulations are also similar. Indeed, the Rhines scale (computed using the EKE, Eq. 2.13) is found to be similar for each rotation rate in the full and QL simulations (Fig. 3.50, blue dots). The increase in baroclinic conversion to the barotropic mode in the QL simulations is consistent with the tendency of the eddy-eddy interactions to make the stratification less uniform (not shown). A more uniform stratification, as occurs in the atmosphere compared to the ocean, enables a stronger baroclinic conversion (Fu and Flierl, 1980; Smith and Vallis, 2001, 2002; Chemke and Kaspi, 2016b).

The conversion from baroclinic to barotropic EKE not only strengthens, but also shifts to larger zonal wavenumbers in the QL simulations, and reaches higher latitudes (compare gray line between Fig. 3.49a and Fig. 3.49b). The eddy-mean interactions also strengthen and intrude into higher latitudes in the QL simulations (replacing the strong eddy-eddy interactions

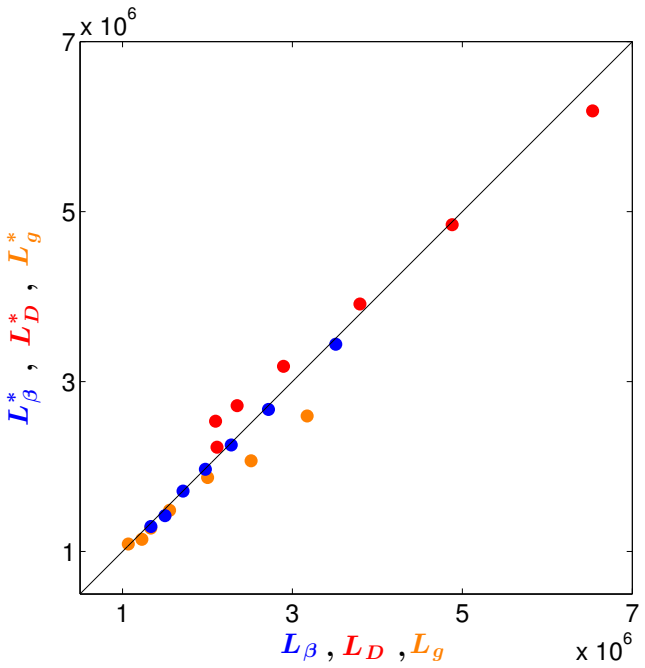

Figure 3.50: The Rhines scale (blue), the Rossby deformation radius (red) and the conversion scale of baroclinic to barotropic EKE (orange) in the QL simulations (denoted with an asterisk) compared to the full simulations, for all rotation rates. For comparing the scales in the QL and full simulations, the meridional average of each scale is taken over the jet region calculated from the full simulations (defined as the distance between the most equatorward and poleward jet).

poleward of the supercriticality latitude, Fig. 8d in Chemke and Kaspi, 2015a), and maintain the jets there (Figs. 3.46 and 3.49c and d). Thus, by weakening the baroclinic conversion and efficiently spreading it locally in spectral space, the eddy-eddy interactions *inhibit* jet formation at high latitudes. Not only the transfer of barotropic EKE to the mean flow increases in the QL simulation, but also the addition of barotropic EKE to large scales from the mean flow increases (Figs. 3.49c and 3.49d). While in the QL simulations the addition of barotropic EKE by the eddy-mean interactions at large scales coincides with the Rhines scale (blue line, Fig. 3.49d), in the full simulations, on the other hand, the addition of barotropic EKE by eddy-eddy interactions coincides with the Rhines scale (Chemke and Kaspi, 2015a).

In the QL simulations, as in the full simulations, the Rossby deformation radius does not coincide with the conversion scale of baroclinic to barotropic EKE (white and gray lines in Figs. 3.49a and 3.49b). This differs from the classic two-layer phenomenology of Salmon (1978), and can be more robustly seen in Fig. 3.50, by comparing the deformation radius (red) and conversion scale (orange) at each rotation rate simulation, where all scales decrease monotonically with rotation rate. At low rotation rates (larger scales in Fig. 3.50), both the conversion scale and the Rossby deformation radius are larger in the full simulations. At high rotation rates, on the other hand, while the conversion scale better coincides in the QL and full simulations (although still larger in the full simulation), the Rossby deformation radius is larger in the QL simulations (Fig. 3.50). The conversion scale decreases with rotation rate, as the inverse cascade of the barotropic EKE is being arrested at smaller Rhines scales (Chai and Vallis, 2014).

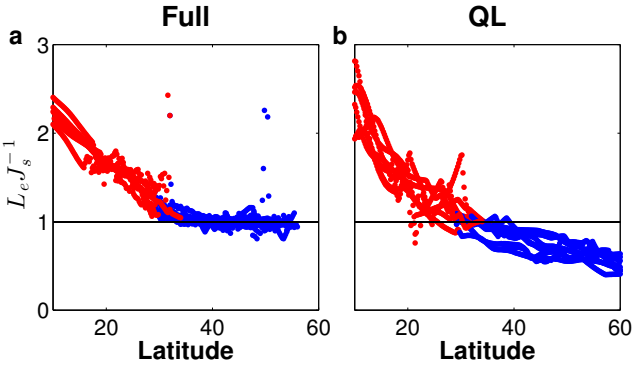

Figure 3.51: The ratio of the length scale of the energy-containing zonal wavenumber, calculated from the zonal spectrum of the barotropic meridional velocity (Eq. 2.10), and the jet space as a function of latitude for all rotation rates presented in Fig. 3.47b for simulations with eddy-eddy interactions (a) and without eddy-eddy interactions (b). The blue (red) dots represents latitudes poleward (equatorward) of the supercriticality latitude.

The green line in Fig. 3.49 shows the scale of maximum baroclinic growth, which is the wavenumber corresponding to the fastest growth rate computed using a linear normal-mode instability analysis (Smith, 2007). This is done by solving the linearized QG potential vorticity equation, at each latitude, using the meridional potential vorticity gradient, mean zonal wind and density from the idealized GCM simulations. Similar to the filtering method of Smith (2007), in order to consider only the most unstable wavenumbers that are energetically important, we normalized the maximum growth rate of all levels by the eddy available potential energy (EAPE). The EAPE is estimated using the variance of the potential temperature field (e.g., Lorenz, 1955; Saltzman, 1957; Boer, 1975; Schneider and Walker, 2006)[9]. Even though the Rossby deformation radius does not coincide with the conversion scale, the scale of maximum baroclinic growth does show a similar latitudinal behavior as the conversion scale, consistent with Jansen and Ferrari (2012), but here also through all latitudes (Figs. 3.49a and 3.49b). In the QL simulation the conversion scale is smaller than the scale of maximum baroclinic growth (Fig. 3.49b), as in the full simulation equatorward of the supercriticality latitude, where eddy-eddy interactions are weaker (Fig. 3.49b). On the other hand, poleward of the supercriticality latitude in the full simulation, the scale of maximum baroclinic growth coincides with the conversion scale (Fig. 3.49a).

Similar to the meridional direction, the energy-containing zonal wavenumber also increases in the QL simulations (Fig. 3.48c). As in O'Gorman and Schneider (2008c) and Chemke and Kaspi (2015a), the energy-containing zonal wavenumber is computed using the "squared inverse centroid" of the zonal spectrum of the barotropic eddy meridional velocity (Eq. 2.10)[10].

The length scale of the energy-containing zonal wavenumber is not only larger in the full simulations, (consistent with Chai and Vallis, 2014 QL simulations under strong supercriticality),

[9] Applying a shortwave cutoff at each latitude by filtering out the unstable wavenumbers where the conversion from baroclinic to barotropic EKE is less than 85% of the maximum conversion, produces the same results.

[10] This definition produces an energy-containing zonal wavenumber closest to the peak of the zonal spectrum of the barotropic eddy meridional velocity, and its length scale (Eq. 2.11) best coincides with the jets scale (Fig. 3.51a, blue dots).

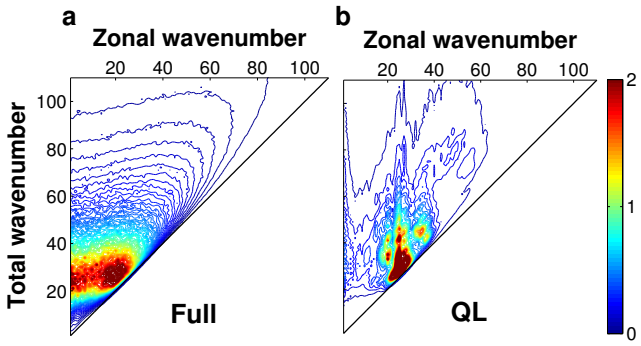

Figure 3.52: The 2D spectrum, computed using spherical harmonics as basis functions (Boer and Shepherd, 1983), of the barotropic EKE (10^{-2} m^2s^{-2}) as a function of zonal and total wavenumbers in the $8\Omega_e$ simulation with eddy-eddy interactions (a) and without eddy-eddy interactions (b).

but also its ratio with the length scale of the energy-containing zonal wavenumber in the QL simulations increases with latitude (Fig. 3.48c, blue dots). Equatorward of the supercriticality latitude the length scale of the energy-containing zonal wavenumber is found to be larger in the full simulations by a factor of ~ 1.3 (Fig. 3.48c, red dots). At these latitudes, the width of the jet is smaller than the length scales of the energy-containing zonal wavenumbers in both full and QL simulations (Fig. 3.51, red dots). On the other hand, poleward of the supercriticality latitude the jet and energy-containing scales coincide only in the full simulations (Fig. 3.51, blue dots).

The effect of eddy-eddy interactions on the ratio between the zonal energy-containing and meridional width of the jets, can be explained by the tendency of the eddy-eddy interactions to spread the barotropic EKE along lines of constant total wavenumbers (Fig. 3.52a, turbulence isotropization) as discussed in Shepherd (1987a) and Huang and Robinson (1998). In the QL simulation, the lack of eddy-eddy interactions reduces the isotropization of the flow, and the barotropic EKE is no longer spread along lines of constant total wavenumbers (Fig. 3.52b). As a result, the meridional width of the jet does no longer coincide with the zonal energy-containing scale poleward of the supercriticality latitude (Fig. 3.51, blue dots). Furthermore, the energy containing wavenumber is isolated in the spectral space (Fig. 3.52b), once these interactions are removed.

3.6.3 Conclusions

In this study we show that eddy-eddy interactions have a large effect on both the meridional and zonal structure of jets in a series of idealized GCM simulations where we systematically compare simulations with (full simulations) and without eddy-eddy interactions (quasi-linear simulations, QL), at different rotation rates. The different rotation rates allow preforming the analysis over a continuous range of latitudes, eddy scales and jet widths. Our main conclusions are as follows:

- The eddy-eddy interactions are found to decrease the number and intensity of eddy-driven jets in the atmosphere (Figs. 3.46 and 3.47a), by limiting the latitudinal extent of the region where these jets appear (Fig. 3.47b). This implies that not only that eddy-eddy interactions are not a prerequisite for the formation of zonal jets in the atmosphere, but also that they act to inhibit jet formation.

- Eddy-eddy interactions are found to limit the barotropization of the flow mostly poleward of the supercriticality latitude (Figs. 3.49a and 3.49b). Consistently, in the QL simulations stronger barotropic eddy-mean flow interactions intrude into these latitudes (Figs. 3.49c and 3.49d). These interactions replace the eddy-eddy interactions (which efficiently spread the input of baroclinic EKE locally in spectral space) and maintain the jets (transfer energy to the zero zonal wavenumber) at high latitudes, and thus, widen the jet region (Fig. 3.47b).

- In the full Earth-like simulation, the supercriticality latitude was found to occur poleward of the baroclinic zone. As a result, eddy-eddy interactions were found to play a negligible role in the balance (Chemke and Kaspi, 2015a). Nonetheless, in the QL Earth-like simulation, an additional jet emerges at high latitudes (Fig. 3.47a) as in O'Gorman and Schneider (2007) and Chai and Vallis (2014). This implies that eddy-eddy interactions do have some effect on the zonal mean flow, even under Earth's parameters.

- The eddy-eddy interactions are found to have a minor effect on the meridional width of the jets through all latitudes and rotation rates (Fig. 3.48a). As in the full simulations Chemke and Kaspi (2015a), also in the QL simulations the width of the jet coincides with the Rhines scale through all latitudes and rotation rates (Fig. 3.48b). Thus, the Rhines scale also remains similar in both full and QL simulations. This congruity implies that the jet scale is not determined by a turbulence inverse cascade.

- The conversion scale of baroclinic to barotropic EKE does not coincide with the Rossby deformation radius, for all rotation rates, both in the full and QL simulations (Figs. 3.49a, 3.49b and 3.50). It does, however, better coincide with the scale of maximum baroclinic growth, mostly poleward of the supercriticality latitude.

- The eddy-eddy interaction are found to make the flow more isotropic; as they both spread the barotropic energy along lines of constant total wavenumber (Fig. 3.52), and increase the energy-containing zonal wavenumber (Fig. 3.48c) such that it coincides with the meridional jet scale (Fig. 3.51a).

Chapter 4

Atmospheric mass

4.1 The thermodynamic effect of atmospheric mass on early Earth's temperature

Various indirect observations suggest that Earth's early atmospheric mass may have differed from its present-day value (e.g., Nishizawa et al., 2007; Goldblatt et al., 2009; Som et al., 2012; Marty et al., 2013; Johnson and Goldblatt, 2015; Kavanagh and Goldblatt, 2015; Som et al., 2016), though whether the atmosphere was more or less massive than present remains a topic of debate. Negligible atmospheric O_2 concentrations in Earth's early atmosphere (e.g., Kasting, 1993) suggest total pressure lower by about 20%, which is unlikely to be compensated for by higher CO_2 concentrations required to explain a relatively warm climate under a weaker early Sun (Sagan and Chyba, 2010; von Paris et al., 2008; Kienert et al., 2012; Wolf and Toon, 2013; Wordsworth and Pierrehumbert, 2013). The early abundance of the main component of the atmosphere, N_2, is less clear. Earth's geologic N_2 budget suggests that the mantle has been a net sink of N_2, implying greater-than-present Archean atmospheric pressure (Goldblatt et al., 2009; Johnson and Goldblatt, 2015), in agreement with upper limits from rain droplet imprints of $2-10$ times the current atmospheric density ~ 2.7 billion year ago (Ga)(Som et al., 2012; Kavanagh and Goldblatt, 2015). Studies of fluid inclusions in hydrothermal quartz disagree on whether early Archaean atmospheric mass was half today's value or up to 3.3 times greater (Nishizawa et al., 2007; Marty et al., 2013). Recently, using gas bubbles in basaltic lava, Som et al. (2016) suggested an upper limit on surface pressure of only half the present-day value. In aggregate, it appears from existing constraints that the total pressure of the early atmosphere may have been as little as half or as much as ten times its present-day value.

In this study, we use an idealized moist GCM to elucidate the effects of atmospheric mass on thermodynamical processes and early Earth's near-surface temperature (Sec. 2.1.4). The advantage of using an idealized GCM to study the behavior of temperature under variations of atmospheric mass is that compared to 1D radiative-convective models, an idealized GCM provides a more complete description of the dynamic and thermodynamic structures of the atmosphere (e.g., more realistic vertical and meridional processes). Yet, in comparison with full GCMs, which contain a large number of variables that affect the dynamics (e.g., clouds, chemical reactions, etc.), the relative simplicity of the idealized GCM enables isolation of the basic physics

that contribute most to the dynamic-thermodynamic processes in the atmosphere. We neglect the effects of atmospheric mass on the radiative transfer (e.g., Rayleigh scattering and pressure broadening), which have been previously studied, and focus exclusively on thermodynamic effects.

4.1.1 Simulation setup

Surface pressure is systematically varied using an idealized GCM (Sec. 2.1.4) from 0.5 to 10 times Earth's present-day value ($p_{s_e} = 1\,\text{bar}$), in order to examine the effects of atmospheric mass on the thermodynamics. As the majority of observations constrain Earth's early surface pressure to $0.5 - 4 \times p_{s_e}$, we show the results for this range of p_s in the main text, and show the results for $0.5 - 10 \times p_{s_e}$ in appendix 6.2 (Figs. 6.3 and 6.4). The simulations up to $10 \times p_{s_e}$ are similar to the simulations of Kaspi and Showman (2015), but with a solar luminosity of 80% of its present-day value to simulate a weaker early Sun. Each simulation has 30 vertical σ layers at T42 horizontal resolution ($2.8° \times 2.8°$). Increasing the resolution does not have a significant effect on the results. Simulation results presented here are zonally averaged and represent the time average of the last 500 days out of a 1500-day simulation. The major role of the atmospheric heat capacity in these simulations can affect the time it takes the model to reach a thermal and kinetic energy statistically steady-state, and in all simulations it is verified that such a steady-state is in fact reached. Note that due to the model's simplicity, it may not exactly capture the temperature and wind fields in early Earth's atmosphere. Nevertheless, it enables study of the 3D behavior of the dynamic and thermodynamic components of the atmosphere.

Changes in temperature due to increasing atmospheric mass are best understood by studying the model's temperature tendency equation (Eq. 2.2). In a steady state ($\partial/\partial t = 0$), the two types of processes in Eq. 2.2 that are most affected by a change in p_s are moist processes (Q_{conv}), as these involve temperature relaxation toward a moist adiabatic lapse rate (Betts, 1986; Betts and Miller, 1986; Frierson et al., 2006), and the radiative forcing (Q_{rad}, Eq. 2.3), as it is affected by the atmospheric heat capacity ($C_p dm$), which increases with increasing atmospheric mass. Studying the temperature tendency equation rather than the energy equation, provides a straight-forward understanding of the temperature variations due to changes in atmospheric mass, especially as the atmospheric mass affects the heat capacity of the atmosphere, and thus the conversion between energy and temperature.

To isolate the effects of the atmospheric heat capacity and moisture on near-surface (lowest atmospheric level) temperature, under p_s variations, three types of idealized GCM simulations are compared: I. simulations where both atmospheric heat capacity and moisture effects are taken into account (Frierson et al., 2006), with an active hydrological cycle (i.e., moist convection affects the temperature tendency), and using the radiative forcing term in Eq. 2.3. II. simulations without moist convection, and using the radiative forcing term in Eq. 2.3, and III. simulations without moist convection, and with a forcing scheme based on a Newtonian cool-

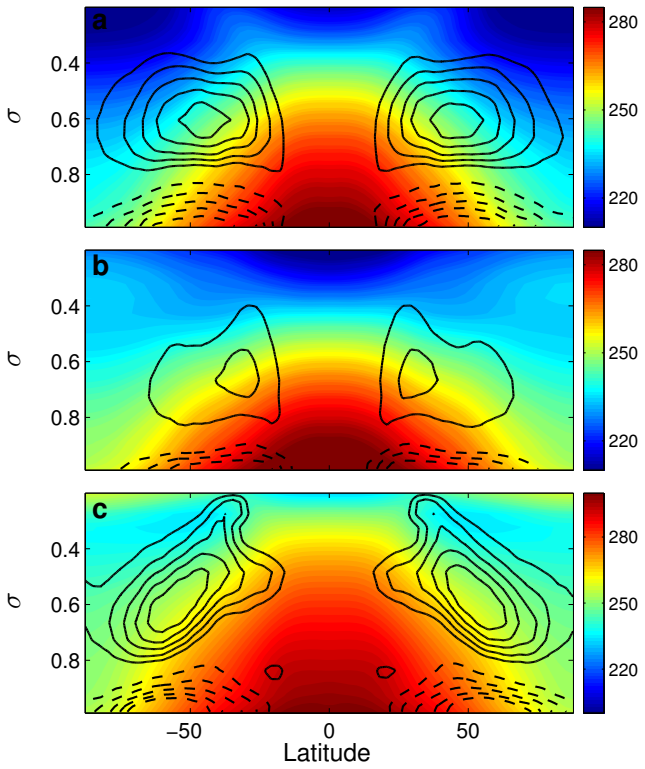

Figure 4.1: The zonal and time mean temperature (K, color contours) and vertical advection of temperature by eddies (Ks^{-1}, black contours) as a function of height and latitude. Solid and dashed contours denote positive and negative temperature tendencies, respectively. (a) Type I simulation of early Earth climate, with solar luminosity of $1088\,\mathrm{Wm}^{-2}$ (80% its present value) and surface pressure of 1 bar. (b) Type I simulation of early Earth climate, with solar luminosity of $1088\,\mathrm{Wm}^{-2}$ and surface pressure of 4 bar. (c) Simulation of present-day climate, which includes the greenhouse gas effect of water vapor and ice-albedo feedback, with solar luminosity of $1360\,\mathrm{Wm}^{-2}$, surface pressure of 1 bar and 40 Pa of CO_2 at the surface. Minimum and maximum contours correspond to -2.5×10^{-5} and $1\times10^{-5}\,\mathrm{Ks}^{-1}$ in panels a and c, and to -1×10^{-5} and $0.5\times10^{-5}\,\mathrm{Ks}^{-1}$ in panel b.

ing ($\frac{T_{\mathrm{relax}}-T}{\lambda}$, instead of Eq. 2.3) which does not depend on atmospheric mass (Held and Suarez, 1994; Frierson, 2005) and where the temperature is relaxed towards a fixed profile (T_{relax}) with a relaxation time λ ($\lambda_i = 150$ days and $\lambda_s = 15$ days are the interior and near-surface relaxation times, respectively), as described in (Schneider, 2004). In these dry simulations, convection acts to relax the temperature towards a constant convective profile of $\sim 6.8\,\mathrm{K\,km}^{-1}$. Note, that varying λ in type III simulations is equivalent to varying the atmospheric mass in type I and II simulations, and thus produces similar results (Fig. 6.5 in appendix 6.2).

After evaluating the effects of an atmospheric mass different than today's on Earth's early climate using type I-III simulations (Sec. 4.1.2.1), we then show and discuss an amplification of the climatic effect of changing atmospheric mass by the positive water-vapor and ice-albedo feedbacks (type IA simulations, Sec. 4.1.2.2). Since in type I simulations the optical thickness only varies spatially and the planetary albedo is constant, we investigate the effect of these feedbacks, by allowing the water-vapor and surface temperature to affect the optical thickness and planetary albedo, respectively (type IA). The setup of type IA simulations is described in Sec. 4.1.2.2. Finally, we map the ice-line latitude in a parameter space of total and CO_2 surface

pressures (Sec. 4.1.3).

4.1.2 Results and Discussion

4.1.2.1 Warming due to an increase in atmospheric mass

The reduction in solar flux to 80% of its present-day value decreases the global mean near-surface temperature to 275 K and pushes the ice-line latitude equatorward (the latitude where the near-surface temperature equals the temperature at the triple-point of water, $T_0 = 273.16$ K, Fig. 4.1a). Fig. 4.2a shows the change of the mean near-surface temperature in type I simulations with respect to present-day reference simulation (p_{s_e}). When both moisture and atmospheric heat capacity effects are included (type I simulation), the increase in p_s increases the global mean near-surface temperature (Fig. 4.1b) by up to ~ 4.5 K (at $4 \times p_{s_e}$, red circles in Fig. 4.2a). The convective fluxes may decrease with increasing p_s, due to an increase of the moist adiabatic lapse rate, and thereby increase the near-surface temperature (Goldblatt et al., 2009). To examine this effect of moisture on the mean near-surface temperature we performed type II simulations. In these simulations there are no convection processes, and the atmospheric mass only affect the radiative forcing term (Eq. 2.3) through the atmospheric heat capacity ($C_p dm$). In these simulations the temperature increases with surface pressure to $\sim 70 - 75\%$ of the temperature increase in the moist, type I simulations (blue circles in Fig. 4.2a), demonstrating that moist convection is not the primary cause for the increase of mean near-surface temperature with atmospheric mass. With a radiation scheme independent of pressure (type III simulation), the mean near-surface temperature does not change with p_s (black circles in Fig. 4.2a). Hence, the effects on the mean near-surface temperature due to changes in atmospheric mass are mostly through a change in the atmospheric heat capacity (Eq. 2.3).

The dimmer Sun in Earth's early history leads to stronger global net radiative cooling in the lower atmosphere (i.e., $Q_{\text{rad}} < 0$). The inverse relation between Q_{rad} and the atmospheric mass (Eq. 2.3) decreases net radiative cooling with increasing p_s, thereby increasing the mean near-surface temperature (Figs. 4.1a, b and 4.2a). The presence of the temperature in the radiative forcing term (in the net longwave radiative flux), opposes this warming effect, as the warming itself acts to increase the net radiative cooling, but the overall effect is still a surface warming. Examination of the meridional and vertical temperature distributions reveals a decreased meridional temperature gradient with larger atmospheric mass (compare Figs. 4.1a and b). While the near-surface temperature in the tropics warms by ~ 4 K when the atmospheric mass is quadrupled, at the poles it warms by ~ 10 K. The meridional distribution of solar heating imposes a net radiative warming at low latitudes, but a net cooling at high latitudes, and overall cooling in the global net, as discussed above. Thus, higher atmospheric mass, which depresses low-latitude radiative warming and high-latitude cooling, tends to flatten the meridional temperature gradient. This may limit baroclinic instability processes (e.g., Eady, 1949; Phillips, 1954), and, as shown below, may suppress midlatitude vertical eddy tempera-

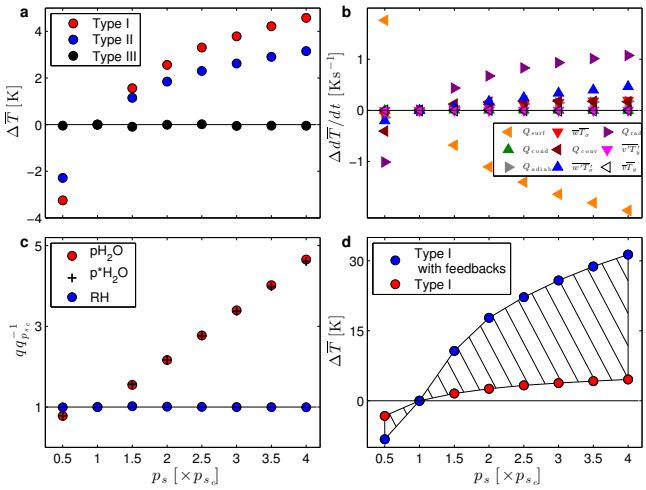

Figure 4.2: The dependence of zonal, meridional and time mean near-surface temperature, components of its tendency equation (Eq. 2.2) and moisture parameters on surface pressure relative to the $1\times p_{s_e}$ simulation with solar luminosity 80% its present value. (a) Mean near-surface temperature from simulations with the effect of heat capacity, and with (type I, red) and without (type II, blue) moist convection, and dry simulations without both moist convection and the effect of heat capacity (type III, black). (b) Mean components of the mean near-surface temperature tendency equation (10^{-5}) in type I simulation at a statistically steady state (i.e., all components add to approximately zero); Radiation (purple), vertical advection of eddy temperature fluxes (blue), adiabatic term (gray), vertical advection of mean temperature fluxes (red), meridional advection of mean temperature fluxes (black), meridional advection of eddy temperature fluxes (magenta), surface fluxes (orange), condensation (green) and convection (maroon). (c) The ratio of the tropospheric mean water vapor partial pressure (red), saturated water vapor partial pressure (black crosses), and relative humidity (blue). Shown are simulations with optical thickness calculated using water vapor concentrations and 500 Pa of CO_2 at the surface (type IA). (d) Mean near-surface temperature from simulations with optical thickness calculated using water vapor concentrations and 500 Pa of CO_2 at the surface (blue, type IA), and using parameterized optical thickness (type I, red). The hatched area shows the effect of the water vapor and ice-albedo feedbacks on the mean near-surface temperature.

ture fluxes (Kaspi and Showman, 2015), thereby trapping heat at the surface and flattening the meridional temperature gradient even further (Fig. 4.1a and b), which acts to destabilize the atmosphere (Stone, 1978; Held, 1982; Juckes, 2000; Schneider, 2004; Frierson, 2006). Flattening of the gradient is not due to net meridional advection, but due to radiative processes and decreased vertical eddy fluxes.

To better understand the effects of the different components in Eq. 2.2 on the mean near-surface temperature at steady state, we calculate their mean values for each value of p_s and compare the results to the present-day reference simulation (p_{s_e}). These results are shown in Fig. 4.2b, where the magnitude of several components in the temperature tendency equation are shown to increase with increasing atmospheric mass. Thus, these components act to warm the near-surface with increasing mass. The increase in magnitude of the warming components is balanced, at a steady state, by a decrease in surface fluxes (orange), leading to less near-surface warming, but this balance is achieved at higher near-surface temperatures with increasing p_s. The radiative component (purple), which contains the effect of the atmospheric heat capacity

($C_p dm$, Eq. 2.3), is the main contributor to near-surface warming. It becomes less negative with increasing p_s, as it decreasingly cools the lower layers of the atmosphere. An associated decrease in vertical eddy advection (blue) traps more heat in the lower atmosphere (compare black contours in Fig. 4.1a and b), and contributes to warming with increasing p_s (Kaspi and Showman, 2015). The convection (maroon), mean vertical temperature advection (red) and the adiabatic term (gray) contribute similarly to warming the surface with atmospheric mass, but with a smaller magnitude than the radiation and vertical eddy temperature fluxes. The findings for convection (increased warming with increasing p_s) are similar to the suggested tendency of convective fluxes, at a given surface temperature, to decrease with p_s due to an increase of the moist adiabatic lapse rate (Goldblatt et al., 2009). However, in relatively massive atmospheres (beyond $3.5 \times p_{s_e}$), the convective fluxes become increasingly negligible, which results in a weaker warming with increasing p_s (Fig. 6.3b in appendix 6.2). The fact that on one hand the warming solely due to convection plays a minor role in the temperature tendency equation (maroon circles in Fig. 4.2b), but on the other hand, convection is responsible for almost a third of the warming effect (Fig. 4.2a), suggests that it triggers other processes that contribute to the warming. These warming effects in the lower atmosphere suppress the sensible and diffusive heat fluxes from the ocean (orange). Changes in the other terms in Eq. 2.2 with increasing p_s are of lesser importance (Fig. 4.2b).

4.1.2.2 Amplification by positive feedbacks

Previous full GCM studies found an increase of $\sim 7\,\mathrm{K}$ in the global sea surface temperature for a doubling of surface pressure (Charnay et al., 2013; Wolf and Toon, 2014). Here, a doubling of surface pressure produces an increase of only $\sim 2\,\mathrm{K}$. This difference is likely related to two factors. First, the idealized GCM lacks radiative responses to changes in atmospheric mass, such as changes in Rayleigh scattering and importantly, pressure broadening of infrared absorption by greenhouse gases (e.g., CO_2 and H_2O). Second, positive feedbacks were absent from the simulations in Sec. 4.1.2.1, which were aimed at elucidating the thermodynamic effects of different atmospheric mass only. Of these feedbacks, the water vapor and ice-albedo feedbacks are both expected to amplify the temperature response to changes in atmospheric mass. According to the Clausius-Clapeyron relation, the warmer atmospheric column (due to a higher atmospheric mass) holds more water vapor, which increases the infrared opacity of the atmosphere, and may result in additional warming (Hartmann, 1994). Additionally, a warmer surface results in decreased ice cover, and the albedo of the ice itself decreases with increasing temperature (Griffies et al., 2011). Both effects decrease the planetary albedo, increase the fraction of solar radiation absorbed at the surface, and result in additional warming.

To account for the greenhouse effect of water vapor and its response to warming (cooling) by an increase (decrease) in atmospheric mass, we run an additional set of simulations (type IA), where the optical depth is not only parameterized spatially as in type I simulations (Sec. 4.1.2.1), but also as a function of the water vapor content (Thuburn and Craig,

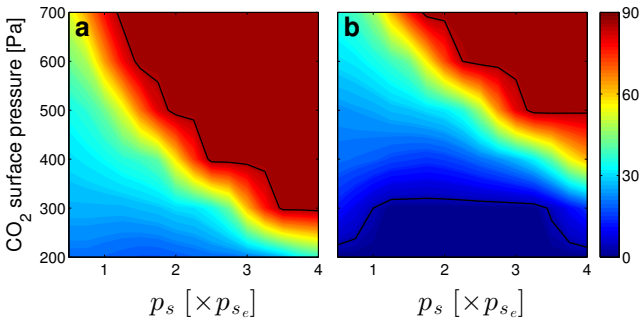

Figure 4.3: Ice-line latitude as a function of pCO_2 and total surface pressure. Shown are simulations with the water vapor and ice-albedo feedbacks, and with a solar luminosity of (a) 80%; (b) 75% its present value. The black contours represent the 90° and 0° ice-line latitudes. The total surface pressure and pCO_2 simulations are conducted in intervals of $0.25 \times p_{s_e}$ and 100 Pa, respectively.

2000; Merlis and Schneider, 2010) and CO_2 concentrations. The optical depth varies with height as described in Frierson et al. (2006), $\tau = \tau_{CO_2}\sigma + \tau_{H_2O}\sigma^4$, where the linear term represents the relative global contribution of a well-mixed longwave absorber, such as CO_2 and the quadric term represents the relative global contribution of an absorber with a scale height that is one quarter of the pressure scale, such as water vapor. The surface optical depths of CO_2 and water-vapor are calculated as the full vertical integral of the absorption coefficient, C, and the number density of the absorber (Hartmann, 1994), η, $\tau_{CO_2} = C_1 \int_{p_{top}}^{p_s} \frac{R_d T}{pg} \eta_{CO_2} dp$, and $\tau_{H_2O} = C_2 \int_{p_{top}}^{p_s} \frac{R_d T}{pg} \eta_{H_2O} dp$, respectively. η_{CO_2} and η_{H_2O} are the CO_2 and water vapor number density, respectively. The absorption coefficients, $C_1 = 0.5 \times 10^{-3}\,\mathrm{m}^2$ and $C_2 = 5 \times 10^{-3}\,\mathrm{m}^2$, are empirical constants chosen to best produce Earth's current climate (mean near-surface temperature of 289 K, mean meridional temperature gradient between 50 and 60 K, and ice-line latitude of $\sim 60°$, Fig. 4.1c), with global contributions of water vapor and CO_2 to the net longwave absorption for clear-sky conditions of $\sim 70\%$ and $\sim 30\%$, respectively (Kiehl and Trenberth, 1997; Schmidt et al., 2010), and an increase of $3 - 4$ K for a CO_2 doubling, consistent with the Intergovernmental Panel on Climate Change Fifth Assessment Report IPCC (2013). This, together with the fact that in all simulations the relative humidity changes only by less than $\sim 2\%$ (Hartmann, 1994; Held and Soden, 2006) (Fig. 4.2c), provide confidence that the qualitative results presented here do not depend on the above adaptation of the radiation scheme.

To account for the ice-albedo feedback, in these simulations (type IA) the albedo is no longer constant but changes with surface temperature (Griffies et al., 2011; Pierrehumbert et al., 2010), T_s, as

$$\alpha(T_s) = \begin{cases} \alpha_l & T_s \geq T_0 \\ \alpha_h + (\alpha_l - \alpha_h)\frac{(T_s - T_i)}{T_0 - T_i} & T_i < T_s < T_0 \\ \alpha_h & T_s \leq T_i \end{cases} \tag{4.1}$$

where $\alpha_l = 0.26$ and $\alpha_h = 0.45$ are the surface ice-free and ice-cover albedo values, respectively, above T_0 the surface is assumed to be ice-free, and $T_i = 263.16$ K is the temperature below which the surface is ice-covered.

Although this parameterized radiation scheme is more realistic compared to Type I simulations, as it includes water vapor and ice-albedo feedbacks, it still lacks key radiative responses to changes in atmospheric mass (e.g., Rayleigh scattering and pressure broadening of gaseous absorption lines), as well as any responses related to clouds. Changes in cloud cover and, consequently, the planetary albedo, may offset some of the warming due to the water vapor and ice-albedo feedbacks. Thus, the radiation scheme used in this study likely tends to underestimate the CO_2 concentrations required to sustain a given mean climate. Conversely, use of this radiation scheme tends to overestimate near-surface temperatures for a given concentration of CO_2. Nevertheless, the idealized GCM with the improved radiation scheme allows an exploration of the thermodynamic response of the atmosphere to changes in mass, and we expect the actual temperature response to be intermediate between the response with and without the water vapor and ice-albedo feedbacks, as parameterized here.

For a constant CO_2 concentration of 500 Pa, including the water vapor and ice-albedo feedbacks results in substantial warming as the mass of Earth's atmosphere increases (Fig. 4.2d, blue). For example, with $p_s = 2 \times p_{s_e}$ the global average near-surface temperature increases by more than 15 K (compared to ~ 2 K without the feedbacks). With $p_s = 4 \times p_{s_e}$ the global average near-surface temperature increases by ~ 30 K (compared to ~ 4.5 K without the feedbacks). This is double the warming found in full GCMs (Charnay et al., 2013; Wolf and Toon, 2014), probably due to the absence of Rayleigh scattering in our simulations, which increases with atmospheric mass (Wolf and Toon, 2014). The warming can be divided into effects arising only from the increased atmospheric mass (Fig. 4.2d, red), which are discussed in Sec. 4.1.2.1, and those arising from positive feedbacks due to the atmospheric water vapor content and the albedo of ice, which together account for the majority of the warming (Fig. 4.2d, hatched area). It is important to note, however, that the positive feedbacks are only pushed into operation by the warming associated with an increase in atmospheric mass.

4.1.3 Ice-line latitude and Earth's habitability

A necessary condition for Earth's early habitability is that the ice-line latitude is poleward of the tropics and global glaciation is avoided. The ice-line latitude shifts poleward with increasing pCO_2 due to a stronger greenhouse effect (Fig. 4.3), consistent with the findings of previous studies (Pierrehumbert et al., 2010). In addition, even with constant pCO_2, the ice-line latitude shifts poleward with increasing p_s. At ~ 3 Ga (80% present luminosity) and pCO_2 between 300 and 600 Pa (within observational constraints, Kasting, 2010 and references therein), an atmospheric mass 1 to 3 times its present-day value is sufficient to achieve a present-day ice-line latitude of $\sim 60°$. At ~ 3.8 Ga (75% present luminosity) an atmospheric mass 2 to 5 times its present value is sufficient for the same range of pCO_2 (Fig. 4.3b). Overall, a more massive early atmosphere may help to explain the existence of liquid water on Earth's surface in the face of a less luminous early Sun.

The rate of increase of the ice-line latitude with surface pressure depends on pCO_2 (see the

contour gradient upon a horizontal transect in Fig. 4.3). As mentioned above, the decrease in both net radiative cooling and vertical eddy temperature fluxes, which is more pronounced in the extratropics (Vallis, 2006), preferentially warms the high latitudes as surface pressure is increased. As a result, when pCO_2 is high and the ice line resides at relatively high latitudes, which are more sensitive to a change in atmospheric mass, the change in ice-line latitude due to changing atmospheric mass is more pronounced. This also affects the termination of global glaciations. The global net warming due to increasing p_s leads to a requirement of less CO_2 to initiate deglaciation. In addition, as discussed above, once deglaciation starts, as the ice-line latitude resides further poleward, for a given pCO_2 it increases more rapidly with increasing p_s. This effect can be seen in Fig. 4.3b, where a shift in the ice-line from snowball (lower black line) to ice-free (upper black line) conditions requires smaller ΔpCO_2 with increasing p_s. Note, that at low p_s and CO_2 concentrations the ice-line latitude decreases with atmospheric mass (bottom-left corner in Fig. 4.3b). This may be related to near-surface condensation, due to the low temperatures. The associated release of latent heat may result in a poleward shift of the ice line with decreasing atmospheric mass.

4.1.4 Conclusions

An increase (decrease) in atmospheric mass causes an increase (decrease) in near-surface temperatures and a decrease (increase) of the equator-to-pole near-surface temperature gradient. Warming is caused mostly by the increase in atmospheric heat capacity with mass, which decreases the net radiative cooling of the atmosphere. Also important is a decrease in vertical eddy heat fluxes, which traps more heat in the lower atmosphere and heats the surface. As both net radiative cooling and vertical heat fluxes are more pronounced at mid-high latitudes, the meridional temperature gradient decreases with increasing atmospheric mass. A more massive atmosphere would have required lower greenhouse gas abundances to maintain a warm climate on early Earth, perhaps to within constraints on paleo-pCO_2 levels. On the other hand, if Earth's early atmosphere were less massive, as suggested in some recent studies, then higher abundances of greenhouse gases, or other warming mechanisms would have been required to keep Earth's surface warm.

4.2 Atmospheric dynamics of massive atmospheres

In this study we explore the effects of atmospheric mass on the general circulation. Atmospheric mass varies greatly between planets, and is clearly crucial for the atmospheric dynamics and habitability, and therefore understanding its affect on planetary climate is essential. Here, the dynamical-thermodynamical role of atmospheric mass on the planet's atmospheric circulation is studied using an idealized 3D ocean slab GCM, where the surface pressure is systematically varied (which is equivalent of changing the entire atmospheric mass) between 0.5 bar and

100 bar. In order to keep the analysis and simulations as simple as possible in the vast planetary parameter space, we keep all planetary parameters similar to Earth, and only vary the surface pressure (Sec. 2.1.4).

The top row in Fig. 4.4 shows the zonal and time mean meridional streamfunction (in colors),

$$\Psi = 2\pi a \int_0^1 \overline{v} \cos\varphi d\sigma, \tag{4.2}$$

where a is Earth's radius, v is the meridional velocity, φ is latitude, and overbar ($\bar{\cdot}$) represents a zonal and time mean; and the mean zonal wind, $\overline{u}$ (in contours), as a function of sigma and latitude for four simulations with different surface pressure (1, 10, 30 and 100 bar in panels a, b, c and d, respectively). The blue (red) colors correspond to clockwise (counterclockwise) circulation.

The 1 bar simulation (Fig 4.4a), which represents Earth's present-day atmosphere, has two major zonally symmetric meridional cells in each hemisphere; the tropical Hadley cell and extratropical Ferrel cell (as in Earth's atmosphere, disregarding the seasonal cycle). The Hadley cell (most equatorward blue colors in Fig. 4.4a) is driven by the differential heating between low and high latitudes, which results in rising warm air at the equatorial troposphere. The stable stratosphere above the tropopause halts this equatorial ascending air, which then propagate poleward, cools and descends at the subtropics. As the poleward movement flow at the upper branch of the Hadley cell conserves angular momentum, while its distance from the planet's axis of rotation decreases, a strong zonal flow forms at the edge of the Hadley cell. This flow is referred to as the subtropical jet.

In the extratropics, the circulation is driven by eddies (deviations from zonal mean), which maintain the indirect circulation of the Ferrel cell by meridionally converging heat and momentum. The eddies are driven by baroclinic instability (e.g., meridional temperature gradient, Pedlosky, 1987), and in their life cycle go through a growing and decaying phases (Simmons and Hoskins, 1978). In their growing phase, the eddies extract available potential energy from the mean flow, and grow on the expense of the meridional temperature gradient (through eddy heat fluxes). As the meridional temperature gradient is directly related to the vertical shear of the zonal wind, through thermal wind balance, the eddies act to weaken the vertical shear in their growing phase as well. Then, by converting their available potential energy to kinetic energy, the eddies return the energy to the mean flow by strengthening the mean zonal shear through eddy momentum flux convergence, thus maintaining the extratropical eddy-driven jets (Vallis, 2006).

4.2.1 Tropical circulation

Increasing atmospheric mass results in two robust changes of the mean tropical circulation (Fig. 4.4). First, the circulation contracts as the atmospheric mass increases. Second, the strength of the mean meridional circulation decreases as the atmospheric mass increases. Note,

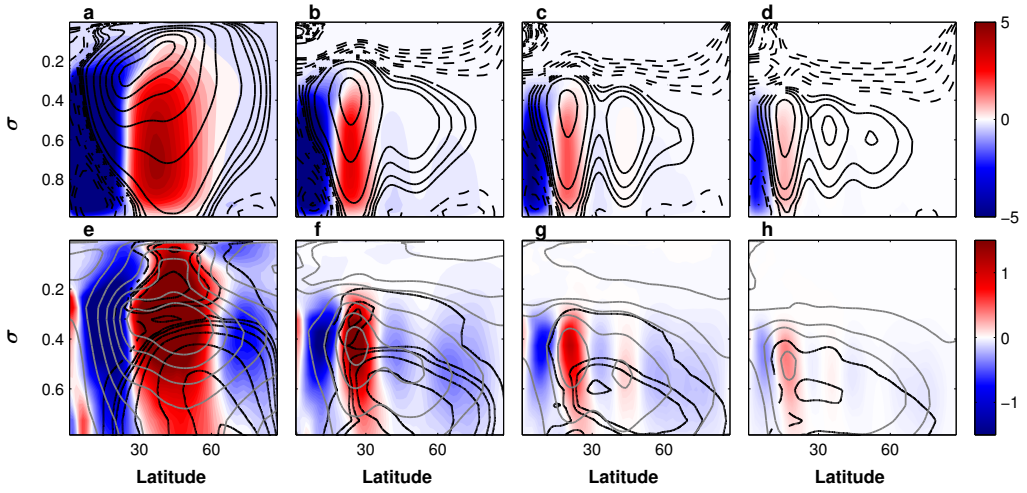

Figure 4.4: Mean fields from simulations of 1 bar (first column), 10 bar (second column), 30 bar (third column) and 100 bar (fourth column) as a function of sigma and latitude. First row (a-d) shows the mean meridional streamfunction ($10^5\,\mathrm{m^2 s^{-1}}$, colors) and mean zonal wind ($\mathrm{ms^{-1}}$, contours). Solid and dashed contours correspond to positive (easterly) and negative (westerly) flows, respectively. Second row (e-h) shows the meridional ($10^{-5}\,\mathrm{ms^{-2}}$, colors) and vertical ($\mathrm{ms^{-2}}$, black contours) EP flux components (Eqs. 4.9-4.10) and the mean eddy kinetic energy (gray contours).

that different than Kaspi and Showman (2015), here we do not plot the mean meridional mass streamfunction, which was shown to increase with atmospheric mass (i.e., mass transfer increases with atmospheric mass), but rather only the strength of the mean circulation.

4.2.1.1 Hadley cell width

To understand the contraction of the Hadley cell with atmospheric mass (most left blue colors in the top row of Fig. 4.4), we first parametrize the latitudinal extent of the Hadley cell, and then study the different parametrization as a function of atmospheric mass. Figure 4.5a shows the latitudinal extent of the Hadley cell, calculated as the latitude where the mean meridional streamfunction first changes sign at the height of its maximum value, as a function of the surface pressure. The Hadley cell width decreases with atmospheric mass following $\propto p_s^{-0.164}$.

The first parameterization studied here for the Hadley cell width is that of Held and Hou (1980), which assumes that the upper branch of the Hadley cell conserves angular momentum and that the cell is thermally closed. They suggest that the latitudinal extent of the Hadley cell scales as,

$$Y_{\mathrm{HH}} \propto \left(\frac{5 \Delta_h \theta g H|_{\mathrm{Hadley}}}{3 \Omega^2 a^2 \theta_0} \right)^{1/2}, \tag{4.3}$$

where $\Delta_h \theta$ is the tropospheric equator-to-pole potential temperature difference, $H|_{\mathrm{Hadley}}$ is the mean tropopause height in the Hadley cell, Ω is Earth's rotation rate and θ_0 is the global mean tropospheric potential temperature. This scaling (Eq. 4.3), with a constant of proportionality of $C_{\mathrm{HH}} = 0.782$, is found to linearly follow the Hadley cell's edge in our simulations (red dots

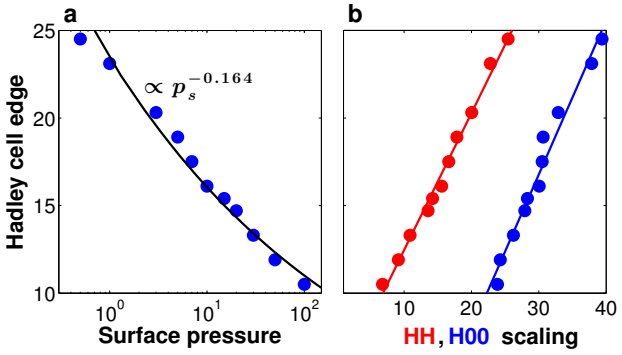

Figure 4.5: The Hadley cell edge (latitude, see text for definition), as a function of (a) surface pressure (bar) and (b) Held and Hou (1980) scaling (Eq. 4.3, red) and Held (2000) scaling (Eq. 4.5, blue). The red and blue lines in panel b show the best linear fit and correspond to $y_{\mathrm{HH}} = x + 4.6$ with $R^2 = 0.99$ and $y_{\mathrm{H00}} = x - 9.6$ with $R^2 = 0.97$, respectively.

in Fig. 4.5b), $y = x + 4.6$ with $R^2 = 0.99$. The 4.6 degrees difference between the two scaling might be either related to the Held and Hou (1980) theory assumptions, or to the fact that in Held and Hou (1980) the $\Delta_h\theta$ is calculated as the radiative equilibrium temperature difference, while here it is the steady state temperature difference.

The zonal mean angular momentum equation, after neglecting the vertical advection and frictional processes, can be written as,

$$\frac{D\overline{m}}{Dt} = -\frac{1}{a\cos\varphi}\frac{\partial}{\partial\varphi}(\overline{v'm'}\cos\varphi), \tag{4.4}$$

where $m = (u + \Omega a\cos\varphi)a\cos\varphi$ is angular momentum, u is the zonal wind and prime denotes deviation from zonal mean (i.e., the eddy component). The eddies (righthand side of Eq. 4.4), thus, may overcome the conservation of mean angular momentum. This led Held (2000) to introduce a second parametrization, which estimated the latitudinal extent of the Hadley cell as the latitude where the vertical shear of the angular momentum conserving flow first encounters the baroclinically unstable shear of midlatitudes (according to the two-layer model criterion of Phillips, 1954),

$$Y_{\mathrm{H00}} \propto \left(\frac{NH|_{\Psi=0}}{\Omega a}\right)^{1/2}, \tag{4.5}$$

where $N^2 = -\frac{g^2\rho}{\theta}\frac{\partial\theta}{\partial p}$ is the mean extratropical static stability and $H|_{\Psi=0}$ is the tropopause height at the edge of the Hadley cell (i.e., where the mean meridional streamfunction first changes sign at the height of its maximum value). The scaling of Held (2000) (Eq. 4.5) with a constant of proportionality of $C_{\mathrm{H00}} = 0.879$ is also found to linearly follow the Hadley cell edge in our simulations (blue dots in Fig. 4.5b), $y = x - 9.6$ with $R^2 = 0.97$, but with more than a double latitudinal shift of 9.6 degrees than using Eq. 4.3.

The linear relation of both scalings (Fig. 4.5b) with the latitudinal extent of the Hadley cell enables further investigation of its decrease with atmospheric mass, by studying the different components of each scaling. To understand which of the components of each scaling contributes most to the contraction of the Hadley cell we normalize both Eqs. 4.3 and 4.5 by their values in

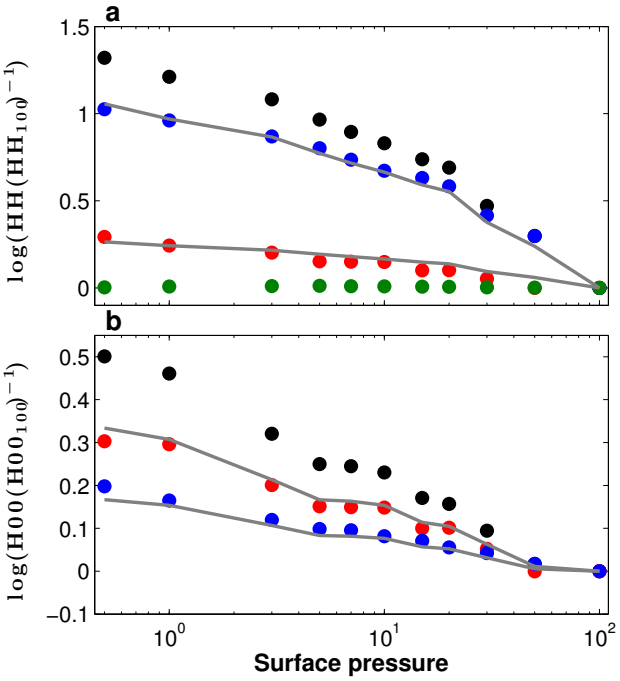

Figure 4.6: The log of the ratio of (a) the HH scaling (black), tropospheric equator-to-pole potential temperature difference ($\Delta_h\theta$, blue), tropopause height ($H|_{\mathrm{Hadley}}$, red) and the global mean tropospheric potential temperature (θ_0, green), and (b) The H00 (Held, 2000) scaling (black), tropopause height ($H|_{\Psi=0}$, red) and the static stability (N, blue) with their corresponding values in the most massive atmosphere simulation (100 bar surface pressure) as a function of surface pressure (bar). In panels (a) and (b) the gray lines show the 0.8 and 0.2 and the 0.6 and 0.3 values of the black dots, respectively.

the most massive simulation of 100 bar surface pressure, and take the logarithm of the equations. This produces the following two equations,

$$\log\left(\frac{Y_{\mathrm{HH}}}{Y_{\mathrm{HH}_{100}}}\right) = 0.5\log\left(\frac{\Delta_h\theta}{\Delta_h\theta_{100}}\right) + 0.5\log\left(\frac{H|_{\mathrm{Hadley}}}{H|_{\mathrm{Hadley}_{100}}}\right) + 0.5\log\left(\frac{\theta_{0_{100}}}{\theta_0}\right), \tag{4.6}$$

and

$$\log\left(\frac{Y_{\mathrm{H00}}}{Y_{\mathrm{H00}_{100}}}\right) = 0.5\log\left(\frac{N}{N_{100}}\right) + 0.5\log\left(\frac{H|_{\Psi=0}}{H|_{\Psi=0_{100}}}\right), \tag{4.7}$$

where all the contributions from variables that do not change with atmospheric mass (e.g., rotation rate, radius, gravitational acceleration) vanish. Plotting the above components as a function of surface pressure (Fig. 4.6) shows that 80% of the decrease in the Held and Hou (1980) scaling (black dots in Fig. 4.6a) can be explained by the decrease of the tropospheric equator-to-pole potential temperature difference ($\Delta_h\theta$, blue dots in Fig. 4.6a) and the other 20% by the decrease in the mean tropopause height in the Hadley cell ($H|_{\mathrm{Hadley}}$, red dots in Fig. 4.6a). For the Held (2000) scaling (black dots in Fig. 4.6b) two-thirds of the decrease in his scaling can be explained using the reduction of the tropopause height at the edge of the Hadley cell ($H|_{\Psi=0}$, red dots in Fig. 4.6b), and one third using the reduction of the mean extratropical

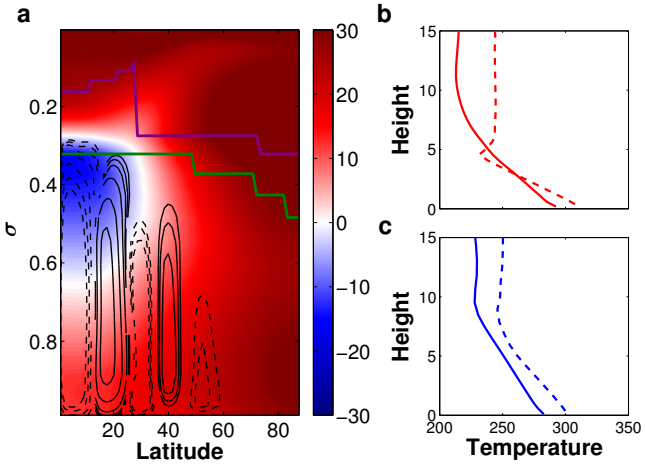

Figure 4.7: (a) Mean temperature difference (K, colors) between simulations with surface pressure of 50 bar and 1 bar as a function of sigma (p/p_s) and latitude. The solid and dashed lines respectively show the counterclockwise and clockwise circulation based on the streamfunction (m^2s^{-1}) in the simulation with surface pressure of 50 bar. The purple and green lines show the tropopause height in the simulation with surface pressure of 1 bar and 50 bar, respectively. Panels (b) and (c) show respectively the tropical (at the edge of the Hadley cell, red lines) and extratropical ($\sim 40°$, blue lines) temperature profiles as a function of height (km). The solid and dashed lines correspond to simulations with surface pressure of 1 bar and 50 bar, respectively.

static stability (N, blue dots in Fig. 4.6b).

This indicates that the reductions in the meridional temperature gradient and the tropopause height both in the tropics and in the extratropics (Fig.4.6), is strongly related to the decrease in the scaling of the Hadley cell width (Fig. 4.5). Figure 4.7a shows the temperature difference between two simulations of different atmospheric mass ($T_{50\,\mathrm{bar}} - T_{1\,\mathrm{bar}}$). The contours correspond to the mean streamfunction from the simulation with a surface pressure of 50 bar, where the solid and dashed contours respectively correspond to clockwise and counterclockwise circulation. The purple and green lines show the tropopause height in the simulation of 1 bar and 50 bar surface pressure, respectively. The tropopause height is calculated as the lowest height where the temperature lapse rate decreases below $2\mathrm{kmK}^{-1}$, following the definition of the World Meteorological Organization.

As the atmospheric mass increases, the temperature increases substantially at mid-high latitudes and less strongly near the surface at low latitudes, and decreases at low latitudes below the tropopause. This results in two main outcomes; First, the mean tropospheric meridional temperature gradient decreases, as shown in Fig. 4.6a (blue dots), and second, at low-mid latitudes the vertical temperature gradient increases. The increase of the temperature lapse rate can also be seen in Fig. 4.7b and c, where the vertical temperature profiles at the edge of the Hadley cell (red lines) and at midlatitudes ($\sim 40°$, blue lines) are shown for simulations of 1 bar (solid lines) and 50 bar (dashed lines) surface pressure. At low-mid latitudes, due to the warming of lower layers and cooling of the upper layers, the temperature lapse rate increases as the atmospheric mass increases, resulting in a lower tropopause height (compare solid and dashed red lines in Fig. 4.7b). Similarly, at high latitudes the lower troposphere warms more

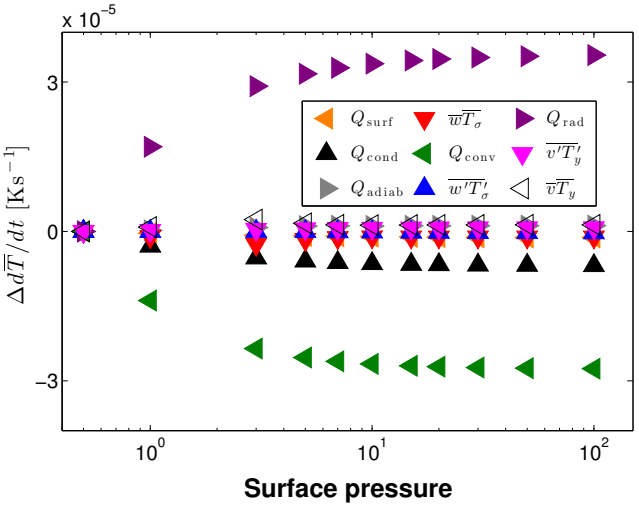

Figure 4.8: Mean tropospheric components of the temperature tendency equation relative to the lightest atmosphere simulation (0.5 bar surface pressure) as a function of surface pressure (bar); radiation (purple), vertical advection of eddy temperature fluxes (blue), adiabatic term (gray), vertical advection of mean temperature fluxes (red), meridional advection of mean temperature fluxes (black), meridional advection of eddy temperature fluxes (magenta), surface fluxes (orange), condensation (black), and convection (green).

than the upper troposphere, which also increases the temperature lapse rate with atmospheric mass (compare solid and dashed blue lines in Fig. 4.7c). Different from low-mid latitudes where there is a strong cooling below the tropopause, at high latitudes both upper and lower layers warm, resulting in a reduced change in the temperature lapse rate. Still, the decrease in the temperature lapse rate also reduces the tropopause height even at high latitudes. Thus, throughout all latitudes, the tropopause height decreases (compare the purple and green lines in Fig. 4.7a) as was shown in Fig. 4.6 (red dots). The reduction in the temperature lapse rate with atmospheric mass also reduces the static stability (N), resulting in a less stable atmosphere (blue dots in Fig. 4.6b).

What are the mechanisms behind the tropospheric cooling of low-mid latitudes, and the warming of low altitudes and high latitudes? Understanding these temperature changes with atmospheric mass can further elucidate the changes in tropopause height and meridional temperature gradient, and the contraction of the Hadley cell. The effects of surface pressure on the temperature can be understood by studying the temperature tendency equation (Eq. 2.2).

Figure 4.8 shows the tropospheric mean of the terms of the righthand side of Eq. 2.2 as a function of surface pressure, with respect to the lightest atmospheric mass simulation of 0.5 bar surface pressure. At steady state the lefthand side of Eq. 2.2 is zero, thus the sum of all components at each surface pressure simulation is zero. The term that contributes mostly to warming the troposphere is the radiative term (purple triangles, Eq. 2.3), which is mainly balanced by cooling due to convective processes (green triangles).

An increase in atmospheric mass, increases the heat capacity of the atmosphere, and following Eq. 2.3, tends to decrease the radiative heating (Chemke et al., 2016b). Thus, at places where there is a net radiative cooling, the radiation term will act to cool the atmosphere at a

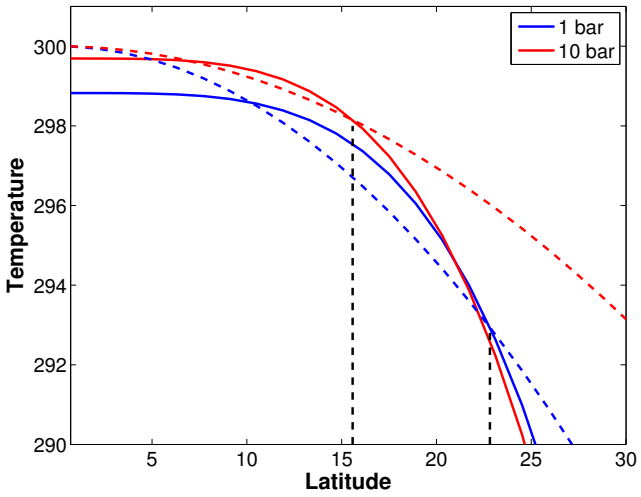

Figure 4.9: The temperature from the angular momentum conserving solution (θ_m, solid lines) and the radiative equilibrium temperature (θ_e, dashed lines, with $\theta_{e_0} = 300$K), from Held and Hou (1980) theory, as a function of latitude for simulations with surface pressure of 1 bar (blue lines) and 10 bar (red lines). The vertical black dashed lines indicate the latitudinal extent of the Hadley cell of 22.8° and 15.6° in simulations with surface pressure of 1 bar and 10 bar, respectively.

lesser rate. As net radiative cooling occurs through most of the troposphere, except near the surface around the equator, most of the troposphere warms as the atmospheric mass increases (red colors in Fig. 4.7a). Moreover, since in the lower atmosphere net radiative cooling is more pronounced in the extratropics, heating becomes stronger at higher latitudes, and contributes both to the reduction in the meridional temperature gradient (blue dots in Fig. 4.6a), and to the increase of the lapse rate at high latitudes (Fig. 4.7c).

The convective scheme in the model acts to relax the temperature profile towards a moist adiabatic lapse rate (Betts, 1986; Betts and Miller, 1986). An increase in surface pressure then increase the moist adiabatic lapse rate, bringing it closer to the dry adiabatic lapse rate, thus reducing the positive buoyancy of an air parcel and weakening the convective fluxes (Goldblatt et al., 2009). As the atmospheric mass increases, the convective fluxes thus tend to warm the surface (i.e., less heat is transferred upwards), and cool the upper level (blue colors in Fig. 4.7, and green triangles in Fig. 4.8). As convection occurs mostly at low-mid latitudes, this cooling effect contributes both to the weakening of the meridional temperature gradient and to an increase in the vertical temperature gradient at low-mid latitudes (Fig. 4.7b). Note, that in low latitudes the convective fluxes and radiative cooling have opposite effects to respectively increase and decrease the vertical temperature gradient.

In aggregate, the effect of atmospheric mass to reduce both the convective fluxes and the radiative cooling effect (Fig. 4.8), tends to weaken the meridional temperature gradient and increase the temperature lapse rate in both low and high latitudes, which decreases the tropopause height (Fig. 4.7a). Following the scaling of both Held and Hou (1980) and Held (2000), and consistent with our simulations, these changes act to contract the latitudinal extent of the Hadley cell (Figs. 4.5 and 4.6). These effects can also be seen by comparing the temperature's

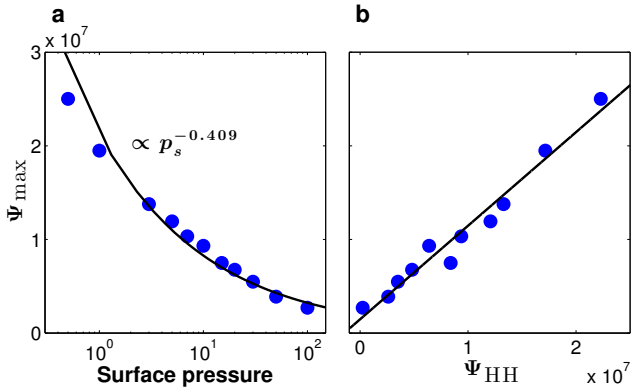

Figure 4.10: The Hadley cell strength, calculated as the maximum absolute value of the streamfunction (m^2s^{-1}, Eq. 4.2), as a function of (a) surface pressure (bar) and (b) Held and Hou (1980) scaling (Eq. 4.8). The black line in panel b shows the best linear fit ($y_{\mathrm{HH}_\Psi} = x + 1.46 \cdot 10^6$, with $R^2 = 0.966$).

solutions from Held and Hou (1980) theory (Fig. 4.9). In their theory, the Hadley cell is thermally closed such that the total radiative equilibrium temperature (i.e., diabatic forcing) in the Hadley cell, $\theta_e = \theta_{e_0} - \Delta_h \theta \varphi^2$, where θ_{e_0} is the equilibrium temperature at the equator, equals the total temperature from the angular momentum conserving solution, $\theta_m = \theta(0) - \frac{\theta_0 \Omega^2 a^2 \varphi^4}{2gH|_{\mathrm{Hadley}}}$, where $\theta(0) = \theta_{e_0} - \frac{5\Delta_h \theta^2 gH|_{\mathrm{Hadley}}}{18\Omega^2 a^2 \theta_0}$ is the potential temperature at the equator. Thus, the Hadley cell edge is predicted by where the solid and dashed blue lines intersect, such that the areas between the solid and dashed lines are equal inside the Hadley cell. For a given θ_{e_0}, θ_e changes slower with latitude as the atmospheric mass increases (compare blue and red dashed lines in Fig. 4.9), due to the decrease in the meridional temperature gradient with atmospheric mass (Figs. 4.6 and 4.7), which is associated with the reduction of the radiative cooling effect. θ_m, on the other hand, changes faster with latitude as the atmospheric mass increases (compare blue and red solid lines in Fig. 4.9), due to the decrease in the tropopause height with atmospheric mass (Figs. 4.6 and 4.7). As the atmospheric mass increases, the steepening of θ_e with latitude together with the more moderate change of θ_m, result in an equatorward shift of the Hadley cell edge (compare vertical black dashed lines in Fig. 4.9).

4.2.1.2 Hadley cell strength

As was shown in Fig. 4.4a-d, the Hadley cell circulation weakens with atmospheric mass following $\propto p_s^{-0.409}$ (Fig. 4.10a). The Hadley cell strength is calculated as the maximum of the mean meridional streamfunction (Eq. 4.2). According to Held and Hou (1980) scaling theory, the strength of the Hadley circulation follows,

$$\Psi \propto \frac{\Delta_h \theta^{2.5} g^{1.5} H^{2.5}|_{\mathrm{Hadley}}}{\Omega^3 a^2 \theta_0^{1.5} \Delta_v \theta}, \tag{4.8}$$

where $\Delta_v \theta$ is the vertical tropopause-to-surface potential temperature difference in the Hadley cell. The Hadley cell strength shows a linear relation with the scaling of Held and Hou (1980)

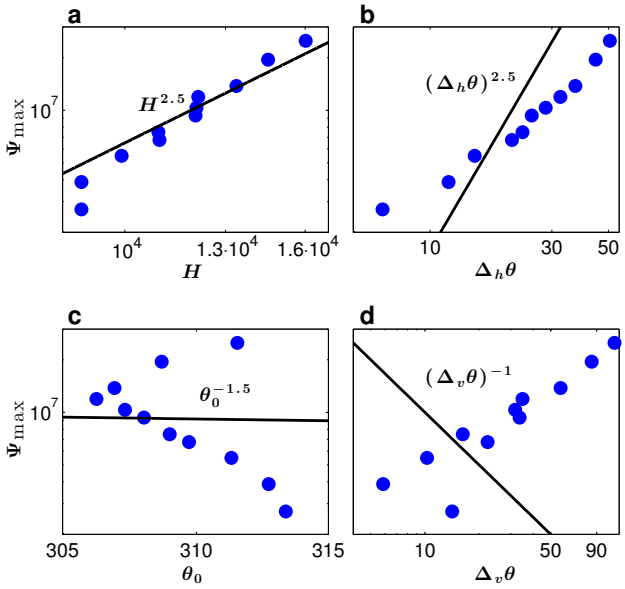

Figure 4.11: Hadley cell circulation strength (maximum mean meridional streamfunction, m^2s^{-1}, Eq. 4.2) as a function (a) averaged tropopause height in the Hadley cell ($H|_{\text{Hadley}}$), (b) tropospheric equator-to-pole potential temperature difference ($\Delta_h\theta$), (c) global mean potential temperature (θ_0) and (d) vertical tropopause-to-surface potential temperature difference in the Hadley cell ($\Delta_v\theta$). The black lines at each panel show the scaling relation based on Held and Hou (1980) (Eq. 4.8).

(Eq. 4.8) and using a constant of proportionality of $C_{\text{HH}_\Psi} = 1.22 \times 10^{-2}$.

To elucidate which of the components in Eq. 4.8 contributes mostly to the agreement between the Hadley cell strength and the scaling of Held and Hou (1980) (Eq. 4.8), the Hadley cell strength is plotted as a function of each of the Held and Hou (1980) scaling components (Fig. 4.11). While the tropopause height (Fig. 4.11a) and the meridional temperature gradient (Fig. 4.11b) show similar scaling to Eq. 4.8, the mean potential temperature (Fig. 4.11c) and the vertical temperature gradient (Fig. 4.11d) are poorly correlated (and even have an opposite sign) with the scaling of Held and Hou (1980) (Eq. 4.8). Thus, the decrease of both the tropopause height and meridional temperature gradient, as discussed earlier, contribute mostly to the weakening of the Hadley circulation with atmospheric mass.

4.2.2 Extratropical circulation

4.2.2.1 Strength of the extratropical circulation

Similar to the mean tropical circulation discussed in Sec. 4.2.1, the mean extratropical circulation and eddy fields also weaken with atmospheric mass (Fig. 4.4). Due to angular momentum conservation, the contraction of the Hadley cell with surface pressure weakens the subtropical jet (i.e., the most equatorward jet, contours in Fig. 4.4a-d). Concomitantly, not only the subtropical jet weakens but also the eddy-driven jets. As these jets are maintained by convergence of eddy momentum fluxes, these fluxes also weaken with atmospheric mass (colors in Fig. 4.4e-h). The bottom row in Fig. 4.4 shows the divergence of the two components of the

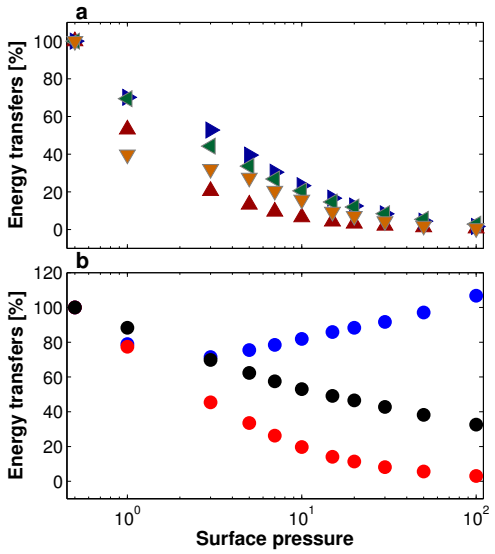

Figure 4.12: The energy conversions in the Lorenz's energy cycle in percentage of their corresponding values in the lightest atmospheric mass simulation of 0.5 bar as a function of surface pressure (bar); (a) MAPE to EAPE (red, Eq. 4.11), EAPE to EKE (green, Eq. 4.12), EKE to MKE (blue, Eq. 4.13) and MAPE to MKE (orange, Eq. 4.14). (b) Components of MAPE to EAPE (Eq. 4.11); Γ (blue), mean meridional temperature gradient (black) and mean meridional eddy temperature flux (red).

Eliassen–Palm flux (EP flux, Edmon et al., 1980),

$$-\frac{1}{a\cos^2\varphi}\frac{\partial}{\partial\varphi}\left(\overline{u'v'}\cos^2\varphi\right), \tag{4.9}$$

in colors, and

$$\frac{\partial}{\partial p}\left(f\overline{v'\theta'}\left(\frac{\partial\overline{\theta}}{\partial p}\right)^{-1}\right), \tag{4.10}$$

in black contours, where f is the Coriolis parameter. The red (blue) colors in Fig. 4.4e-h correspond to convergence (divergence) of eddy momentum fluxes (Eq. 4.10), and are associated with the acceleration (deceleration) of the eddy-driven jets (solid contours in Fig. 4.4a-d). The reduction of the eddy-mean flow interactions is also observed in the vertical component of the EP flux (Eq. 4.10) as well as in the eddy kinetic energy, EKE $= u'^2 + v'^2$ (gray contours).

Since eddy-mean flow interactions play an important role in the extratropics, studying the eddy-mean energy cycle helps explain the reduction in the strength of both the eddy fields and mean circulation. For each simulation we calculate the tropospheric mean energy conversions of the Lorenz (1955)'s energy cycle, following Peixoto and Oort (1992) where,

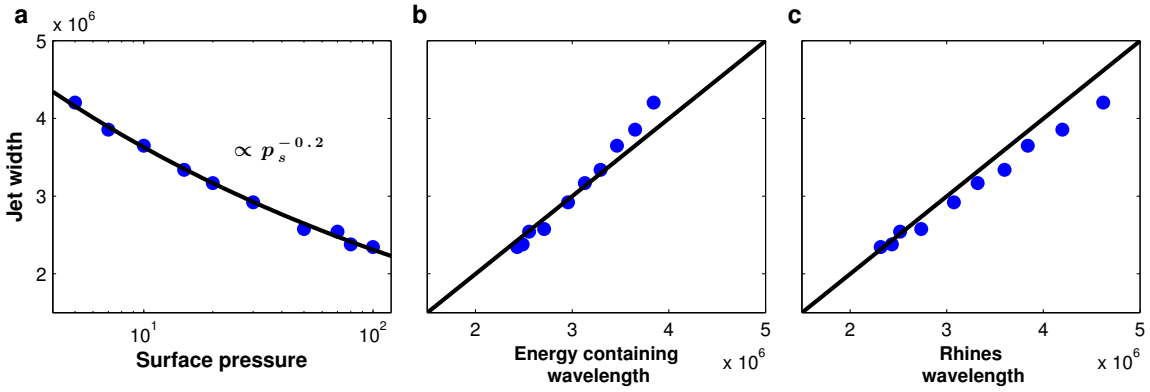

Figure 4.13: (a) The jet width (m, see text for definition) as a function of (a) surface pressure, (b) the energy containing wavelength (Eq. 4.16) and (c) the Rhines wavelength.

$$\begin{aligned} \text{MAPE} \rightarrow \text{EAPE} \quad = \quad & -C_p \Bigg\langle \frac{\Gamma \overline{v'T'}}{a} \frac{\partial \overline{T}}{\partial \varphi} \\ & + p^{-k} \overline{w'T'} \frac{\partial}{\partial p} \Gamma p^k \left(\overline{T} - [T] \right) \Bigg\rangle, \end{aligned} \tag{4.11}$$

is the conversion of mean available potential energy (MAPE) to eddy available potential energy (EAPE),

$$\text{EAPE} \rightarrow \text{EKE} = - \left\langle \overline{\frac{v'}{a} \frac{\partial \phi'}{\partial \varphi}} + \overline{\frac{u'}{a \cos \varphi} \frac{\partial \phi'}{\partial \lambda}} \right\rangle, \tag{4.12}$$

is the conversion of EAPE to EKE,

$$\begin{aligned} \text{EKE} \rightarrow \text{MKE} \quad = \quad & \Bigg\langle \frac{\overline{u'v'} \cos \varphi}{a} \frac{\partial \left(\overline{u} / \cos \varphi \right)}{\partial \varphi} + \overline{u'w'} \frac{\partial \overline{u}}{\partial p} \\ & + \frac{\overline{v'^2}}{a} \frac{\partial \overline{v}}{\partial \varphi} + \overline{v'w'} \frac{\partial \overline{v}}{\partial p} - \frac{\overline{v} \overline{u'^2} \tan \varphi}{a} \Bigg\rangle, \end{aligned} \tag{4.13}$$

is the conversion of EKE to mean kinetic energy (MKE), and

$$\text{MAPE} \rightarrow \text{MKE} = - \left\langle \overline{v} \frac{\partial \overline{\phi}}{a \partial \varphi} \right\rangle, \tag{4.14}$$

is the conversion of MAPE to MKE, where squared brackets denote a horizontal mean, angle brackets denote a global mean, $\Gamma = -\frac{k\theta}{pT} \left(\frac{\partial [\theta]}{\partial p} \right)^{-1}$, w is the vertical velocity, ϕ is the geopotential and λ is longitude.

As the atmospheric mass increases the entire eddy-mean flow energy cycle weakens (Fig. 4.12a). The conversions of energy out of the MAPE (red and orange triangles in Fig. 4.12a) reduce faster than the conversion of energy in and out of the EKE (blue and green triangles in Fig. 4.12a). As the extratropical circulation is driven by baroclinic instability (e.g., Charney, 1947; Eady,

1949; Phillips, 1954; Charney and Stern, 1962; Simmons and Hoskins, 1978), a key in understanding the weakening of the entire energy cycle resides in the conversion of MAPE to EAPE (Eq. 4.11). The dominant term in Eq. 4.11 that contributes mostly to the production of EAPE is, $\frac{\Gamma\overline{v'T'}}{a}\frac{\partial\overline{T}}{\partial\varphi}$. Separating the different components of this term shows that while Γ increases with atmospheric mass (blue dots in Fig. 4.12b), the mean meridional eddy temperature flux (red dots in Fig. 4.12b) as well as the meridional temperature gradient (black dots in Fig. 4.12b) decrease with atmospheric mass. Among these, the mean meridional eddy temperature flux seems to show a stronger and more similar reduction as the conversion of MAPE to EAPE (Eq. 4.11), than the meridional temperature gradient.

The reduction in the meridional temperature gradient is a direct consequence of increasing atmospheric mass, as discussed in Sec. 4.2.1.1, due to the reduction in both the net radiative cooling at high latitudes and convective warming at low latitudes. Assuming that the meridional eddy temperature fluxes are diffusive (e.g., Green, 1970; Held, 1978; Held and Larichev, 1996), a decrease in the meridional temperature gradient results in a weakening of the meridional eddy temperature fluxes, which further weakens the temperature gradient and the energy cycle.

Using hydrostatic balance and assuming small variation of density with latitude, the conversion between MAPE and MKE can be written as, $\text{MAPE} \rightarrow \text{MKE} \approx -R_d \left\langle \overline{v}\frac{\partial\overline{T}}{a\partial\varphi} \right\rangle$. This is similar to thermal wind balance, where a decrease in the meridional temperature gradient, is associated with a weakening of the vertical shear of the mean zonal wind. As the winds vanish at the surface, a reduction in the meridional temperature gradient is associated with a decrease in the MKE (i.e., the mean zonal winds, contours in Fig. 4.4a-d). In summary, the reduction of the mean meridional temperature gradient with atmospheric mass reduces the extraction of MAPE both to the eddy fields and mean flow. The strong baroclinicity of the upper troposphere was found to explain why a reduction in the meridional temperature gradient at these levels (as occurs in our simulations, Fig. 4.7a), results in a reduction in the eddy fields as well (Yuval and Kaspi, 2016).

4.2.2.2 The width of the extratropical circulation

The extratropical circulation not only shifts equatorward together with the contraction of the Hadley cell as the atmospheric mass increases, but also contracts, leading to the formation of multiple alternating extratropical circulations (Fig. 4.4). Concomitantly, the jet width decreases with atmospheric mass following $\propto p_s^{-0.2}$ (Fig. 4.13a). The jet's width is calculated as the meridional distance between two consecutive minima of the eddy-driven jets. This leads to multiple consecutive direct and indirect cells (colors in Fig. 4.4a-d), eddy-driven jets (contours in Fig. 4.4a-d) along with their corresponding momentum flux convergence (colors in Fig. 4.4e-h). Note that while the indirect cells in the extratropics (red colors in Fig. 4.4a-d) are correlated with eddy momentum flux convergence (red colors in Fig. 4.4e-h), and their associated eddy-driven jets (contours in Fig. 4.4a-d), the direct cells in the extratropics (blue colors in Fig. 4.4a-d) are correlated with eddy momentum flux divergence (blue colors in Fig. 4.4e-h),

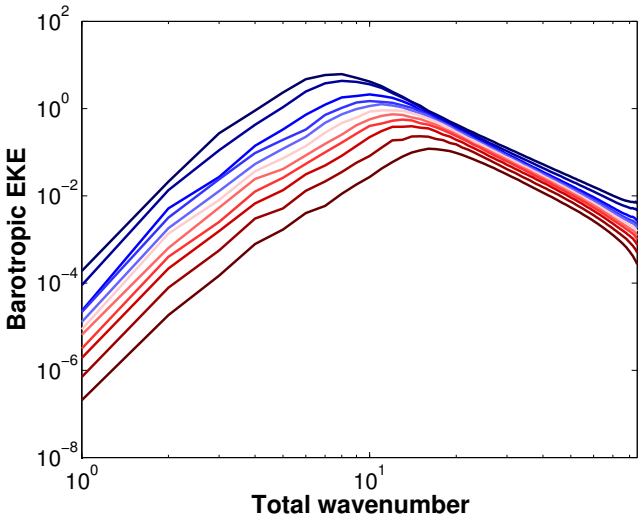

Figure 4.14: (a) The spectrum of the barotropic eddy kinetic energy (bEKE, m^2s^{-2}) as a function of total wavenumber for different atmospheric mass simulations. Red (blue) colors correspond to heavier (lighter) atmospheres.

and minimum zonal wind values. What causes these extratropical features to contract with atmospheric mass? To answer this we first parametrize their meridional scale.

The contraction of the prominent flows in the atmosphere is also seen in spectral space, where the distribution of the barotropic kinetic energy is shifted to smaller wavenumbers as the atmospheric mass increases (going from blue to red colors in Fig. 4.14). The barotropic EKE is calculated following Boer and Shepherd (1983) as,

$$\mathrm{bEKE}_n = \frac{1}{2}\sum_m \frac{n(n+1)}{a^2}\left|\chi_m^n\right|^2, \tag{4.15}$$

where n and m are the zonal and total wavenumbers, respectively, and χ is the horizontal barotropic streamfunction. Consistently, Kaspi and Showman (2015) showed that as the atmospheric mass increases the energy-containing wavenumber increases as well (cf. their Fig. 15b). As atmospheric jets hold most of the kinetic energy in the atmosphere their meridional scale is found to follow the energy-containing wavelength (Fig. 4.13b). The energy-containing wavelength is calculated as,

$$L_e = 2\pi\left(\frac{a^2}{n_e(n_e+1)}\right)^{1/2}, \tag{4.16}$$

where n_e is the energy-containing wavenumber calculated as the inverse centroid of Eq. 4.15,

$$n_e(n_e+1) = \frac{\sum_n \mathrm{bEKE}_n}{\sum_n \mathrm{bEKE}_n[n(n+1)]^{-1}}. \tag{4.17}$$

According to the Rhines-Salmon two-layer phenomenology (Rhines, 1977; Salmon, 1978), as energy cascades from the baroclinic mode (depth-dependent flow), which extracts potential

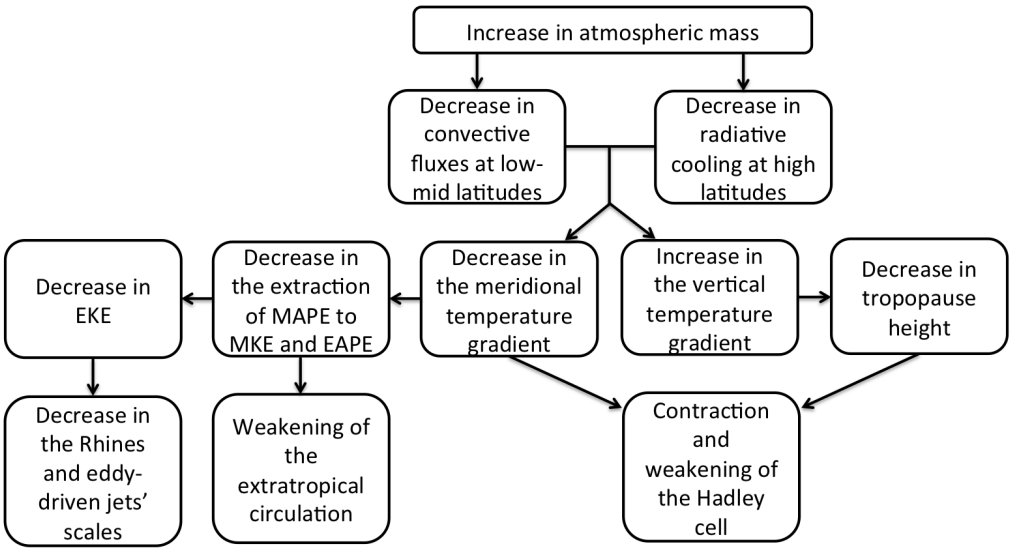

Figure 4.15: Flow chart summarizing the effects of atmospheric mass on both tropical and extratropical circulations.

energy from the mean flow, to the barotropic mode (depth-independent flow), it behaves as a two-dimensional fluid with an inverse energy and a forward enstrophy cascades. The inverse energy cascade is suppressed at the Rhines scale (Rhines, 1975), which separates two flow regimes dominated by Rossby waves and turbulent eddies. The inverse energy cascade, however, is not entirely suppressed, but keeps cascading in the zonal direction until reaching the zero zonal wavenumber, and zonal jets are formed. Thus, as substantial amount of MKE comes from barotropic eddies, the eddy-driven jets tend to have a more barotropic nature then the subtropical jets (Fig. 4.4a-d). This suggests that the Rhines scale should follow both the energy-containing and jet scales, as was shown to occur in 2D flow on a β-plane (e.g., Rhines, 1975; Vallis and Maltrud, 1993), two-layer models (e.g., Panetta, 1993; Held and Larichev, 1996; Lee, 2005), idealized GCMs (e.g., Jansen and Ferrari, 2012; Chai and Vallis, 2014; O'Gorman and Schneider, 2008c; Chemke and Kaspi, 2015a, 2016a) and reanalysis data (e.g., Chemke et al., 2016a; Chemke and Kaspi, 2016b).

The Rhines wavelength indeed follows the jet width through all atmospheric mass simulations (Fig. 4.13c). The Rhines wavelength is calculated as,

$$L_\beta = 2\pi \left(\frac{(\text{bEKE})^{1/2}}{\beta} \right)^{1/2},$$

where β is the meridional derivative of the Coriolis parameter. As the β parameter does not vary between the different simulations, the change in the Rhines wavelength is due to the reduction of the barotropic EKE with atmospheric mass (Fig. 4.14). As discussed in Sec. 4.2.2.1, this reduction is associated with the decrease in the meridional temperature gradient, which suppresses baroclinic instability processes that reduce the conversion of potential energy from the mean flow to kinetic energy.

4.2.3 Conclusions

In this study we explore the effects of atmospheric mass on the general circulation. Atmospheric mass varies greatly between planets, and is clearly crucial for the atmospheric dynamics and habitability, and therefore understanding its affect on planetary climate is essential. Here, the dynamical-thermodynamical role of atmospheric mass on the planet's atmospheric circulation is studied using an idealized 3D ocean slab GCM, where the surface pressure is systematically varied (which is equivalent of changing the entire atmospheric mass) between 0.5 bar and 100 bar.

Two main thermodynamic processes vary with atmospheric mass (Fig. 4.8). First, an increase in atmospheric mass reduces the convective fluxes, as suggested by Goldblatt et al. (2009), leading to a cooler upper troposphere at mid-low latitudes. Second, the increase in the atmospheric heat capacity reduces the net radiative cooling (leading to warming) of the lower troposphere at high latitudes (Chemke et al., 2016b). These processes reduce the meridional temperature gradient and increase the vertical temperature gradient, which reduces the tropopause height (Fig. 4.7).

The resulting changes in the temperature field directly affect the circulation in both the tropics and extratropics (Fig. 4.15). The Hadley circulation contracts as the atmospheric mass increases (Fig. 4.5a). As its latitudinal extent is found to roughly follow the scaling of Held and Hou (1980) (Fig. 4.5b), the reduction of the meridional temperature gradient and tropopause height explain its contraction with atmospheric mass (Fig. 4.6a). Similarly, the reduction in these parameters (Fig. 4.11) also explains the weakening of the Hadley cell strength with atmospheric mass as it is also found to follow the scaling of Held and Hou (1980) (Fig. 4.10).

In the extratropics, the circulation also weakens with atmospheric mass (Fig. 4.4). Studying the eddy-mean flow energy cycle shows that the reduction in the meridional temperature gradient reduces the extraction of mean available potential energy both to the eddies (e.g., by baroclinic instability processes through the reduction of the meridional eddy temperature fluxes), and to the mean kinetic energy (thermal wind balance) (Fig. 4.12). As the extratropical circulation is driven by the differential warming of low and high latitudes, its reduction weakens the circulation.

An increase in atmospheric mass also contracts the extratropical circulation (Fig. 4.4). The jets' width decreases with atmospheric mass, and is found to follow both the energy-containing and Rhines wavelengths (Fig. 4.13). Again, the reduction of the meridional temperature gradient, and its associated reduction in the contraction of available potential energy, reduces the EKE (Fig. 4.14) (e.g., Yuval and Kaspi, 2016), which decreases the Rhines wavelength and hence the jets' width as well.

The main goal of this study is to better understand the dynamical-thermodynamical role of atmospheric mass on the circulation. Thus, in order to keep the simulations as simple as possible, the simplified two-stream gray radiation scheme used in this study does not account for pressure broadening and Rayleigh scattering processes. As these processes were also found to modulate the temperature field with atmospheric mass (Goldblatt et al., 2009; Wolf and

Toon, 2014), for a full understanding of the habitability of planets with different atmospheric mass, it is important to examine the flow properties in a full GCM, which accounts all the radiative ingredients that vary with atmospheric mass. Moreover, as the variety of exoplanets have a wide range of planetary parameters that differ from Earth's, it is also important to explore the effects of atmospheric mass under different planetary parameters (e.g., different obliquity and rotation rate, non-terrestrial planets, etc.) (e.g., Kaspi and Showman, 2015; Kilic et al., 2017). Nonetheless, this study shows that high atmospheric mass planets may be more habitable due to both their higher surface temperature, and weaker meridional temperature gradient, which allows higher temperature at high latitudes, that may help to maintain liquid water on their surface. For example, the low meridional surface temperature gradient on Venus, in contrast to the high values on Mars, may be a result of the different atmospheric masses in these planets (e.g., Prinn and Fegley, 1987; Read et al., 2015). Nevertheless, the lower rotation rate and obliquity of Venus, may also contribute to the lower meridional temperature gradient on Venus.

Chapter 5

Summary and concluding remarks

The flow of the atmosphere spans a wide range of scales. Going from dissipation processes that occur over millimeters, to weather systems and zonal jets that cover thousands of kilometers, these phenomena have different effects on weather and climate. Thus, studying how the energy is distributed among these different scales/phenomena in the atmosphere is key for better understanding the turbulent flow of the atmosphere and its climatic effects. It is important to understand the energy cycle not only in Earth's present-day atmosphere, but also under different planetary parameters, which allows both to develop a deeper understanding of the energy cycle and its sensitivity to these parameters and of the atmospheric flow in different configurations (e.g., in giant planets, exoplanets, past and future climates).

For many questions in this thesis I used the idealized GCM (Sec. 2.1). Most studies to date investigated the energy cycle of geostrophic turbulence either using QG two-layer models (e.g., Larichev and Held, 1995) or continually stratified models (e.g., Smith and Vallis, 2001, 2002). These models do not take into an account the latitudinal changes in the energy cycle and its important macroturbulent scales, nor a realistic vertical structure of the flow. The idealized GCM thus enables studying in a realistic framework (enables a more complete description of the dynamic and thermodynamic structures of the atmosphere), the latitudinal behavior of geostrophic turbulence in the atmosphere. Different than comprehensive GCM, which account for the full complexity of the flow in the atmosphere, and thus contain a large number of variables that affect the dynamics (e.g., clouds, CO_2, land, seasonality, chemistry, etc.), the relative simplicity of the idealized GCM, which solves the primitive equations, enables isolation of the basic physics that contribute most to the dynamic and thermodynamic processes in the atmosphere. Therefore, the intermediate complexity of the GCM gave us a forward leap in complexity compared to previous work, but also allowed the flexibility to study these questions over a wide range of scales that were necessary to isolate the governing physics.

For the geostrophic turbulence questions I addressed in this thesis we used an idealized GCM at high rotation rates to allow a clear separation between the eddy-driven jet and the subtropical jet in the atmosphere. As the meridional jet spacing (latitudinal location) has an important effect on climate and weather systems, this separation enables us to scale the meridional spacing of the eddy-driven jets and study the macroturbulence behavior. We show that at high rotation rates eddy-driven jets tend to migrate poleward with time, due to the

poleward biased baroclinicity around the jet's core, which is found to be driven by the sphericity of the planet. These migrating jets enable studying the barotropic energy cycle as a function of latitude. Using both the above simulations and atmospheric and oceanic reanalysis data, we show the presence of the supercriticality latitude: a latitude where the Rhines scale is equal to the Rossby deformation radius, and the QG supercriticality approaches unity. Poleward of this latitude, the length scale of the energy-containing zonal wavenumber coincides with the width of the jet and the Rhines scale, and the eddy–eddy interactions play an important role in transferring energy both upscale and downscale. Equatorward of the supercriticality latitude, the eddy–mean flow interactions become dominant and the energy-containing zonal scale is found to be larger than the jets and Rhines scales. The agreement of the Rhines and jet's scales is found not to be related to inverse energy cascade arguments, as also in quasi-linear simulations the jet's scale follows the Rhines scale. The eddy-eddy interactions, however, do affect the number of eddy-driven jets in the atmosphere, by suppressing energy transfer through eddy-mean interactions. The barotropic energy cycle also shows interesting features in various climates. The barotropic energy cycle shifts poleward and shows a non-monotonic behavior as the climate becomes warmer. In future projected climates the eddy flow should be dominated by eddy-mean flow interactions, and have a more baroclinic nature.

Using idealized GCM simulations we show that atmospheric mass tends to increase surface temperature, mostly due to a decrease in net radiative cooling, which together with the reduction of convective fluxes reduce the meridional temperature gradient. These changes in surface temperature with atmospheric mass affect the habitability of both early Earth's atmosphere and heavy atmosphere exoplanets. The reduction in the meridional temperature gradient is found both to weaken the tropical circulation and contract it equatorward, and to weaken and narrow the extratropical circulation by limiting the extraction of mean potential energy.

List of publications resulting from this thesis:

- **Chemke, R.**, and Y. Kaspi, 2017. Atmospheric dynamics of massive atmospheres (in revision, *Astrophys. J.*).
- **Chemke, R.**, 2017. Atmospheric energy transfer response to global warming (in revision, *Quart. J. Roy. Meteor. Soc.*).
- **Chemke, R.**, Y. Kaspi, and I. Halevy, 2016. The thermodynamic effect of atmospheric mass on early Earth's temperature, *Geophys. Res. Lett.*, 43, 11,414–11,422. [link].
- Dagan, G., and **R. Chemke**, 2016. The effect of subtropical aerosol loading on equatorial precipitation, *Geophys. Res. Lett.*, 43, 11,048–11,056. [link].
- **Chemke, R.**, T. Dror, and Y. Kaspi, 2016. Barotropic kinetic energy and enstrophy transfers in the atmosphere, *Geophys. Res. Lett.*, 43, 7725-7734. [link].
- **Chemke, R.**, and Y. Kaspi, 2016. The latitudinal dependence of the oceanic barotropic eddy kinetic energy and macroturbulence energy transport, *Geophys. Res. Lett.*, 43, 2723-2731. [link].

- **Chemke, R.**, and Y. Kaspi, 2016. The effect of eddy-eddy interactions on jet formation and macroturbulent scales, *J. Atmos. Sci.*, 73 (5), 2049-2059. [link].
- **Chemke, R.**, and Y. Kaspi, 2015. The Latitudinal Dependence of Atmospheric Jet Scales and Macroturbulent Energy Cascades. *J. Atmos. Sci.*, 72 (10), 3891–3907. [link].
- **Chemke, R.**, and Y. Kaspi, 2015. Poleward migration of eddy-driven jets, *J. Adv. Model. Earth Syst.*, 07, 1457-1471. [link].

Chapter 6

Appendix

6.1 Residual barotropic kinetic energy transfers in the atmosphere

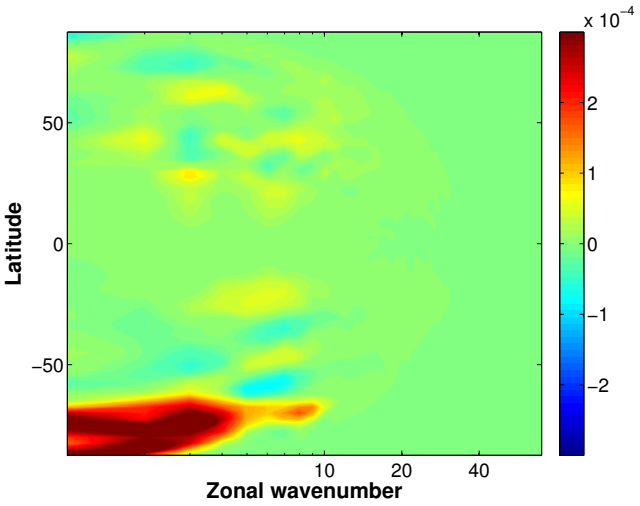

Figure 6.1: Conversion of barotropic eddy potential energy to barotropic eddy kinetic energy ($\mathrm{m^2 s^{-3}}$), $P = -\left\langle \mathrm{Re}[\mathbf{u_h}]_k'^{*} \cdot \left(\nabla_h[\phi]'\right)_{\mathbf{k}} \right\rangle$, as a function of latitude and zonal wavenumber.

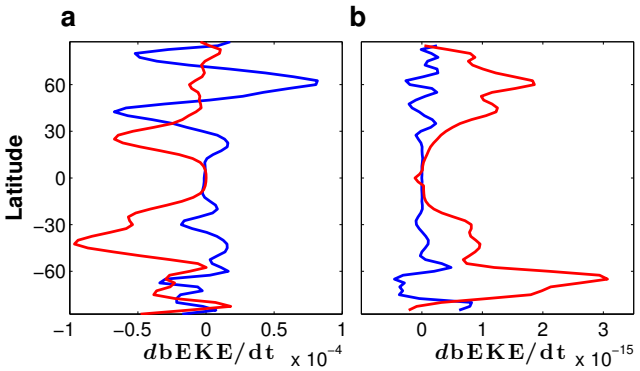

Figure 6.2: Components of (a) the barotropic EKE equation ($\mathrm{m^2 s^{-3}}$) and (b) the barotropic eddy potential enstrophy equation ($\mathrm{s^{-3}}$), summed over all zonal wavenumber, as a function of latitude. Blue and red lines correspond to transfers by barotropic eddy-eddy interactions and eddy-mean flow interactions, respectively.

6.2 Early Earth atmospheric mass simulations up to 10 bar

Extending the simulations to 10 times present atmospheric pressure shows the same trend observed up to 4 times present pressure; the temperature increases with atmospheric mass, mostly due to a reduction in the radiative cooling effect near the surface, and a reduction in the vertical eddy heat fluxes. With $p_s = 10 \times p_{s_e}$ the global average near-surface temperature increases by $\sim$ 47 K (compared to $\sim$ 7.5 K without the feedbacks). In addition, the non-monotonic behavior of the convective fluxes to increase with surface pressure up to $\sim$ 3.5 Pa and decrease beyond is clearly seen.

The poleward movement of the ice-line latitude with surface pressure continues until the entire planet is ice-free. In simulations with solar luminosity 80% and 75% its present value the ice-line latitude reaches the poles, through all CO_2 simulations, at 4 and $7.5 \times p_{s_e}$, respectively.

Varying the atmospheric mass in the moist simulations is equivalent to varying the relaxation time scale in the dry simulations, as both tend to reduce the radiative cooling in the lower layers of the atmosphere. Thus, similar to changes in surface pressure, increasing the relaxation time scale, increases the mean near-surface temperature and reduces the meridional temperature gradient.

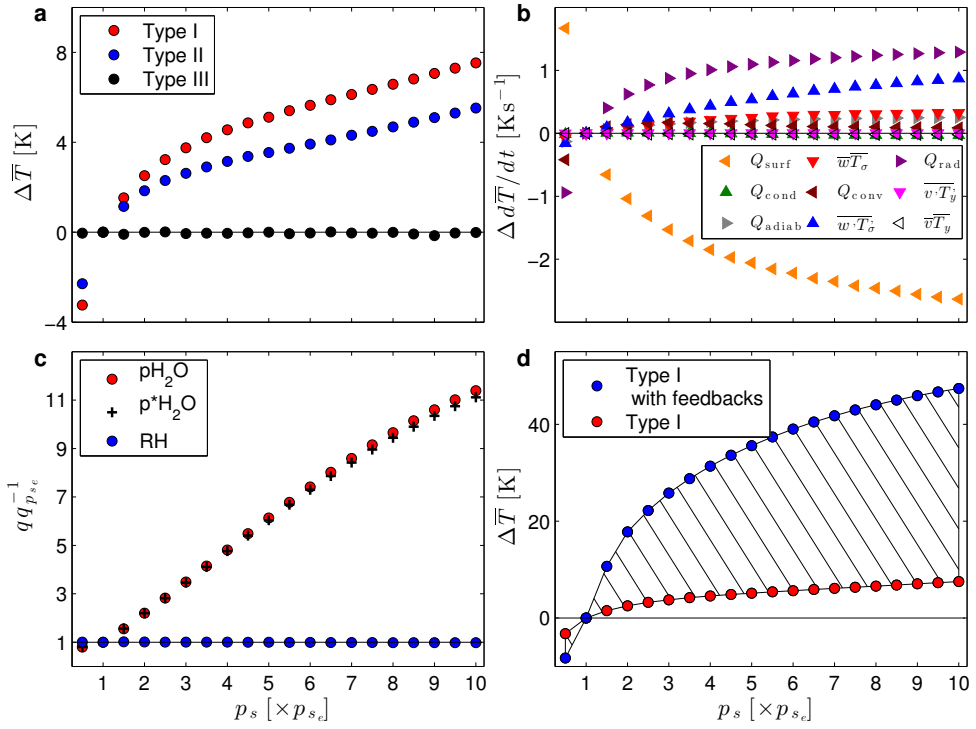

Figure 6.3: The dependence of zonal, meridional and time mean near-surface temperature, components of its tendency equation (Eq. 2.2) and moisture parameters on surface pressure relative to the $1\times p_{s_e}$ simulation with solar luminosity 80% its present value. (a) Mean near-surface temperature from simulations with the effect of heat capacity, and with (type I, red) and without (type II, blue) moist convection, and dry simulations without both moist convection and the effect of heat capacity (type III, black). (b) Mean components of the mean near-surface temperature tendency equation in type I simulation at a statistically steady state (i.e., all components add to approximately zero); Radiation (purple), vertical advection of eddy temperature fluxes (blue), adiabatic term (gray), vertical advection of mean temperature fluxes (red), meridional advection of mean temperature fluxes (black), meridional advection of eddy temperature fluxes (magenta), surface fluxes (orange), condensation (green) and convection (maroon). (c) The ratio of the tropospheric mean water vapor partial pressure (red), saturated water vapor partial pressure (black crosses), and relative humidity (blue). Shown are simulations with optical thickness calculated using water vapor concentrations and 500 Pa of CO_2 at the surface (type IA). (d) Mean near-surface temperature from simulations with optical thickness calculated using water vapor concentrations and 500 Pa of CO_2 at the surface (blue, type IA), and using parameterized optical thickness (type I, red). The hatched area shows the effect of the water vapor and ice-albedo feedbacks on the mean near-surface temperature.

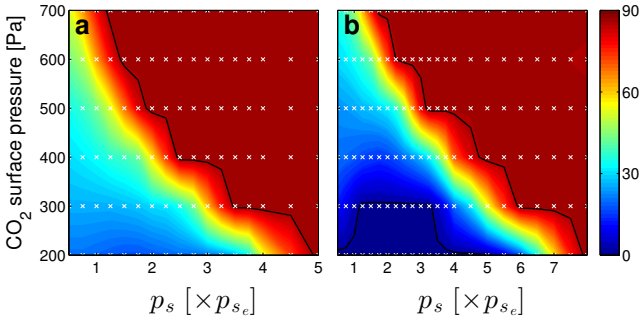

Figure 6.4: Ice-line latitude as a function of pCO_2 and total surface pressure. Shown are simulations with the water vapor and ice-albedo feedbacks, and with a solar luminosity of (a) 80%; (b) 75% its present value. Note the different abscissa values in panels˜a and b. The black contours represent the 90° and 0° ice-line latitudes. White crosses show simulation data points.

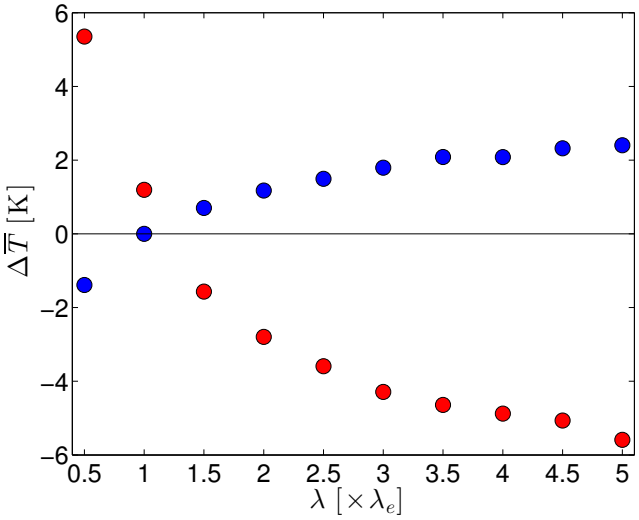

Figure 6.5: Mean near-surface temperature (blue) and equator-to-pole surface temperature difference (red) relative to the reference relaxation time scale, $1\lambda_e$ (for the interior $\lambda_i = 150$ days and for near the surface $\lambda_s = 15$ days), as a function of the relaxation time scale, λ, from dry simulations (type III).

Bibliography

Abernathey, R. and Wortham, C. (2015). Phase speed cross spectra of eddy heat fluxes in the eastern Pacific. *J. Phys. Oceanogr.*, 45:1285–1301.

Adams, E. R., Seager, S., and Elkins-Tanton, L. (2008). Ocean Planet or Thick Atmosphere: On the Mass-Radius Relationship for Solid Exoplanets with Massive Atmospheres. *Astrophys. J.*, 673:1160–1164.

Adcroft, A., Campin, J.-M., Hill, C., and Marshall, J. (2004). Implementation of an atmosphere ocean general circulation model on the expanded spherical cube. *Mon. Weath. Rev.*, 132:2845.

Adcroft, A., Hill, C., and Marshall, J. (1997). Representation of topography by shaved cells in a height coordinate ocean model. *Mon. Weath. Rev.*, 125:2293.

Ait-Chaalal, F. and Schneider, T. (2015). Why eddy momentum fluxes are concentrated in the upper troposphere. *J. Atmos. Sci.*, 72:1585–1604.

Arbic, B. K. and Flierl, G. R. (2004). Baroclinically unstable geostrophic turbulence in the limits of strong and weak bottom ekman friction: Application to midocean eddies. *J. Phys. Oceanogr.*, 34:2257–2273.

Arbic, B. K., Flierl, G. R., and Scott, R. B. (2007). Cascade inequalities for forced-dissipated geostrophic turbulence. *J. Phys. Oceanogr.*, 37(6):1470–1487.

Arbic, B. K. and Scott, R. B. (2008). On quadratic bottom drag, geostrophic turbulence, and oceanic mesoscale eddies. *J. Phys. Oceanogr.*, 38:84.

Baer, F. (1972). An alternate scale representation of atmospheric energy spectra. *J. Atmos. Sci.*, 29(4):649–664.

Bakas, N. A. and Ioannou, P. J. (2014). A theory for the emergence of coherent structures in beta-plane turbulence. *J. Fluid Mech.*, 750:312–341.

Balasubramanian, G. and Garner, S. T. (1997). The role of momentum fluxes in shaping the life cycle of a baroclinic wave. *J. Atmos. Sci.*, 54(4):510–533.

Barnes, E. A. and Thompson, D. W. (2014). Comparing the roles of barotropic versus baroclinic feedbacks in the atmosphere's response to mechanical forcing. *J. Atmos. Sci.*, 71(1):177–194.

Barry, L., Craig, G. C., and Thuburn, J. (2002). Poleward heat transport by the atmospheric heat engine. *Nature*, 415(6873):774–777.

Beckmann, A., Böning, C. W., Köberle, C., and Willebrand, J. (1994). Effects of increased horizontal resolution in a simulation of the north atlantic ocean. *J. Phys. Oceanogr.*, 24:326–344.

Bengtsson, L. and Hodges, K. I. (2006). Storm tracks and climate change. *J. Climate*, 19:3518–3543.

Berloff, P. and Kamenkovich, I. (2013a). On spectral analysis of mesoscale eddies. part i: Linear analysis. *J. Phys. Oceanogr.*, 43:2505–2527.

Berloff, P. and Kamenkovich, I. (2013b). On spectral analysis of mesoscale eddies. part ii: Nonlinear analysis. *J. Phys. Oceanogr.*, 43:2528–2544.

Betts, A. K. (1986). A new convective adjustment scheme. part i: Observational and theoretical basis. *Q. J. R. Meteorol. Soc.*, 112:677–691.

Betts, A. K. and Miller, M. J. (1986). A new convective adjustment scheme. part ii: Single column tests using gate wave, bomex, atex and arctic air-mass data sets. *Q. J. R. Meteorol. Soc.*, 112:693–709.

Blackmon, M. L. (1976). A climatological spectral study of the 500 mb geopotential height of the northern hemisphere. *J. Atmos. Sci.*, 33(8):1607–1623.

Blackmon, M. L., Wallace, J. M., Lau, N., and Mullen, S. L. (1977). An observational study of the northern hemisphere wintertime circulation. *J. Atmos. Sci.*, 34(7):1040–1053.

Boer, G. J. (1975). Zonal and eddy forms of the available potential energy equations in pressure coordinates. *Tellus*, 27(5):433–442.

Boer, G. J. and Shepherd, T. G. (1983). Large-scale two-dimensional turbulence in the atmosphere. *J. Atmos. Sci.*, 40(1):164–184.

Böning, C. W., Bryan, F. O., Holland, W. R., and Döscher, R. (1996). Deep-water formation and meridional overturning in a high-resolution model of the north atlantic. *Journal of Physical Oceanography*, 26:1142–1164.

Bühler, O., Callies, J., and Ferrari, R. (2014). Wave-vortex decomposition of one-dimensional ship-track data. *J. Fluid Mech.*, 756:1007–1026.

Burgess, B. H., Erler, A. R., and Shepherd, T. G. (2013). The troposphere-to-stratosphere transition in kinetic energy spectra and nonlinear spectral fluxes as seen in ECMWF analyses. *J. Atmos. Sci.*, 70:669–687.

Cai, M. and Shin, C. S. (2014). Total flow perspective of atmospheric mass and angular momentum circulations: boreal winter mean state. *J. Atmos. Sci.*, 71(6):2244–2263.

Chai, J. and Vallis, G. K. (2014). The role of criticality on the horizontal and vertical scales of extratropical eddies in a dry GCM. *J. Atmos. Sci.*, 71(7):2300–2318.

Chan, C. J., Plumb, R. A., and Cerovecki, I. (2007). Annular modes in a multiple migrating zonal jet regime. *J. Atmos. Sci.*, 64(11):4053–4068.

Charnay, B., Forget, F., Wordsworth, R., Leconte, J., Millour, E., Cordon, F., and Spiga, A. (2013). Exploring the faint young sun problem and the possible climates of the archean earth with a 3-d GCM. *J. Geophys. Res.*, 118(18):10–414.

Charney, J. G. (1947). The dynamics of long waves in a baroclinic westerly current. *J. of Meteorology*, 4(5):136–162.

Charney, J. G. (1971). Geostrophic turbulence. *J. Atmos. Sci.*, 28(6):1087–1095.

Charney, J. G. and Stern, M. E. (1962). On the stability of internal baroclinic jets in a rotating atmosphere. *J. Atmos. Sci.*, 19(2):159–172.

Chelton, D. B., Deszoeke, R. A., Schlax, M. G., Naggar, E., and Siwertz, N. (1998). Geographical variability of the first baroclinic rossby radius of deformation. *J. Phys. Oceanogr.*, 28(3):433–460.

Chelton, D. B., Schlax, M. G., Samelson, R. M., and de Szoeke, R. A. (2007). Global observations of large oceanic eddies. *Geophys. Res. Lett.*, 34:L15606.

Chemke, R., Dror, T., and Kaspi, Y. (2016a). Barotropic kinetic energy and enstrophy transfers in the atmosphere. *Geophys. Res. Lett.*, 43:7725–7734.

Chemke, R. and Kaspi, Y. (2015a). The latitudinal dependence of atmospheric jet scales and macroturbulent energy cascades. *J. Atmos. Sci.*, 72(10):3891–3907.

Chemke, R. and Kaspi, Y. (2015b). Poleward migration of eddy driven jets. *J. Adv. Mod. Earth Syst.*, 7:1457–1471.

Chemke, R. and Kaspi, Y. (2016a). The effect of eddy-eddy interactions on jet formation and macroturbulent scales. *J. Atmos. Sci.*, 73(5):2049–2059.

Chemke, R. and Kaspi, Y. (2016b). The latitudinal dependence of the oceanic barotropic eddy kinetic energy and macroturbulence energy transport. *Geophys. Res. Lett.*, 43:2723–2731.

Chemke, R., Kaspi, Y., and Halevy, I. (2016b). The thermodynamic effect of atmospheric mass on early Earth's temperature. *Geophys. Res. Lett.*, 43:11.

Chen, G. and Held, I. M. (2007). Phase speed spectra and the recent poleward shift of southern hemisphere surface westerlies. *Geophys. Res. Lett.*, 34:L21805.

Chen, G., Held, I. M., and Robinson, W. A. (2007). Sensitivity of the latitude of the surface westerlies to surface friction. *J. Atmos. Sci.*, 64:2899–2915.

Cho, J. and Polvani, L. M. (1996). The formation of jets and vortices from freely-evolving shallow water turbulence on the surface of a sphere. *Phys. of Fluids*, 8:1531–1552.

Choi, D. S. and Showman, A. P. (2011). Power spectral analysis of Jupiter's clouds and kinetic energy from Cassini. *Icarus*, 216(2):597–609.

Constantinou, N. C., Farrell, B. F., and Ioannou, P. J. (2014). Emergence and equilibration of jets in beta-plane turbulence: applications of stochastic structural stability theory. *J. Atmos. Sci.*, 71(5):1818–1842.

Coronel, B., Ricard, D., RiviÃšre, G., and Arbogast, P. (2015). Role of moist processes in the tracks of idealized midlatitude surface cyclones. *J. Atmos. Sci.*, 72(8):2979–2996.

Danilov, S. and Gurarie, D. (2002). Rhines scale and spectra of the beta plane turbulence with bottom drag. *Phys. Rev. E*, 65(6):067301.

Danilov, S. D. and Gurarie, D. (2000). Quasi-two-dimensional turbulence. *Uspekhi Fizicheskikh Nauk*, 170(9):921–968.

Dickey, J. O., Marcus, S. L., and Hide, R. (1992). Global propagation of interannual fluctuations in atmospheric angular momentum. *Nature*, 357(6378):484–488.

Eady, E. T. (1949). Long waves and cyclone waves. *Tellus*, 1(3):33–52.

Eden, C. (2007). Eddy length scales in the north atlantic ocean. *J. Geophys. Res.*, 112.

Edmon, J. H. J., Hoskins, B. J., and McIntyre, M. E. (1980). Eliassen-palm cross sections for the troposphere. *J. Atmos. Sci.*, 37(12):2600–2612.

Elkins-Tanton, L. T. and Seager, S. (2008). Ranges of Atmospheric Mass and Composition of Super-Earth Exoplanets. *Astrophys. J.*, 685:1237–1246.

Farrell, B. F. and Ioannou, P. J. (2007). Structure and spacing of jets in barotropic turbulence. *J. Atmos. Sci.*, 64(10):3652–3665.

Feldstein, S. B. (1998). An observational study of the intraseasonal poleward propagation of zonal mean flow anomalies. *J. Atmos. Sci.*, 55(15):2516–2529.

Ferrari, R. and Wunsch, C. (2009). Ocean circulation kinetic energy: Reservoirs, sources, and sinks. *Ann. Rev. Fluid Mech.*, 41:253–282.

Fjortoft, R. (1953). On the changes in the spectral distribution of kinetic energy for twodimensional, nondivergent flow. *Tellus*, 5(3):225–230.

Forget, F. and Pierrehumbert, R. T. (1997). Warming Early Mars with Carbon Dioxide Clouds That Scatter Infrared Radiation. *Science*, 278:1273.

Frierson, D. M. W. (2005). *Studies of the general circulation with a simplified moist general circulation model*. PhD thesis, Princeton University, 218 pp., New Jersey, USA.

Frierson, D. M. W. (2006). Robust increases in midlatitude static stability in simulations of global warming. *Geophys. Res. Lett.*, 33:L24816.

Frierson, D. M. W. (2008). Midlatitude static stability in simple and comprehensive general circulation models. *J. Atmos. Sci.*, 65:1049.

Frierson, D. M. W., Held, I. M., and Zurita-Gotor, P. (2006). A gray-radiation aquaplanet moist GCM. part I: Static stability and eddy scale. *J. Atmos. Sci.*, 63(10):2548–2566.

Frierson, D. M. W., Held, I. M., and Zurita-Gotor, P. (2007). A gray-radiation aquaplanet moist GCM. part II: Energy transports in altered climates. *jas*, 64:1680.

Fu, L.-L. and Flierl, G. R. (1980). Nonlinear energy and enstrophy transfers in a realistically stratified ocean. *Dyn. Atmos. Oceans*, 4(4):219–246.

Gill, A. E. (1982). *Atmosphere-ocean dynamics*. pp. 662. Academic Press., San Diego, California, USA.

Goldblatt, C., Claire, M. W., Lenton, T. M., Matthews, A. J., Watson, A. J., and Zahnle, K. J. (2009). Nitrogen-enhanced greenhouse warming on early earth. *Nature Geoscience*, 2(12):891–896.

Goody, R. M. and Yung, Y. L. (1995). *Atmospheric radiation: Theoretical basis*. pp. 519. Oxford University Press, New York.

Green, J. S. A. (1970). Transfer properties of the large-scale eddies and the general circulation of the atmosphere. *Q. J. R. Meteorol. Soc.*, 96(408):157–185.

Grianik, N., Held, I. M., Smith, K. S., and Vallis, G. K. (2004). The effects of quadratic drag on the inverse cascade of two-dimensional turbulence. *Phys. of Fluids*, 16(1):73–78.

Griffies, S. M., Winton, M., Donner, L. J., Horowitz, L. W., Downes, S. M., Farneti, R., Gnanadesikan, A., Hurlin, W. J., Lee, H.-C., Liang, Z., Palter, J. B., Samuels, B. L., Wittenberg, A. T., Wyman, B. L., Yin, J., and Zadeh, N. (2011). The GFDL CM3 Coupled Climate Model: Characteristics of the Ocean and Sea Ice Simulations. *J. Climate*, 24:3520–3544.

Haidvogel, D. B. and Held, I. M. (1980). Homogeneous quasi-geostrophic turbulence driven by a uniform temperature gradient. *J. Atmos. Sci.*, 37(12):2644–1660.

Hall, N. M. J., Hoskins, B. J., Valdes, P. J., and Senior, C. A. (1994). Storm tracks in a high-resolution GCM with doubled carbon dioxide. *Q. J. R. Meteorol. Soc.*, 120:1209–1230.

Hamilton, K., Takahashi, Y. O., and Ohfuchi, W. (2008). Mesoscale spectrum of atmospheric motions investigated in a very fine resolution global general circulation model. *J. Geophys. Res.*, 113(D12):D18110.

Hartmann, D. L. (1994). *Global Physical Climatology*. Academic Press, San Diego, California, USA.

Held, I. M. (1975). Momentum transport by quasi-geostrophic eddies. *J. Atmos. Sci.*, 32:1494–1496.

Held, I. M. (1978). The Vertical Scale of an Unstable Baroclinic Wave and Its Importance for Eddy Heat Flux Parameterizations. *J. Atmos. Sci.*, 35:572–576.

Held, I. M. (1982). On the height of the tropopause and the static stability of the troposphere. *J. Atmos. Sci.*, 39(2):412–417.

Held, I. M. (2000). The general circulation of the atmosphere. *Program in Geophysical Fluid Dynamics, Woods Hole, MA, Woods Hole Oceanographic Institute*. [Available online at http://www.whoi.edu].

Held, I. M. and Hoskins, B. J. (1985). Large-scale eddies and the general circulation of the troposphere. *Adv. Geophys.*, 28:3–31.

Held, I. M. and Hou, A. Y. (1980). Nonlinear axially symmetric circulations in a nearly inviscid atmosphere. *J. Atmos. Sci.*, 37:515–533.

Held, I. M. and Larichev, V. D. (1996). A scaling theory for horizontally homogeneous, baroclinically unstable flow on a beta plane. *J. Atmos. Sci.*, 53(7):946–952.

Held, I. M. and Soden, B. J. (2006). Robust responses of the hydrological cycle to global warming. *J. Climate*, 19:5686–5699.

Held, I. M. and Suarez, M. J. (1994). A proposal for the intercomparison of the dynamical cores of atmospheric general circulation models. *Bull. Am. Meteor. Soc.*, 75:1825–1830.

Holloway, G. and Hendershott, M. C. (1977). Stochastic closure for nonlinear rossby waves. *J. Fluid Mech.*, 82(4):747–765.

Hoskins, B. J., James, I. N., and White, G. H. (1983). The shape, propagation and mean-flow interaction of large-scale weather systems. *J. Atmos. Sci.*, 40(7):1595–1612.

Hoskins, B. J., McIntyre, M. E., and Robertson, A. W. (1985). On the use and significance of isentropic potential vorticity maps. *Q. J. R. Meteorol. Soc.*, 111:877–946.

Hoskins, B. J. and Valdes, P. J. (1990). On the existence of storm-tracks. *J. Atmos. Sci.*, 47:1854–1864.

Huang, H. P., Galperin, B., and Sukoriansky, S. (2001). Anisotropic spectra in two-dimensional turbulence on the surface of a rotating sphere. *Phys. of Fluids*, 13:225–240.

Huang, H. P. and Robinson, W. A. (1998). Two-dimentional turbulence and persistent jets in a global barotropic model. *J. Atmos. Sci.*, 55(4):611–632.

Hunt, B. G. (1979). The influence of the earth's rotation rate on the general circulation of the atmosphere. *J. Atmos. Sci.*, 36(7):1392–1408.

Ioannou, P. and Lindzen, R. S. (1986). Baroclinic instability in the presence of barotropic jets. *J. Atmos. Sci.*, 43(2):2999–3014.

IPCC (2013). Summary of policymakers. *Climate Change 2013: The Physical Basis.* T. F. Stocker et al., Eds., Cambridge University Press, 1-29.

James, I. N. and Dodd, J. P. (1996). A mechanism for the low frequency variability of the mid latitude troposphere. *Q. J. R. Meteorol. Soc.*, 122(533):1197–1210.

James, I. N. and Gray, L. J. (1986). Concerning the effect of surface drag on the circulation of a baroclinic planetary atmosphere. *Q. J. R. Meteorol. Soc.*, 112(474):1231–1250.

Jansen, M. and Ferrari, R. (2012). Macroturbulent equilibration in a thermally forced primitive equation system. *J. Atmos. Sci.*, 69(2):695–713.

Jansen, M. and Ferrari, R. (2013). Equilibration of an atmosphere by adiabatic eddy fluxes. *J. Atmos. Sci.*, 70(9):2948–2962.

Jansen, M. and Ferrari, R. (2015). Diagnosing the vertical structure of the eddy diffusivity in real and idealized atmospheres. *Q. J. R. Meteorol. Soc.*, 141(687):631–641.

Jansen, M. F. and Held, I. M. (2014). Parameterizing subgrid-scale eddy effects using energetically consistent backscatter. *Ocean Modeling*, 80:36–48.

Johnson, B. and Goldblatt, C. (2015). The nitrogen budget of earth. *Earth-Science Reviews*, 148:150–173.

Juckes, M. N. (2000). The static stability of the midlatitude troposphere: The relevance of moisture. *J. Atmos. Sci.*, 57:3050–3057.

Kaltenegger, L., Segura, A., and Mohanty, S. (2011). Model spectra of the first potentially habitable Super-Earth - Gl581d. *Astrophys. J.*, 733:35.

Kanamitsu, M., Ebisuzaki, W., Woollen, J., Yang, S.-K., Hnilo, J. J., Fiorino, M., and Potter, G. L. (2002). Ncep-doe amip-ii reanalysis (r-2). *Bull. Am. Meteor. Soc.*, 83:1631–1643.

Kaspi, Y. (2013). Inferring the depth of the zonal jets on Jupiter and Saturn from odd gravity harmonics. *Geophys. Res. Lett.*, 40:676–680.

Kaspi, Y. and Flierl, G. R. (2007). Formation of jets by baroclinic instability on gas planet atmospheres. *J. Atmos. Sci.*, 64(9):3177–3194.

Kaspi, Y. and Schneider, T. (2011). Downstream self-destruction of storm tracks. *J. Atmos. Sci.*, 68:2459–2464.

Kaspi, Y. and Schneider, T. (2013). The role of stationary eddies in shaping midlatitude storm tracks. *J. Atmos. Sci.*, 70:2596–2613.

Kaspi, Y. and Showman, A. P. (2015). Three dimensional atmospheric dynamics of terrestial exoplanets over a wide range of orbital and atmospheric parameters. *Astrophys. J.*, 804:60.

Kasting, J. F. (1993). Earth early atmosphere. *Science*, 259(5097):920–926.

Kasting, J. F. (2010). Early earth: faint young sun redux. *Nature*, 464(7289):687–689.

Kasting, J. F. and Catling, D. (2003). Evolution of a habitable planet. *Ann. Rev. Astron. Astrophy.*, 41:429.

Kavanagh, L. and Goldblatt, C. (2015). Using raindrops to constrain past atmospheric density. *Earth Planet. Sci. Lett.*, 413:51–58.

Kidston, J., Dean, S. M., Renwick, J. A., and Vallis, G. K. (2010). A robust increase in the eddy length scale in the simulation of future climates. *Geophys. Res. Lett.*, 37:L03806.

Kidston, J. and Vallis, G. K. (2010). Relationship between eddy-driven jet latitude and width. *Geophys. Res. Lett.*, 37(21).

Kidston, J. and Vallis, G. K. (2012). The relationship between the speed and the latitude of an eddy-driven jet in a stirred barotropic model. *J. Atmos. Sci.*, 69:3251–3263.

Kidston, J., Vallis, G. K., Dean, S. M., and Renwick, J. A. (2011). Can the increase in the eddy length scale under global warming cause the poleward shift of the jet streams? *J. Climate*, 24(14):3764–3780.

Kiehl, J. T. and Trenberth, K. E. (1997). Earth's annual global mean energy budget. *Bull. Am. Meteor. Soc.*, 78(2):197–208.

Kienert, H., Feulner, G., and Petoukhov, V. (2012). Faint young sun problem more severe due to ice-albedo feedback and higher rotation rate of the early earth. *Geophys. Res. Lett.*, 39(23).

Kilic, C., Raible, C. C., Stocker, T. F., and Kirk, E. (2017). Impact of variations of gravitational acceleration on the general circulation of the planetary atmosphere. *Planet. Space Sci.*, 135:1–16.

Klocker, A. and Abernathey, R. (2014). Global patterns of mesoscale eddy properties and diffusivities. *J. Phys. Oceanogr.*, 44(3):1030–1046.

Kodama, C. and Iwasaki, T. (2009). Influence of the sst rise on baroclinic instability wave activity under an aquaplanet condition. *J. Atmos. Sci.*, 66:2272.

Koshyk, J. N. and Hamilton, K. (2001). The horizontal kinetic energy spectrum and spectral budget simulated by a high-resolution troposphere-stratosphere-mesosphere GCM. *J. Atmos. Sci.*, 58(4):329–348.

Kraichnan, R. H. (1967). Inertial ranges in two-dimensional turbulence. *Phys. of Fluids*, 10:1417–1423.

Kuo, H. L. (1949). Dynamic instability of two-dimensional nondivergent flow in a barotropic atmosphere. *J. Meteor.*, 6(2):105–122.

Kushner, P. J., Held, I., and Delworth, T. (2001). Southern hemisphere atmospheric circulation response to global warming. *J. Climate*, 14:2238–2249.

Lambert, S. J. (1984). A global available potential energy-kinetic energy budget in terms of the two-dimensional wavenumber for the fgge year. *Atmosphere-Ocean*, 22(3):265–282.

Larichev, V. D. and Held, I. M. (1995). Eddy amplitudes and fluxes in a homogeneous model of fully developed baroclinic instability. *J. Phys. Oceanogr.*, 25(10):2285–2297.

Lee, S. (2005). Baroclinic multiple zonal jets on the sphere. *J. Atmos. Sci.*, 62(7):2482–2498.

Lee, S. and Kim, H. (2003). The dynamical relationship between subtropical and eddy-driven jets. *J. Atmos. Sci.*, 60:1490–1503.

Lee, S., Son, S. W., Grise, K., and Feldstein, S. B. (2007). A mechanism for the poleward propagation of zonal mean flow anomalies. *J. Atmos. Sci.*, 64(3):849–868.

Lindborg, E. (1999). Can the atmospheric kinetic energy spectrum be explained by two-dimensional turbulence? *J. Fluid Mech.*, 388:259–288.

Lindzen, R. S. (1988). Instability of plane parallel shear flow (toward a mechanistic picture of how it works). *Pure Appl. Geophys.*, 126:103–121.

Lindzen, R. S. and Farrell, B. (1980). A simple approximate result for the maximum growth rate of baroclinic instabilities. *J. Atmos. Sci.*, 37(7):1648–1654.

Liu, J. and Schneider, T. (2014). Scaling of off-equatorial jets in giant planet atmospheres. *J. Atmos. Sci.*, 72(1):389–408.

Lorenz, D. J. (2014a). Understanding mid-latitude jet variability and change using rossby wave chromatography: Poleward shifted jets in response to external forcing. *J. Atmos. Sci.*, 71:2370–2389.

Lorenz, D. J. (2014b). Understanding midlatitude jet variability and change using rossby wave chromatography: Wave-mean flow interaction. *J. Atmos. Sci.*, 71(10):3684–3705.

Lorenz, D. J. and DeWeaver, E. T. (2007). Tropopause height and zonal wind response to global warming in the IPCC scenario integrations. *J. Geophys. Res.*, 112(D11):D10119.

Lorenz, D. J. and Hartmann, D. L. (2001). Eddy-zonal flow feedback in the southern hemisphere. *J. Atmos. Sci.*, 58(21):3312–3327.

Lorenz, E. N. (1955). Available potential energy and the maintenance of the general circulation. *Tellus*, 7(2):157–167.

Lu, J., Chen, G., and Frierson, D. M. W. (2008). Response of the zonal mean atmospheric circulation to El Niño versus global warming. *J. Climate*, 21:5835.

Marshall, J., Adcroft, A., Hill, C., Perelman, L., and Heisey, C. (1997). Hydrostatic, quasi-hydrostatic and nonhydrostatic ocean modeling. *J. Geophys. Res.*, 102, C3:5,753–5,766. mars-eta:97b.

Marston, J. B. (2012). Planetary atmospheres as non-equilibrium condensed matter. *Ann. Rev. Condens. Matter Phys.*, 3:285–310.

Marty, B., Zimmermann, L., Pujol, M., Burgess, R., and Philippot, P. (2013). Nitrogen isotopic composition and density of the archean atmosphere. *Science*, 342:101–104.

Masich, J., Chereskin, T. K., and Mazloff, M. R. (2015). Topographic form stress in the southern ocean state estimate. *J. Geophys. Res.*, 120:7919–7933.

Meehl, G. A., Stocker, T. F., Collins, W. D., Friedlingstein, P., Gaye, A. T., Gregory, J. M., Kitoh, A., Knutti, R., Murphy, J. M., Noda, A., Raper, S. C. B., Watterson, I. G., Weaver, A. J., and Zhao, Z.-C. (2007). Global climate projections. In Solomon, S., Qin, D., Manning, M., Chen, Z., Marquis, M., Averyt, K., Tignor, M., and Miller, H., editors, *Climate Change 2007: The Physical Science Basis. Contribution of Working Group I to the Fourth Assessment Report of the Intergovernmental Panel on Climate Change*, pages 747–845. Cambridge Univ. Press, Cambridge, UK, and New York, NY, USA.

Menemenlis, D., Campin, J., Heimbach, P., Hill, C., Lee, T., Nguyen, A., Schodlok, M., and Zhang, H. (2008). Ecco2: High resolution global ocean and sea ice data synthesis. *Mercator Ocean Quarterly Newsletter*, 31:13–21.

Menemenlis, D., Fukumori, I., and Lee, T. (2005). Using green's functions to calibrate an ocean general circulation model. *Mon. Weath. Rev.*, 133:1224.

Merlis, T. M. and Schneider, T. (2009). Scales of linear baroclinic instability and macroturbulence in dry atmospheres. *J. Atmos. Sci.*, 66(6):1821–1833.

Merlis, T. M. and Schneider, T. (2010). Atmospheric dynamics of earth-like tidally locked aquaplanets. *J. Adv. Mod. Earth Syst.*, 2(4).

Mitchell, J. L. and Vallis, G. K. (2010). The transition to superrotation in terrestrial atmospheres. *J. Geophys. Res.*, 115(14):12008.

Nakamura, N. (1993). Momentum flux, flow symmetry, and the nonlinear barotropic governor. *J. Atmos. Sci.*, 50(14):2159–2179.

Nastrom, G. D. and Gage, K. A. (1985). A climatology of atmospheric wavenumber spectra of wind and temperature observed by commercial aircraft. *J. Atmos. Sci.*, 42(9):950–960.

Navarra, A. and Boccaletti, G. (2002). Numerical general circulation experiments of sensitivity to earth rotation rate. *Clim. Dyn.*, 19(5-6):467–483.

Nishizawa, M., Sano, Y., Ueno, Y., and Maruyama, S. (2007). Speciation and isotope ratios of nitrogen in fluid inclusions from seafloor hydrothermal deposits at $\sim$ 3.5 ga. *Earth Planet. Sci. Lett.*, 254:332–344.

O'Gorman, P. A. (2011). The effective static stability experienced by eddies in a moist atmosphere. *J. Atmos. Sci.*, 68:75–90.

O'Gorman, P. A. and Schneider, T. (2007). Recovery of atmospheric flow statistics in a general circulation model without nonlinear eddy-eddy interactions. *Geophys. Res. Lett.*, 34(22):L22801.

O'Gorman, P. A. and Schneider, T. (2008a). Energy in midlatitude transient eddies in idealized simulations of changed climates. *J. Climate*, 21:5797–5806.

O'Gorman, P. A. and Schneider, T. (2008b). The hydrological cycle over a wide range of climates simulated with an idealized GCM. *J. Climate*, 21(15):3815–3832.

O'Gorman, P. A. and Schneider, T. (2008c). Weather-layer dynamics of baroclinic eddies and multiple jets in an idealized general circulation model. *J. Atmos. Sci.*, 65(2):524–535.

Orlanski, I. (1998). Poleward deflection of storm tracks. *J. Atmos. Sci.*, 55:2577–2602.

Orlanski, I. (2003). Bifurcation in eddy life cycles: Implications for storm track variability. *J. Atmos. Sci.*, 60(8):993–1023.

Orr, W. M. F. (1907). The stability or instability of the steady motions of a perfect liquid and of a viscous liquid. part i: A perfect liquid. *Proc. Roy. Ir. Acad.*, 27A:9–68.

Panetta, R. L. (1993). Zonal jets in wide baroclinically unstable regions: Persistence and scale selection. *J. Atmos. Sci.*, 50(14):2073–2106.

Pedlosky, J. (1987). *Geophysical Fluid Dynamics*. New York, Springer-Verlag.

Peixoto, J. P. and Oort, A. H. (1992). *Physics of Climate*. American Institute of Physics.

Phillips, N. A. (1954). Energy transformations and meridional circulations associated with simple baroclinic waves in a two level quasi-geostrophic model. *Telus*, 6(3):273–286.

Phillips, N. A. (1956). The general circulation of the atmosphere: A numerical experiment. *Q. J. R. Meteorol. Soc.*, 82(352):123–164.

Pierrehumbert, R. T., Abbot, D. S., Voigt, A., and Koll, D. (2010). Climate of the neoproterozoic. *Ann. Rev. Earth Planetary Sci.*, 39(1):417.

Prinn, R. G. and Fegley, B. (1987). The atmospheres of Venus, earth, and Mars - A critical comparison. *Ann. Rev. Earth Planetary Sci.*, 15:171–212.

Qiu, B., Scott, R. B., and Chen, S. (2008). Length scales of eddy generation and nonlinear evolution of the seasonally modulated south pacific subtropical countercurrent. *J. Phys. Oceanogr.*, 38:1515.

Randel, W. J. and Held, I. M. (1991). Phase speed spectra of transient eddy fluxes and critical layer absorption. *J. Atmos. Sci.*, 48:688–697.

Read, P. L., Lewis, S. R., and Mulholland, D. P. (2015). The physics of Martian weather and climate: a review. *Rep. Prog. Phys.*, 78(12):125901.

Rhines, P. B. (1975). Waves and turbulence on a beta plane. *J. Fluid Mech.*, 69(03):417–443.

Rhines, P. B. (1977). The dynamics of unsteady currents. *The sea*, 6:189–318.

Rhines, P. B. (1994). Jets. *Chaos*, 4(2):313–339.

Riehl, H., Yeh, T. C., and La Seur, N. E. (1950). A study of variations of the general circulation. *J. of Meteorology*, 7(3):181–194.

Rivera, M. and Wu, X. L. (2000). External dissipation in driven two-dimensional turbulence. *Phys. Rev. Let.*, 85(5):976.

Riviere, G. (2009). Effect of latitudinal variations in low level baroclinicity on eddy life cycles and upper tropospheric wave breaking processes. *J. Atmos. Sci.*, 66(6):1569–1592.

Rivière, G. (2011). A dynamical interpretation of the poleward shift of the jet streams in global warming scenarios. *J. Atmos. Sci.*, 68:1253–1272.

Rivière, P., Treguier, A. M., and Klein, P. (2004). Effects of bottom friction on nonlinear equilibration of an oceanic baroclinic jet. *J. Phys. Oceanogr.*, 34:416.

Robinson, W. A. (1996). Does eddy feedback sustain variability in the zonal index? *J. Atmos. Sci.*, 53(23):3556–3569.

Robinson, W. A. (2000). A baroclinic mechanism for the eddy feedback on the zonal index. *J. Atmos. Sci.*, 57(3):415–422.

Robinson, W. A. (2006). On the self maintenance of midlatitude jets. *J. Atmos. Sci.*, 63(8):2109–2122.

Sagan, C. and Chyba, C. (2010). The early faint sun paradox: Organic shielding of ultraviolet-labile greenhouse gases. *Science*, 276(5316):1217–1221.

Salmon, R. (1978). Two-layer quasi-geostrophic turbulence in a simple special case. *Geophys. Astrophys. Fluid Dyn.*, 10(1):25–52.

Saltzman, B. (1957). Equations governing the energetics of the larger scales of atmospheric turbulence in the domain of wave number. *J. of Meteorology*, 14(6):513–523.

Salyk, C., Ingersoll, A. P., Lorre, J., Vasavada, A., and Del Genio, A. D. (2006). Interaction between eddies and mean flow in Jupiter's atmosphere: Analysis of Cassini imaging data. *Icarus*, 185:430–442.

Sayanagi, K. M., Showman, A. P., and Dowling, T. E. (2008). The emergence of multiple robust zonal jets from freely evolving, three-dimensional stratified geostrophic turbulence with applications to jupiter. *J. Atmos. Sci.*, 65(12):3947–3962.

Schlösser, F. and Eden, C. (2007). Diagnosing the energy cascade in a model of the north atlantic. *Geophys. Res. Lett.*, 34:2604.

Schmidt, G. A., Ruedy, R. A., Miller, R. L., and Lacis, A. A. (2010). Attribution of the present-day total greenhouse effect. *J. Geophys. Res.*, 155.

Schneider, T. (2004). The tropopause and the thermal stratification in the extratropics of a dry atmosphere. *J. Atmos. Sci.*, 61(12):1317–1340.

Schneider, T. (2006). The general circulation of the atmosphere. *Ann. Rev. Earth Planetary Sci.*, 34:655–688.

Schneider, T. and Liu, J. (2009). Formation of jets and equatorial superrotation on Jupiter. *J. Atmos. Sci.*, 66:579–601.

Schneider, T. and Walker, C. C. (2006). Self-organization of atmospheric macroturbulence into critical states of weak nonlinear eddy eddy interactions. *J. Atmos. Sci.*, 63(6):1569–1586.

Schneider, T. and Walker, C. C. (2008). Scaling laws and regime transitions of macroturbulence in dry atmospheres. *J. Atmos. Sci.*, 65:2153–2173.

Scott, R. B. (2001). Evolution of energy and enstrophy containing scales in decaying, two-dimensional turbulence with friction. *Phys. of Fluids*, 13(9):2739–2742.

Scott, R. B. and Arbic, B. K. (2007). Spectral energy fluxes in geostrophic turbulence: Implications for ocean energetics. *J. Phys. Oceanogr.*, 37(3):673–688.

Scott, R. B. and Polvani, L. M. (2007). Forced-dissipative shallow-water turbulence on the sphere and the atmospheric circulation of the giant planets. *J. Atmos. Sci.*, 64(9):3158–3176.

Scott, R. B. and Wang, F. (2005). Direct evidence of an oceanic inverse kinetic energy cascade from satellite altimetry. *J. Phys. Oceanogr.*, 35(9):1650–1666.

Seager, S. (2013). Exoplanet Habitability. *Science*, 340:577–581.

Selsis, F., Kasting, J. F., Levrard, B., Paillet, J., Ribas, I., and Delfosse, X. (2007). Habitable planets around the star Gliese 581? *Astronomy and Astrophys.*, 476:1373–1387.

Shepherd, T. G. (1987a). Rossby waves and two-dimensional turbulence in a large-scale zonal jet. *J. Fluid Mech.*, 183:467–509.

Shepherd, T. G. (1987b). A spectral view of nonlinear fluxes and stationary-transient interaction in the atmosphere. *J. Atmos. Sci.*, 44(8):1166–1147.

Simmons, A. J. (1974). The meridional scale of baroclinic waves. *J. Atmos. Sci.*, 31(6):1515–1525.

Simmons, A. J. and Hoskins, B. J. (1978). The life cycles of some nonlinear baroclinic waves. *J. Atmos. Sci.*, 35(3):414–432.

Smith, K. S. (2007). The geography of linear baroclinic instability in earth's oceans. *J. Mar. Res.*, 65(5):655–683.

Smith, K. S. and Vallis, G. K. (2001). The scales and equilibration of midocean eddies: Freely evolving flow. *J. Phys. Oceanogr.*, 31(2):554–571.

Smith, K. S. and Vallis, G. K. (2002). The scales and equilibration of midocean eddies: Forced-dissipative flow. *J. Phys. Oceanogr.*, 32(6):1699–1720.

Smith, L. T., Chassignet, E. P., and Bleck, R. (2000). The impact of lateral boundary conditions and horizontal resolution on north atlantic water mass transformations and pathways in an isopycnic coordinate ocean model. *J. Phys. Oceanogr.*, 30:137–159.

Som, S. M., Buick, R., Hagadorn, J. W., Blake, T. S., Perreault, J. M., Harnmeijer, J. P., and Catling, D. C. (2016). Earth's air pressure 2.7 billion years ago constrained to less than half of modern levels. *Nature Geoscience*, 9:448–451.

Som, S. M., Catling, D. C., Harnmeijer, J. P., Povlika, P. M., and Buick, R. (2012). Air density 2.7 billion years ago limited to less than twice modern levels by fossil raindrop imprints. *Nature*, 484(7394):359–362.

Son, S.-W. and Lee, S. (2006). Preferred modes of variability and their relationship with climate change. *J. Climate*, 19(10):2063–2075.

Srinivasan, K. and Young, W. R. (2012). Zonostrophic instability. *J. Atmos. Sci.*, 65(9):1633–1656.

Stammer, D. (1997). Global characteristics of ocean variability estimated from regional topex/poseidon altimeter measurements. *J. Phys. Oceanogr.*, 27(8):1743–1769.

Stone, P. H. (1966). On non-geostrophic baroclinic stability. *J. Atmos. Sci.*, 23(4):390–400.

Stone, P. H. (1978). Baroclinic adjustment. *J. Atmos. Sci.*, 35(4):561–571.

Straus, D. M. and Ditlevsen, P. (1999). Two-dimensional turbulence properties of the ecmwf reanalyses. *Tellus*, 51:749.

Theiss, J. (2004). Equatorward energy cascade, critical latitude, and the predominance of cyclonic vortices in geostrophic turbulence. *J. Phys. Oceanogr.*, 34(7):1663–1678.

Theiss, J. (2006). A generalized rhines effect and storms on jupiter. *Geophys. Res. Lett.*, 33(8).

Thompson, A. F. (2010). Jet formation and evolution in baroclinic turbulence with simple topography. *J. Phys. Oceanogr.*, 40(2):257–278.

Thompson, A. F. and Young, W. R. (2006). Scaling baroclinic eddy fluxes: Vortices and energy balance. *J. Phys. Oceanogr.*, 36:720–738.

Thompson, A. F. and Young, W. R. (2007). Two-layer baroclinic eddy heat fluxes: Zonal flows and energy balance. *J. Phys. Oceanogr.*, 64:3214–3231.

Thompson, D. W. J., Wallace, J. M., and Hegerl, G. C. (2000). Annular modes in the extratropical circulation. part II: Trends. *J. Climate*, 13:1018–1036.

Thorncroft, C. D., Hoskins, B. J., and McIntyre, M. E. (1993). Two paradigms of baroclinic-wave life-cycle behaviour. *Q. J. R. Meteorol. Soc.*, 119:17–55.

Thuburn, J. and Craig, G. C. (1997). GCM tests of theories for the height of the tropopause. *J. Atmos. Sci.*, 54:869–882.

Thuburn, J. and Craig, G. C. (2000). Stratospheric Influence on Tropopause Height: The Radiative Constraint. *J. Atmos. Sci.*, 57:17–28.

Tobias, S. M., Dagon, K., and Marston, J. B. (2011). Astrophysical fluid dynamics via direct statistical simulation. *Astrophys. J.*, 727(2):127.

Tobias, S. M. and Marston, J. B. (2013). Direct statistical simulation of out-of-equilibrium jets. *Phys. Rev. Let.*, 110(10):104502.

Treguier, A. M. and Hua, B. L. (1988). Influence of bottom topography on stratified quasi-geostrophic turbulence in the ocean. *Geophys. Astrophys. Fluid Dyn.*, 43:265–305.

Trenberth, K. E. and Solomon, A. (1993). Implications of global atmospheric spatial spectra for processing and displaying data. *J. Climate*, 6:531–545.

Tsang, Y. K. and Young, W. R. (2009). Forced-dissipative two-dimensional turbulence: A scaling regime controlled by drag. *Phys. Rev. E*, 79(4):045308.

Tulloch, R., Marshall, J., Hill, C., and Smith, K. S. (2011). Scales, growth rates, and spectral fluxes of baroclinic instability in the ocean. *J. Phys. Oceanogr.*, 41(6):1057–1076.

Vallis, G. K. (2006). *Atmospheric and Oceanic Fluid Dynamics*. pp. 770. Cambridge University Press, Cambridge, U.K.

Vallis, G. K. and Maltrud, M. E. (1993). Generation of mean flows and jets on a beta plane and over topography. *J. Phys. Oceanogr.*, 23(7):1346–1362.

Vallis, G. K., Zurita-Gotor, P., Cairns, C., and Kidston, J. (2015). Response of the large-scale structure of the atmosphere to global warming. *Q. J. R. Meteorol. Soc.*, 141:1479–1501.

Vasavada, A. R. and Showman, A. P. (2005). Jovian atmospheric dynamics: An update after Galileo and Cassini. *Reports of Progress in Physics*, 68(8):1935–1996.

Venaille, A., Nadeau, L.-P., and Vallis, G. (2014). Ribbon turbulence. *Phys. of Fluids*, 26(12):126605.

Venaille, A., Smith, K. S., and Vallis, G. K. (2011). Baroclinic turbulence in the ocean: Analysis with primitive equation and quasigeostrophic simulations. *J. Phys. Oceanogr.*, 41(9):1605–1623.

Venaille, A., Vallis, G. K., and Griffies, S. M. (2012). The catalytic role of the beta effect in barotropization processes. *J. Fluid Mech.*, 709:490–515.

von Paris, P., Gebauer, S., Godolt, M., Grenfell, J. L., Hedelt, P., Kitzmann, D., Patzer, A. B. C., Rauer, H., and Stracke, B. (2010). The extrasolar planet Gliese 581d: a potentially habitable planet? *Astronomy and Astrophys.*, 522:A23.

von Paris, P., Rauer, H., Lee Grenfell, J., Patzer, B., Hedelt, P., Stracke, B., and Schreier, F. (2008). Warming of the early earth - co2 reconsidered. *Planatary and Space Science*, 56(9):1244–1259.

Walker, C. C. and Schneider, T. (2006). Eddy influences on Hadley circulations: Simulations with an idealized GCM. *J. Atmos. Sci.*, 63:3333–3350.

Williams, G. P. (1978). Planetary circulations: 1. barotropic representation of the Jovian and terrestrial turbulence. *J. Atmos. Sci.*, 35(8):1399–1426.

Williams, G. P. (2003). Jovian dynamics. part iii: Multiple, migrating, and equatorial jets. *J. Atmos. Sci.*, 60(10):1270–1296.

Williams, G. P. and Holloway, J. L. (1982). The range and unity of planetary circulations. *Nature*, 297(5864):295–299.

Wittman, M. A. H., Charlton, A. J., and Polvani, L. M. (2007). The Effect of Lower Stratospheric Shear on Baroclinic Instability. *J. Atmos. Sci.*, 64:479.

Wolf, E. T. and Toon, O. B. (2013). Hospitable archean climates simulated by a general circulation model. *Astrobiology*, 13(7):656–673.

Wolf, E. T. and Toon, O. B. (2014). Controls on the Archean Climate System Investigated with a Global Climate Model. *Astrobiology*, 14:241–253.

Wordsworth, R. and Pierrehumbert, R. (2013). Hydrogen-nitrogen greenhouse warming in earth's early atmosphere. *Science*, 339(6115):64–67.

Wordsworth, R. D., Forget, F., Selsis, F., Madeleine, J.-B., Millour, E., and Eymet, V. (2010). Is Gliese 581d habitable? Some constraints from radiative-convective climate modeling. *Astronomy and Astrophys.*, 522:A22.

Wordsworth, R. D., Forget, F., Selsis, F., Millour, E., Charnay, B., and Madeleine, J.-B. (2011). Gliese 581d is the first discovered terrestrial-mass exoplanet in the habitable zone. *Astrophys. J. Let.*, 733:L48.

Wu, Y., Ting, M., Seager, R., Huang, H., and Cane, M. A. (2010). Changes in storm tracks and energy transports in a warmer climate simulated by the GFDL CM2.1 model. *Clim. Dyn.*, pages 203–222.

Wunsch, C. (1997). The vertical partition of oceanic horizontal kinetic energy. *J. Phys. Oceanogr.*, 27:1770–1794.

Wunsch, C. and Ferrari, R. (2004). Vertical mixing, energy, and the general circulation of the oceans. *Ann. Rev. Fluid Mech.*, 36:281–314.

Yin, J. H. (2005). A consistent poleward shift of the storm tracks in simulations of 21st century climate. *Geophys. Res. Lett.*, 32:L18701.

Yuval, J. and Kaspi, Y. (2016). Eddy Activity Sensitivity to Changes in the Vertical Structure of Baroclinicity. *J. Atmos. Sci.*, 73:1709–1726.

Zurita-Gotor, P. (2008). The sensitivity of the isentropic slope in a primitive equation dry model. *J. Atmos. Sci.*, 65(1):43–65.

Zurita-Gotor, P., Blanco-Fuentes, J., and Gerber, E. P. (2014). The impact of baroclinic eddy feedback on the persistence of jet variability in the two-layer model. *J. Atmos. Sci.*, 71(1):410–429.

Zurita-Gotor, P. and Vallis, G. K. (2009). Equilibration of baroclinic turbulence in primitive equations and quasigeostrophic models. *J. Atmos. Sci.*, 66(4):837–863.